

Modeling and Control of a Dual-Voltage Synchronous Machine

Stanko Gradev

Vollständiger Abdruck der von der Fakultät für Elektrotechnik und Informationstechnik der Technischen Universität München zur Erlangung des akademischen Grades eines

Doktor-Ingenieurs

genehmigten Dissertation.

Vorsitzender: Prof. Dr.-Ing. Klaus Diepold

Prüfer der Dissertation:

1. Prof. Dr.-Ing. Hans-Georg Herzog
2. Prof. Emil Levi, Ph.D.

Die Dissertation wurde am 22.04.2020 bei der Technischen Universität München eingereicht und durch die Fakultät für Elektrotechnik und Informationstechnik am 05.01.2021 angenommen.

Abstract

This dissertation focuses on two main topics in the field of electrical engineering: machine modeling and control development. The thesis makes a contribution in both fields as it introduces a new six-phase dual-voltage machine model and develops a model-based control for the machine.

The dual-voltage electric machine is employed with the goal to supply simultaneously a 12V and a 48V network in a vehicle. The intention of this new machine topology is to replace fully a conventional 48V power supply, which employs a DC/DC converter to enable the bi-directional power flow between the 12V and the 48V sides. The DC/DC converter ensures an independent power transfer between both power supplies. The DC/DC converter decouples the 48V power supply from the dynamics of the 12V power supply or vice versa.

The dual-voltage machine is connected directly to both power supplies and thus both stator systems are strongly coupled to each other. Therefore the power generation at each of both stator systems is influenced by the other one.

An advanced control software is required because of the electromagnetic coupling of both stator systems. The software should be able to decouple the control of each side from the other one. A model-based approach is chosen for the development of the control algorithm. Therefore, a very detailed machine model is required beforehand, which is able to adequately reproduce the behavior of the machine prototype. The model-based control is developed for the dual-voltage machine and designed such, that it counteracts the coupling occurring in the machine air-gap. The scholarly thesis consists of five chapters in total. Chapter 1 and Chapter 5 represent the introduction and the summary. The main body of the thesis is documented in chapters 2, 3 and 4.

Chapter 1 presents the conventional 48V power supply architecture in comparison to the 48V architecture with a dual-voltage machine power supply. The chapter explains the motivation behind the research project and points out the main challenges encompassing the integration of the new dual-voltage machine topology in a 48V power supply.

Chapter 2 explains state of the art modeling principles for three-phase synchronous machines. After a detailed introduction into the modeling of three-phase machines, the model for a six-phase dual-voltage synchronous machine is derived. The derived model is implemented according to two different modeling approaches: the Direct Quadrature (DQ) and Voltage Behind Reactance (VBR) methods. Both models reproduce the dynamics of the dual-voltage machine and include a saturation behavior of the main inductance. The

models are also extended to replicate the iron losses of the machine. At the end of the chapter the presented machine model is parametrized through measurements from the test bench.

Chapter 3 handles the current control design for the dual-voltage machine. In order to achieve a torque control at both stator systems, five current controllers are required. Each current controller should be able to set its current reference independently and should be able to counteract disturbances caused by the electromagnetic coupling. The chapter handles the tuning of the controllers for all five currents (I_{q12V} , I_{d12V} , I_{q48V} , I_{d48V} and I_{fd}). A Field Oriented Control (FOC) is implemented to control the four stator current references. In order to improve the control performance a decoupling network is derived, which improves the control performance. The current controllers are verified in a simulation as well as through measurements on a test bench. The control is implemented on a dSpace Autobox used as a rapid control prototyping environment. Chapter 3 investigates new methods for decoupling control design and presents a new Dynamic Decoupling Matrix (DDM), which is able to counteract the dynamic disturbances resulting from the controller interactions. The DDM is verified successfully in the simulation environment and improves the decoupling control significantly.

Chapter 4 handles the torque and power control development for the dual-voltage machine. The torque control is developed for two control references T_{e12V}^* and T_{e48V}^* . The developed control is based on pre-calculated working points and is verified through simulations and measurements in the Base Speed (BS) range. A comparison between the simulations and the measurements is performed and the observed discrepancies between model and measurements in edge areas are explained through the observed iron losses of the claw-pole machine. Therefore the models from Chapter 2 are extended in the aftermath to replicate the iron losses of the machine. For the Field Weakening (FW) region a new Voltage Angle Control (VAC) is derived for the dual-voltage machine. Based on the rotation of the maximum voltage vectors the new angle control is able to set power references at both stator systems (P_{e12V}^* and P_{e48V}^*). A switching mechanism between both control areas, FOC and VAC, is developed and implemented in the machine control. The VAC and the switching mechanism are verified as well in the simulation as through measurements on the test bench.

Chapter 5 summarizes the findings of the presented work and proposes topics, which can be addressed in some future research.

Acknowledgment

“Logic will get you from A to B. Imagination will take you everywhere.”

Albert Einstein

It is my pleasure to acknowledge several persons, who have each played an important role during my Ph.D. research.

I would like to express my gratitude to my supervisor Univ.-Prof. Dr.-ing. Hans-Georg Herzog for supporting me during the years of my research. The talks and discussions with Prof. Herzog were always constructive and brought different perspective to the solutions of the problems being discussed. Prof. Herzog always encouraged me in critical moments during my research, when decisions about the research direction had to be taken.

I would like to thank the second examiner, Prof. Emil Levi from the John Moores University in Liverpool, for his participation in the examination board and his work in the field of electric machine modeling. His research work on saturation modeling helped me to develop the dual-voltage machine models.

I wish to thank the whole alternator development department at BMW Group, who guided me through my research and enabled the project in terms of financing and hardware procurement. In person I wish to thank to Dr. Friedrich Haslinger, team-lead of the alternator development department. My thanks go also to Daniel Findeisen and Jörg Reuss, supervisors of the research project on the dual-voltage machine topology, for the many technical discussions we have had.

During the years of research, not only professional support was highly appreciated, but also support in my private life. I am thankful to my lovely girlfriend Vera, who supported me to keep going through all the years of my research. I wish to thank also my family. My deepest gratitude goes to my mother, Valentina Popova, and my father, Valkan Popov, who is also an electrical engineer, for encouraging me to finish my research. My thanks go also to my sister Kalina Gradeva for her positivity and supportive nature during all the years.

Stanko Gradev

Munich, April 2020

Contents

List of Figures	V
List of Tables	XI
Nomenclature	XIII
1 Introduction	1
1.1 Project Motivation	1
1.2 Thesis Objective and Structure	3
1.3 Nomenclature	4
2 Machine Modeling	7
2.1 Three-Phase Salient-Pole Machine Model	8
2.1.1 Magnetomotive Forces of a Salient-Pole Machine	8
2.1.2 Deriving Flux Linkages and Inductances	13
2.1.3 Machine Voltage Equations in Stator and Rotor Reference Frame	16
2.1.4 Deriving the Torque Equation	21
2.1.5 Saturation and Cross-Magnetization	23
2.1.6 Direct-Quadrature Axis Model with Saturation	28
2.1.7 Voltage-Behind-Reactance Model with Saturation	30
2.1.8 Mechanical Modeling	33
2.2 Six-Phase Dual-Voltage Salient-Pole Machine Model	34
2.2.1 Six-Phase Dual-Voltage DQ Machine Model	34
2.2.2 Six-Phase Dual-Voltage VBR Model	42
2.3 Iron Losses Modeling	44
2.3.1 Iron Losses in the DQ Equivalent Circuit	45
2.3.2 DQ Model Formulation with Iron Losses	48
2.3.3 VBR Formulation with Iron Losses	50
2.4 Model Parametrization with Measurements	52
3 Current Control Design	63
3.1 Introduction into Feedback Control	64
3.1.1 Stability of a Closed Loop	64
3.1.2 State Space Representation	67
3.1.3 Loop Shaping Design	68

3.2	Current Control for the Dual-Voltage Machine	72
3.2.1	Inverse-Based Controller Design	73
3.2.2	Tuning the Proportional Integral (PI) Controllers	78
3.2.3	PI Control Implementation	81
3.2.4	Simulation Results	85
3.2.5	Static Decoupling Action	90
3.2.6	Simulation Results Summary of the Controller Tests	97
3.2.7	Measurement Setup	99
3.2.8	Measurements in a Current Control Loop	102
3.2.9	Conclusion from the Simulation and Measurement Results	108
3.2.10	Dynamic Decoupling	110
4	Torque and Power Control Development	121
4.1	Torque Control - State of the Art	122
4.1.1	Torque Control in the BS Range for an EESM	123
4.1.2	Torque Control in the FW Range for an EESM	130
4.2	Torque Control in the BS Range for the Dual-Voltage Machine	140
4.3	Torque Control in the FW Range for the Dual-Voltage Machine	148
4.3.1	Torque Control Based with Linear Parameters	148
4.3.2	Torque Control with Non-Linear Parameters	154
4.4	Simulations and Measurements in the BS Range	162
4.4.1	Optimal Currents for a 12V Torque Reference	164
4.4.2	Optimal Currents for a 48V Torque Reference	166
4.4.3	Analysis Summary of the Optimal Current References	169
4.4.4	Torque Control Simulations in the BS Range	170
4.4.5	Torque Control Measurements in the BS Range	174
4.4.6	Summary of the Torque Control Results in the BS Range	180
4.5	Power Control - Voltage Angle Control in the Field-Weakening Range	181
4.5.1	Voltage Angle Control Theory	183
4.5.2	Switching Method between the FOC and the VAC	193
4.5.3	Simulations Results with the Voltage Angle Control	196
4.5.4	Measurement Results with the Voltage Angle Control	200
5	Summary and Outlook	205
5.1	Summary	205
5.2	Outlook	208
A	Calculating Inductances of a Three-Phase Machine	209
A.1	Deriving the Inductances of a Three-Phase Linear Machine Model	209
A.2	Saturation of the Main Inductance	215
B	Deriving State Space Representation for the Dual-Voltage Machine	217
C	Tuning the Current Control Loops - Parameters and Nyquist Plots	221

D Simulation Results of the Controller Tests	225
E Star Point Current Controller - Tuning and Simulations	229
F Offline Calculated Working Points	233
References	235

List of Figures

1.1	Conventional 48V Architecture Employing a DC/DC Converter	2
1.2	Dual-Voltage Machine Architecture Eliminating a DC/DC converter	2
2.1	Schematic Drawing of a Three-Phase Salient-Pole Machine	8
2.2	Three-Phase ABC Equivalent Circuit	9
2.3	Three-Phase $d-q$ Equivalent Circuit	22
2.4	Two Coupled Inductors	22
2.5	B-H Curve	23
2.6	Slope of a Saturation Curve	24
2.7	Sat. Curve $i_{md} = F(\lambda_{md})$	24
2.8	Three-Phase DQ Model Overview	29
2.9	Three-Phase VBR Model Overview	31
2.10	Schematic Drawing of a Dual-Voltage Salient-Pole Machine	35
2.11	ABC -Schematic of the Dual-Voltage Salient-Pole Machine	36
2.12	Six-Phase DQ Model Overview	37
2.13	$d-q$ Equivalent Circuit of the Dual-Voltage Machine	38
2.14	Six-Phase VBR Model Overview	43
2.15	Six-Phase DQ Equivalent Circuit with Iron Losses	45
2.16	Six-Phase DQ Model Overview with Iron Losses	49
2.17	Six-Phase VBR Model Overview with Iron Losses	50
2.18	q Voltages over i_{fd}	57
2.19	Calc. d -flux	57
2.20	Calc. q -flux	57
2.21	Magn. Flux 12V and 48V over i_{fd}	57
2.22	Aprox. vs. Meas. Flux 48V	58
2.23	Aprox. vs. Meas. Magn. Flux 12V	58
2.24	L_{ls2} over i_{ds2}	58
2.25	$v_{ds1}(i_{qs1}), v_{ds2}(i_{qs1})$ @ $i_{fd} = 1,5$ A	58
2.26	Iron Loss Power at No-Load	60
2.27	Loss Torque at No-Load	60
2.28	Iron Loss Voltage at No-Load	60
2.29	Iron Loss Resistance Look-Up-Table (LUT)(i_{fd}, n_{rpm})	60
2.30	Resistance LUT(λ_{md1}, n_{rpm})	61
2.31	Simulated Back-Emf Voltage	61
2.32	Simulated Iron Losses	61
2.33	Simulated Iron Loss Torque	61

2.34	Simulation of the Controlled Dual-Voltage Machine with Power Electronics	61
3.1	Signal flow diagram of a control loop	64
3.2	Bode Plot of $G_0(s) = \frac{K_p(1-4s)}{s(1+2s)(1+3s)}$	67
3.3	Nyquist Plot of $G_0(s) = \frac{K_p(1-4s)}{s(1+2s)(1+3s)}$	67
3.4	Signal Flow Diagram of a Control Loop with Disturbance and Noise	69
3.5	PI-Controller for a Plant with Two First Order Low-Pass Transfer Functions	70
3.6	Current Control Loop	74
3.7	Nyquist Plot of the Open Loop (OL) Transfer Function i_{qs1}	80
3.8	Nyquist Plot of the Closed Loop (CL) Transfer Function i_{qs1}	80
3.9	Tuning the Decentralized PI Controllers	81
3.10	PI Controllers with Decoupling	84
3.11	Simulation @0rpm: $i_{qs1} = 100$ A, $i_{ds1} = 0$ A, $i_{qs2} = 0$ A, $i_{ds2} = 0$ A and $i_{fd} = 0$ A MO Tuning	86
3.12	Simulation @0rpm: $i_{qs1} = 0$ A, $i_{ds1} = 0$ A, $i_{qs2} = 100$ A, $i_{ds2} = 0$ A and $i_{fd} = 0$ A MO Tuning	87
3.13	Simulation @0rpm: $i_{qs1} = 0$ A, $i_{ds1} = 0$ A, $i_{qs2} = 0$ A, $i_{ds2} = 0$ A and $i_{fd} = 2$ A MO Tuning	88
3.14	Simulation @1000rpm: $i_{qs1} = 100$ A, $i_{ds1} = 0$ A, $i_{qs2} = 0$ A, $i_{ds2} = 0$ A and $i_{fd} = 0$ A MO Tuning	89
3.15	Simulation @1000rpm: $i_{qs1} = 0$ A, $i_{ds1} = 0$ A, $i_{qs2} = 100$ A, $i_{ds2} = 0$ A and $i_{fd} = 0$ A MO Tuning	89
3.16	Simulation @1000rpm: $i_{qs1} = 0$ A, $i_{ds1} = 0$ A, $i_{qs2} = 0$ A, $i_{ds2} = 0$ A and $i_{fd} = 2$ A MO Tuning	90
3.17	Simulation @1000rpm: $i_{qs1} = 100$ A, $i_{ds1} = 0$ A, $i_{qs2} = 0$ A, $i_{ds2} = 0$ A and $i_{fd} = 0$ A MO with a Decoupling Network (DN) $L(I_{act})$	92
3.18	Simulation @1000rpm: $i_{qs1} = 0$ A, $i_{ds1} = 0$ A, $i_{qs2} = 100$ A, $i_{ds2} = 0$ A and $i_{fd} = 0$ A MO with a DN $L(I_{act})$	92
3.19	Simulation @1000rpm: $i_{qs1} = 0$ A, $i_{ds1} = 0$ A, $i_{qs2} = 0$ A, $i_{ds2} = 0$ A and $i_{fd} = 2$ A MO with a DN $L(I_{act})$	93
3.20	Simulation @1000rpm: $i_{qs1} = 100$ A, $i_{ds1} = -50$ A, $i_{qs2} = 0$ A, $i_{ds2} = 0$ A and $i_{fd} = 2$ A MO-FN $L(I_{rqst})$	94
3.21	Simulation @1000rpm: $i_{qs1} = 0$ A, $i_{ds1} = 0$ A, $i_{qs2} = 100$ A, $i_{ds2} = -50$ A and $i_{fd} = 2$ A MO-FN $L(I_{rqst})$	96
3.22	Simulation @1000rpm: $i_{qs1} = 100$ A, $i_{ds1} = -50$ A, $i_{qs2} = 100$ A, $i_{ds2} = -50$ A and $i_{fd} = 2$ A MO-FN $L(I_{rqst})$	97
3.23	Simulation @1000rpm: $i_{qs1} = -100$ A, $i_{ds1} = -50$ A, $i_{qs2} = 100$ A, $i_{ds2} = -50$ A and $i_{fd} = 2$ A MO-FN $L(I_{rqst})$	98
3.24	Test Bench Schematic	102
3.25	Measurements @1000rpm: $i_{qs1} = 100$ A, $i_{ds1} = -50$ A, $i_{qs2} = 0$ A, $i_{ds2} = 0$ A and $i_{fd} = 2$ A MO with a Feedforward Network (FN)	104
3.26	Measurements @1000rpm: $i_{qs1} = 0$ A, $i_{ds1} = 0$ A, $i_{qs2} = 100$ A, $i_{ds2} = -50$ A and $i_{fd} = 2$ A MO with a FN	105

3.27	Measurements @1000rpm: $i_{qs1} = 100$ A, $i_{ds1} = -50$ A, $i_{qs2} = 100$ A, $i_{ds2} = -50$ A and $i_{fd} = 2$ A MO with a FN	107
3.28	Measurements @1000rpm: $i_{qs1} = -100$ A, $i_{ds1} = -50$ A, $i_{qs2} = 100$ A, $i_{ds2} = -50$ A and $i_{fd} = 2$ A MO with a FN	108
3.29	Example a Two-Input Two-Output (TITO) Plant with Decoupling Controller	112
3.30	Signal Flow Diagram of a Controller with a Pre-Compensator	113
3.31	Current Control Signal Flow Diagram with a Pre-Compensator	113
3.32	Simulation @1000rpm: $i_{qs1} = 100$ A, $i_{ds1} = -50$ A, $i_{qs2} = 0$ A, $i_{ds2} = 0$ A and $i_{fd} = 2$ A MO with a DDM (Stator) $L(I_{rqst})$	117
3.33	Simulation @1000rpm: $i_{qs1} = 0$ A, $i_{ds1} = 0$ A, $i_{qs2} = 100$ A, $i_{ds2} = -50$ A and $i_{fd} = 2$ A MO with a DDM (Stator) $L(I_{rqst})$	117
3.34	Simulation @1000rpm: $i_{qs1} = 100$ A, $i_{ds1} = -50$ A, $i_{qs2} = 100$ A, $i_{ds2} = -50$ A and $i_{fd} = 2$ A MO with a DDM (Stator) $L(I_{rqst})$	118
3.35	Simulation @1000rpm: $i_{qs1} = -100$ A, $i_{ds1} = -50$ A, $i_{qs2} = 100$ A, $i_{ds2} = -50$ A and $i_{fd} = 2$ A MO with a DDM (Stator) $L(I_{rqst})$	119
3.36	Simulation @1000rpm: $i_{qs1} = -100$ A, $i_{ds1} = -50$ A, $i_{qs2} = 100$ A, $i_{ds2} = -50$ A and $i_{fd} = 2$ A MO with a DDM (Stator) $L(I_{rqst})$	119
4.1	Constant Torque Curves and Constant Current Curves	124
4.2	Constant Torque Curves and Maximum Torque-per-Ampere (MTPA) Curves with i_{fd} as a Parameter	126
4.3	Illustration of the Maximum Torque-per-Copper Losses (MTPCL) Curve in 2-D and 3-D	128
4.4	Constant Torque Surfaces in 3-D	129
4.5	Constant Torque Curves and Voltage Ellipses for $i_{fd}=2$ A	132
4.6	Maximum Torque-per-Voltage (MTPV) for a Fixed Field Winding Current	136
4.7	Maximum Torque-per-Voltage (MTPV) Curves for Two Different Field Winding Currents, $i_{fd} = 1$ A and 3 A	137
4.8	MTPV Trajectory with a Variable Field Winding Current i_{fd}	139
4.9	Constant Torque Lines for T_{e12V} and T_{e48V} at $i_{fd} = 2$ A	143
4.10	Voltage Ellipses for the Dual-Voltage Machine, $i_{fd} = 2$ A and $n_{rpm} = 4500$ rpm and zero torque control	150
4.11	Voltage Ellipses for the Dual-Voltage Machine, $i_{fd} = 2$ A and $n_{rpm} = 4500$ rpm and generative torque control	151
4.12	Voltage Ellipses for the Dual-Voltage Machine, $i_{fd} = 2$ A and $n_{rpm} = 4500$ rpm and motoring torque control	153
4.13	Working Points	160
4.14	Voltage Ellipses at variable Direct Current (DC) Link Voltages	161
4.15	Working Points for MTPCL: 12V Currents	164
4.16	MTPCL: 12V Cross Reluctance Torque	165
4.17	MTPCL: 12V Reluctance Torque	165
4.18	Working Points for MTPCL: I_{exc}	167
4.19	Working Points for MTPCL: 48V Currents	167

4.20	MTPCL: 48V Cross Reluctance Torque	168
4.21	MTPCL: 48V Reluctance Torque	169
4.22	MTPCL Simulation @1000rpm: $T_{e12V} = -8 \text{ Nm}$, $T_{e48V} = -20 \text{ Nm}$	170
4.23	MTPCL Simulation @1000rpm: $T_{e12V} = 8 \text{ Nm}$, $T_{e48V} = -20 \text{ Nm}$	171
4.24	MTPCL Simulation @1000rpm: $T_{e12V} = -8 \text{ Nm}$, $T_{e48V} = 20 \text{ Nm}$	172
4.25	MTPCL Simulation @1000rpm: $T_{e12V} = -8 \text{ Nm}$, $T_{e48V} = 8 \text{ Nm}$	173
4.26	Simulations for MTPCL: $T_{LV,act}$	174
4.27	Simulations for MTPCL: $T_{HV,act}$	174
4.28	Measurements @1000rpm: $T_{e12V} = -8 \text{ Nm}$, $T_{e48V} = -20 \text{ Nm}$ MTPCL Control	175
4.29	Measurements @1000rpm: $T_{e12V} = 8 \text{ Nm}$, $T_{e48V} = -20 \text{ Nm}$ MTPCL Control	176
4.30	Measurements @1000rpm: $T_{e12V} = -8 \text{ Nm}$, $T_{e48V} = 20 \text{ Nm}$ MTPCL Control	177
4.31	Measurements @1000rpm: $T_{e12V} = -8 \text{ Nm}$, $T_{e48V} = 8 \text{ Nm}$ MTPCL Control	178
4.32	Measurements for Torque Control MTPCL: T_{meas}	179
4.33	Measurements for Torque Control MTPCL: T_{meas}	179
4.34	Measurements for Torque Control MTPCL: $T_{meas,err} = T_{emech} - (Te_{LV}^* + Te_{HV}^*)$ [Nm]	180
4.35	Angle Control Principle with 12V and 48V Voltage Vectors	184
4.36	Power as a Function of the Voltage Angles.	189
4.37	Power as Function of Voltage Angles.	191
4.38	Block Diagram Power Voltage Angle Control	192
4.39	Activation and Deactivation of the VAC based on M_{idx}	193
4.40	Switching Mechanism between FOC and VAC	193
4.41	Transition from VAC to FOC	194
4.42	Transition from VAC to FOC	194
4.43	PI Controller with a Pre-Charge Function	195
4.44	Working Points for MPPF: I_{exc}	197
4.45	VAC Simulation @3000rpm: $P_{e12V} = 0 \text{ W}$, $P_{e48V} = -4000 \text{ W}$	198
4.46	VAC Simulation @3000rpm: $P_{e12V} = -1000 \text{ W}$, $P_{e48V} = -4000 \text{ W}$	199
4.47	Voltage Angle Control Measurement @3000rpm: $P_{e12V} = 0 \text{ W}$, $P_{e48V} = -4000 \text{ W}$	201
4.48	Voltage Angle Control Measurement @3000rpm: $P_{e12V} = -1000 \text{ W}$, $P_{e48V} = -4000 \text{ W}$	203
A.1	Schematic Drawing of a Three-Phase Salient-Pole machine	210
C.1	Nyquist Plot of the Open Loop Transfer Function i_{ds1}	223
C.2	Nyquist Plot of the Closed Loop Transfer Function	223
C.3	Nyquist Plot of the Open Loop Transfer Function i_{qs2}	223
C.4	Nyquist Plot of the Closed Loop Transfer Function	223
C.5	Nyquist Plot of the Open Loop Transfer Function i_{ds2}	224
C.6	Nyquist Plot of the Closed Loop Transfer Function	224
C.7	Nyquist Plot of the Open Loop Transfer Function i_{fd}	224
C.8	Nyquist Plot of the Closed Loop Transfer Function	224

D.1	Simulation @1000rpm: $i_{qs1} = 0$ A, $i_{ds1} = 0$ A, $i_{qs2} = 100$ A, $i_{ds2} = 0$ A and $i_{fd} = 0$ A MO Tuning	225
D.2	Simulation @1000rpm: $i_{qs1} = 100$ A, $i_{ds1} = 0$ A, $i_{qs2} = 0$ A, $i_{ds2} = 0$ A and $i_{fd} = 0$ A MO Tuning	225
D.3	Simulation @1000rpm: $i_{qs1} = 0$ A, $i_{ds1} = 0$ A, $i_{qs2} = 0$ A, $i_{ds2} = 0$ A and $i_{fd} = 2$ A MO Tuning	225
D.4	Simulation @1000rpm: $i_{qs1} = 0$ A, $i_{ds1} = 0$ A, $i_{qs2} = 100$ A, $i_{ds2} = 0$ A and $i_{fd} = 0$ A MO with a DN $L(I_{act})$	226
D.5	Simulation @1000rpm: $i_{qs1} = 100$ A, $i_{ds1} = 0$ A, $i_{qs2} = 0$ A, $i_{ds2} = 0$ A and $i_{fd} = 0$ A MO with a DN $L(I_{act})$	226
D.6	Simulation @1000rpm: $i_{qs1} = 0$ A, $i_{ds1} = 0$ A, $i_{qs2} = 0$ A, $i_{ds2} = 0$ A and $i_{fd} = 2$ A MO with a DN $L(I_{act})$	226
D.7	Simulation @1000rpm: $i_{qs1} = 0$ A, $i_{ds1} = 0$ A, $i_{qs2} = 100$ A, $i_{ds2} = 0$ A and $i_{fd} = 0$ A MO with a DN $L(I_{rqst})$	226
D.8	Simulation @1000rpm: $i_{qs1} = 100$ A, $i_{ds1} = 0$ A, $i_{qs2} = 0$ A, $i_{ds2} = 0$ A and $i_{fd} = 0$ A MO with a DN $L(I_{rqst})$	226
D.9	Simulation @1000rpm: $i_{qs1} = 0$ A, $i_{ds1} = 0$ A, $i_{qs2} = 0$ A, $i_{ds2} = 0$ A and $i_{fd} = 2$ A MO with a DN $L(I_{rqst})$	227
D.10	Simulation @1000rpm: $i_{qs1} = 0$ A, $i_{ds1} = 0$ A, $i_{qs2} = 100$ A, $i_{ds2} = 0$ A and $i_{fd} = 0$ A MO-FN $L(I_{rqst})$	227
D.11	Simulation @1000rpm: $i_{qs1} = 100$ A, $i_{ds1} = 0$ A, $i_{qs2} = 0$ A, $i_{ds2} = 0$ A and $i_{fd} = 0$ A MO-FN $L(I_{rqst})$	227
D.12	Simulation @1000rpm: $i_{qs1} = 0$ A, $i_{ds1} = 0$ A, $i_{qs2} = 0$ A, $i_{ds2} = 0$ A and $i_{fd} = 2$ A MO-FN $L(I_{rqst})$	227
D.13	Simulation @1000rpm: $i_{qs1} = 0$ A, $i_{ds1} = 0$ A, $i_{qs2} = 100$ A, $i_{ds2} = 0$ A and $i_{fd} = 0$ A MO with a DDM (Stator) $L(I_{rqst})$	227
D.14	Simulation @1000rpm: $i_{qs1} = 100$ A, $i_{ds1} = 0$ A, $i_{qs2} = 0$ A, $i_{ds2} = 0$ A and $i_{fd} = 0$ A MO with a DDM (Stator) $L(I_{rqst})$	228
D.15	Simulation @1000rpm: $i_{qs1} = 0$ A, $i_{ds1} = 0$ A, $i_{qs2} = 0$ A, $i_{ds2} = 0$ A and $i_{fd} = 2$ A MO with a DDM (Stator) $L(I_{rqst})$	228
D.16	Simulation @1000rpm: $i_{qs1} = 0$ A, $i_{ds1} = 0$ A, $i_{qs2} = 100$ A, $i_{ds2} = 0$ A and $i_{fd} = 0$ A MO with a DDM $L(I_{rqst})$	228
D.17	Simulation @1000rpm: $i_{qs1} = 100$ A, $i_{ds1} = 0$ A, $i_{qs2} = 0$ A, $i_{ds2} = 0$ A and $i_{fd} = 0$ A MO with a DDM $L(I_{rqst})$	228
D.18	Simulation @1000rpm: $i_{qs1} = 0$ A, $i_{ds1} = 0$ A, $i_{qs2} = 0$ A, $i_{ds2} = 0$ A and $i_{fd} = 2$ A MO with a DDM $L(I_{rqst})$	228
E.1	Dual-Voltage Machine with a Star Point Connected to 12V+	229
E.2	Star Point Current Control Loop	230
E.3	Controller Test: $i_{0s2} = 100$ A, $I_{12V,DC}^{ref} = -300$ A.	231
E.4	Controller Test: $I_{48V,DC} = -100$ A, $I_{12V,DC}^{ref} = 300$ A.	231
F.1	MTPCL: 12V Cross Reluctance Left Right Torques	233

List of Figures

F.2 MTPCL: 48V Cross Reluctance Left Right Torques 234

List of Tables

2.1	Machine Model Parameters	59
3.1	Controller Parameters	80

Nomenclature

The most commonly used symbols are listed here. Symbols used but not listed here are clarified in their respective contexts.

List of Abbreviations

Abbreviation	Description
AC	Air Conditioning
AGM	Absorbent Glass Mat
BEV	Battery Electric Vehicle
BS	Base Speed
CAN	Control Area Network
CC	Coupled-Circuit
CL	Closed Loop
CO ₂	Carbon Dioxide
DC	Direct Current
DC/DC	Direct-Current to Direct-Current
DDM	Dynamic Decoupling Matrix
DLRO	Digital Low Resistance Ohmmeter
DN	Decoupling Network
DOF	Degree-of-Freedom
DQ	Direct Quadrature
EC	European Commission
EDC	Electronic Damper Control
EESM	Externally-Excited Synchronous Machine
EHC	Electrically Heated Catalyst
emf	electromotive force
EPS	Electric Power Steering
EU	European Union
FEA	Finite Element Analysis

(Abbreviations continued)

Abbreviation	Description
FEM	Finite Element Method
FN	Feedforward Network
FOC	Field Oriented Control
FPGA	Field-Programmable Gate Array
FW	Field Weakening
GA	Genetic Algorithm
GM	Gain Margin
HIL	Hardware in the Loop
HS	High-Side
HV	High Voltage
ICE	Internal Combustion Engine (ICE)
IM	Induction Machine (IM)
IMC	Internal Model Control
IPM	Interior Permanent Magnet
IPMSM	Interior Permanent Magnet Synchronous Machine
KKT	Karush-Kuhn-Tucker
LS	Low-Side
LUT	Look-Up-Table
LV	Low Voltage
MCU	Motor Control Unit
MIL	Model in the Loop
MIMO	Multiple-Input Multiple-Output
MMF	Magnetomotive Force
mmf	magnetomotive force
MO	Modulus Optimum
MOSFET	Metal-Oxide-Semiconductor Field-Effect Transistor (MOSFET)
MSA	Motor Start-Stop Automatic
MTPA	Maximum Torque-per-Ampere
MTPCL	Maximum Torque-per-Copper Losses
MTPF	Maximum Torque-per-Flux
MTPV	Maximum Torque-per-Voltage
OEM	Original Equipment Manufacturer (OEM)
OL	Open Loop

(Abbreviations continued)

Abbreviation	Description
P	Proportional
PD	Proportional Derivative
PHEV	Plug-in Hybrid Electric Vehicle
PHS	Peripheral High Speed
PI	Proportional Integral
PID	Proportional Integral Derivative
PLECS	Piecewise-Linear Electrical Circuit Simulation
PM	Phase Margin
PMSM	Permanent-Magnet Synchronous Machine (PMSM)
PTC	Positive Temperature Coefficient Heater
PWM	Pulse Width Modulation
QD	Quadrature Direct
RCP	Rapid Control Prototyping
RDE	Real Driving Emissions
RHP	Right-Half Plane
SCR	Single Current Controller
SISO	Single-Input Single-Output
SM	Synchronous Machine
SO	Symmetrical Optimum
SOC	State of Charge
SOSC	Second-Order-Sufficient Condition
SSFR	Standstill Frequency-Response
SVM	Space Vector Modulation
SW	Software
SynRM	Synchron Reluctance Machine
TFC	Torque Flux Control
TITO	Two-Input Two-Output
VAC	Voltage Angle Control
VBR	Voltage Behind Reactance
VCC	Vector Current Control

Symbols

Symbol	Description	Unit
Constants		
μ_0	permeability of the air = $4\pi \cdot 10^{-7}$	$\frac{T \cdot m}{A}$

Mathematical Symbols

λ	Lagrange multiplier for equality condition
s	Laplace operator
μ	Lagrange multiplier for inequality condition
p	Heaviside's operator

Six-Phase Machine Modeling - Parameters

α_{12}	displacement angle between stator 1 and stator 2	
L_{dd1}	d -axis inductance referred to stator 1	H
L_{ls1}	leakage stator inductance for system 1 (12V)	H
L_{ls2}	leakage stator inductance for system 2 (48V)	H
$L_{md1,0}$	unsaturated magnetizing inductance	Wb
L_{qd1}	cross-magnetizing inductance between q - and d -axis referred to stator 1	H
L_{qq1}	q -axis inductance referred to stator 1	H
N_{sf1}	effective number of turns ratio from rotor to stator 1 $N_{s1f} = \frac{N_{s1}}{N_f}$	
N_{s1}	effective number of turns for stator 1	
N_{s1f}	effective number of turns ratio from stator 1 to rotor $N_{s1f} = \frac{N_{s1}}{N_f}$	
N_{s12}	effective number of turns ratio from stator 1 to 2 $N_{s12} = \frac{N_{s1}}{N_{s2}}$	
N_{s2}	effective number of turns for stator 2	
N_{s2f}	effective number of turns ratio from stator 2 to f $N_{s2f} = \frac{N_{s2}}{N_f}$	
r_{s1}	stator winding resistance of stator system 1 (12V)	Ω
r_{s2}	stator winding resistance of stator system 2 (48V)	Ω

Six-Phase Machine Modeling - Quantities

i_{ds1}	d -axis stator current for system 1 (12V)	A
i_{ds2}	d -axis stator current for system 2 (48V)	A
i'_{ds2}	d -axis stator current for system 2 (48V) referred to stator 1 (12V)	A

(Symbols continued)

Symbol	Description	Unit
i_{mdfe1}	d -axis iron loss current referred to stator 1 (12V)	A
i_{mqfe1}	q -axis iron loss current referred to stator 1 (12V)	A
i_{qs1}	q -axis stator current for system 1 (12V)	A
i_{qs2}	q -axis stator current for system 2 (48V)	A
i'_{qs2}	q -axis stator current for system 2 (48V) referred to stator 1 (12V)	A
i_{0s1}	0-axis stator current for system 1 (12V)	A
i_{0s2}	0-axis stator current for system 2 (48V)	A
λ_{mag1}	magnetizing flux generated by the permanent magnets in the rotor referred to stator 1 (12V)	Wb
λ_{md1}	d -magnetizing flux referred to stator 1 (12V)	Wb
λ_{md2}	d -magnetizing flux referred to stator 1 (48V)	Wb
λ_{mq1}	q -magnetizing flux referred to stator 1 (12V)	Wb
λ_{mq2}	q -magnetizing flux referred to stator 1 (48V)	Wb
T_{e1}	electromagnetic torque for stator system 1 (12V)	Nm
T_{e2}	electromagnetic torque for stator system 2 (48V)	Nm
v_{ds1}	d -axis stator voltage for system 1 (12V)	V
v_{ds2}	d -axis stator voltage for system 2 (48V)	V
v_{qs1}	q -axis stator voltage for system 1 (12V)	V
v_{qs2}	q -axis stator voltage for system 2 (48V)	V

Three-Phase Modeling - Parameters

g	air-gap length	m
L_d	linear d -axis inductance	H
L_{dd}	d -axis stator inductance	H
l	axial length of stator	m
L_{lf}	rotor leakage inductance	H
L_{ls}	stator leakage inductance	H
\mathbf{L}_{mi}	incremental inductance matrix describing the saturation and cross-saturation	H
L_q	linear q -axis inductance	H
L_{qq}	q -axis stator inductance	H
N_f	effective number of turns for the field winding	
N_p	maximum turns density for the sinusoidal winding distribution	rad ⁻¹
N_s	effective number of turns for the stator winding	
ϕ_r	angle from f_q -axis in counterclockwise manner	rad
ϕ_s	angle from u_s -axis in counterclockwise manner	rad
\mathbf{P}_m	permutation matrix for back-emf d - q cross-coupling	
p	number of poles pairs	

(Symbols continued)

Symbol	Description	Unit
P	number of poles	
r_{fd}	field winding resistance	Ω
r	mean air-gap radius	m
r_s	stator winding resistance	Ω

Saturation Modeling

α	anisotropic factor: $\alpha = \sqrt{\frac{L_{qq1}}{L_{dd1}}}$	
f_T	form factor of the saturation curve	
$\lambda_{mT,LV}$	transition magnetizing flux	Wb
λ_T	transition magnetizing flux	Wb
L_{md1s}	saturated magnetizing inductance	Wb
L_{mds}	saturated d -axis magnetizing inductance	H
L_{md0}	unsaturated d -axis magnetizing inductance	H

Three-Phase Machine Modeling - Quantities

F	viscous friction	Nm · s
i_{ds}	d -axis stator current	A
i_{fd}	field winding current	A
i_m	magnetizing current	A
i_{mag}	magnetizing current offset due to the permanent magnets	A
i_{md}	d -magnetizing current	A
i_{mdfe1}	q -axis magnetizing iron loss current	A
i_{mqfe1}	q -axis magnetizing iron loss current	A
i_{qs}	q -axis stator current	A
i_{0s}	0-axis stator current	A
J	inertia	kg · m ²
λ_{ls}	leakage stator flux	Wb
λ_m	magnetizing flux	Wb
λ_{md}	d -magnetizing flux	Wb
λ_{mf}	rotor magnetizing flux	Wb
λ_{mq}	q -magnetizing flux	Wb
n_{rpm}	mechanical speed in rounds per minute	$\frac{1}{\text{min}}$
τ_T	form factor for the saturation curve	
T_e	electromagnetic torque	Nm
θ_m	mechanical rotor position	rad
θ_r	rotor displacement	rad
T_m	mechanical torque	Nm

(Symbols continued)

Symbol	Description	Unit
v_{ds}	d -axis stator voltage	V
v_{qs}	q -axis stator voltage	V
v_{fd}	field winding voltage	V
ω_e	electrical angular speed	$\frac{\text{rad}}{\text{s}}$
ω_m	mechanical angular speed	$\frac{\text{rad}}{\text{s}}$
ω_r	rotor angular speed	$\frac{\text{rad}}{\text{s}}$

VBR Modeling

\mathbf{R}_m	matrix describing the inductive terms
\mathbf{L}_m	matrix describing the resistive terms
$\mathbf{e}_{abc,12f}$	back-emf voltage vector

Control Theory - Symbols

M_{idx}	modulation index	
K_p	proportional factor	
$L(j\omega)$	transfer function around a closed loop	
ω_{180}	phase crossover frequency	Hz
ω_c	gain crossover frequency	Hz
ω_b	bandwidth frequency	Hz
T_1	large time constant for modulus optimum	s
T_σ	small time constant for modulus optimum	s
K_s	plant gain	
K_r	controller gain	
T_n	time constant of the PI controller	s
t_r	rise time	s
$T_{sw,ph}$	switching time for the inverter phase currents	s
$T_{sw,f}$	switching time for the inverter field winding current	s
$K_p^{\omega_b}$	proportional factor after the Modulus Optimum criterion for a certain closed loop bandwidth ω_b	
$K_{i\omega_b}$	integral factor after the Modulus Optimum criterion for a certain closed loop bandwidth ω_b	
K_i	integral factor	
T_s	sampling time	s
β_{fw}	field weakening angle β_{fw}	
β_1	VAC field weakening angle for stator 1 (12V)	rad
β_2	VAC field weakening angle for stator 2 (48V)	rad
α_1	voltage angle for stator 1 (12V)	

(Symbols continued)

Symbol	Description	Unit
α_2	voltage angle for stator 2 (48V)	
α	VAC field weakening angle	rad
β_1^{FW}	VAC field weakening angle for stator 1 (12V)	rad
β_2^{FW}	VAC field weakening angle for stator 2 (48V)	rad

Control Theory - Plant Matrices

$\mathbf{G}_p(s)$	plant model matrix for the dual-voltage machine - relates voltages to currents: $\mathbf{i}_{s,\text{qd},12\text{f}} = \mathbf{G}_p(s)\mathbf{v}_{s,\text{qd},12\text{f}}$
$\mathbf{G}_p^{-1}(s)$	inverse plant model matrix for the dual-voltage machine - relates currents to voltages: $\mathbf{v}_{s,\text{qd},12\text{f}} = \mathbf{G}_p^{-1}(s)\mathbf{i}_{s,\text{qd},12\text{f}}$
$\mathbf{G}_{p,\text{dyn},\text{dcpl}}(s)^{-1}$	inverse dynamic decoupling matrix for the dual-voltage machine
$\mathbf{G}_{p,\text{stat},\text{dcpl}}(s)^{-1}$	static decoupling matrix for the dual-voltage machine
$\mathbf{G}_{p,\text{diag}}(s)^{-1}$	inverse diagonal matrix for the dual-voltage machine
$\mathbf{G}_{p,\text{inv}}(s)$	matrix plant model of the inverter for the dual-voltage machine
$\mathbf{G}_{c,\text{PI}}(s)$	PI current controller matrix for the dual-voltage machine
$\mathbf{G}_{c,\text{diag}}(s)$	diagonal current controller matrix for the dual-voltage machine
$\mathbf{P}_{\text{dyn}}(s)$	pre-compensator matrix for the dual-voltage machine dynamic decoupling control
$\mathbf{G}_{p,\text{diag}}(s)$	diagonal plant model matrix for the dual-voltage machine

Iron Loss Modeling

R_{mfe1}	iron loss resistance referred to stator 1 (12V)	Ω
-------------------	---	----------

Physical Quantities

\vec{H}	magnetic field strength	T
\vec{B}	magnetic field density	T
W_f	field energy	Ws
μ_r	magnetic permeability	

1 Introduction

1.1 Project Motivation

According to the European Commission (EC) personal transportation is responsible for 12% of total European Union (EU) emissions of Carbon Dioxide (CO₂). The target set by the EU law requires that new vehicles emit no more than 130 grams of CO₂ per kilometre by 2015 and no more than 95 grams of CO₂ per kilometre for new cars released after 2021. Every single gram over this limit costs the manufacturer 95€ from 2019 [58]. Battery Electric Vehicles (BEVs) and Plug-in Hybrid Electric Vehicles (PHEVs) have the potential to reduce the CO₂ emissions even to 67-84 $\frac{\text{g}}{\text{km}}$, when using the energy mix from 2010 and up to 0-4 $\frac{\text{g}}{\text{km}}$, when using purely renewable energy sources [24]. The transition to pure electric transportation will be a slow process and the short term goals for 2020 by the EU commission cannot be met only with the introduction of BEVs and PHEVs. Therefore Original Equipment Manufacturer (OEM)s (OEMs) have to come up with innovations also for their Internal Combustion Engine (ICE) (ICE) cars [14]. The introduction of mild-hybrid technologies like the 48V system can help OEMs to meet emission targets by 2020 [3].

The introduction of the new 48V power supply enables the use of high power loads as an electric compressor and electrically heated catalyst. The electrically heated catalyst alone has the potential to reduce CO₂ footprint by 3-4% [62] [72]. Further, the increase of the voltage and the introduction of actively controlled Metal-Oxide-Semiconductor Field-Effect Transistor (MOSFET) (MOSFET) technology for the generator control increases the efficiency of the conventional alternator. The 12V power supply is well established nowadays in the automotive industry. Therefore a dual-voltage power supply (12V/48V) is required as a hybrid solution. Thus, a Direct-Current to Direct-Current (DC/DC) converter is required to enable the power flow between both power supply networks. Figure 1.1 shows a schematic of a conventional 48V power supply architecture. A 48V generator supplies the 48V side, comprising of a Li-Ion battery and possible 48V loads. The 12V battery can be a Lead-Acid one, a dual-storage system comprising of Lead-Acid and Li-ion cells [35] or a pure Li-Ion battery[51]. The DC/DC converter is designed to transfer power of up to 3kW between both power supplies, covering the energy supply of all loads on the 12V side [1]. The additional DC/DC converter increases the costs for the OEMs. Further, it requires additional efforts for its integration and placement in the car. Therefore, a competitive architecture, which eliminates the use of a DC/DC converter is a very attractive option.

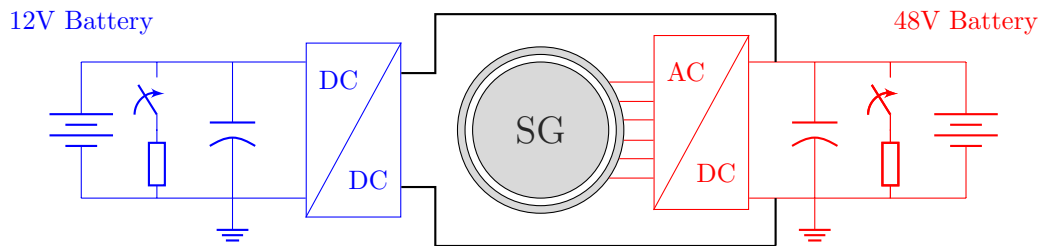


Figure 1.1 – Conventional 48V Architecture Employing a DC/DC Converter

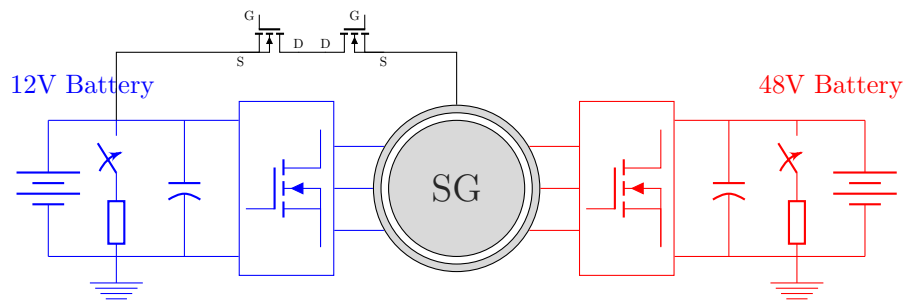


Figure 1.2 – Dual-Voltage Machine Architecture Eliminating a DC/DC converter

One possible solution would be to design a machine, which naturally generates two voltage levels as shown in Fig. 1.2. Since most of the alternators are six-phase machines, they can be split in two three-phase systems. In Fig. 1.2 also a star point switch is illustrated, which connects the 12V plus with the star point of the 48V system. This switch is employed, when a power transfer at standstill is required. However the focus of this thesis is not the investigation of the power transfer at standstill, which is performed in another work [31], but rather the power transfer at rotation and the decoupling control for the machine. From Fig. 1.2 is evident, that one sub-system supplies the 12V side and the other sub-system supplies the 48V side. Through the use of actively controlled power electronics, based on a MOSFET technology, the power can be controlled at both three-phase systems. This way the alternator, driven by the ICE, can be used to supply both power supply networks at the same time (dual-generation). The power sources at both sides can be used simultaneously to provide mechanical torque on the belt and assist the engine. This competitive architecture entails a challenge in terms of machine control. The control needs to handle the coupling of both stator systems and counteract it, such that the power is controlled at each side as far as possible independently. A very detailed knowledge about the machine is required in order to implement model-based control algorithms, which manage to decouple and control the power flow in both directions at both sides.

1.2 Thesis Objective and Structure

The focus of this thesis is to develop a machine model, which is able to replicate the machine behavior of a dual-voltage prototype machine and to develop a control, which is stable and is able to decouple the 12V and the 48V sides. The control should be able to control the power flow at both stator windings as well in the Base Speed (BS) range as in the Field Weakening (FW) area.

Although the thesis documentation follows in its biggest part the time-line of the project, the documentation is rather content-oriented than time-line oriented. Chapter 2 includes all findings throughout the research related to the machine modeling part of the work. Chapter 3 covers respectively all theory and findings related to the current control design and Chapter 4 examines the torque and power control for the dual-voltage machine. The content of the chapters is described briefly in the following paragraphs.

Chapter 2 handles the model development of the dual-voltage machine. The chapter describes in its first half a three-phase machine model with one voltage level as the state of the art and an introduction into the modeling of six-phase machines. The second half of the chapter presents the machine theory for a six-phase dual-voltage synchronous machine model. The machine voltage equations are explained in detail and derived according to the VBR and DQ modeling principles. Based on the findings in this chapter two research papers are published: “A general voltage-behind-reactance formulation of a multivoltage $n \times 3$ -phase hybrid-excited synchronous machine” [29] and “Integration of iron-loss resistance into dynamic models of 2×3 -phase hybrid-excited synchronous machine” [28] in the Transactions on Energy Conversion. The machine model equations are implemented in the PLECS blockset and the model is used further for control purposes. The iron losses extension of the models is performed after the torque and current control for the machine is developed and as a result of the findings observed during the torque control measurements in Chapter 4. Therefore this part of the model development is performed at the end of the project but included in the first chapter because of the content structure of the thesis. During the beginning of the project also a six-phase dual-voltage induction machine model has been derived and a conference paper based on the derived model is published: “A voltage-behind-reactance model of a dual-voltage six-phase induction machine” [27]. The modeling of the induction machine is not included in the thesis, because the induction machine does not show promising results in terms of power density and is excluded from further research. In case the reader is interested into the modeling of the six-phase dual-voltage induction machine, one can refer to the research paper [27].

Chapter 3 handles the current control design for the dual-voltage machine. Five PI current controllers, the 12V d - and q -axis currents, the 48V d - and q -axis currents and the field winding current, have to be tuned. The chapter handles the tuning of all five current controllers after the Modulus Optimum (MO) criterion and tests these in a simulation environment with the already programmed model from Chapter 2. The controllers are

tested also with a dSpace rapid control prototyping Autobox on the test bench and verified successfully. The chapter investigates also decoupling networks, which attempt to improve the control performance at speed and minimize the controller interactions. The improvement in control performance through the decoupling network, which takes the magnetic coupling of all five currents into account, is confirmed in the simulation as well as through measurements. The decoupling network has also some limitations and can only compensate the static coupling between the axis. For the dynamic coupling a new dynamic decoupling control is designed for the dual-voltage machine. The dynamic decoupling is developed at the end of the project and therefore only simulations are performed to verify the developed decoupling control. The dynamic decoupling network shows extraordinary results in the simulation and is one of the main contributions of the thesis in the field of current control design.

Chapter 4 handles the torque control development for the dual-voltage machine. The first half of the chapter introduces some state of the art torque control methods like the MTPA control for the BS range and the Maximum Torque-per-Flux (MTPF) control for the FW range on the example of a three-phase machine with one voltage level. The second half of the chapter handles the development of the torque control for the dual-voltage machine based on two torque references: T_{e12V}^* and T_{e48V}^* . The developed torque control aims to set independently two air-gap torque references in order to control the power at both stator systems. The control is verified in the simulation and on the test bench. Due to the considerable iron losses of the claw-pole dual-voltage machine, these have been afterwards measured and included as iron loss torques for both air-gap torque references. The implemented optimization algorithm searches for optimal current references for all five currents in respect to the copper losses of the machine. The field weakening control for the dual-voltage machine is extremely challenging, as the maximum available voltages can vary independently at both sides and also the inaccuracies in the parameter identification of the machine can lead to saturation of the PI controllers. Therefore, a new concept, not based on pre-calculated working points, is investigated. A Voltage Angle Control (VAC) for both stator systems is derived and implemented in the simulation environment and on the test bench. The proof of concept for the new VAC is successfully confirmed. A switching mechanism between the FOC and the VAC is implemented and verified. With this third main chapter the bulk of the thesis and the project is finished.

Chapter 5 represents a summary of the main findings from chapters 2, 3 and 4. The last chapter points out some of the areas, which can be addressed in a further research.

1.3 Nomenclature

In this section a nomenclature is defined, which is valid throughout the whole thesis. The use of vectors is denoted with bold small letters (e.g. \mathbf{v}) or with an arrow over the symbol (e.g. \vec{v}) and a matrix is written out with bold capital letter (e.g. \mathbf{M}). Since the dual-voltage machine comprises of two stator systems, these have to be identified by

some indexing. Throughout the whole thesis the index 1 refers to the 12V side and the index 2 denotes the 48V side. Quantities related to the 12V stator system are either indexed with 1 or the 12V abbreviation is included in the subscript of the quantities. In an analogous way the quantities for the 48V system are indexed with 2 or explicitly with the 48V abbreviation in the subscript. For example, a current flowing along the q -axis of the 12V system is written out as i_{qs1} . The index s denotes the stator system. A current flowing through the d -axis of the 48V system is symbolized with i_{ds2} . During the machine modeling some physical quantities need to be referred to one stator reference system. All referred quantities are denoted by an uppercase prime symbol $'$. For example, the q -axis current of the 48V system referred to the 12V system is denoted by i'_{qs2} . Analogically the d -axis 48V current referred to the 12V side is symbolized with i'_{ds2} . Mainly in Chapter 2, which handles the machine modeling, but also throughout the whole thesis, physical quantities and equations are written out in matrix and vector form in order to save space and improve the legibility of the thesis. When an equation is written in matrix-vector form the following nomenclature is employed. A vector \mathbf{f}_{qd0} symbolizes a certain physical quantity f (e.g. current i , voltage v or flux λ), which consists of components along the q -, d - and 0-axis ($\mathbf{f}_{qd0} = [f_q, f_d, f_0]^T$). The ABC domain is used as a synonym for the stationary stator domain. The rotor frame is described as the d - q domain.

Reference values, which are mainly used in Chapters 3 and 4, are denoted by an upper asterisk $*$ above the physical quantity or directly include the abbreviation *ref* in its subscript. Following this logic a torque reference is symbolized as T_e^* and a current reference as I_q^* .

The Heaviside's operator p is employed for the differentiation time. The Laplace operator is denoted by the symbol s .

2 Machine Modeling

The chapter presents the theory for the development of the six-phase externally-excited dual-voltage machine model. The chapter explains some basic modeling terminology and derives the three-phase machine model for an externally-excited synchronous machine, before the machine equations for the dual-voltage machine are derived.

In the beginning of the chapter the terms *magnetomotive force*, *effective number of turns* and *air-gap length* are explained. It derives the *self* and *mutual inductances* of a three-phase salient-pole machine based on a cross-section of a salient-pole machine. Thereafter the DQ and VBR model equations for the three-phase model are derived as a basis for the six-phase model. The terms *saturation* and *cross-magnetization* are explained and a saturation model of the main inductance is added to both three-phase models.

In the second half of the chapter, the machine equations used to describe the dual-voltage machine behavior are derived from the three-phase model. All required equations for both formulations, the DQ and the VBR, are derived for the 2×3 -phase dual-voltage machine. The machine equations are derived based from a cross-section of the six-phase dual-voltage machine. Afterwards *iron losses* are added to the dynamic models in order to increase the accuracy of the simulated machine torque. At the end of the chapter, the presented six-phase dual-voltage machine model is parametrized through measurements from a test bench.

The presented theory in the current chapter is also published in the following papers:

- Gradev, S.; Findeisen, D.; Toennesen, T. L., ; et al.: “A voltage-behind-reactance model of a dual-voltage six-phase induction machine”. In: *2014 International Conference on Electrical Machines (ICEM)*. Sept. 2014, pp. 672–678. DOI: [10.1109/ICELMACH.2014.6960253](https://doi.org/10.1109/ICELMACH.2014.6960253)
- Gradev, S.; Reuss, J.; Herzog, H. G.: “A general voltage-behind-reactance formulation of a multivoltage $n \times 3$ -phase hybrid-excited synchronous machine”. In: *IEEE Transactions on Energy Conversion* 31.4 (Dec. 2016), pp. 1452–1461. ISSN: 0885-8969. DOI: [10.1109/TEC.2016.2597258](https://doi.org/10.1109/TEC.2016.2597258)
- Gradev, S.; Herzog, H.: “Integration of iron-loss resistance into dynamic models of 2×3 -phase hybrid-excited synchronous machine”. In: *IEEE Transactions on Energy Conversion* (2018), pp. 1–1. ISSN: 0885-8969. DOI: [10.1109/TEC.2018.2841856](https://doi.org/10.1109/TEC.2018.2841856)

2.1 Three-Phase Salient-Pole Machine Model

In order to derive the three-phase salient-pole machine model, first the term Magnetomotive Forces (MMFs) is explained and the fluxes of each coil are derived from the spatial arrangement of the stator coils and their rotor displacement relative to the field winding. The self- and mutual inductances of the three-phase salient-pole machine model are derived. The employed approach for the derivation of the three-phase model is based on methods explained in detail in referece [38].

2.1.1 Magnetomotive Forces of a Salient-Pole Machine

A schematic cross-section drawing of the three-phase salient-pole machine with one pole pair is shown in Fig. 2.1 and used to derive the three-phase machine model.

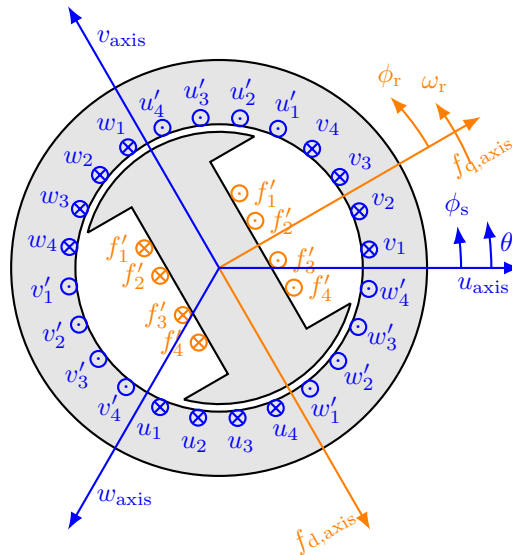


Figure 2.1 – Schematic Drawing of a Three-Phase Salient-Pole Machine

The stator coils are represented by the letters u , v and w and the field coil by the letter f . The stator coils are usually embedded in the stator slots. The stator coils are assumed to be physically identical and are displaced by 120° each in the stator slots. Therefore, the inductances and resistances of the coils have equal values. The field coil is wound on the rotor core and produces a magnetic field, which is carried by the rotor iron and passed into the stator through the air-gap. The field winding rotates at an angular speed ω_r . In Fig. 2.1. the sign \otimes represents a positive current flowing down along the stator slot (into the paper) and the sign \odot represents a negative current flowing backwards along the stator slot (out of the paper) [38]. For example, winding $u_1 - u'_1$ consists of n_x number of turns and spans an area of the stator of π radians. If the Ampere's right

hand rule is applied to the current flowing in the winding u_s it is evident from Fig. 2.1 that a positive flux along the u_s axis is created. Positive flux is also produced along the v_s and w_s axis when the current flows with the described directions from Fig. 2.1. Each stator coil consists of multiple windings, which have certain number of turns. Thus the number of turns of a coil is calculated by the product of the number of windings and number of turns of each winding n_x . In the drawing from Fig 2.1 the number of windings is 4: u_1 to u_4 . The windings are placed in such a way in the stator slots, that the end of u'_1 is connected to u_2 . This is illustrated in the equivalent circuit in Fig. 2.2. The same arrangement holds also for the windings v_s and w_s . The end turns of u'_s , v'_s and w'_s are connected together and form a star-point connection. In Fig. 2.1 the windings span the

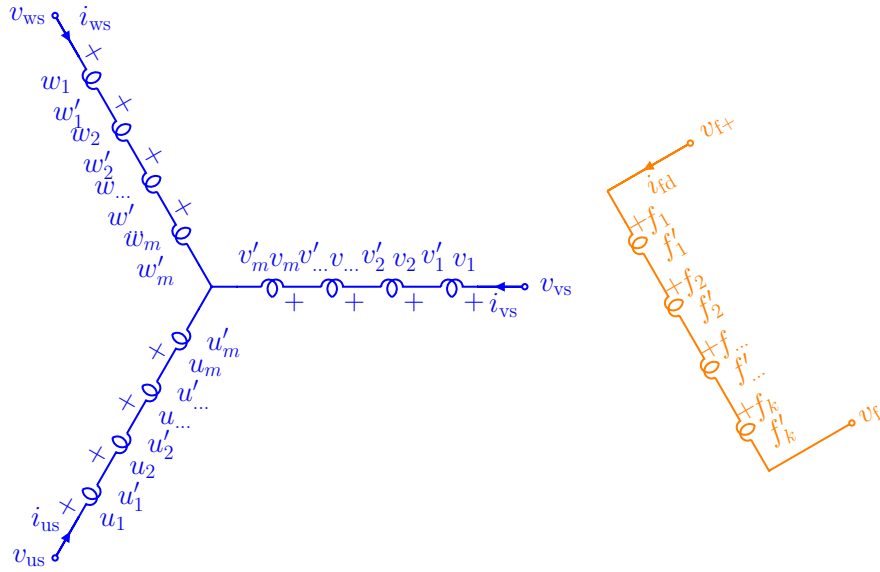


Figure 2.2 – Three-Phase ABC Equivalent Circuit

whole pitch of the pole, which in a two-pole machine is π radians. For a four-pole machine the windings would span $\frac{\pi}{2}$ radians. For an n -pole machine the windings would span an angle of $\frac{2\pi}{n}$ radians. Often machines have a fractional pitch winding. This means that the windings do not cover the whole pitch of the pole but slightly less. In the two-pole example, this would be slightly less than π radians. In order to produce a sinusoidal MMF different number of turns are used for each of the four coils u_1 , u_2 , u_3 and u_4 . With the example from Fig. 2.1 this would be the cause for example with windings u_1 and u_4 , which would have less turns than u_2 and u_3 . The illustration from Fig. 2.1, where the windings of each phase are separated strictly by 60° is not true in a real machine. It is also often the case, that windings of two neighboring coils, for example u_s and v_s , share the same slots. Thus one coil side spans more space from the stator circumference than 60° . In a practical design, a coil side spans an area of 120° [38]. Thus, for the equivalent dynamic models an *effective number of turns* for a coil is of interest, and not the actual number of turns placed in the stator.

The air-gap MMF for the two-pole machine from Fig. 2.1 is derived in order to derive afterwards the torque equation. The MMF expression can be easily extended to P -pole machines. First, a displacement angle between rotor and stator is defined for this purpose in equation (2.1.1.1).

$$\phi_s = \phi_r + \theta_r \quad (2.1.1.1)$$

The angle ϕ_s denotes an angular displacement relative to the u_s axis along the stator circumference. The angle ϕ_r denotes an angular displacement relative to the f_q axis along the rotor circumference. The magnetic flux strength \vec{H} and flux density \vec{B} are assumed to be radial. This is true due to the fact, that the permeability of the stator and rotor material μ is much larger than the permeability of the air μ_0 and the flux lines cross perpendicularly to the rotor and stator circumferences. Thus, the flux densities \vec{H} and \vec{B} in the air-gap have only a radial component and their amplitudes are functions of ϕ_s . The relationship between B_r and H_r is shown in equation (2.1.1.2).

$$B_r(\phi_s) = \mu_0 H_r(\phi_s) \quad (2.1.1.2)$$

The direction of the current i_{us} from Fig. 2.1 indicates that the rotor flux lines in the air-gap flows from the stator to the rotor for $\frac{\pi}{2} < \phi_s < \frac{3\pi}{2}$ and from rotor to stator for $-\frac{\pi}{2} < \phi_s < \frac{\pi}{2}$. According to Ampere's Law the magnetic flux strength enclosed in the covered area by the winding u_s is integrated and equal to the flowing current as shown in equation (2.1.1.3).

$$\int \vec{H} d\vec{L} = i \quad (2.1.1.3)$$

It is assumed that no flux from the winding can escape out of the whole air-gap. If Gauss's Law is applied to (2.1.1.3) for the whole surface spanned by the winding, equation (2.1.1.4) is derived.

$$\int_s \vec{B} d\vec{S} = 0 \quad (2.1.1.4)$$

When the law is applied for winding u_s , equation (2.1.1.5) is derived.

$$\int_0^{2\pi} B_r(\phi_s) r l d\phi_s = 0 \quad (2.1.1.5)$$

The parameter r is the mean radius of the air-gap and l is the axial length of the stator. Thus, the product $r l d\phi_s$ is the incremental area of the cylindrical surface over the air-gap of the machine, over which the magnetic flux density $B_r(\phi_s)$ is integrated. The air-gap length g for the two-pole salient-pole machine is a periodical function of π and is expressed in equation (2.1.1.6).

$$g(\phi_r) = g(\phi_r + \pi) \quad (2.1.1.6)$$

The stator displacement angle relative to the u_s axis is substituted in equation (2.1.1.6) and equation (2.1.1.7) is derived.

$$g(\phi_s - \theta_r) = g(\phi_s - \theta_r + \pi) \quad (2.1.1.7)$$

Considering Gauss' Law, shown in equation (2.1.1.4), and the periodicity of the air-gap length function, shown in equation (2.1.1.7), the conclusion can be made that both MMFs have to be in opposite direction at a periodicity of π for the two-pole machine (2.1.1.8).

$$MMF(\phi_s) = -MMF(\phi_s + \pi) \quad (2.1.1.8)$$

It is assumed, that the designed machine produces a sinusoidal MMF. Therefore, the number of turns of the windings are also distributed sinusoidally. The effective number of turns for the two-pole machine is calculated according the sinusoidal distribution of the u_s winding in equation (2.1.1.9). [38].

$$N_{us} = N_p \sin \phi_s, \quad 0 \leq \phi_s \leq \pi \quad N_{us} = -N_p \sin \phi_s, \quad \pi \leq \phi_s \leq 2\pi \quad (2.1.1.9)$$

The negative sign in equation (2.1.1.9) results from the relationship shown in equation (2.1.1.8). The parameter N_p is the maximum turns density in turns per radian. Then the effective number of turns would be the integral over ϕ_s for the range of $0 < \phi_s < \pi$.

$$N_s = \int_0^\pi N_p \sin \phi_s d\phi_s = 2N_p \quad N_p = \frac{N_s}{2} \quad (2.1.1.10)$$

The parameter N_s is the effective number of turns used in the machine equations. The current flow direction from Fig. 2.1 in winding u_s can be implemented in the distribution of the winding, shown in equation (2.1.1.11), such that a positive current produces a positive flux in the u_s axis direction.

$$N_{us} = -\frac{N_s}{2} \sin \phi_s \quad (2.1.1.11)$$

The MMF is then calculated according to Ampere's Law for all windings as the integral up to the angle ϕ_s . The peak of the MMF for winding u_s is in the direction of the u_s axis. The MMF for the winding u_s is a cosine function of the angle ϕ_s . The MMF is an integral of the winding distribution from equation (2.1.1.11) multiplied by the current flowing in the winding i_{us} . All three MMF expressions for each winding are shown in equations (2.1.1.12), (2.1.1.13) and (2.1.1.14).

$$MMF_{u_s} = \frac{N_s}{2} \cdot i_{us} \cos \phi_s \quad (2.1.1.12)$$

$$MMF_{v_s} = \frac{N_s}{2} \cdot i_{vs} \cos \left(\phi_s - \frac{2\pi}{3} \right) \quad (2.1.1.13)$$

$$MMF_{w_s} = \frac{N_s}{2} \cdot i_{ws} \cos \left(\phi_s + \frac{2\pi}{3} \right) \quad (2.1.1.14)$$

The total MMF at the angle displacement ϕ_s is expressed as the sum of all winding's MMFs according to equation (2.1.1.15).

$$MMF_{uvw_s} = \frac{N_s}{2} \cdot i_{us} \cos \phi_s + \frac{N_s}{2} \cdot i_{vs} \cos \left(\phi_s - \frac{2\pi}{3} \right) + \frac{N_s}{2} \cdot i_{ws} \cos \left(\phi_s + \frac{2\pi}{3} \right) \quad (2.1.1.15)$$

In a balanced steady state condition the stator currents are expressed as shown in equations (2.1.1.16), (2.1.1.17) and (2.1.1.18).

$$i_{\text{us}} = \sqrt{2}I_s \cos(\omega_e t + \theta_{t0}) \quad (2.1.1.16)$$

$$i_{\text{vs}} = \sqrt{2}I_s \cos\left(\omega_e t + \theta_{t0} - \frac{2\pi}{3}\right) \quad (2.1.1.17)$$

$$i_{\text{ws}} = \sqrt{2}I_s \cos\left(\omega_e t + \theta_{t0} + \frac{2\pi}{3}\right) \quad (2.1.1.18)$$

The derived MMF is set for a two-pole machine. The expression can be extended to more poles P or pole pairs p . The air-gap MMF generated by each phase is shown in equations (2.1.1.19), (2.1.1.20) and (2.1.1.21). The sum of all MMFs for a P -pole machine is provided in equation (2.1.1.22).

$$MMF_{\text{us}} = \frac{N_s}{P} \cdot i_{\text{us}} \cos \frac{P}{2} \phi_s \quad (2.1.1.19)$$

$$MMF_{\text{vs}} = \frac{N_s}{P} \cdot i_{\text{vs}} \cos\left(\frac{P}{2} \phi_s - \frac{2\pi}{3}\right) \quad (2.1.1.20)$$

$$MMF_{\text{ws}} = \frac{N_s}{P} \cdot i_{\text{ws}} \cos\left(\frac{P}{2} \phi_s + \frac{2\pi}{3}\right) \quad (2.1.1.21)$$

$$\begin{aligned} MMF_{\text{uvw}} &= \frac{N_s}{P} \cdot i_{\text{us}} \cos \frac{P}{2} \phi_s + \frac{N_s}{P} \cdot i_{\text{vs}} \cos\left(\frac{P}{2} \phi_s - \frac{2\pi}{3}\right) \\ &+ \frac{N_s}{P} \cdot i_{\text{ws}} \cos\left(\frac{P}{2} \phi_s + \frac{2\pi}{3}\right) \end{aligned} \quad (2.1.1.22)$$

Equation (2.1.1.22) represents an air-gap MMF rotating in a counterclockwise manner at the speed of $\frac{\omega_m}{p}$ radians. This is the MMF produced by the currents flowing in the stator windings.

The *self-* and *mutual inductances* have to be derived based on the spatial arrangement from Fig. 2.1, in order to derive the machine voltage equations. A self inductance of a winding x is defined as the ratio between the generated flux λ_{xs} by its own current i_{xs} and divided through the same current i_{xs} , while all other currents are zero. The mutual inductance is the ratio between the flux λ_{xs} of a certain winding x , produced by a current flowing in an another winding, for example i_{ys} , and divided by the current i_{ys} . In order to calculate the flux produced by a stator winding it is necessary to have an expression of the air-gap length. The air-gap length of a salient-pole machine is a periodical function. The expression is derived in reference [38] and shown in equation (2.1.1.23).

$$g(\phi_r) = \frac{1}{\alpha_1 - \alpha_2 \cos 2\phi_r} \quad g(\phi_s - \theta_r) = \frac{1}{\alpha_1 - \alpha_2 \cos(2(\phi_s - \theta_r))} \quad (2.1.1.23)$$

The minimum air-gap length is then $(\alpha_1 + \alpha_2)^{-1}$ and the maximum $(\alpha_1 - \alpha_2)^{-1}$. The MMF is defined as the integral of \vec{H} . This way the relationship between MMF and magnetic flux density is derived in equation (2.1.1.24).

$$B_r(\phi_s) = \mu_0 H_r(\phi_s) \quad B_r = \mu_0 \frac{MMF}{g} \quad (2.1.1.24)$$

The magnetic flux density, shown in equation (2.1.1.25), is derived with the MMF expression from equation (2.1.1.12) and the air-gap length described through equation (2.1.1.23). The expression is dependent on the stator angle ϕ_s and rotor displacement angle θ_r .

$$B_r(\phi_s, \theta_r) = \mu_0 \frac{MMF_{us}(\phi_s)}{g(\phi_s - \theta_r)} = \mu_0 \frac{N_s}{2} i_{us} \cos \phi_s [\alpha_1 - \alpha_2 \cos 2(\phi_s - \theta_r)] \quad (2.1.1.25)$$

The magnetic flux densities produced by the other windings and their currents are derived in a similar way. The expression for the flux density produced by the current i_{vs} , while all other currents are zero, is shown in equation (2.1.1.26).

$$B_r(\phi_s, \theta_r) = \mu_0 \frac{N_s}{2} i_{vs} \cos \left(\phi_s - \frac{2\pi}{3} \right) [\alpha_1 - \alpha_2 \cos 2(\phi_s - \theta_r)] \quad (2.1.1.26)$$

The magnetic flux density produced by the current i_{ws} is shown in equation (2.1.1.27).

$$B_r(\phi_s, \theta_r) = \mu_0 \frac{N_s}{2} i_{ws} \cos \left(\phi_s + \frac{2\pi}{3} \right) [\alpha_1 - \alpha_2 \cos 2(\phi_s - \theta_r)] \quad (2.1.1.27)$$

The field winding also produces an MMF. The air-gap MMF generated by the field winding is assumed to be sinusoidal and is expressed in equation (2.1.1.28). The turns of the field winding are uniformly wound around the rotor and the rotor poles are shaped in a such a way that they produce a sinusoidal MMF, when the field winding current is flowing. Therefore, the distribution of the field winding is sinusoidal with equivalent number of turns N_f . The angle ϕ_r is referred to the f_q -axis. The peak MMF is generated at the angle $\phi_r - \frac{\pi}{2}$ in direction of the f_d -axis as it is illustrated in Fig. 2.1. The MMF of the field winding is shown in equation (2.1.1.28).

$$MMF_{fd} = -\frac{N_f}{2} i_{fd} \sin \phi_r \quad (2.1.1.28)$$

The magnetic flux density produced by the rotor winding is also calculated according to the given relationship between MMF, B_r and air-gap length g in equation (2.1.1.24). The magneto-motive force of the field winding, shown in equation (2.1.1.28), is substituted in the relationship between the magnetic flux density and the MMF shown in equation (2.1.1.24). This way the magnetic flux density of the field winding is derived in equation (2.1.1.29).

$$B_r(\phi_r) = -\mu_0 \frac{N_f}{2} i_{fd} \sin \phi_r (\alpha_1 - \alpha_2 \cos 2\phi_s) \quad (2.1.1.29)$$

2.1.2 Deriving Flux Linkages and Inductances

The expressions for the self inductances can be derived, when a formula for the flux linkage produced by the winding's own current is derived and divided by this current. In order to derive an expression for the mutual inductance between two stator windings the flux linkage in a winding produced by a current flowing in a neighboring winding has to be derived and divided by this current. The flux linkage of a single turn is the integral of

the magnetic flux density over the area covered by this turn. This relation is expressed through equation (2.1.2.1).

$$\Phi(\phi_s, \theta_r) = \int_{\phi_s}^{\phi_s + \pi} B_r(\zeta, \theta_r) r l d\zeta \quad (2.1.2.1)$$

The flux linkage produced by the whole winding can be calculated when all flux linkages of each turn are summed up. The turns of the windings have a sinusoidal distribution, as shown in equation (2.1.1.10), and therefore the flux linkage of the whole winding is calculated as an integral over the sinusoidal distribution of the winding. This way the whole flux linkage of the winding u_s is calculated. The result is shown in equation (2.1.2.2). It is assumed that the winding has a leakage inductance L_{ls} and a leakage flux λ_{ls} .

$$\begin{aligned} \lambda_{us} &= L_{ls} i_{us} + \int N_{us}(\phi_s) \Phi(\phi_s, \theta_r) d\phi_s \\ &= L_{ls} i_{us} + \int N_{us}(\phi_s) \int_{\phi_s}^{\phi_s + \pi} B_r(\zeta, \theta_r) r l d\zeta d\phi_s \end{aligned} \quad (2.1.2.2)$$

The magnetic flux density is described as a function of the stator angle ϕ_s , which is described through equation (2.1.1.25), and the distribution of the u_s winding turns, described in equation (2.1.1.9), are both substituted in equation (2.1.2.2) to derive the full expression of the flux linkage λ_{us} in equation (2.1.2.3).

$$\begin{aligned} \lambda_{us} &= L_{ls} i_{us} + \int_{\pi}^{2\pi} \left(-\frac{N_s}{2} \right) \sin \phi_s \cdot \int_{\phi_s}^{\phi_s + \pi} \mu_0 \frac{N_s}{2} i_{us} \cdot \cos \zeta [\alpha_1 - \alpha_2 \cos 2(\zeta - \theta_r)] r l d\zeta d\phi \\ &= L_{ls} i_{us} + \left(\frac{N_s}{2} \right)^2 \pi \mu_0 r l \left(\alpha_1 - \frac{\alpha_2}{2} \cos 2\theta_r \right) i_{us} \end{aligned} \quad (2.1.2.3)$$

The self inductance is then obtained from equation (2.1.2.3). The expression for the self inductance $L_{l,usus}$ of winding u_s is shown in equation (2.1.2.4).

$$L_{l,usus} = L_{ls} \left(\frac{N_s}{2} \right)^2 \pi \mu_0 r l \left(\alpha_1 - \frac{\alpha_2}{2} \cos 2\theta_r \right) \quad (2.1.2.4)$$

The mutual inductance is derived in an analogical way. The magnetic flux density produced by the current i_{vs} is integrated over the winding distribution of u_s . The derivation can be followed in detail in reference [38]. In order to derive an expression for the mutual inductance between the windings u_s and v_s , L_{usvs} , the expression of the stator flux linkage λ_{us} , caused by the current i_{vs} , is required. According to reference [38] the flux linkage is expressed as a function of the current i_{vs} through equation (2.1.2.5).

$$\lambda_{us} = \int_{\pi}^{2\pi} \left(-\frac{N_s}{2} \right) \sin \phi_s \cdot \int_{\phi_s}^{\phi_s + \pi} \mu_0 \frac{N_s}{2} i_{vs} \cos \left(\zeta - \frac{2\pi}{3} \right) (\alpha_1 - \alpha_2 \cos 2(\zeta - \theta_r)) r l d\zeta d\phi \quad (2.1.2.5)$$

The expression for the inductance can be derived, when the double integral from equation (2.1.2.5) is solved and the expression is divided by the current i_{vs} . This way the mutual inductance L_{usvs} is calculated as shown in equation (2.1.2.6).

$$L_{usvs} = - \left(\frac{N_s}{2} \right)^2 \pi \mu_0 r l \left(\alpha_1 + \frac{\alpha_2}{2} \cos \left(2\theta_r + \frac{\pi}{3} \right) \right) \quad (2.1.2.6)$$

The mutual inductance L_{usws} from equation (2.1.2.7) is calculated in a similar way.

$$L_{usws} = - \left(\frac{N_s}{2} \right)^2 \pi \mu_0 r l \left(\alpha_1 + \frac{\alpha_2}{2} \cos 2 \left(\theta_r + \frac{\pi}{3} \right) \right) \quad (2.1.2.7)$$

The mutual inductance between stator winding u_s and the rotor field winding f_d is derived in a similar way and the result is given in equation (2.1.2.8). The flux linkage produced by the current i_{fd} into the winding u_s is expressed through equation (2.1.2.9). The presented expressions for the flux linkages and the inductances are verified through matlab scripts, which are employed to solve the double integrals with the Matlab Symbolic Toolbox [49].

$$L_{usfd} = \frac{N_s}{2} \frac{N_f}{2} \pi \mu_0 r l \left(\alpha_1 + \frac{\alpha_2}{2} \right) \sin \theta_r \quad (2.1.2.8)$$

$$\lambda_{us} = \int_{\pi}^{2\pi} \frac{N_s}{2} \sin \phi_s \int_{\phi_s}^{\phi_s + \pi} \mu_0 \frac{N_f}{2} i_{fd} \sin (\zeta - \theta_r) [\alpha_1 - \alpha_2 \cos 2 (\zeta - \theta_r)] r l d\zeta d\phi \quad (2.1.2.9)$$

The rotor flux linkage produced by the rotor current only is provided in equation (2.1.2.11). It is assumed that the field winding is also sinusoidally distributed. From Fig. 2.1 is obvious that the sinusoidal distribution of the rotor winding turns into a cosine integration over the rotor angle from $\frac{\pi}{2}$ to $\frac{3\pi}{2}$. The field winding distribution and the flux linkage of one turn of the field winding are substituted in equation (2.1.2.10). The calculated flux linkage is shown in equation (2.1.2.11).

$$\lambda_{fd} = \int N_f(\phi_r) \Phi(\phi_r) d\phi \quad (2.1.2.10)$$

$$\lambda_{fd} = L_{lfd} i_{fd} + \int_{\frac{\pi}{2}}^{\frac{3\pi}{2}} \frac{N_f}{2} \cos \phi_r \int_{\phi_r}^{\phi_r + \pi} \mu_0 \frac{N_f}{2} i_{fd} \sin \zeta (\alpha_1 - \alpha_2 \cos 2\zeta) r l d\zeta d\phi \quad (2.1.2.11)$$

The flux, which does not penetrate into the stator, but leaks out, is defined through the product of the leakage inductance L_{lfd} and the current i_{fd} . After the integration of equation (2.1.2.11), the rotor self inductance is derived in equation (2.1.2.12).

$$L_{l,fdfd} = L_{lfd} + \frac{N_f^2}{2} \pi \mu_0 r l \left(\alpha_1 + \frac{\alpha_2}{2} \right) \quad (2.1.2.12)$$

The mutual inductance between the field winding f_d and the stator winding u_s will be derived also as an example. The mutual inductances between the field winding and the

other stator windings can be derived analogically. The distribution of the rotor winding and the flux linkage generated by i_{us} are substituted in equation (2.1.2.13).

$$\lambda_{fd} = \int_{\frac{\pi}{2}}^{\frac{3\pi}{2}} \frac{N_f}{2} \cos \phi_r \int_{\phi_r}^{\phi_r + \pi} \mu_0 \frac{N_s}{2} i_{us} \cos(\zeta + \theta_r) [\alpha_1 - \alpha_2 \cos 2(\zeta + \theta_r)] r l d\zeta d\phi \quad (2.1.2.13)$$

If equation (2.1.2.13) is integrated and divided by the current i_{us} , one gets the mutual inductance L_{fdus} in equation (2.1.2.14).

$$L_{fdus} = -\frac{N_f N_s}{2} \pi \mu_0 r l (\alpha_1 + \frac{\alpha_2}{2}) \sin \theta_r \quad (2.1.2.14)$$

The expressions in equations (2.1.2.15) and (2.1.2.16) are valid for the inductances L_{fdvs} and L_{fdws} .

$$L_{fdvs} = \frac{N_f N_s}{2} \pi l \mu_0 r (\alpha_1 - \frac{\alpha_2}{2}) \sin(\theta_r + \frac{\pi}{3}) \quad (2.1.2.15)$$

$$L_{fdws} = \frac{N_f N_s}{2} \pi l \mu_0 r (\alpha_1 - \frac{\alpha_2}{2}) \sin(\theta_r - \frac{\pi}{3}) \quad (2.1.2.16)$$

The procedure for deriving the self and mutual inductances of a three-phase salient-pole machine has been explained on some of the inductances. This procedure is adapted to all self- and mutual inductance of the three-phase salient-pole machine. The results are provided in equation (2.1.2.17). All flux linkages and inductances of the three-phase salient-pole machine are derived in Appendix A for the interested reader.

$$\begin{aligned} L_A &= \frac{N_s^2}{2} \pi \mu_0 r l \alpha_1 & L_B &= \frac{1}{2} \frac{N_s^2}{2} \pi \mu_0 r l \alpha_2 \\ L_{sfd} &= \frac{N_s N_f}{2} \pi \mu_0 r l (\alpha_1 + \frac{\alpha_2}{2}) & L_{mfd} &= \frac{N_f^2}{2} \pi \mu_0 r l (\alpha_1 + \frac{\alpha_2}{2}) \\ L_{l,us} &= L_{ls} + L_A - L_B \cos 2\theta_r & L_{l,vs} &= L_{ls} + L_A - L_B \cos 2\left(\theta_r - \frac{2\pi}{3}\right) \\ L_{l,ws} &= L_{ls} + L_A - L_B \cos 2\left(\theta_r + \frac{2\pi}{3}\right) & L_{l,dfd} &= L_{lfd} + L_{mfd} \\ L_{usvs} &= -\frac{1}{2} L_A - L_B \cos 2\left(\theta_r - \frac{\pi}{3}\right) & L_{usws} &= -\frac{1}{2} L_A - L_B \cos 2\left(\theta_r + \frac{\pi}{3}\right) \\ L_{vs} &= -\frac{1}{2} L_A - L_B \cos 2\left(\theta_r + \pi\right) & L_{usfd} &= L_{sfd} \sin \theta_r \\ L_{vsfd} &= L_{sfd} \sin\left(\theta_r - \frac{2\pi}{3}\right) & L_{wsfd} &= L_{sfd} \sin\left(\theta_r + \frac{2\pi}{3}\right) \end{aligned} \quad (2.1.2.17)$$

2.1.3 Machine Voltage Equations in Stator and Rotor Reference Frame

The voltage equations for the stator windings v_{us} , v_{vs} , v_{ws} and the field winding v_{fd} are functions of the voltage drops over the resistances and the rate of change of the flux

linkages. The voltage equations in the stator reference frame are provided in equations (2.1.3.1) to (2.1.3.4).

$$v_{us} = r_s i_{us} + \frac{d\lambda_{us}}{dt} \quad (2.1.3.1)$$

$$v_{vs} = r_s i_{vs} + \frac{d\lambda_{vs}}{dt} \quad (2.1.3.2)$$

$$v_{ws} = r_s i_{ws} + \frac{d\lambda_{ws}}{dt} \quad (2.1.3.3)$$

$$v_{fd} = r_{fd} i_{fd} + \frac{d\lambda_{fd}}{dt} \quad (2.1.3.4)$$

The voltage equations consist of the voltage drops over the stator and rotor resistances and the corresponding flux linkages. The stator resistance is symbolized with r_s in the equations and the field winding resistance with r_{fd} . The flux linkages are expressed as functions of the already in Subsection 2.1.2 derived self and mutual inductances and stator and rotor currents. The expressions of the flux linkages are given in equations (2.1.3.5) to (2.1.3.8). It is assumed that the relationship between currents and flux linkages is linear and thus saturation and cross-magnetization are neglected at this moment. The saturation modeling is handled in Subsection 2.1.5.

$$\lambda_{us} = L_{l,usus} i_{us} + L_{usvs} i_{vs} + L_{usws} i_{ws} + L_{usfd} i_{fd} \quad (2.1.3.5)$$

$$\lambda_{vs} = L_{vsus} i_{us} + L_{l,vsvs} i_{vs} + L_{vsws} i_{ws} + L_{vsfd} i_{fd} \quad (2.1.3.6)$$

$$\lambda_{ws} = L_{wsus} i_{us} + L_{wsvs} i_{vs} + L_{l,wsws} i_{ws} + L_{wsfd} i_{fd} \quad (2.1.3.7)$$

$$\lambda_{fd} = L_{fdus} i_{us} + L_{fdvs} i_{vs} + L_{fdws} i_{ws} + L_{l,fdfd} i_{fd} \quad (2.1.3.8)$$

The inductances from equations (2.1.3.5) to (2.1.3.8) are functions of the rotor displacement angle θ_r and respectively also by the rotor angular speed ω_r . This is evident from the derived inductance terms shown in equation (2.1.2.17).

This complexity can be reduced if a suitable transformation for the stator quantities is defined to transform them into a stationary rotor reference frame. Different transformations are described in the literature, which try to eliminate the time varying terms of the machine equations. The most commonly used transformation is the one defined by R.H. Park [54] in 1929. Park's transformation converts all voltage equations to a reference frame fixed to the rotor. This way the rotor displacement relative to the stator windings is eliminated from the voltage equations. The torque equation does not depend on the rotor angle in its steady state. The torque equation is the cross-product of the magnetic flux vector and the current vector in the rotor reference frame - called also a d - q frame. The transformation, which eliminates the rotor position dependency of the voltage equations in the stator reference frame, is shown in equation (2.1.3.9). The reverse transformation is called the backwards Park transformation and is shown in equation (2.1.3.10).

$$\mathbf{K}_s(\theta_r) = \frac{2}{3} \begin{bmatrix} \cos(\theta_r) & \cos(\theta_r - \frac{2\pi}{3}) & \cos(\theta_r + \frac{2\pi}{3}) \\ \sin(\theta_r) & \sin(\theta_r - \frac{2\pi}{3}) & \sin(\theta_r + \frac{2\pi}{3}) \\ \frac{1}{2} & \frac{1}{2} & \frac{1}{2} \end{bmatrix} \quad (2.1.3.9)$$

$$\mathbf{K}_s^{-1}(\theta_r) = \begin{bmatrix} \cos(\theta_r) & \sin(\theta_r) & 1 \\ \cos(\theta_r - \frac{2\pi}{3}) & \sin(\theta_r - \frac{2\pi}{3}) & 1 \\ \cos(\theta_r + \frac{2\pi}{3}) & \sin(\theta_r + \frac{2\pi}{3}) & 1 \end{bmatrix} \quad (2.1.3.10)$$

In order to derive the d - q representation of the three-phase machine model, the voltage equations (2.1.3.1) to (2.1.3.4) are brought into a matrix form as shown in equation (2.1.3.11). The flux linkages are substituted with their expressions from equations (2.1.3.5) to (2.1.3.8). The expressions of the inductance terms are the ones calculated in Appendix A.

$$\begin{bmatrix} v_{us} \\ v_{vs} \\ v_{ws} \\ v_{fd} \end{bmatrix} = \begin{bmatrix} r_s & 0 & 0 & 0 \\ 0 & r_s & 0 & 0 \\ 0 & 0 & r_s & 0 \\ 0 & 0 & 0 & r_{fd} \end{bmatrix} \cdot \begin{bmatrix} i_{us} \\ i_{vs} \\ i_{ws} \\ i_{fd} \end{bmatrix} + \frac{d}{dt} \left(\begin{bmatrix} L_{l,usus} & L_{usvs} & L_{usws} & L_{usfd} \\ L_{vsus} & L_{l,vsvs} & L_{vsws} & L_{vsfd} \\ L_{wsus} & L_{wsvs} & L_{l,wsws} & L_{wsfd} \\ L_{fdus} & L_{fdvs} & L_{fdws} & L_{l,fdfd} \end{bmatrix} \cdot \begin{bmatrix} i_{us} \\ i_{vs} \\ i_{ws} \\ i_{fd} \end{bmatrix} \right) \quad (2.1.3.11)$$

The derived inductance terms from equation (2.1.2.17) are arranged in a matrix as shown in equation (2.1.3.12).

$$\mathbf{L}_{ls} = \begin{bmatrix} L_{l,usus} & L_{usvs} & L_{usws} & L_{usfd} \\ L_{vsus} & L_{l,vsvs} & L_{vsws} & L_{vsfd} \\ L_{wsus} & L_{wsvs} & L_{l,wsws} & L_{wsfd} \\ L_{fdus} & L_{fdvs} & L_{fdws} & L_{l,fdfd} \end{bmatrix} \quad (2.1.3.12)$$

The inductance matrix (2.1.3.12) is separated into a constant leakage matrix, shown in equation (2.1.3.13), and a main time-varying inductance matrix, shown in (2.1.3.14). The matrix \mathbf{L}_s contains entries, which depend on the rotor position θ_r .

$$\mathbf{L}_l = \begin{bmatrix} L_{ls} & 0 & 0 & 0 \\ 0 & L_{ls} & 0 & 0 \\ 0 & 0 & L_{ls} & 0 \\ 0 & 0 & 0 & L_{lfd} \end{bmatrix} \quad (2.1.3.13) \quad \mathbf{L}_s = \begin{bmatrix} L_{usus} & L_{usvs} & L_{usws} & L_{usfd} \\ L_{vsus} & L_{vsvs} & L_{vsws} & L_{vsfd} \\ L_{wsus} & L_{wsvs} & L_{wsws} & L_{wsfd} \\ L_{fdus} & L_{fdvs} & L_{fdws} & L_{lfdfd} \end{bmatrix} \quad (2.1.3.14)$$

The angle dependency from equation (2.1.3.11) is removed, when the equation is transformed in the d - q rotor reference frame. The Park transformation from equation (2.1.3.9) and the backwards transformation, shown in equation (2.1.3.10), are extended with one more diagonal entry to consider the field winding. The additional entry is equal to 1, because the field winding quantities are fixed with the rotor axis. The extended matrices are shown in equations (2.1.3.15) and (2.1.3.16). A primed notation, $\mathbf{K}_s(\theta_r)'$ and $\mathbf{K}_s^{-1}(\theta_r)'$, is employed on the transformation matrices to denote the inclusion of the field winding. The forwards transformation is applied on vectors in the stator reference

frame, \mathbf{f}_{uvwf} and the backwards transformation is applied on vectors in the rotor reference frame, \mathbf{f}_{qdof} . Equations (2.1.3.17) and (2.1.3.18) show this relationship, where f can be voltage, current or flux linkage.

$$\mathbf{K}_s(\theta_r)' = \frac{2}{3} \begin{bmatrix} \cos(\theta_r) & \cos(\theta_r - \frac{2\pi}{3}) & \cos(\theta_r + \frac{2\pi}{3}) & 0 \\ \sin(\theta_r) & \sin(\theta_r - \frac{2\pi}{3}) & \sin(\theta_r + \frac{2\pi}{3}) & 0 \\ \frac{1}{2} & \frac{1}{2} & \frac{1}{2} & 0 \\ 0 & 0 & 0 & \frac{3}{2} \end{bmatrix} \quad (2.1.3.15)$$

$$\mathbf{K}_s^{-1}(\theta_r)' = \begin{bmatrix} \cos(\theta_r) & \sin(\theta_r) & 1 & 0 \\ \cos(\theta_r - \frac{2\pi}{3}) & \sin(\theta_r - \frac{2\pi}{3}) & 1 & 0 \\ \cos(\theta_r + \frac{2\pi}{3}) & \sin(\theta_r + \frac{2\pi}{3}) & 1 & 0 \\ 0 & 0 & 0 & 1 \end{bmatrix} \quad (2.1.3.16)$$

$$\begin{bmatrix} f_{qs} \\ f_{ds} \\ f_{0s} \\ f_{fd} \end{bmatrix} = \frac{2}{3} \begin{bmatrix} \cos(\theta_r) & \cos(\theta_r - \frac{2\pi}{3}) & \cos(\theta_r + \frac{2\pi}{3}) & 0 \\ \sin(\theta_r) & \sin(\theta_r - \frac{2\pi}{3}) & \sin(\theta_r + \frac{2\pi}{3}) & 0 \\ \frac{1}{2} & \frac{1}{2} & \frac{1}{2} & 0 \\ 0 & 0 & 0 & \frac{3}{2} \end{bmatrix} \cdot \begin{bmatrix} f_{us} \\ f_{vs} \\ f_{ws} \\ f_{fd} \end{bmatrix} \quad (2.1.3.17)$$

$$\begin{bmatrix} f_{us} \\ f_{vs} \\ f_{ws} \\ f_{fd} \end{bmatrix} = \begin{bmatrix} \cos(\theta_r) & \sin(\theta_r) & 1 & 0 \\ \cos(\theta_r - \frac{2\pi}{3}) & \sin(\theta_r - \frac{2\pi}{3}) & 1 & 0 \\ \cos(\theta_r + \frac{2\pi}{3}) & \sin(\theta_r + \frac{2\pi}{3}) & 1 & 0 \\ 0 & 0 & 0 & 1 \end{bmatrix} \cdot \begin{bmatrix} f_{qs} \\ f_{ds} \\ f_{0s} \\ f_{fd} \end{bmatrix} \quad (2.1.3.18)$$

The d - q voltage equations are derived, when the primed transformations $\mathbf{K}_s^{-1}(\theta_r)'$ and $\mathbf{K}_s(\theta_r)'$ are applied on equation (2.1.3.11). Equation (2.1.3.19) is written in matrix-vector form due to space considerations. The bold font denotes a matrix or a vector and the subscripts denote the indices of the vectors. For example, the vector \mathbf{f}_{uvwf} has four elements in the u , v , w and f axis.

$$\begin{aligned} \mathbf{K}_s(\theta_r)' \mathbf{v}_{uvwf} &= \mathbf{K}_s(\theta_r)' \mathbf{r}_s \mathbf{K}_s^{-1}(\theta_r)' \mathbf{K}_s(\theta_r)' \mathbf{i}_{uvwf} + \mathbf{K}_s(\theta_r)' \frac{d}{dt} \left(\mathbf{L}_l \mathbf{K}_s^{-1}(\theta_r)' \mathbf{K}_s(\theta_r)' \mathbf{i}_{uvwf} \right) \\ &+ \mathbf{K}_s(\theta_r)' \frac{d}{dt} \left(\mathbf{L}_s \mathbf{K}_s^{-1}(\theta_r)' \mathbf{K}_s(\theta_r)' \mathbf{i}_{uvwf} \right) \end{aligned} \quad (2.1.3.19)$$

The stator current vector \mathbf{i}_{uvwf} is transformed to the d - q frame as shown in equation (2.1.3.20) to derive the d - q current vector \mathbf{i}_{qdof} . The stator voltage vector \mathbf{v}_{uvwf} is transformed to the d - q frame according to equation (2.1.3.21) to derive the voltage vector in the d - q reference frame \mathbf{v}_{qdof} . Equations (2.1.3.20) and (2.1.3.21) are substituted into equation (2.1.3.19) to derive equation (2.1.3.22).

$$\mathbf{i}_{\text{qdof}} = \mathbf{K}_s(\theta_r)' \mathbf{i}_{\text{uvwf}} \quad (2.1.3.20) \quad \mathbf{v}_{\text{qdof}} = \mathbf{K}_s(\theta_r)' \mathbf{v}_{\text{uvwf}} \quad (2.1.3.21)$$

$$\begin{aligned} \mathbf{v}_{\text{qdof}} = & \mathbf{K}_s(\theta_r)' \mathbf{r}_s \mathbf{K}_s^{-1}(\theta_r)' \mathbf{i}_{\text{qdof}} + \mathbf{K}_s(\theta_r)' \frac{d}{dt} \left(\mathbf{L}_l \mathbf{K}_s^{-1}(\theta_r)' \mathbf{i}_{\text{qdof}} \right) \\ & + \mathbf{K}_s(\theta_r)' \frac{d}{dt} \left(\mathbf{L}_s \mathbf{K}_s^{-1}(\theta_r)' \mathbf{i}_{\text{qdof}} \right) \end{aligned} \quad (2.1.3.22)$$

Equation (2.1.3.22) can be further simplified with the expressions from equations (2.1.3.23) and (2.1.3.24). Equation (2.1.3.23) is equal to the resistance matrix \mathbf{r}_s and equation (2.1.3.24) is derived, when the differential product rule is applied.

$$\mathbf{r}_s = \mathbf{K}_s(\theta_r)' \mathbf{r}_s \cdot \mathbf{K}_s^{-1}(\theta_r)' \quad (2.1.3.23)$$

$$\mathbf{K}_s(\theta_r)' \frac{d}{dt} \left(\mathbf{L}_l \mathbf{K}_s^{-1}(\theta_r)' \mathbf{i}_{\text{qdof}} \right) = \mathbf{L}_l \frac{d}{dt} \mathbf{i}_{\text{qdof}} + \omega_e \mathbf{P}'_m \mathbf{L}_l \mathbf{i}_{\text{qdof}} \quad (2.1.3.24)$$

The permutation matrix \mathbf{P}'_m used in equation (2.1.3.24) is defined through equation (2.1.3.25) and introduces the cross-coupling between the d - and q -axis. The matrix is extended to take into account the field winding quantities.

$$\mathbf{P}'_m = \begin{bmatrix} 0 & 1 & 0 & 0 \\ -1 & 0 & 0 & 0 \\ 0 & 0 & 0 & 0 \\ 0 & 0 & 0 & 0 \end{bmatrix} \quad (2.1.3.25)$$

The rotor angle dependency is eliminated from equation (2.1.3.22) and the inductance matrix \mathbf{L}_s , when the matrix multiplication in the third part of the equation is performed. The result after the multiplication is shown in equation (2.1.3.26).

$$\begin{aligned} \mathbf{K}_s(\theta_r)' \frac{d}{dt} \left(\mathbf{L}_s \mathbf{K}_s^{-1}(\theta_r)' \mathbf{i}_{\text{qdof}} \right) = & \\ \begin{bmatrix} \frac{3}{2} \frac{N_s^2}{2} \pi l r \mu_0 \left(\alpha_1 - \frac{\alpha_2}{2} \right) \frac{d}{dt} i_q + \frac{N_s}{2} \frac{N_f}{2} \pi l r \mu_0 \left(\alpha_1 + \frac{\alpha_2}{2} \right) \omega_e i_{fd} + \frac{3}{2} \frac{N_s^2}{2} \pi l r \mu_0 \left(\alpha_1 + \frac{\alpha_2}{2} \right) \omega_e i_d \\ \frac{3}{2} \frac{N_s^2}{2} \pi l r \mu_0 \left(\alpha_1 + \frac{\alpha_2}{2} \right) \frac{d}{dt} i_d + \frac{N_s}{2} \frac{N_f}{2} \pi l r \mu_0 \left(\alpha_1 + \frac{\alpha_2}{2} \right) \frac{d}{dt} i_{fd} - \frac{3}{2} \frac{N_s^2}{2} \pi l r \mu_0 \left(\alpha_1 - \frac{\alpha_2}{2} \right) \omega_e i_q \\ 0 \\ \frac{N_f^2}{2} \pi l r \mu_0 \left(\alpha_1 + \frac{\alpha_2}{2} \right) \frac{d}{dt} i_{fd} + \frac{3}{2} \frac{N_f}{2} \frac{N_s}{2} \pi l r \mu_0 \left(\alpha_1 + \frac{\alpha_2}{2} \right) \frac{d}{dt} i_d \end{bmatrix} & \end{aligned} \quad (2.1.3.26)$$

The d - q self and mutual inductances can be derived from equation (2.1.3.26). The explicit form of the d - q inductances is shown in equation (2.1.3.27).

$$\begin{aligned} L_q = \frac{3}{2} \frac{N_s^2}{2} \pi l r \mu_0 \left(\alpha_1 - \frac{\alpha_2}{2} \right) \quad L_d = \frac{3}{2} \frac{N_s^2}{2} \pi l r \mu_0 \left(\alpha_1 + \frac{\alpha_2}{2} \right) \quad L_{fd} = \frac{2}{3} \frac{N_f}{N_s} L_d \\ M_{fdd} = \frac{N_f}{N_s} L_d \quad M_{dfd} = \frac{2}{3} \frac{N_f}{N_s} L_d \quad M_{qfd} = \frac{2}{3} \frac{N_f}{N_s} L_d \end{aligned} \quad (2.1.3.27)$$

Equation (2.1.3.26) can be transformed into a matrix form with the derived mutual and self inductances. The result is shown in equation (2.1.3.28).

$$\begin{aligned}
 \mathbf{K}_s(\theta_r)' \frac{d}{dt} \left(\mathbf{L}_s \mathbf{K}_s^{-1}(\theta_r)' \mathbf{i}_{qd0f} \right) &= \overbrace{\begin{bmatrix} L_{qq} & 0 & 0 & M_{qfd} \\ 0 & L_{dd} & 0 & M_{dfd} \\ 0 & 0 & 0 & 0 \\ 0 & M_{fdd} & 0 & L_{fd} \end{bmatrix}}^{\mathbf{L}_{sQD}} \cdot \frac{d}{dt} \begin{bmatrix} i_{qs} \\ i_{ds} \\ i_{0s} \\ i_{fd} \end{bmatrix} \\
 + \omega_e \begin{bmatrix} 0 & 1 & 0 & 0 \\ -1 & 0 & 0 & 0 \\ 0 & 0 & 0 & 0 \\ 0 & 0 & 0 & 0 \end{bmatrix} \overbrace{\begin{bmatrix} L_{qq} & 0 & 0 & 0 \\ 0 & L_{dd} & 0 & 0 \\ 0 & 0 & 0 & 0 \\ 0 & 0 & 0 & 0 \end{bmatrix}}^{\mathbf{L}_{sQD,emf}} \cdot \begin{bmatrix} i_{qs} \\ i_{ds} \\ i_{0s} \\ i_{fd} \end{bmatrix} & \quad (2.1.3.28)
 \end{aligned}$$

Equation (2.1.3.28) shows, that the transformations from equations (2.1.3.9) and (2.1.3.10) remove the rotor angle dependency in the inductance terms. Equation (2.1.3.28) can be then rewritten with matrix symbols as shown in equation (2.1.3.29).

$$\mathbf{K}_s(\theta_r)' \frac{d}{dt} \left(\mathbf{L}_s \mathbf{K}_s^{-1}(\theta_r)' \mathbf{i}_{qd0f} \right) = \mathbf{L}_{sQD} \frac{d}{dt} \mathbf{i}_{qd0f} + \omega_e \mathbf{P}'_m \mathbf{L}_{sQD,emf} \cdot \mathbf{i}_{qd0f} \quad (2.1.3.29)$$

After the performed mathematical reformulations, described through equations (2.1.3.29), (2.1.3.24) and (2.1.3.23), the d - q voltage equations are transformed into their final d - q form in a matrix-vector notation. The result is shown in equation (2.1.3.30).

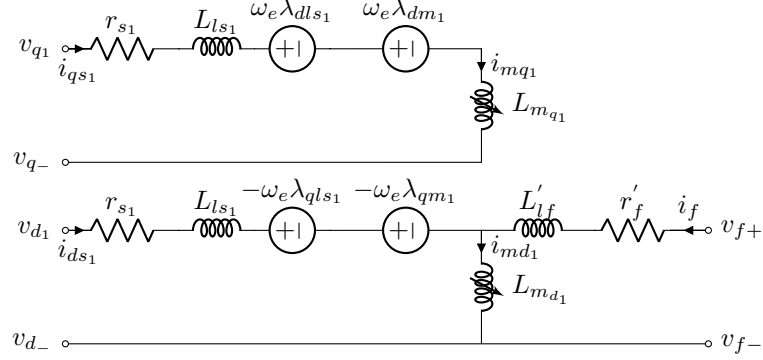
$$\mathbf{v}_{qd0f} = \mathbf{r}_s \mathbf{i}_{qd0f} + \mathbf{L}_l \frac{d}{dt} \mathbf{i}_{qd0f} + \mathbf{L}_{sQD} \frac{d}{dt} \mathbf{i}_{qd0f} + \omega_e \mathbf{P}'_m \mathbf{L}_l \mathbf{i}_{qd0f} + \omega_e \mathbf{P}'_m \mathbf{L}_{sQD,emf} \mathbf{i}_{qd0f} \quad (2.1.3.30)$$

The derived voltage equations correspond to the d - q equivalent circuit scheme of the three-phase machine shown in Fig. 2.3. The figure includes also a symbol for a variable main inductance, which takes into account saturation of the main inductance. The saturation and cross-magnetization are included in the voltage equations in Subsection 2.1.5.

2.1.4 Deriving the Torque Equation

In this subsection an expression of the generated machine torque is derived for the linear three-phase machine model. The torque expression is derived starting from the general expression for the energy, W_f , coupled in an inductor (2.1.4.1). This approach is described in detail in referece [38].

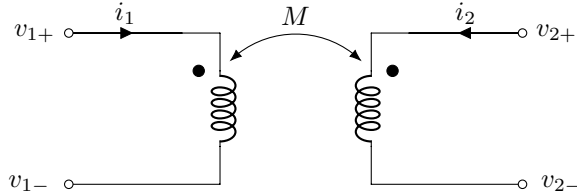
$$W_f = \frac{1}{2} L(t) i(t)^2 \quad (2.1.4.1)$$


Figure 2.3 – Three-Phase d - q Equivalent Circuit

Equation (2.1.4.1) can be extended to take into account two coupled inductors. The energy in the whole system from Fig. 2.4 is then the sum of the stored energy in both inductors due to their own currents and the energy stored in the mutual inductance due to the product of both currents. This relationship is described mathematically through equation (2.1.4.2).

$$W_{\text{fL1L2}} = \frac{1}{2}L_1I_1^2 + \frac{1}{2}L_2I_2^2 + \frac{1}{2}M_{12}I_1I_2 \quad (2.1.4.2)$$

A schematic of both inductors with their electromagnetic coupling is provided in Fig. 2.4. If the system has a leakage inductance, which is the case with the three-phase machine, the leakage inductances do not store energy in the coupling field and do not contribute to the generated torque. The energy of the three-phase salient-pole machine is stored


Figure 2.4 – Two Coupled Inductors

in the air-gap of the machine and results from the coupling between the three stator windings and the field winding. The stored energy in the coupled field is expressed in equation (2.1.4.3) with the matrix \mathbf{L}_s from equation (2.1.3.14). The matrix contains all self and mutual inductances of the machine.

$$W_f = \frac{1}{2} \mathbf{i}_{\text{uvw}f}^T \mathbf{L}_s \mathbf{i}_{\text{uvw}f} \quad (2.1.4.3)$$

When Newton's Law is applied to equation (2.1.4.3), one derives equation (2.1.4.4).

$$dW_f = T_e d\theta_m \quad \text{with} \quad \theta_m = \frac{2}{P} \theta_e \quad \Rightarrow \quad T_e = \frac{P}{2} \frac{dW_f}{d\theta_e} \quad (2.1.4.4)$$

The coupled field energy in the air-gap of the machine W_f is substituted in equation (2.1.4.4) to derive equation (2.1.4.5). Equation (2.1.4.5) describes the torque as a function of currents and inductances.

$$T_e = \frac{P}{2} \frac{1}{2} \mathbf{i}_{uvwf}^T \frac{d\mathbf{L}_s}{d\theta_e} \mathbf{i}_{uvwf} \quad (2.1.4.5)$$

If the current vector \mathbf{i}_{uvwf} is substituted with the product of the backwards transformation and the \mathbf{i}_{qd0f} current vector, then the torque equation in the d - q frame is derived. The result is shown in equations (2.1.4.6) and (2.1.4.7).

$$T_e = \frac{3}{2} \frac{P}{2} \left(\frac{N_f N_s}{2} \pi r l \mu_0 (\alpha_1 + \frac{\alpha_2}{2}) i_{fd} i_q + \frac{3}{2} \frac{N_s^2}{2} \pi r l \mu_0 \alpha_2 i_d i_q \right) \quad (2.1.4.6)$$

$$T_e = \frac{3}{2} \frac{P}{2} (L'_{fd} \cdot i'_{fd} \cdot i_q + (L_d - L_q) i_d i_q) \quad (2.1.4.7)$$

2.1.5 Saturation and Cross-Magnetization

The linear voltage equations, as shown in equation (2.1.3.28), do not include the effects of saturation and cross-magnetization. These physical properties are of a non-linear nature and their exact behavior depends on the material used for the stator and rotor. Figure 2.5 shows a typical relationship between the magnetic field strength \vec{H} , which is generated by the flowing current, and the magnetic flux density \vec{B} , which is an amplification of the field \vec{H} and depends on the magnetic permeability μ_r of the material used. The magnetic materials exhibit also hysteresis and eddy current losses, which are considered in Section 2.3.2. This subsection handles only the non-linear relationship between magnetizing current and magnetic flux. The non-linearity is typical only for the main inductance and not for the stator leakage inductances [15].

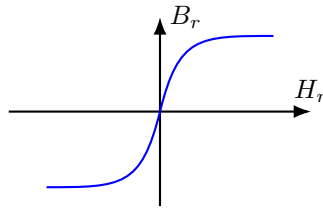


Figure 2.5 – B-H Curve

The non-linear relationship between the magnetizing current i_m and magnetizing flux λ_m is described through an arcustangens function [15]. In reference [15], it is assumed that the relationship between flux linkage and magnetizing current is linear in the unsaturated

and fully saturated regions. A mathematical formulation of this assumption is shown in equation (2.1.5.1).

$$\frac{dF(\lambda_{md})}{d\lambda_{md}} = \frac{2}{\pi} M_d \arctan(\tau_T (\lambda_{md} - \lambda_T)) + M_a \quad (2.1.5.1)$$

The parameters M_d and M_a are defined in equations (2.1.5.2) and (2.1.5.3) as functions of the initial M_i and final M_f slope of the arcustangens function.

$$M_d = \frac{M_f - M_i}{2} \quad (2.1.5.2) \quad M_a = \frac{M_f + M_i}{2} \quad (2.1.5.3)$$

Equation (2.1.5.1) is plotted in Fig. 2.6. The slope of the saturation curve is initially constant, then it undergoes a transition around the flux λ_T . At higher fluxes ($\lambda_m \gg \lambda_T$) the slope is also constant. The parameter τ_T is the form factor of the transition

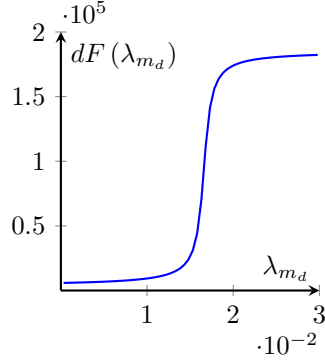


Figure 2.6 – Slope of a Saturation Curve

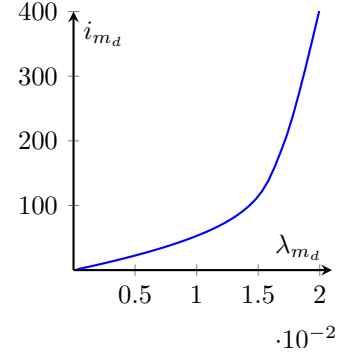


Figure 2.7 – Sat. Curve $i_{md} = F(\lambda_{md})$

between unsaturated and saturated region. The transition flux λ_T is the flux linkage at the intersection point between both tangents - the linear unsaturated region and the linear saturated region. When equation (2.1.5.1) is integrated over the magnetizing flux λ_{md} , equation (2.1.5.4) is derived.

$$F(\lambda_{md}) = \frac{2M_d}{\pi} [(\lambda_{md} - \lambda_T) \arctan \tau_T (\lambda_{md} - \lambda_T) - \lambda_T \arctan \tau_T \lambda_T] + \frac{M_d}{\pi \tau_T} \left[\ln \left(1 + \tau_T^2 \lambda_T^2 \right) - \ln \left(1 + \tau_T^2 (\lambda_{md} - \lambda_T)^2 \right) \right] + M_a \lambda_{md} \quad (2.1.5.4)$$

The parameters describing the plotted saturation curve are derived from measurements in Section 2.4. Equation (2.1.5.4) describes only the saturation of the d -axis as a function of the d -axis magnetizing flux. One approach to consider also the saturation of the q -axis is to introduce an anisotropic factor α . The anisotropic factor is defined in equation (2.1.5.5) as the square root of the ratio between the q - and d -axis inductances. Reference [46] converts the anisotropy of the salient-pole machine into an equivalent isotropic

machine through this method. This way one is able to calculate the saturated q - and d -axis inductances only through one saturation curve of the d -axis [46].

$$\alpha = \sqrt{\frac{L_{mq0}}{L_{md0}}} = \sqrt{\frac{L_{mq}}{L_{md}}} = \text{constant} \quad (2.1.5.5)$$

According to reference [46] the anisotropic salient-pole machine can be converted into an equivalent isotropic one and thus the saturation and cross-magnetization of both axes can be taken into account. For this purpose the equivalent magnetizing flux λ'_m , the equivalent magnetizing current i'_m and the equivalent magnetizing inductance L'_m are introduced through equation (2.1.5.6) [45].

$$\lambda'_m = \sqrt{\lambda_{md}^2 + \frac{\lambda_{mq}^2}{\alpha^2}} \quad i'_m = \sqrt{i_{md}^2 + i_{mq}^2 \alpha^2} \quad L'_m = \frac{\lambda'_m}{i'_m} \quad (2.1.5.6)$$

The magnetization curve, which can be calculated from the back-emf voltage induced during no-load tests, is set equal to $\lambda'_m = f(i'_m)$, where f is the inverse function of the saturation curve from equation (2.1.5.4). The relationship between the q - and d -axis magnetizing fluxes, λ_{mq} and λ_{md} , the q - and d -axis magnetizing inductances, L_{mq} and L_{md} , and q - and d -axis magnetizing currents, i_{mq} and i_{md} , are derived through equation (2.1.5.7) and the definition from equation (2.1.5.6) .

$$\lambda_{md} = L_{md} i_{md} = L'_m i_{md} \quad \lambda_{mq} = L_{mq} i_{mq} = L'_m \alpha^2 i_{mq} \quad (2.1.5.7)$$

Both fluxes along the d - and q -axis, $\lambda_{md}(t)$ and $\lambda_{mq}(t)$, are functions of time¹. Therefore the saturation function from equation (2.1.5.4) has partial derivatives after the d - and q -axis magnetizing fluxes λ_{mq} and λ_{md} . This is symbolically illustrated through equation (2.1.5.8).

$$\begin{bmatrix} di_{mq} \\ di_{md} \end{bmatrix} = \begin{bmatrix} dF_{qq} & dF_{qd} \\ dF_{dq} & dF_{dd} \end{bmatrix} \cdot \begin{bmatrix} d\lambda_{mq} \\ d\lambda_{md} \end{bmatrix} \quad (2.1.5.8)$$

Equation (2.1.3.28) is derived with the assumption for linear inductances. The flux linkage derivatives do not depend only on the current derivatives $\frac{d}{dt} i_{qd}$ but also on the inductance derivatives $\frac{d}{dt} L_{sQD}$ because of the non-linear function shown in equation (2.1.5.4), . This matrix is called a differential inductance matrix. The matrix is derived, when the differential rule is applied to the product of the inductances and currents as shown in equation (2.1.5.9).

$$\frac{d}{dt} \lambda(t) = \frac{d}{dt} (L(t) \cdot i(t)) = \frac{d}{dt} L(t) \cdot i(t) + \frac{d}{dt} i(t) \cdot L(t) \quad (2.1.5.9)$$

It is assumed that the explicit expression of the saturation function is unknown and that, it is a function of both currents i_{md} and i_{mq} . Then the inductance derivative is calculated

¹Due to the change of the rotor position or the change of the currents along the d - and q -axis also the fluxes change with time.

through the formula shown in equation (2.1.5.10) after applying a partial differentiation [44].

$$\frac{d}{dt} L'_m = \left(\overbrace{\frac{d\lambda'_m}{di'_m}}^{L'_{m,diff}} - L'_m \right) \cdot \frac{1}{i_m^2} \left(i_{md} \frac{d}{dt} i_{md} + \alpha^2 i_{mq} \frac{d}{dt} i_{mq} \right) \quad (2.1.5.10)$$

The expressions for the inductances L_{dd} , L_{qq} , L_{qd} and L_{dq} are derived from equation (2.1.5.10) and shown in equation (2.1.5.11).

$$\begin{aligned} dL_{dd} &= L'_{m,diff} \frac{i_{md}^2}{i_m} + L'_m \frac{\alpha i_{mq}^2}{i'_m} & dL_{qq} &= \alpha^2 \left(L'_m \frac{i_{md}^2}{i_m} + L'_{m,diff} \frac{i_{md}^2}{i_m} \right) \\ dL_{dq} &= dL_{qd} = \alpha \left(L'_{m,diff} - L'_m \right) \frac{i_{md} i_{mq}}{i_m i_m} \end{aligned} \quad (2.1.5.11)$$

Equation (2.1.5.11) shows that the model with saturation and cross-saturation includes the q - and d -axis differential inductances and the cross-coupling differential inductances between the d - and q -axis: dL_{qd} and dL_{dq} . The saturation model, defined through equation (2.1.5.4), describes the magnetizing current as a function of the magnetizing flux linkage $i_{md} = F(\lambda_{md})$. Therefore the inductance derivatives, as shown in equation (2.1.5.11), cannot be explicitly derived. The differential inductances can be calculated indirectly through the calculation of the differential inverse inductances $d\Gamma_{qq}$, $d\Gamma_{dd}$, $d\Gamma_{qd}$ and $d\Gamma_{dq}$.

The relationship between the equivalent magnetizing current i'_m and the equivalent magnetizing flux λ'_m is derived with the saturation function from equation (2.1.5.4) and with equation (2.1.5.6), which describes the conversion from an anisotropic to an isotropic machine.

$$i'_m = F(\lambda'_m) \quad (2.1.5.12)$$

$$\Gamma'_{diff} = \frac{d}{dt} \frac{1}{L'_m} = \left(\frac{di'_m}{d\lambda'} - \Gamma' \right) \cdot \frac{1}{\lambda_m^2} \left(\lambda_{md} \frac{d}{dt} \lambda_{md} + \frac{1}{\alpha^2} \lambda_{mq} \frac{d}{dt} \lambda_{mq} \right) \quad (2.1.5.13)$$

$$\begin{aligned} d\Gamma_{dd} &= \frac{1}{dL_{dd}} = \Gamma'_{diff} \frac{\lambda_{md}^2}{\lambda_m} + \Gamma' \frac{\lambda_{mq}^2}{\alpha \lambda'_m} & d\Gamma_{qq} &= \frac{1}{dL_{qq}} = \frac{1}{\alpha^2} \left(\Gamma' \frac{\lambda_{md}^2}{\lambda_m} + \Gamma'_{diff} \frac{\lambda_{md}^2}{\lambda_m} \right) \\ d\Gamma_{qd} &= d\Gamma_{dq} = \frac{1}{dL_{qd}} = \frac{1}{\alpha} (\Gamma'_{diff} - \Gamma') \frac{\lambda_{md} \lambda_{mq}}{\lambda_m \lambda_m} \end{aligned} \quad (2.1.5.14)$$

The differential inverse inductance from equation (2.1.5.13) and the derivatives of the inverse inductances from equation (2.1.5.14) are used to derive the differential magnetizing inductances dL_{qq} , dL_{dd} and dL_{qd} as shown in equation (2.1.5.15). Equation (2.1.5.15)

does not contain the expression of the saturation function F due to space considerations. The full form, also with the expression for F , is included in Appendix A.

$$\begin{aligned}
 d\Gamma_{\text{qq}} &= \frac{dF}{d\lambda'_m} \frac{\alpha \lambda_{\text{mq}}^2}{\lambda'_m} + \alpha \frac{F}{\lambda'_m} \left(1 - \alpha \left(\frac{\lambda_{\text{mq}}}{\lambda'_m} \right)^2 \right) & d\Gamma_{\text{qd}} &= \left(\frac{dF}{d\lambda'_m} - \frac{F}{\lambda'_m} \right) \alpha \lambda_{\text{mq}} \frac{\lambda_{\text{md}} + \lambda_{\text{mag}}^2}{\lambda'_m} \\
 \Gamma_{\text{dd}} &= \frac{dF}{d\lambda'_m} \left(\frac{(\lambda_{\text{md}} + \lambda_{\text{mag}})^2}{\lambda'_m} \right) + F/\lambda'_m \left(1 - ((\lambda_{\text{md}} + \lambda_{\text{mag}})/\lambda'_m)^2 \right) \\
 \Gamma_{\text{det}} &= d\Gamma_{\text{qq}} d\Gamma_{\text{dd}} - d\Gamma_{\text{qd}}^2 & dL_{\text{qq}} &= \frac{d\Gamma_{\text{dd}}}{\Gamma_{\text{det}}} & dL_{\text{qd}} &= -\frac{d\Gamma_{\text{qd}}}{\Gamma_{\text{det}}} & dL_{\text{dd}} &= \frac{d\Gamma_{\text{qq}}}{\Gamma_{\text{det}}}
 \end{aligned} \tag{2.1.5.15}$$

Equation (2.1.5.15) defines the differential inductances dL_{qq} , dL_{dd} and $dL_{\text{qd}} = dL_{\text{dq}}$. They can be integrated in one incremental inductance matrix \mathbf{L}_{mi} , which describes the non-linearity between the magnetizing currents vector, the magnetizing flux vector and the cross-coupling between d - and q -axis as shown in equation (2.1.5.16).

$$\begin{bmatrix} \lambda_{\text{mq}} \\ \lambda_{\text{mq}} \end{bmatrix} = \overbrace{\begin{bmatrix} dL_{\text{qq}} & dL_{\text{qd}} \\ dL_{\text{qd}} & dL_{\text{dd}} \end{bmatrix}}^{\mathbf{L}_{\text{mi}}} \cdot \begin{bmatrix} i_{\text{mq}} \\ i_{\text{md}} \end{bmatrix} \tag{2.1.5.16}$$

These inductances are integrated in the already derived linear model. This way, equation (2.1.3.28) can be adapted to take into account the magnetic saturation and cross-magnetization. The product of the differential inductance matrix $d\mathbf{L}_{\text{sQD}}$ and the differential currents are used to replace the differential magnetizing fluxes in the machine model. Equation (2.1.5.17) illustrates how the model is extended to include the non-linearity of the main inductance.

$$\mathbf{K}_s(\theta_r)' \frac{d}{dt} \left(\mathbf{L}_s \mathbf{K}_s^{-1}(\theta_r)' i_{\text{qdof}} \right) = \overbrace{\begin{bmatrix} dL_{\text{qq}} & dL_{\text{qd}} & 0 & dM_{\text{qfd}} \\ dL_{\text{qd}} & dL_{\text{dd}} & 0 & dM_{\text{dfd}} \\ 0 & 0 & 0 & 0 \\ dM_{\text{fdq}} & dM_{\text{fdd}} & 0 & dL_{\text{fdd}} \end{bmatrix}}^{d\mathbf{L}_{\text{sQD}}} \cdot \frac{d}{dt} \begin{bmatrix} i_{\text{qs}} \\ i_{\text{ds}} \\ i_{\text{0s}} \\ i_{\text{fd}} \end{bmatrix} + \omega_e \mathbf{P}'_{\text{m}} \cdot \begin{bmatrix} \lambda_{\text{mq}} \\ \lambda_{\text{md}} \\ \lambda_{\text{m0}} \\ \lambda_{\text{mf}} \end{bmatrix} \tag{2.1.5.17}$$

The mutual differential inductances with saturation are shown in equation (2.1.5.18). They take into account the effective number of turns of the rotor N_f and the stator N_s . The factor $\frac{2}{3}$ is included due to the Park's transformation for the mutual inductances, M_{qfd} and M_{dfd} , in the stator d - q reference frame. The mutual inductances, M_{fdq} and M_{fdd} , employed in the field winding equation do not have to be scaled with the factor as they are written out in the rotor reference frame.

$$M_{\text{fdq}} = \frac{N_f}{N_s} dL_{\text{qd}} \quad M_{\text{fdd}} = \frac{N_f}{N_s} dL_{\text{dd}} \quad M_{\text{qfd}} = \frac{2}{3} \frac{N_f}{N_s} dL_{\text{qd}} \quad M_{\text{dfd}} = \frac{2}{3} \frac{N_f}{N_s} dL_{\text{dd}} \tag{2.1.5.18}$$

2.1.6 Direct-Quadrature Axis Model with Saturation

The current subsection introduces the formulation of the DQ model for the three-phase synchronous machine with saturation and cross-magnetization of the main inductance. The linear voltage equations in the d - q frame are already derived in equation (2.1.3.30). The linear voltage equations are extended to take into account the saturation with the theory presented in Subsection 2.1.5. The differential inductances are integrated in the voltage equations, as shown in equation (2.1.6.1), to include the saturation modeling.

$$\mathbf{v}_{\text{qdof}} = \mathbf{r}_s \mathbf{i}_{\text{qdof}} + \mathbf{L}_1 \mathbf{p} \mathbf{i}_{\text{qdof}} + \overbrace{\mathbf{d} \mathbf{L}_{\text{sQD}} \mathbf{p}}^{d\lambda_{\text{mqdof}}} \mathbf{i}_{\text{qdof}} + \omega_e \mathbf{P}'_{\text{m}} \mathbf{L}_1 \mathbf{i}_{\text{qdof}} + \omega_e \mathbf{P}'_{\text{m}} \lambda_{\text{mqdof}} \quad (2.1.6.1)$$

The DQ model offers the advantage of an easy calculation of the machine variables and is described as a voltage-in-current-out type. For this type of models the voltages are applied as input quantities to the model and the current is calculated after solving the differential equations. The equations are calculated in the rotor reference frame and cannot be easily interfaced with the stationary ABC frame. Other electric components, like batteries and loads, are however modeled in the stationary ABC frame. Software programs like PLECS [68] provide solvers and simulation environment for the stationary ABC domain. If the model has to be employed in a system simulation studies with the interaction of other loads in the electrical system fictitious snubber $R - C$ elements, as illustrated in Fig. 2.8, have to be added in parallel to the controlled current sources [5]. The current sources are controlled by the currents, which are the solution from the voltage equations written out in (2.1.6.1). Figure 2.8 shows the block diagram of a three-phase DQ model. On the left side of the plot the ABC domain (or UVW) is illustrated. The machine model in the ABC domain is represented through voltage-controlled sources. The signals “driving” the voltage-controlled sources are calculated in the d - q domain on the right side. In order to calculate the control signals the applied UVW and field winding voltages are transformed to the d - q frame. These voltages are used to calculate the magnetizing fluxes λ_{mq} and λ_{md} and the stator currents \mathbf{i}_{qdof} . The model derivation is explained based on the d - q voltage equations shown in (2.1.6.1). The derivation of the model is based on two differential equations, which are solved for the magnetizing fluxes λ_{mq} and λ_{md} , and four differential equations, which are solved for the stator currents contained in the stator currents vector \mathbf{i}_{qdof} .

Equation (2.1.6.1) is rearranged in such a way, that the differential stator currents $\mathbf{p} \mathbf{i}_{\text{qdof}}$ are taken out of the brackets and the voltage equations are solved for the differential currents vector $\mathbf{p} \mathbf{i}_{\text{qdof}}$ as shown in equation (2.1.6.2).

$$\mathbf{p} \mathbf{i}_{\text{qdof}} = [\mathbf{L}_1 + \mathbf{d} \mathbf{L}_{\text{sQD}}]^{-1} \cdot [\mathbf{v}_{\text{qdof}} - (\mathbf{r}_s \mathbf{i}_{\text{qdof}} + \omega_e \mathbf{P}'_{\text{m}} (\mathbf{L}_1 \mathbf{i}_{\text{qdof}} + \lambda_{\text{mqdof}}))] \quad (2.1.6.2)$$

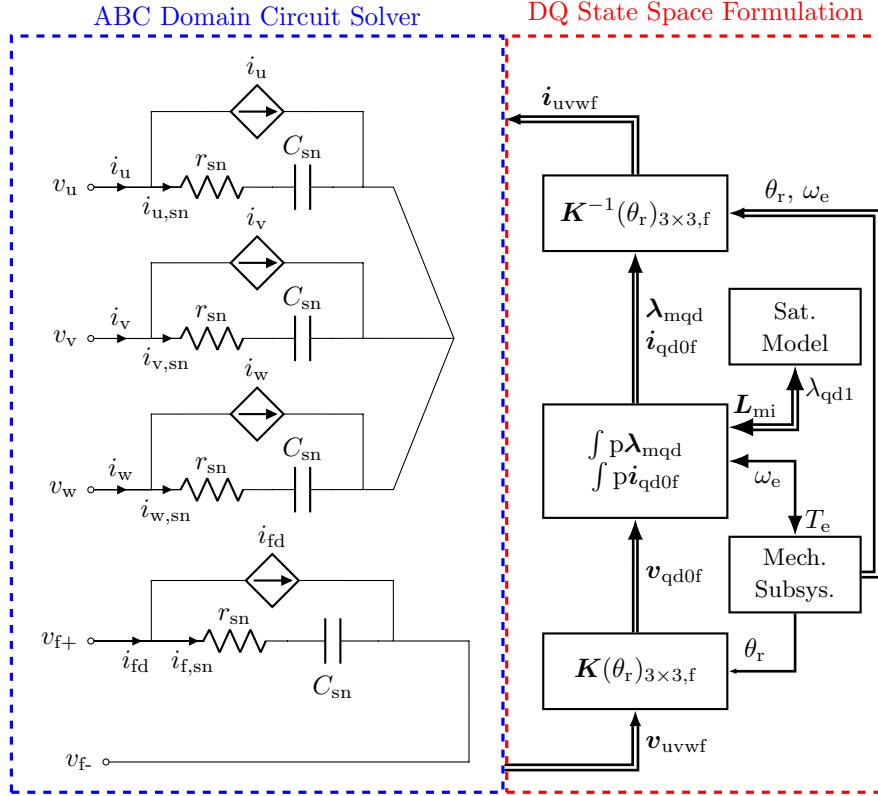


Figure 2.8 – Three-Phase DQ Model Overview

Equation (2.1.6.2) contains the magnetic flux vector λ_{mqd0f} as unknown variables, which can be derived from equation (2.1.5.17).

$$\frac{d}{dt} \begin{bmatrix} \lambda_{mq} \\ \lambda_{md} \\ \lambda_{m0} \\ \lambda_{mf} \end{bmatrix} = \begin{bmatrix} dL_{qq} & dL_{qd} & 0 & dM_{qfd} \\ dL_{qd} & dL_{dd} & 0 & dM_{dfd} \\ 0 & 0 & 0 & 0 \\ M_{fdq} & M_{fdd} & 0 & dL_{fdd} \end{bmatrix} \cdot \frac{d}{dt} \begin{bmatrix} i_{qs} \\ i_{ds} \\ i_{0s} \\ i_{fd} \end{bmatrix} \quad (2.1.6.3)$$

The magnetic flux in 0-direction is not relevant for the energy conversion and the torque production in the machine. The magnetic flux referred to the field winding λ_{mf} is linearly dependent through the turns ratio between stator and rotor from the magnetizing flux in d -direction λ_{md} . Therefore, only the λ_{mq} and λ_{md} fluxes are calculated. The differential magnetic fluxes $\frac{d}{dt}\lambda_{mq}$ and $\frac{d}{dt}\lambda_{md}$ from equation (2.1.6.3) are integrated through a differential solver and the magnetic fluxes λ_{md} and λ_{mq} are derived. Both differential

equations, resulting from the two upper rows from equation (2.1.6.3), are shown in equation (2.1.6.4).

$$\frac{d}{dt} \begin{bmatrix} \lambda_{mq} \\ \lambda_{md} \end{bmatrix} = \begin{bmatrix} dL_{qq} & dL_{qd} & 0 & dM_{qfd} \\ dL_{qd} & dL_{dd} & 0 & dM_{dfd} \end{bmatrix} \frac{d}{dt} \begin{bmatrix} i_{qs} \\ i_{ds} \\ i_{0s} \\ i_{fd} \end{bmatrix} \quad (2.1.6.4)$$

The state space model for the three-phase DQ machine model is set up with equations (2.1.6.2) and (2.1.6.4). All six equations are taken into account and thus the model consists of six independent state space variables: i_{qs} , i_{ds} , i_{0s} , i_{fd} , λ_{mq} and λ_{md} . A computer simulation program is used to solve the six differential equations and the result is the state space variables as outputs from the model. The calculated currents in d - q frame are transformed back to the ABC frame as illustrated in Fig. 2.8 and used as inputs to the controlled current sources. Through the parallel connected R - C snubber circuits, a back-emf voltage is generated, which acts against the applied voltage at the machine terminals. In order to connect the electrical subsystem to the mechanical domain, the electromagnetic torque T_e is calculated in the d - q frame according to equation (2.1.6.5).

$$T_e = \frac{3}{2} \frac{P}{2} (\lambda_{md} i_{mq} - \lambda_{mq} i_{md}) \quad (2.1.6.5)$$

2.1.7 Voltage-Behind-Reactance Model with Saturation

The introduction of a suitable d - q transformation removes the angle dependency in the inductances and enables an easy and efficient way of calculation of the machine voltages, torque, fluxes and power. The interaction with the rest of the power electronics takes places in the stationary ABC domain. Therefore, a way is required to connect both domains:

- the d - q domain, where the calculation of machine quantities is performed.
- the ABC domain, where the simulation of the stationary elements like power switches, capacitors and resistances takes place.

There are a couple of methods known in the electric machine modeling literature, which enable the interconnection with stationary elements [71]:

- the Coupled-Circuit (CC) method.
- the VBR method.
- the DQ method with voltage-controlled current sources and snubber R - C elements.

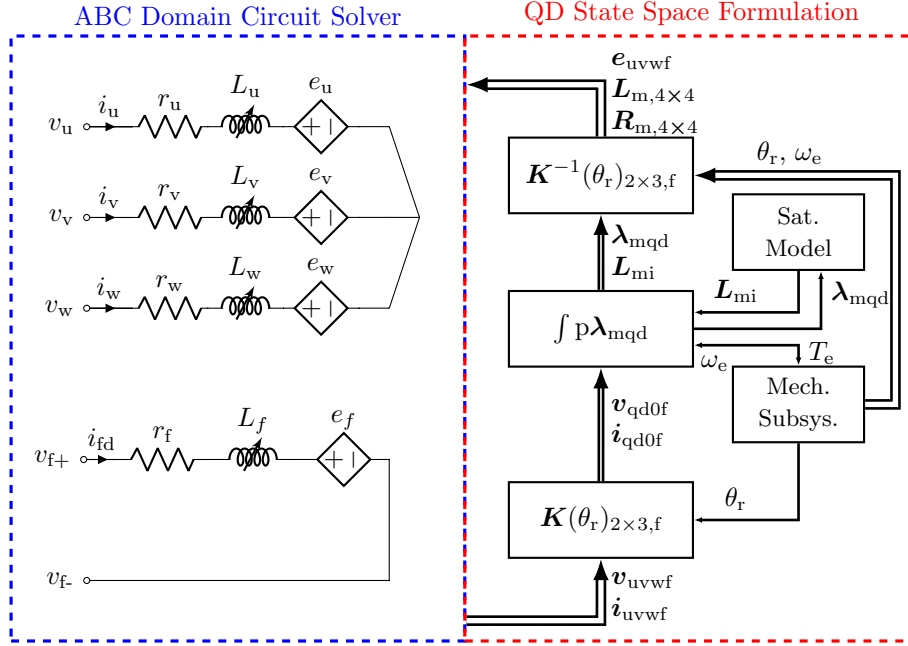


Figure 2.9 – Three-Phase VBR Model Overview

The CC method is represented by the machine equations without applying any transformation and is calculated directly in the ABC stator reference frame. Thus, for salient-pole machines, the rotor dependency is present in the voltage and torque equations due to the angle dependent inductance terms. Therefore, this method is not suitable for fast dynamic simulations [71]. The DQ method with snubber R - C elements is described in Subsection 2.1.6. The VBR method [55, 75] is a machine model implemented as a back-emf voltage behind a R - L reactance as shown in Fig. 2.9. The machine behavior is hidden behind time-varying controlled voltage sources, representing the machine behavior in the ABC domain. In contrast to this method the DQ method is an implementation of the machine behavior through controlled current sources. The dynamic machine behavior is represented through a controlled-coupled inductances approach [68]. The coupled inductances are illustrated in the ABC domain in Fig. 2.9 and include the mutual coupling between the machine windings. The voltage drop over a single controlled inductance is shown in equation (2.1.7.1) in order to clarify better the usage of coupled inductances in the VBR machine model [68]. The principle is based on the product differentiation rule. The inductive term is emphasized with a red rectangle and the resistive term with a blue rectangle.

$$v = \frac{di}{dt} (L \cdot i) = \boxed{L} \cdot \frac{di}{dt} + \boxed{\frac{dL}{dt}} \cdot i \quad (2.1.7.1)$$

When a coupling between multiple n phases is introduced, the control signals increase up to $2 \cdot n^2$. The voltage drops over two coupled variable inductors are shown in equation

(2.1.7.2). The signals for the variable inductances are then provided as a control vector with the following entries: $\left[L_{11} \ L_{12} \ L_{21} \ L_{22}, \frac{d}{dt}L_{11} \ \frac{d}{dt}L_{12} \ \frac{d}{dt}L_{21} \ \frac{d}{dt}L_{22} \right]$.

$$\begin{bmatrix} v_1 \\ v_2 \end{bmatrix} = \begin{bmatrix} L_{11} & L_{12} \\ L_{21} & L_{22} \end{bmatrix} \cdot \frac{d}{dt} \begin{bmatrix} i_1 \\ i_2 \end{bmatrix} + \frac{d}{dt} \begin{bmatrix} L_{11} & L_{12} \\ L_{21} & L_{22} \end{bmatrix} \cdot \begin{bmatrix} i_1 \\ i_2 \end{bmatrix} \quad (2.1.7.2)$$

For the representation of the three-phase externally-excited machine through the VBR method the coupled inductances have to have $2 \cdot 4^2$ control signals. The voltage drop over the stator resistances is straightforward and does not need any further clarification. The right side of Figure 2.9 represents schematically the steps required to calculate the control signals for the back-emf voltages and the inductance terms. These are summarized here in five steps:

1. Forwards transformation of the ABC currents and voltages.
2. Setting forth and solving differential equations after λ_{md} and λ_{mq} .
3. Calculating the saturated differential inductance matrix with the saturation model based on the magnetic fluxes λ_{md} and λ_{mq} .
4. Solving the mechanical equations to calculate the rotor position θ_r and the angular speed ω_e .
5. Applying the backwards transformation on the voltage equations in order to calculate the back-emf voltages e_{uvw1f} and the control signals for the coupled inductances.

As Fig. 2.9 shows, one difference in the state space part of the VBR model in comparison to the DQ model, is that the currents in the VBR model are no longer state variables. The currents are “measured” via virtual ampere meters in the simulation program and transformed in the d - q reference frame. They are used in solving the differential equations after λ_{md} and λ_{mq} . The backwards transformation is applied to the d - q voltage equations for deriving the VBR model. In contrast to that, the backwards transformation is applied to the d - q currents for the derivation of the DQ model. This is evident, when Fig. 2.8 and Fig. 2.9 are compared. Through this step the control signals for the coupled inductances and the back-emf voltages are derived. The state-space block consists of equations (2.1.6.2) and (2.1.6.4), which are already derived in Subsection 2.1.6. In order to derive the matrixes $\mathbf{L}_{m,4 \times 4}$ and $\mathbf{R}_{m,4 \times 4}$ and the back-emf terms e_{uvw1f} , the backwards transformation is applied to equation (2.1.6.1). Equation (2.1.7.3) is derived this way.

$$\begin{aligned} \mathbf{K}_s^{-1}(\theta_r)' \mathbf{v}_{qd0f} = & \mathbf{K}_s^{-1}(\theta_r)' (\mathbf{r}_s \mathbf{i}_{qd0f} + \mathbf{L}_l \mathbf{p} \mathbf{i}_{qd0f} + \overbrace{\frac{d\lambda_{mqd0f}}{dt} \mathbf{L}_{sQDP}} \mathbf{i}_{qd0f} \\ & + \omega_e \mathbf{P}'_m \mathbf{L}_l \mathbf{i}_{qd0f} + \omega_e \mathbf{P}'_m \lambda_{mqd0f}) \end{aligned} \quad (2.1.7.3)$$

The transformed d - q currents \mathbf{i}_{qd0f} from equation (2.1.7.3) have to be represented through the currents in the ABC domain (\mathbf{i}_{uvw1f}). The forwards transformation $\mathbf{K}_s(\theta_r)'$ from

equation (2.1.3.15) is used to represent the current vectors $p\mathbf{i}_{\text{qd0f}}$ and \mathbf{i}_{qd0f} through the currents vector \mathbf{i}_{uvw} in the stator reference frame as shown in equations (2.1.7.5) and (2.1.7.4).

$$p\mathbf{i}_{\text{qd0f}} = p\mathbf{K}_s(\theta_r)' \cdot \mathbf{i}_{\text{uvw}} + \mathbf{K}_s(\theta_r)' \cdot p\mathbf{i}_{\text{uvw}} \quad (2.1.7.4)$$

$$\mathbf{i}_{\text{qd0f}} = \mathbf{K}_s(\theta_r)' \cdot \mathbf{i}_{\text{uvw}} \quad (2.1.7.5)$$

Equation (2.1.7.3) is transformed into equation (2.1.7.6) when the substitutions are applied.

$$\begin{aligned} \mathbf{v}_{\text{uvw}} = & r_s \mathbf{i}_{\text{uvw}} + \mathbf{K}_s^{-1}(\theta_r)' ((L_1 + dL_{\text{sQD}}) p\mathbf{K}_s(\theta_r)' + \omega_e \mathbf{P}'_m L_1 \mathbf{K}_s(\theta_r)') \cdot \mathbf{i}_{\text{uvw}} + \\ & \mathbf{K}_s^{-1}(\theta_r)' (L_1 + dL_{\text{sQD}}) \mathbf{K}_s(\theta_r)' \cdot p\mathbf{i}_{\text{uvw}} + \omega_e \mathbf{P}'_m \boldsymbol{\lambda}_{\text{mqd0f}} \end{aligned} \quad (2.1.7.6)$$

The required control signals, shown in Fig. 2.9, are extracted from equation (2.1.7.6) and written out in their explicit form in equations (2.1.7.7), (2.1.7.8) and (2.1.7.9). This way, the VBR three-phase synchronous machine model is derived.

$$\mathbf{R}_{\text{m},4 \times 4} = \mathbf{K}_s^{-1}(\theta_r)' (L_1 + dL_{\text{sQD}}) \mathbf{K}_s(\theta_r)' \quad (2.1.7.7)$$

$$\mathbf{L}_{\text{m},4 \times 4} = \mathbf{K}_s^{-1}(\theta_r)' ((L_1 + dL_{\text{sQD}}) p\mathbf{K}_s(\theta_r)' + \omega_e \mathbf{P}'_m L_1 \mathbf{K}_s(\theta_r)') \quad (2.1.7.8)$$

$$\mathbf{e}_{\text{uvw}} = \omega_e \mathbf{P}'_m \boldsymbol{\lambda}_{\text{mqd0f}} \quad (2.1.7.9)$$

2.1.8 Mechanical Modeling

The mechanical subsystem from Figures 2.8 and 2.9 is modeled through two differential equations (2.1.8.1) and (2.1.8.2). Both equations represent the angular motion of the rotor. These equations are derived when Newton's Law is applied on an angular displacement.

$$p\omega_m = \frac{1}{J} (T_e - F\omega_m - T_m) \quad (2.1.8.1)$$

$$p\theta_m = \omega_m \quad (2.1.8.2)$$

The symbol F is the friction coefficient, T_e is the electromagnetic torque and T_m is the load torque. The mechanical rotor position is represented by θ_m and the mechanical angular speed is ω_m . The rotor inertia is represented by the symbol J .

2.2 Six-Phase Dual-Voltage Salient-Pole Machine Model

Section 2.1 explains the modeling of a three-phase salient-pole machine and sets the base for the six-phase machine model theory. The section introduces the terms MMF, self- and mutual inductances and the torque equation for a three-phase machine. Further it explains the terms effective number of turns and the technique of referring the rotor circuit to the stator system. The terms saturation and cross-magnetization are explained. The saturation behavior of the main inductance is mathematically described. The DQ and VBR models of a dynamic salient-pole three-phase machine are mathematically derived from the machine's physics.

The current section uses as a knowledge base the machine theory derived for three-phase models and extends the equations to describe the behavior of the dual-voltage six-phase machine. For this purpose a suitable six-phase $d-q$ transformation is defined, which transforms the stator machine quantities into the $d-q$ rotor reference frame. The transformation considers the machine specific winding displacement between the 12V stator system and the 48V stator system. The voltage equations are derived in the $d-q$ frame with the electromagnetic coupling between the 12V stator system, the 48V stator system and the field winding. For this purpose all mutual inductances are derived through the use of the effective number of turns for each system. All voltage equations are calculated relative to stator system 1 (12V). The quantities from stator system 2 (48V) and the rotor are referred to the stator system 1 (12V). At the end of the section the torque equation in the $d-q$ frame for the dual-voltage machine is derived, which comprises of two air-gap torques, T_{e12V} and T_{e48V} .

2.2.1 Six-Phase Dual-Voltage DQ Machine Model

The schematic drawing of the three-phase machine model from Fig. 2.1 is modified to represent a six-phase dual-voltage machine model. The cross-section of the synchronous dual-voltage machine is illustrated in Fig. 2.10. Two winding sets are placed in the stator slots. In Fig. 2.10 the UVW winding set represents the 12V stator winding and is illustrated with blue color in the graphic. The abbreviation XYZ stands for the 48V stator winding and is drawn in red color. The field winding is plotted in orange color. The winding set XYZ is displaced with a certain angle α_{12} relative to the 12V winding set. The cross-section of the dual-voltage machine from Fig. 2.10 shows how the windings are disposed in the stator. Each of both winding sets forms a three-phase system and generates a rotating magnetic field, when balanced three-phase stator currents flow in it. The machine possesses only one rotor and therefore each of the stator windings interacts with the rotor field and generates its own air-gap torque. The sum of both torques minus the losses occurring in the machine is equal to the mechanical torque.

The schematic representation of the equivalent machine's circuit in the stator reference frame is illustrated in Fig. 2.11. The machine is designed such, that each three-phase

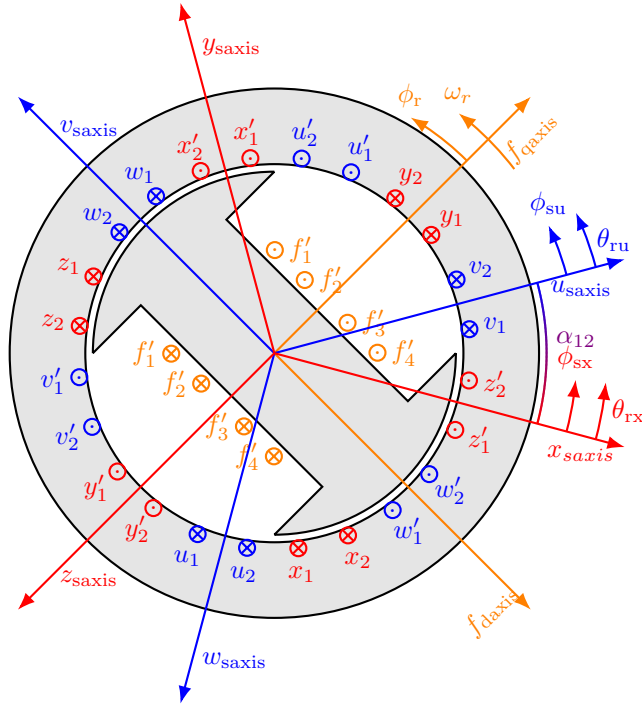


Figure 2.10 – Schematic Drawing of a Dual-Voltage Salient-Pole Machine

system generates a back-emf voltage suitable for the DC voltage range of the battery it is connected to. The winding set with index 1 (12V) produces a back-emf suitable for the 12V system (typically in the range from 11 V to 16 V). The other winding with index 2 is designed to supply a 48V battery and has more turns in order to produce a greater back-emf (typically in the range from 36 V up to 54 V). Depending on the machine design the effective number of turns of the second system relative to the first system can vary.

The first step in the process of deriving the machine model is to define a suitable six-phase transformation, which can remove the angle dependency in the voltage and torque equations. The forwards transformation is shown in equation (2.2.1.1) and the backwards transformation is provided in equation (2.2.1.2). The same transformations are used also in the control of the machine, which is explained in Chapter 3.

$$\mathbf{K}_{s,2 \times 3}(\theta_r) = \begin{bmatrix} \mathbf{K}_s(\theta_r) & \mathbf{0}_{3 \times 3} & \mathbf{0}_{3 \times 1} \\ \mathbf{0}_{3 \times 3} & \mathbf{K}_s(\theta_r + \alpha_{12}) & \mathbf{0}_{3 \times 1} \\ \mathbf{0}_{1 \times 3} & \mathbf{0}_{1 \times 3} & 1 \end{bmatrix} \quad (2.2.1.1)$$

$$\mathbf{K}_{s,2 \times 3}(\theta_r)^{-1} = \begin{bmatrix} \mathbf{K}_s^{-1}(\theta_r) & \mathbf{0}_{3 \times 3} & \mathbf{0}_{3 \times 1} \\ \mathbf{0}_{3 \times 3} & \mathbf{K}_s^{-1}(\theta_r + \alpha_{12}) & \mathbf{0}_{3 \times 1} \\ \mathbf{0}_{1 \times 3} & \mathbf{0}_{1 \times 3} & 1 \end{bmatrix} \quad (2.2.1.2)$$

The 12V and 48V stator windings are placed in different slots. There is a displacement angle α_{12} , which is defined as the angle of stator system 2 (48 V) relative to stator system 1 (12 V). Therefore this displacement angle is considered in the transformations from equations (2.2.1.1) and (2.2.1.2).

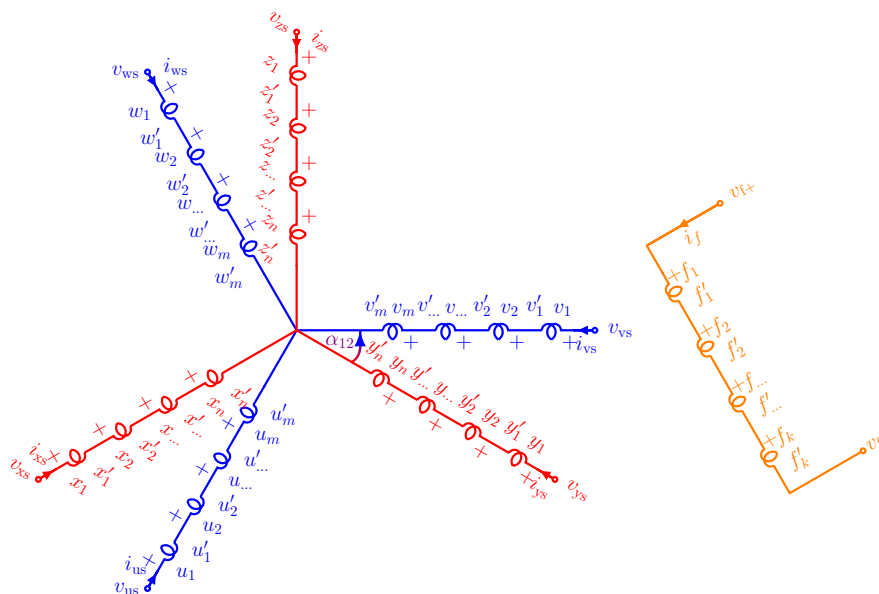


Figure 2.11 – *ABC*-Schematic of the Dual-Voltage Salient-Pole Machine

In Fig. 2.11 the different number of turns of stator system 1 (12V) is denoted by the index m and the number of turns of stator system 2 (48V) is denoted with index n . The number of turns of the field winding is symbolized with the index k . All quantities of stator system 2 (48 V) are referred to stator system 1 (12V) with an effective number of turns ratio. The same principle is used when the mutual inductances of the salient-pole machine between stator and rotor are derived in Subsection 2.1.2. Equations (2.1.2.14), (2.1.2.15) and (2.1.2.16) represent the mutual inductances L_{fdus} , L_{fdvs} and L_{fdws} , where the effective number of turns of the rotor is N_f and the effective number of turns of the stator is N_s . The effective number of turns of stator system 1 (12 V) is denoted by N_{s1} and the effective number of turns for stator system 2 (48 V) is defined with N_{s2} . Thus, the turns ratio between stator system 1 and 2 is given through the parameter $N_{12} = \frac{N_{s1}}{N_{s2}}$. This ratio is used to refer all physical quantities of the 48V system, for example currents, fluxes and voltages, to the stator system 1. The turns ratio between stator system 1 and the rotor is defined as $N_{s1f} = \frac{N_{s1}}{N_f}$.

The machine quantities can be transformed to the d - q equivalent circuit from Fig. 2.13, when the six-phase transformation is applied to the *ABC* circuit from Fig. 2.11. The applied six-phase forwards transformation removes the angle dependency of the machine

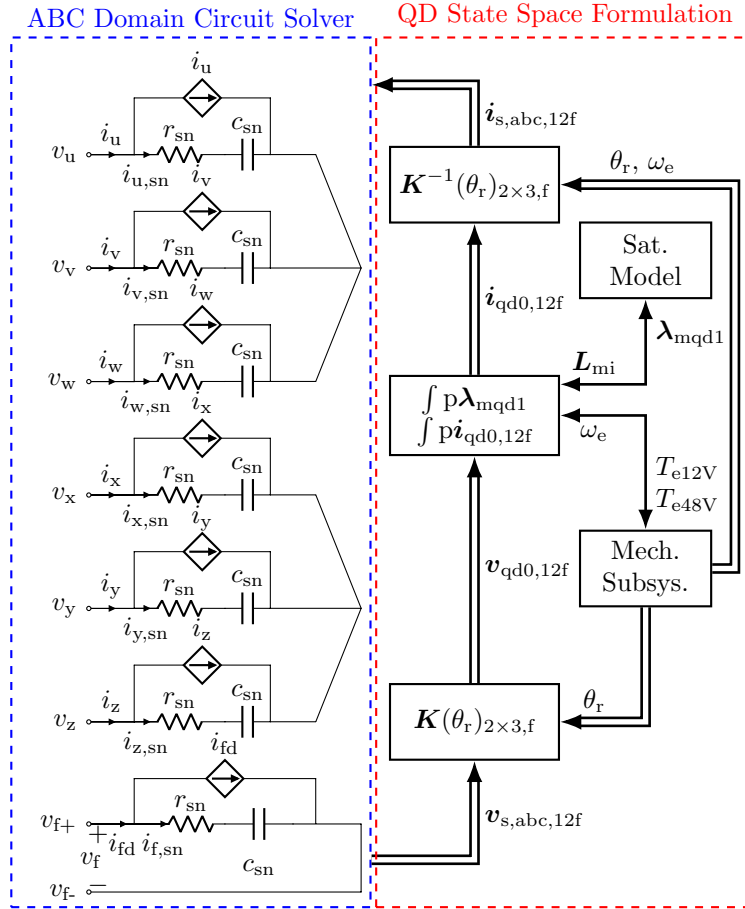


Figure 2.12 – Six-Phase DQ Model Overview

equations. It takes into account also the angle displacement α_{12} between both stator systems, which enables the calculation of the machine voltage equations only in one d - q reference frame. The angle displacement α_{12} is not relevant in the d - q voltage equations of the dual-voltage machine and is not present in the equivalent d - q circuit. From Fig. 2.13 is evident that the physical quantities of stator system 1 (12V) are illustrated without a prime notation. The physical quantities of stator system 2 (48V) are illustrated with a superscript prime notation, which stands for the referred quantities. The same is valid for the rotor quantities, which are marked with a superscript prime notation. Inductances and resistances are referred with the square of the effective turns ratio. For example, the stator resistance 2 is referred to stator system 1 with the expression: $r'_{s2} = r_{s2} N_{s12}^2$. The 48V stator leakage inductance L_{ls2} is referred also with the square of the turns ratio to the stator system 1: $L'_{ls2} = L_{ls2} N_{s12}^2$. The currents are referred with the effective turns ratio. For example, the 48V d -axis stator current is referred to the 12V stator system as follows: $i'_{ds2} = \frac{i_{ds2}}{N_{s12}}$. The voltages and fluxes are referred to stator system 1 by dividing with the effective number of turns ratio N_{s12} . For example, the 48V d -axis stator voltage

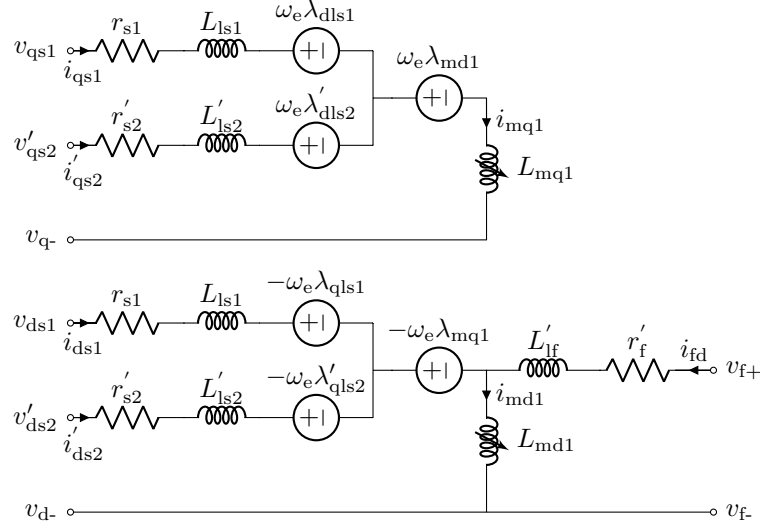


Figure 2.13 – d - q Equivalent Circuit of the Dual-Voltage Machine

is referred with: $v'_{ds2} = \frac{v_{ds2}}{N_{s12}}$. The same holds for the flux. The rotor quantities are referred to stator system 1 with the effective number of turns ratio N_{s1f} .

The machine voltage equations are derived based on the d - q equivalent circuit from Fig. 2.13. The machine equations are derived in matrix-vector form for better legibility with the vectors defined in equation (2.2.1.3).

$$\begin{aligned}
 \mathbf{v}_{s,qd0,12f} &= \begin{bmatrix} \mathbf{v}_{sqd01} & \mathbf{v}_{sqd02} & v_{fd} \end{bmatrix} & \mathbf{i}_{s,qd0,12f} &= \begin{bmatrix} \mathbf{i}_{sqd01} & \mathbf{i}_{sqd02} & i_{fd} \end{bmatrix} \\
 \mathbf{p}\mathbf{i}_{s,qd0,12f} &= \begin{bmatrix} \mathbf{p}\mathbf{i}_{sqd01} & \mathbf{p}\mathbf{i}_{sqd02} & \mathbf{p}i_{fd} \end{bmatrix} & \mathbf{p}\mathbf{i}_{m,qd0,12f} &= \begin{bmatrix} \mathbf{p}i_{mqd0,1} & \mathbf{p}i_{mqd0,2} & \mathbf{p}i_{mqf} & \mathbf{p}i_{mdf} \end{bmatrix} \\
 \boldsymbol{\lambda}_{sqd0,12f} &= \begin{bmatrix} \boldsymbol{\lambda}_{sqd0,1} & \boldsymbol{\lambda}_{sqd0,2} & \lambda_f \end{bmatrix} & \mathbf{p}\boldsymbol{\lambda}_{sqd0,12f} &= \begin{bmatrix} \mathbf{p}\boldsymbol{\lambda}_{sqd0,1} & \mathbf{p}\boldsymbol{\lambda}_{sqd0,2} & \mathbf{p}\lambda_f \end{bmatrix} \\
 \boldsymbol{\lambda}_{m,qd0,12f} &= \begin{bmatrix} \lambda_{mqd0,1} & \lambda_{mqd0,2} & \lambda_{mf} \end{bmatrix} & \mathbf{p}\boldsymbol{\lambda}_{m,qd0,12f} &= \begin{bmatrix} \mathbf{p}\lambda_{mqd0,1} & \mathbf{p}\lambda_{mqd0,2} & \mathbf{p}\lambda_{mf} \end{bmatrix} \\
 \boldsymbol{\lambda}_{lsqd0,12f} &= \begin{bmatrix} \lambda_{lsqd0,1} & \lambda_{lsqd0,2} & \lambda_{lsf} \end{bmatrix} & \mathbf{p}\boldsymbol{\lambda}_{lsqd0,12f} &= \begin{bmatrix} \mathbf{p}\lambda_{lsqd0,1} & \mathbf{p}\lambda_{lsqd0,2} & \mathbf{p}\lambda_{lsf} \end{bmatrix}
 \end{aligned} \tag{2.2.1.3}$$

Each vector consists of two sub-vectors and one scalar value for the field winding. The first sub-vector describes quantities related to stator system 1 and the second sub-vector contains quantities from stator system 2. For example, the voltage vector $\mathbf{v}_{s,qd0,12f}$ consists of two sub-vectors \mathbf{v}_{sqd01} and \mathbf{v}_{sqd02} and the field winding voltage v_{fd} . The vectors \mathbf{v}_{sqd01} and \mathbf{v}_{sqd02} consist each of 3 scalar elements - the voltage components in q , d and 0 direction. The matrices required for the voltage equations are provided in equations (2.2.1.4), (2.2.1.5), (2.2.1.6) and (2.2.1.7),

$$\mathbf{R}_{s,12f} = \begin{bmatrix} r_{s1} \cdot \mathbf{I}_{3 \times 3} & \mathbf{0}_{3 \times 3} & \mathbf{0}_{3 \times 1} \\ \mathbf{0}_{3 \times 3} & r_{s2} \cdot \mathbf{I}_{3 \times 3} & \mathbf{0}_{3 \times 1} \\ \mathbf{0}_{1 \times 3} & \mathbf{0}_{1 \times 3} & r_f \end{bmatrix} \quad \mathbf{L}_{mi,12f} = \begin{bmatrix} \frac{\mathbf{L}_{mi1}}{N_{s11}^2} & \mathbf{0}_{3 \times 3} & \mathbf{0}_{3 \times 1} & \mathbf{0}_{3 \times 1} \\ \mathbf{0}_{3 \times 3} & \frac{\mathbf{L}_{mi1}}{N_{s12}^2} & \mathbf{0}_{3 \times 1} & \mathbf{0}_{3 \times 1} \\ \mathbf{0}_{1 \times 3} & \mathbf{0}_{1 \times 3} & \frac{L_{mqd1}}{N_{s1f}^2} & \frac{L_{mqdd1}}{N_{s1f}^2} \end{bmatrix} \quad (2.2.1.4) \quad (2.2.1.6)$$

$$\mathbf{L}_{ls,12f} = \begin{bmatrix} L_{ls1} \cdot \mathbf{I}_{3 \times 3} & \mathbf{0}_{3 \times 3} & \mathbf{0}_{3 \times 1} \\ \mathbf{0}_{3 \times 3} & L_{ls2} \cdot \mathbf{I}_{3 \times 3} & \mathbf{0}_{3 \times 1} \\ \mathbf{0}_{1 \times 3} & \mathbf{0}_{1 \times 3} & L_{lf} \end{bmatrix} \quad \mathbf{P}_m = \begin{bmatrix} \begin{bmatrix} 0 & 1 & 0 \\ -1 & 0 & 0 \\ 0 & 0 & 0 \end{bmatrix} & \mathbf{0}_{3 \times 3} & \mathbf{0}_{3 \times 1} \\ \mathbf{0}_{3 \times 3} & \begin{bmatrix} 0 & 1 & 0 \\ -1 & 0 & 0 \\ 0 & 0 & 0 \end{bmatrix} & \mathbf{0}_{3 \times 1} \\ \mathbf{0}_{1 \times 3} & \mathbf{0}_{1 \times 3} & 0 \end{bmatrix} \quad (2.2.1.5) \quad (2.2.1.7)$$

where $\mathbf{I}_{3 \times 3}$ is the entity matrix and $\mathbf{0}_{3 \times 3}$ is a zero 3×3 matrix. Respectively, the vectors $\mathbf{0}_{3 \times 1}$ and $\mathbf{0}_{1 \times 3}$ are vectors fulfilling the 7×7 matrices.

The voltage equations of the six-phase dual-voltage machine are provided in matrix-vector form through equation (2.2.1.8). The voltage equations are derived, when Kirchhoff's Voltage Law is applied to the equivalent circuit scheme from Fig. 2.13. Instead of the primed notation from Fig. 2.13 the effective number of turns ratios are directly incorporated in the voltage equations. The main magnetizing inductances and the magnetizing fluxes λ_{md1} and λ_{mq1} have to be referred correctly to each system. The rest of the quantities like resistances and leakage inductances are calculated in the references system they are defined in. The primed notation is used in the equivalent d - q circuit diagram from Fig. 2.13 in order to represent the physical relationship between the quantities correctly. The voltage equations of the dual-voltage machine are explained based on Kirchoff's Voltage Low. The d - q voltages at the terminals consist of the voltage drops over the stator and rotor resistances, the back-emf d - q voltages and the d - q stator flux derivatives. The stator and rotor flux derivatives vector $p\lambda_{s,qd,12f}$ consists of the leakage flux derivatives vector $p\lambda_{lsqd0,12f}$ and the magnetizing flux derivatives vector $p\lambda_{mqd0,12f}$. The leakage flux derivatives vector $p\lambda_{lsqd0,12f}$ is a result of the changing stator current in the leakage inductances and is equal to the product from the leakage inductance matrix $\mathbf{L}_{ls,12f}$ and the differential currents vector $p\mathbf{i}_{qd,12f}$. The magnetizing flux derivatives vector $p\lambda_{mqd0,12f}$ describes the generated voltage due to the changes of the magnetizing fluxes and is equal to the product of the differential main inductance matrix $\mathbf{L}_{mi,12f}$ and the differential magnetizing currents vector $p\mathbf{i}_{m,qd,12f}$. Both expressions are highlighted in equation (2.2.1.8) with an overbrace.

$$\mathbf{v}_{s,qd0,12f} = \mathbf{R}_{s,12f} \cdot \mathbf{i}_{s,qd0,12f} + \underbrace{\omega_e \cdot \mathbf{P}_m \cdot \lambda_{sqd0,12f}}_{\text{back-emf}} + \underbrace{\mathbf{L}_{ls,12f} \cdot p\mathbf{i}_{s,qd0,12f} + \mathbf{L}_{mi,12f} \cdot p\mathbf{i}_{m,qd0,12f}}_{\mathbf{v}_{\lambda s,qd0,12f} = p\lambda_{lsqd0,12f} + p\lambda_{mqd0,12f}} \quad (2.2.1.8)$$

The back-emf voltage term from equation (2.2.1.8) is separated in two terms. The first term is the back-emf voltage vector as a result of the product from the leakage inductance matrix $\mathbf{L}_{ls,12f}$ and the currents vector $\mathbf{i}_{qd,12f}$. The second term is the generated back-emf voltage due to the rotating magnetizing flux vector $\lambda_{m,qd0,12f}$. The permutation matrix

\mathbf{P}_m introduces the cross-coupling between the d - and q -axes of the machine. Both terms are written out in equation (2.2.1.9).

$$\begin{aligned} \mathbf{v}_{s,qd0,12f} = & \mathbf{R}_{s,12f} \cdot \mathbf{i}_{s,qd0,12f} + \overbrace{\omega_e \cdot \mathbf{L}_{ls,12f} \cdot \mathbf{P}_m \cdot \mathbf{i}_{s,qd0,12f} + \omega_e \cdot \mathbf{P}_m \cdot \boldsymbol{\lambda}_{m,qd0,12f}}^{\text{back-emf}} \\ & + \underbrace{\mathbf{L}_{ls,12f} \cdot \mathbf{p}\mathbf{i}_{s,qd0,12f} + \mathbf{L}_{mi,12f} \cdot \mathbf{p}\mathbf{i}_{m,qd0,12f}}_{\mathbf{v}_{\lambda s,qd0,12f} = \mathbf{p}\boldsymbol{\lambda}_{sqd0,12f}} \end{aligned} \quad (2.2.1.9)$$

All parameters from equation (2.2.1.9) are linear except for the differential magnetizing flux vector $\mathbf{p}\boldsymbol{\lambda}_{mqd0,12f}$. This vector describes how the magnetizing flux changes, when the magnetizing current is changed on a small scale. According to the derived equations from Subsection 2.1.5 this relationship is highly non-linear and is described through an arcustangens function. The small-signal behavior of the non-linear inductance is described through the incremental inductance matrix \mathbf{L}_{mi} from equation (2.1.5.16). The derivative of the magnetizing flux vector $\mathbf{p}\boldsymbol{\lambda}_{mqd0,12f}$ is expressed through the product of the extended incremental inductance matrix $\mathbf{L}_{mi,12f}$ and the time derivative of the magnetizing currents vector $\mathbf{p}\mathbf{i}_{m,qd,12f}$. The entries of the differential inductance matrix \mathbf{L}_{mi} are defined in reference to stator system 1 and the 48V and field winding entries are referred by the square of the turns ratio N_{s12}^2 to the 12V system. The magnetizing currents $\mathbf{i}_{m,qd0,12f}$ are expressed as a sum of the stator and rotor currents according to Kirchoff's Currents Law. The expression for the differential magnetizing flux vector is provided in equation (2.2.1.10). The quantities are all referred to the first stator system.

$$\begin{aligned} \mathbf{p}\boldsymbol{\lambda}_{mqd0,12f} = & \mathbf{L}_{mi,12f} \cdot \mathbf{p}\mathbf{i}_{m,qd0,12f} = \underbrace{\mathbf{L}_{mi,12f} \cdot \mathbf{N}_{12f}}_{= \overline{\mathbf{L}}_{mi,12f}} \cdot \mathbf{p}\mathbf{i}_{s,qd0,12f} \end{aligned} \quad (2.2.1.10)$$

The matrix \mathbf{N}_{12f} , shown in equation (2.2.1.11), represents the relationship between the differential currents vector $\mathbf{p}\mathbf{i}_{s,qd0,12f}$ and the magnetizing currents vector $\mathbf{p}\mathbf{i}_{m,qd0,12f}$. The stator and rotor currents have to be scaled with the corresponding turn ratios N_{s12} and N_{s1f} , when Kirchoff's Current Law is used to express the magnetizing currents vector through the stator and rotor currents. The matrix takes into account the mutual coupling between the stator system 1, stator system 2 and the rotor.

$$\mathbf{N}_{12f} = \begin{bmatrix} \frac{1}{N_{s11}} & 0 & 0 & \frac{1}{N_{s12}} & 0 & 0 & 0 \\ 0 & \frac{1}{N_{s11}} & 0 & 0 & \frac{1}{N_{s12}} & 0 & \frac{2}{3} \frac{1}{N_{s1f}} \\ 0 & 0 & 1 & 0 & 0 & 0 & 0 \\ \frac{N_{s12}}{N_{s11}} & 0 & 0 & \frac{N_{s12}}{N_{s12}} & 0 & 0 & 0 \\ 0 & \frac{N_{s12}}{N_{s11}} & 0 & 0 & \frac{N_{s12}}{N_{s12}} & 0 & \frac{2}{3} \frac{N_{s12}}{N_{s1f}} \\ 0 & 0 & 0 & 0 & 0 & 1 & 0 \\ \frac{N_{s1f}}{N_{s11}} & 0 & 0 & \frac{N_{s1f}}{N_{s12}} & 0 & 0 & 0 \\ 0 & \frac{N_{s1f}}{N_{s11}} & 0 & 0 & \frac{N_{s1f}}{N_{s12}} & 0 & \frac{2}{3} \frac{N_{s1f}}{N_{s1f}} \end{bmatrix} \quad (2.2.1.11)$$

The result of the product $\mathbf{N}_{12f} \cdot \mathbf{L}_{mi,12f}$ from equation (2.2.1.10) is a 7×7 matrix denoted with $\overline{\mathbf{L}}_{mi,12f}$, which is shown in equation (2.2.1.12). The sub-matrix \mathbf{L}_{mi1} is the

differential inductance matrix. This matrix describes the saturation and the cross-coupling as explained in Subsection 2.1.5 and is referred to stator system 1.

$$\overline{\mathbf{L}}_{\text{mi},12\text{f}} = \begin{bmatrix} \frac{\mathbf{L}_{\text{mi}1}N_{\text{s}11}}{N_{\text{s}11}^2} & \frac{\mathbf{L}_{\text{mi}1}N_{\text{s}12}}{N_{\text{s}11}^2} & \frac{2}{3} \frac{(\mathbf{L}_{\text{mi}1})_2^T N_{\text{s}1\text{f}}}{N_{\text{s}1\text{f}}^2} \\ \frac{\mathbf{L}_{\text{mi}1}N_{\text{s}21}}{N_{\text{s}12}^2} & \frac{\mathbf{L}_{\text{mi}1}N_{\text{s}22}}{N_{\text{s}12}^2} & \frac{2}{3} \frac{(\mathbf{L}_{\text{mi}1})_2^T N_{\text{s}2\text{f}}}{N_{\text{s}1\text{f}}^2} \\ \frac{(\mathbf{L}_{\text{mi}1})_2 N_{\text{s}1\text{f}}}{N_{\text{s}1\text{f}}^2} & \frac{(\mathbf{L}_{\text{mi}1})_2 N_{\text{s}2\text{f}}}{N_{\text{s}1\text{f}}^2} & \frac{2}{3} \frac{\mathbf{L}_{\text{m}dd1}}{N_{\text{s}1\text{f}}^2} \end{bmatrix} \quad \text{with} \quad \mathbf{L}_{\text{mi}1} = \begin{bmatrix} dL_{\text{qq}1} & dL_{\text{qd}1} & 0 \\ dL_{\text{qd}1} & dL_{\text{dd}1} & 0 \\ 0 & 0 & 0 \end{bmatrix} \quad (2.2.1.12)$$

The d - q voltage equations are brought into the form shown in equation (2.2.1.13), when equation (2.2.1.10) is substituted into equation (2.2.1.9). The differential inductance matrix from equation (2.2.1.12) includes the coupling of the saturated main inductance between all three sub-systems: stator 1 (12V), stator 2 (48V) and the field winding.

$$\begin{aligned} \mathbf{v}_{\text{s},\text{qd}0,12\text{f}} &= [\mathbf{R}_{\text{s},12\text{f}} + \omega_e \cdot \mathbf{L}_{\text{ls},12\text{f}} \cdot \mathbf{P}_m] \cdot \mathbf{i}_{\text{s},\text{qd}0,12\text{f}} + [\mathbf{L}_{\text{ls},12\text{f}} + \overline{\mathbf{L}}_{\text{mi},12\text{f}}] \cdot \mathbf{p}\mathbf{i}_{\text{s},\text{qd}0,12\text{f}} \\ &\quad + \omega_e \cdot \mathbf{P}_m \cdot \boldsymbol{\lambda}_{\text{m},\text{qd}0,12\text{f}} \end{aligned} \quad (2.2.1.13)$$

The voltage equations from (2.2.1.13) are solved for the differential stator and rotor currents vector $\mathbf{p}\mathbf{i}_{\text{s},\text{qd}0,12\text{f}}$. The goal is to derive differential equations after the magnetizing fluxes λ_{mq} and λ_{md} . Therefore, an expression of the differential currents vector $\mathbf{p}\mathbf{i}_{\text{s},\text{qd}0,12\text{f}}$ is derived. The solution after $\mathbf{p}\mathbf{i}_{\text{s},\text{qd}0,12\text{f}}$ is shown in equation (2.2.1.14).

$$\begin{aligned} \mathbf{p}\mathbf{i}_{\text{s},\text{qd}0,12\text{f}} &= [\mathbf{L}_{\text{ls},12\text{f}} + \overline{\mathbf{L}}_{\text{mi},12\text{f}}]^{-1} \cdot \left[\mathbf{v}_{\text{s},\text{qd}0,12\text{f}} - [\mathbf{R}_{\text{s},12\text{f}} \cdot \mathbf{i}_{\text{s},\text{qd}0,12\text{f}} \right. \\ &\quad \left. + \omega_e \cdot \mathbf{L}_{\text{ls},12\text{f}} \cdot \mathbf{P}_m \cdot \mathbf{i}_{\text{s},\text{qd}0,12\text{f}} \quad + \omega_e \cdot \mathbf{P}_m \cdot \boldsymbol{\lambda}_{\text{m},\text{qd}0,12\text{f}} \right] \end{aligned} \quad (2.2.1.14)$$

The differential equations after the magnetizing fluxes derived in equation (2.1.6.4) for the three-phase machine model are adapted according Kirhoff's Law for the six-phase model in equation (2.2.1.15).

$$\frac{d}{dt} \begin{bmatrix} \lambda_{\text{mq}} \\ \lambda_{\text{md}} \end{bmatrix} = \begin{bmatrix} dL_{\text{qq}} & dL_{\text{qd}} & 0 & dL_{\text{qq}}N_{\text{s}21} & dL_{\text{qd}}N_{\text{s}21} & 0 & dM_{\text{qfd}}N_{\text{s}1\text{f}} \\ dL_{\text{qd}} & dL_{\text{dd}} & 0 & dL_{\text{qd}}N_{\text{s}21} & dL_{\text{dd}}N_{\text{s}21} & 0 & dM_{\text{dfd}}N_{\text{s}1\text{f}} \end{bmatrix} \frac{d}{dt} \begin{bmatrix} i_{\text{qs}1} \\ i_{\text{ds}1} \\ i_{\text{0s}1} \\ i_{\text{qs}2} \\ i_{\text{ds}2} \\ i_{\text{0s}2} \\ i_{\text{fd}} \end{bmatrix} \quad (2.2.1.15)$$

The differential currents from equation (2.2.1.15) are calculated from the expression in equation (2.2.1.14) and substituted in the differential equations (2.2.1.15). The differential

equations are solved in the simulation software Piecewise-Linear Electrical Circuit Simulation (PLECS). The DQ model is a voltage-in-current-out type models. Therefore, the currents have to be also calculated through the differential equations from (2.2.1.14). In total, there are 9 independent variables, 7 currents and 2 magnetizing fluxes as illustrated in Fig. 2.12. The electromagnetic torque of the dual-voltage machine results from the electromagnetic coupling between stator system 1 (12V), stator system 2 (48V) and the field winding. The interaction of the stator current vector of system 1 (12V) \vec{i}_{s1} with the magnetic flux vector in the air-gap $\vec{\lambda}_{m1}$ generates the 12V electromagnetic torque T_{e12V} . The interaction between the referred stator current of system 2 (48V) \vec{i}'_{s2} with the magnetic flux vector in the air-gap $\vec{\lambda}_{m1}$ results in a 48V electromagnetic torque T_{e48V} . The whole electromagnetic torque is shown in equation (2.2.1.16). The torque is calculated in reference to stator system 1, but can be also calculated in reference to stator system 2.

$$T_e = \frac{3}{2} \cdot p \cdot \left((\lambda_{md1} + \lambda_{mag1}) \cdot \left(\frac{i_{qs1}}{N_{s11}} + \frac{i_{qs2}}{N_{s12}} \right) - \lambda_{mq1} \cdot \left(\frac{i_{ds1}}{N_{s11}} + \frac{i_{ds2}}{N_{s12}} \right) \right) \quad (2.2.1.16)$$

The d - q currents of system 1 and system 2 can be controlled independently. This way each winding generates a separate torque. The coupling of the torque equations occurs in the generation of the magnetizing fluxes λ_{md1} and λ_{mq1} . The torque equation of the dual-voltage machine, separated into two electromagnetic torques T_{e1} and T_{e2} , is shown in equation (2.2.1.17). Equation (2.2.1.17) considers also the influence of a permanent magnet's flux λ_{mag1} caused by magnets integrated in the rotor of the machine.

$$T_e = \overbrace{\frac{3}{2} \cdot p \cdot \left((\lambda_{md1} + \lambda_{mag1}) \cdot \frac{i_{qs1}}{N_{s11}} - \lambda_{mq1} \cdot \frac{i_{ds1}}{N_{s11}} \right)}^{T_{e1}} + \overbrace{\frac{3}{2} \cdot p \cdot \left((\lambda_{md1} + \lambda_{mag1}) \cdot \frac{i_{qs2}}{N_{s12}} - \lambda_{mq1} \cdot \frac{i_{ds2}}{N_{s12}} \right)}^{T_{e2}} \quad (2.2.1.17)$$

2.2.2 Six-Phase Dual-Voltage VBR Model

The VBR model eliminates the need to solve the differential equations after the stator currents, because the model does not have the currents as output variables. Instead, the currents are “measured” from the stator phases in the ABC domain and transformed to the d - q frame with the six-phase transformation shown in equation (2.2.1.1). This is also evident from Fig. 2.14, where the integration of the differential magnetizing fluxes is illustrated. When the backwards transformation is applied to the d - q voltage equations the matrices $\mathbf{R}_{m,7 \times 7}$ and $\mathbf{L}_{m,7 \times 7}$ and the back-emf terms $\mathbf{e}_{abc,12f}$, are derived. The backwards six-phase transformation is applied to equation (2.2.1.13).

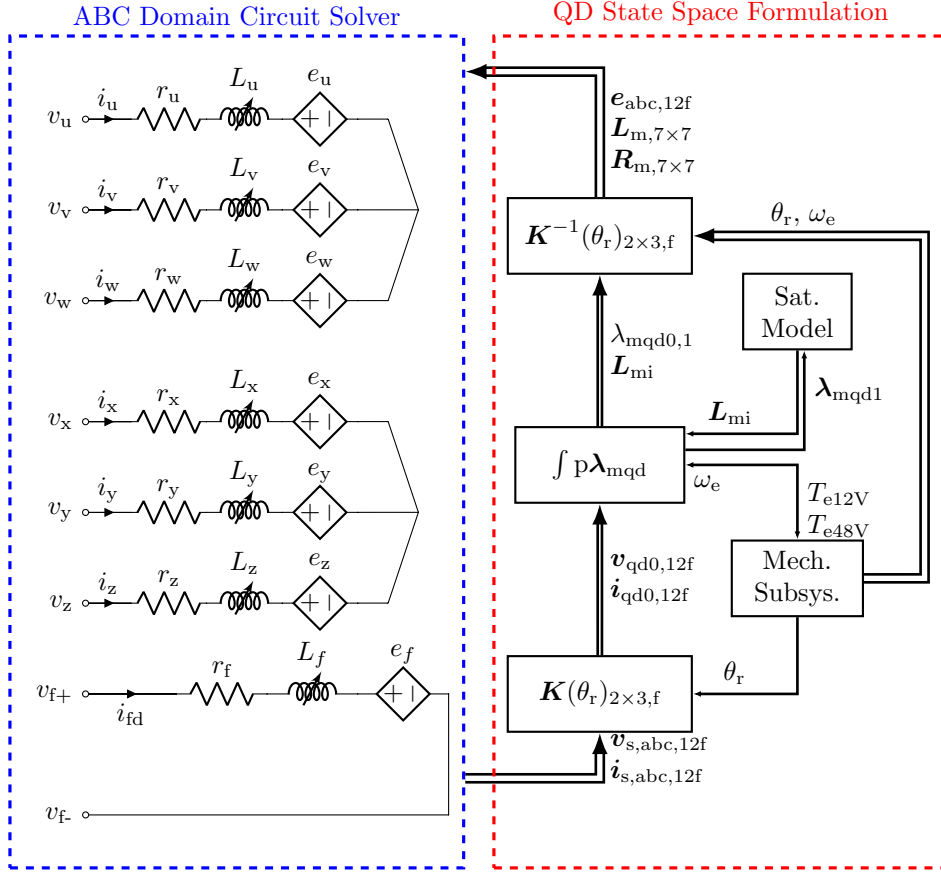


Figure 2.14 – Six-Phase VBR Model Overview

The VBR formulation of the voltage equations is derived from equation (2.2.1.13). The d - q currents are substituted with the transformed ABC currents according to equations (2.2.2.1) and (2.2.2.2).

$$\mathbf{i}_{s,qd0,12f} = \mathbf{K}_{s,2 \times 3}(\theta_r) \cdot \mathbf{i}_{s,abc,12f} \quad (2.2.2.1)$$

$$\mathbf{p}\mathbf{i}_{s,qd0,12f} = \mathbf{p}\mathbf{K}_{s,2 \times 3}(\theta_r) \cdot \mathbf{i}_{s,abc,12f} + \mathbf{K}_{s,2 \times 3}(\theta_r) \cdot \mathbf{p}\mathbf{i}_{s,abc,12f} \quad (2.2.2.2)$$

The voltage equations with the substitutions are rearranged as shown in equation (2.2.2.3).

$$\begin{aligned} \mathbf{v}_{s,qd,12f} = & [\mathbf{R}_{s,12f} + \omega_e \mathbf{L}_{ls,12f} \mathbf{P}_m] \cdot \mathbf{K}_{s,2 \times 3}(\theta_r) \cdot \mathbf{i}_{s,abc,12f} \\ & + [\mathbf{L}_{ls,12f} + \overline{\mathbf{L}}_{mi,12f}] \cdot [\mathbf{p}\mathbf{K}_{s,2 \times 3}(\theta_r) \cdot \mathbf{i}_{s,abc,12f} \\ & + \mathbf{K}_{s,2 \times 3}(\theta_r) \cdot \mathbf{p}\mathbf{i}_{s,abc,12f}] + \omega_e \cdot \mathbf{P}_m \cdot \boldsymbol{\lambda}_{m,qd0,12f} \end{aligned} \quad (2.2.2.3)$$

Equation (2.2.2.3) describes the d - q machine voltages through the currents from the ABC domain. However the voltages are still defined in the d - q domain. The backwards six-phase transformation is applied to equation (2.2.2.3) from the left side in order to

transform the voltages to the stator reference frame. The result is provided in equation (2.2.2.4). Equation (2.2.2.4) describes the machine behavior in the stator domain.

$$\mathbf{v}_{s,abc,12f} = \mathbf{R}_m \cdot \mathbf{i}_{s,abc,12f} + \mathbf{L}_m \cdot p\mathbf{i}_{s,abc,12f} + \mathbf{e}_{abc,12f} \quad (2.2.2.4)$$

The expressions for the matrices \mathbf{R}_m and \mathbf{L}_m are provided in equations (2.2.2.5) and (2.2.2.6). The back-emf voltage vector is shown in equation (2.2.2.7) in the stator domain. The matrix \mathbf{R}_m describes the inductive terms and the matrix \mathbf{L}_m describes the resistive terms in an analogy with equation (2.1.7.1). The back-emf voltage sources from Fig. 2.14 are controlled at each time step through the control signals in the vector $\mathbf{e}_{abc,12f}$. The modeling method is known as a Voltage Behind Reactance (VBR) due to this specific representation of the machine equations.

$$\mathbf{R}_m = \mathbf{K}_{s,2 \times 3}(\theta_r)^{-1} \left[[\mathbf{R}_{s,12f} + \omega_e \mathbf{L}_{ls,12f} \mathbf{P}_m] \mathbf{K}_{s,2 \times 3}(\theta_r) + [\mathbf{L}_{ls,12f} + \overline{\mathbf{L}_{mi,12f}}] \cdot p\mathbf{K}_{s,2 \times 3}(\theta_r) \right] \quad (2.2.2.5)$$

$$\mathbf{L}_m = \mathbf{K}_{s,2 \times 3}(\theta_r)^{-1} \cdot [\mathbf{L}_{ls,12f} + \overline{\mathbf{L}_{mi,12f}}] \cdot \mathbf{K}_{s,2 \times 3}(\theta_r) \quad (2.2.2.6)$$

$$\mathbf{e}_{abc,12f} = \mathbf{K}_{s,2 \times 3}(\theta_r)^{-1} \cdot \omega_e \cdot \mathbf{P}_m \cdot \boldsymbol{\lambda}_{m,qd0,12f} \quad (2.2.2.7)$$

2.3 Iron Losses Modeling

The claw-pole dual-voltage machine exhibits excessive iron losses. This is observed during the torque control tests from Chapter 4 Subsection 4.2. Neglecting the iron loss phenomena introduces inaccuracies in the predicted torque from the machine model. The investigated claw-pole machine has especially prominent iron losses due to the solid iron rotor. Therefore, the current subsection handles the extension of the derived six-phase dual-voltage machine models to the iron loss modeling. Though the inaccuracies are observed further in the project work the modeling of the iron losses is included in this Chapter because it belongs to the machine modeling theory. As noted in the introduction of the thesis, most of the part of the documentation follows the time-line of the research but the thesis structure is topic oriented. Specifically the extension of the iron losses is performed due to the findings documented in the torque control chapter.

The iron losses are already investigated in various publications. The representation of iron losses in dynamic models is achieved by adding parallel resistance along the main inductance. This approach is already used for three-phase models for Interior Permanent Magnet (IPM) machines, Permanent-Magnet Synchronous Machine (PMSM)s (PMSMs) and Induction Machine (IM)s (IMs). The iron loss modeling is achieved with a constant iron loss resistance [11, 26, 50, 52, 57, 61, 69, 73]. The aforementioned machines are built from a stacked stator and rotor and thus possess less iron losses in comparison to the claw-pole machine. The iron losses in claw-pole alternators are mainly investigated through 3D-Finite Element Analysis (FEA), which is computationally very time-consuming, not suitable for system studies and control loop verification. The integration of the iron losses

into dynamic models is not thoroughly investigated for the externally-excited synchronous machine and specifically for the claw-pole machine. The authors from [13] model the claw-pole iron losses through additional R-L branches and verify this model against measurements from a passive rectifications at few operating points. For the purpose of active torque vector control this modeling is not as accurate as required. The presented theory in the current section extends the presented six-phase models to represent also the iron losses as measured at the test bench through the inclusion of a variable iron loss resistance.

The 48V power supply represents a mild-hybrid architecture and presupposes a machine, which is able to actively set the torque demand from the motor control unit. This involves the development of a torque control strategy, which varies i_{fd} , i_{qs} and i_{ds} to achieve an efficient control of the machine. The challenge is thus to develop a model, which represents the iron losses in all possible operating points - all combinations of i_{fd} , i_{qs} and i_{ds} . For the six-phase dual-voltage machine the complexity increases even further, because all five currents, i_{qs1} , i_{ds1} , i_{qs2} , i_{ds2} and i_{fd} , have to be varied to set the torques T_{e12V} and T_{e48V} .

In Subsections 2.3.1, 2.3.2 and 2.3.3 a variable iron loss resistance is added to the DQ and VBR dual-voltage models. For this purpose the derived voltage equations have to be adapted.

2.3.1 Iron Losses in the DQ Equivalent Circuit

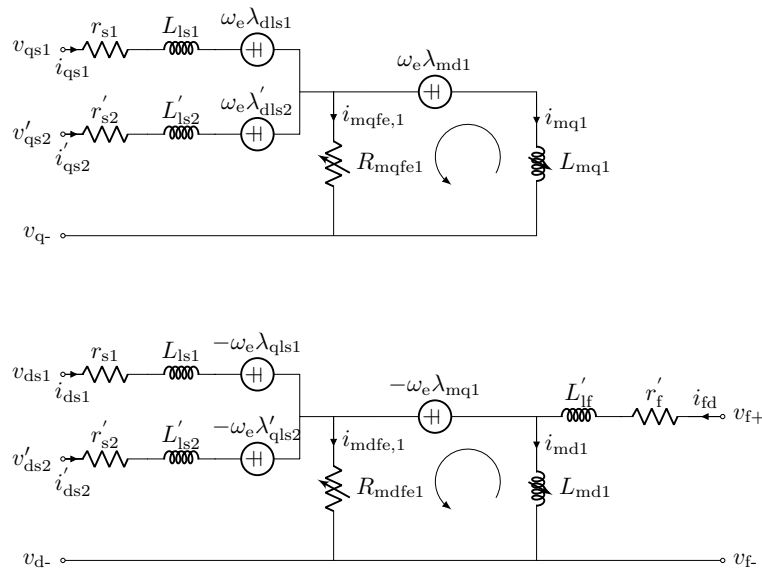


Figure 2.15 – Six-Phase DQ Equivalent Circuit with Iron Losses

The d - q equivalent circuit diagram is extended to represent the iron losses through a parallel iron loss resistance R_{mfe1} placed along the d - and q -axis main inductances of the six-phase model as shown in Fig. 2.15. The authors from reference [20] show that the iron loss resistance is equal for the d - and q -axis, which is used here as a prerequisite. The DQ and VBR machine models with iron losses are derived in the following subsections based on the equations from the equivalent circuit diagram from Fig. 2.15. According to Kirchhoff's Voltage Law two additional voltage loops for the d - and q -axis are added, when Figures 2.13 and 2.15 are compared. The additional voltage loops are shown in equations (2.3.1.1) and (2.3.1.2).

$$0 = -i_{mqfe1}R_{mfe1} + \omega_e(\lambda_{md1} + \lambda_{mag}) + L_{mqq1} \cdot pi_{mq1} + L_{mqd1}pi_{md1} \quad (2.3.1.1)$$

$$0 = -i_{mdfe1}R_{mfe1} - \omega_e\lambda_{mq1} + L_{mqd1} \cdot pi_{mq1} + L_{mdd1} \cdot pi_{md1} \quad (2.3.1.2)$$

The expressions for the magnetizing currents are adapted according to Kirchhoff's Current Law to take into account the iron loss currents i_{mqfe1} and i_{mdfe1} in equations (2.3.1.3) and (2.3.1.4).

$$pi_{md1} = pi_{ds1} + p \frac{i_{ds2}}{N_{s12}} + \frac{2}{3}p \frac{i_{fd}}{N_{s1f}} - pi_{mdfe1} \quad (2.3.1.3)$$

$$pi_{mq1} = pi_{qs1} + p \frac{i_{qs2}}{N_{s12}} - pi_{mqfe1} \quad (2.3.1.4)$$

Equations (2.3.1.3) and (2.3.1.4) are substituted in equations (2.3.1.1) and (2.3.1.2) to eliminate the magnetizing currents. The derived voltage equations, (2.3.1.5) and (2.3.1.6), depend on the differential stator currents, the rotor current and the iron loss currents. These equations can be integrated in the d - q voltage equations without iron losses shown in equation (2.2.1.13).

$$\begin{aligned} i_{mqfe1}R_{mfe1} = & + \omega_e(\lambda_{md1} + \lambda_{mag1}) + L_{mqq1} \left(pi_{qs1} + p \frac{i_{qs2}}{N_{s12}} - pi_{mqfe1} \right) \\ & + L_{mqd1} \left(pi_{ds1} + p \frac{i_{ds2}}{N_{s12}} + \frac{2}{3}p \frac{i_{fd}}{N_{s1f}} - pi_{mdfe1} \right) \end{aligned} \quad (2.3.1.5)$$

$$\begin{aligned} i_{mdfe1}R_{mfe1} = & - \omega_e\lambda_{mq1} + L_{mqd1} \cdot \left(pi_{qs1} + p \frac{i_{qs2}}{N_{s12}} - pi_{mqfe1} \right) \\ & + L_{mdd1} \left(pi_{ds1} + p \frac{i_{ds2}}{N_{s12}} + \frac{2}{3}p \frac{i_{fd}}{N_{s1f}} - pi_{mdfe1} \right) \end{aligned} \quad (2.3.1.6)$$

Both voltage equations, (2.3.1.5) and (2.3.1.6), are added to the d - q voltage equations from (2.2.1.13). All voltage equations, describing the d - q dual-voltage machine model with iron losses, are transformed into a vector-matrix form. The current, voltage and

flux vectors from equation (2.2.1.3) are extended to include the iron loss voltage loops from Fig. 2.15. The extended vectors are summarized in equation (2.3.1.7).

$$\begin{aligned}
 \mathbf{v}_{s,\text{qd0},12\text{f, feq, fed}} &= [\mathbf{v}_{s,\text{qd0},12\text{f}} \quad 0 \quad 0 \quad \quad \quad]^T \\
 \mathbf{i}_{s,\text{qd0},12\text{f, feq, fed}} &= [\mathbf{i}_{s,\text{qd0},12\text{f}} \quad i_{\text{mqfe1}} \quad i_{\text{mdfe1}} \quad \quad \quad]^T \\
 \text{p}\mathbf{i}_{s,\text{qd0},12\text{f, feq, fed}} &= [\text{p}\mathbf{i}_{s,\text{qd0},12\text{f}} \quad \text{p}i_{\text{mqfe1}} \quad \text{p}i_{\text{mdfe1}} \quad \quad \quad]^T \\
 \boldsymbol{\lambda}_{\text{mqd0},12\text{f, feq, fed}} &= [\boldsymbol{\lambda}_{\text{mqd0s},12\text{f}} \quad \lambda_{\text{mq1}} \quad (\lambda_{\text{md1}} + \lambda_{\text{mag1}}) \quad \quad \quad]^T
 \end{aligned} \tag{2.3.1.7}$$

The matrices also have to be extended as shown in equations (2.3.1.8) and (2.3.1.9).

$$\mathbf{R}_{s,12\text{f, feq, fed}} = \begin{bmatrix} \mathbf{R}_{s,12\text{f}} & \mathbf{0}_{7 \times 1} & \mathbf{0}_{7 \times 1} \\ \mathbf{0}_{1 \times 7} & -R_{\text{mfe1}} & 0 \\ \mathbf{0}_{1 \times 7} & 0 & -R_{\text{mfe1}} \end{bmatrix} \quad \mathbf{L}_{\text{ls},12\text{f, feq, fed}} = \begin{bmatrix} \mathbf{L}_{\text{ls},12\text{f}} & \mathbf{0}_{7 \times 1} & \mathbf{0}_{7 \times 1} \\ \mathbf{0}_{1 \times 7} & 0 & 0 \\ \mathbf{0}_{1 \times 7} & 0 & 0 \end{bmatrix} \tag{2.3.1.8}$$

$$\begin{aligned}
 \overline{\mathbf{L}}_{\text{mi},12\text{f, feq, fed}} &= \begin{bmatrix} \overline{\mathbf{L}}_{\text{mi},12\text{f}} & \mathbf{L}'_{\text{mi}} \\ \left(\overline{\mathbf{L}}_{\text{mi},12\text{f}}\right)_{2 \times 7} & \left(\mathbf{L}'_{\text{mi}}\right)_{2 \times 2} \end{bmatrix} \quad \overline{\mathbf{P}}_{\text{m}} = \begin{bmatrix} \mathbf{P}_{\text{m}} & \mathbf{0}_{7 \times 1} & \mathbf{0}_{7 \times 1} \\ \mathbf{0}_{1 \times 7} & 0 & 1 \\ \mathbf{0}_{1 \times 7} & -1 & 0 \end{bmatrix} \\
 \text{with } \mathbf{L}'_{\text{mi}} &= \begin{bmatrix} -L_{\text{mqq1}} & -L_{\text{mqd1}} & 0 & -\frac{L_{\text{mqd1}}}{N_{s12}} & -\frac{L_{\text{mqd1}}}{N_{s12}} & 0 & -\frac{L_{\text{mqd1}}}{N_{s1f}} \\ -L_{\text{mqd1}} & -L_{\text{mdd1}} & 0 & -\frac{L_{\text{mqd1}}}{N_{s12}} & -\frac{L_{\text{mdd1}}}{N_{s12}} & 0 & -\frac{L_{\text{mdd1}}}{N_{s1f}} \end{bmatrix}^T
 \end{aligned} \tag{2.3.1.9}$$

The matrix $\overline{\mathbf{L}}_{\text{mi},12\text{f, feq, fed}}$ contains the mutual coupling between the axis extended to consider the iron losses. The matrix consists of the submatrix $\overline{\mathbf{L}}_{\text{mi},12\text{f}}$, which is already defined in equation (2.2.1.12), and describes the mutual coupling of the dual-voltage machine without iron losses. The matrix is extended to form a 9×9 matrix to consider the iron loss currents. The matrix $\left(\overline{\mathbf{L}}_{\text{mi},12\text{f}}\right)_{2 \times 7}$ denotes the submatrix consisting of the first 2-by-7 rows and columns of the main matrix $\overline{\mathbf{L}}_{\text{mi},12\text{f}}$. The matrix $\left(\mathbf{L}'_{\text{mi}}\right)_{2 \times 2}$ is a submatrix consisting of the first 2-by-2 rows and columns of the main matrix \mathbf{L}'_{mi} . The voltage equations with iron losses are provided in a vector-matrix form in equation (2.3.1.10).

$$\begin{aligned}
 \mathbf{v}_{s,\text{qd0},12\text{f, feq, fed}} &= \left[\mathbf{R}_{s,12\text{f, feq, fed}} + \omega_e \cdot \mathbf{L}_{\text{ls},12\text{f, feq, fed}} \cdot \overline{\mathbf{P}}_{\text{m}} \right] \cdot \mathbf{i}_{s,\text{qd0},12\text{f}} \\
 &+ \left[\mathbf{L}_{\text{ls},12\text{f, feq, fed}} + \overline{\mathbf{L}}_{\text{mi},12\text{f, feq, fed}} \right] \cdot \text{p}\mathbf{i}_{s,\text{qd0},12\text{f, feq, fed}} \\
 &+ \omega_e \cdot \overline{\mathbf{P}}_{\text{m}} \cdot \boldsymbol{\lambda}_{\text{mqd0},12\text{f, feq, fed}}
 \end{aligned} \tag{2.3.1.10}$$

The system of equations (2.3.1.10) is solved for the derivatives of the currents vector $\text{p}\mathbf{i}_{s,\text{qd0},12\text{f, feq, fed}}$. Then the current derivatives are found as a function of the voltages, currents, speed, inductances and resistances of the machine. The iron loss currents i_{mqfe1} and i_{mdfe1} are additional variables, which need to be numerically integrated in the state space model. The additional iron loss currents are illustrated in Fig. 2.16 and Fig. 2.17, where they are added as additional integrals in the state space part of the DQ and

VBR models. Therefore, these currents are defined as continuous state variables and their derivatives $p i_{\text{mfeq1}}$ and $p i_{\text{mfed1}}$ as continuous derivatives in the machine model. The differential equations after the magnetizing fluxes, λ_{md} and λ_{mq} , are adapted to consider the derivatives of the iron loss currents as shown in equation (2.3.1.11).

$$\begin{bmatrix} p\lambda_{\text{mq1}} \\ p\lambda_{\text{md1}} \end{bmatrix} = \begin{bmatrix} L_{\text{mqq1}} & L_{\text{mqd1}} \\ L_{\text{mqd1}} & L_{\text{mdd1}} \end{bmatrix} \cdot \begin{bmatrix} \left(\frac{p i_{\text{qs1}}}{N_{\text{s11}}} + \frac{p i_{\text{qs2}}}{N_{\text{s12}}} - p i_{\text{mfeq}} \right) \\ \left(\frac{p i_{\text{ds1}}}{N_{\text{s11}}} + \frac{p i_{\text{ds2}}}{N_{\text{s12}}} + \frac{2}{3} \cdot \frac{p i_{\text{fd}}}{N_{\text{s1f}}} - p i_{\text{mfed}} \right) \end{bmatrix} \quad (2.3.1.11)$$

This state space model is derived and can be solved for the magnetic fluxes λ_{mq1} and λ_{md1} . The iron loss currents are calculated through two additional state space equations (2.3.1.12). The functions $f_{\text{sol,feq}}$ and $f_{\text{sol,fed}}$ denote the last two rows from the solution vector of equation (2.3.1.10).

$$\begin{aligned} p i_{\text{mfeq1}} &= f_{\text{sol,feq}}(i_{\text{mfeq1}}) \\ p i_{\text{mfed1}} &= f_{\text{sol,fed}}(i_{\text{mfed1}}) \end{aligned} \quad (2.3.1.12)$$

2.3.2 DQ Model Formulation with Iron Losses

The DQ model is of a voltage-in current-out type machine model. The inputs to the model are the applied voltages at the machine terminals and the model calculates through the integration of the differential equations the currents as outputs. Therefore no algebraic loop is introduced, when the iron loss currents are added as state space variables. The additional state space variables are only required to calculate the stator and rotor currents, which are outputs from the DQ model. The d - q voltage equations are shown in equation (2.3.1.10). The voltage equations are solved for the differential currents vector $p \mathbf{i}_{\text{s,qd0,12f,feq,fed}}$. This way one derives the system of differential equations, which are solved by the solver of the PLECS Blockset. The state space variables are the stator currents including the iron loss currents, which are part of the currents vector $\mathbf{i}_{\text{s,qd0,12f,feq,fed}}$. The form of the differential equations is shown in equation (2.3.2.1). The vector function $\mathbf{f}_{\text{QD},9 \times 9}$ symbolizes the solution of the voltage equations as a function of all currents. The vector function $\mathbf{f}_{\text{QD},9 \times 9}$ is derived through a matlab script, which inverts the system of equations and solves them after the differential stator currents vector $p \mathbf{i}_{\text{s,qd0,12f,feq,fed}}$. The explicit form of the function is not presented here for better legibility. The derivation is straightforward and can be performed through a matlab script.

$$p \mathbf{i}_{\text{s,qd0,12f,feq,fed}} = \mathbf{f}_{\text{QD},9 \times 9}(\mathbf{i}_{\text{s,qd0,12f,feq,fed}}) \quad (2.3.2.1)$$

The torque from equation (2.2.1.16) is adapted to take into account the iron loss currents i_{mqfe1} and i_{mdfe1} . In order to consider the effect of the iron loss currents to the torque equation they have to be subtracted from the stator and rotor currents according to Kirchhoff's Currents Law. The currents are illustrated in the equivalent d - q circuit diagram from Fig. 2.15. The whole air-gap torque is shown in equation (2.3.2.2). The

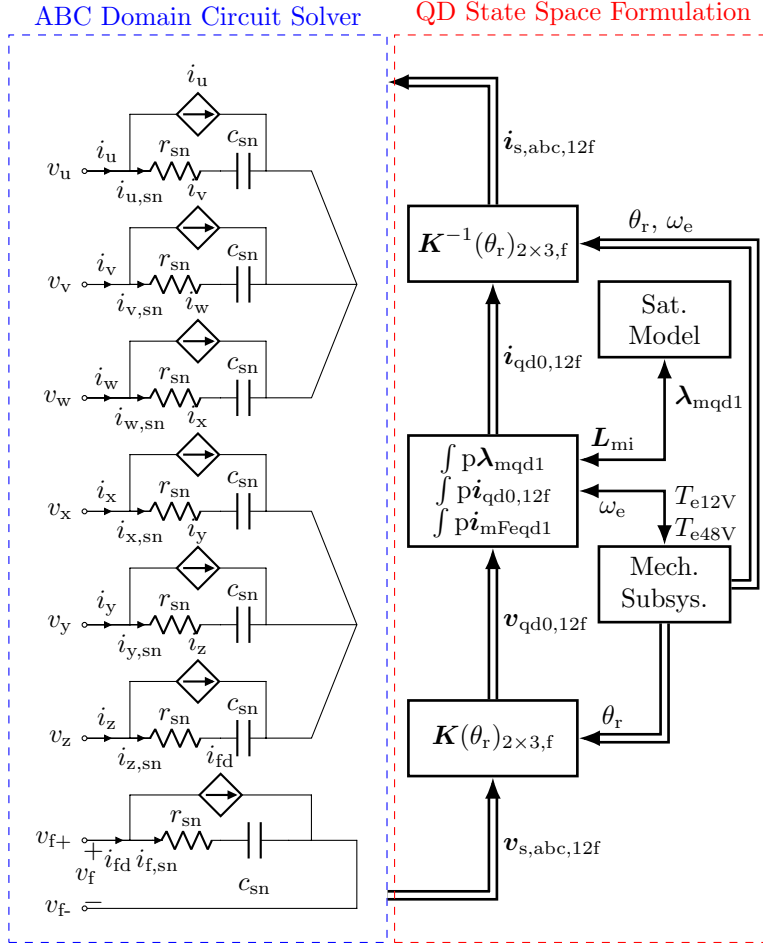


Figure 2.16 – Six-Phase DQ Model Overview with Iron Losses

q -axis iron loss current i_{mqfe1} is subtracted from the sum of both stator q currents, i_{qs1} and i_{qs2} , calculated in reference to the 12V system. The d -axis iron loss current i_{mdfe1} is subtracted from the sum of both d -axis stator currents, i_{ds1} and i_{ds2} , and the rotor current i_{fd} , which are all calculated in reference to stator system 1.

$$\begin{aligned}
 T_e = & \frac{3}{2} \cdot p \cdot \left((\lambda_{md1} + \lambda_{mag1}) \cdot \left(\frac{i_{qs1}}{N_{s11}} + \frac{i_{qs2}}{N_{s12}} - i_{mqfe1} \right) \right. \\
 & \left. - \lambda_{mq1} \cdot \left(\frac{i_{ds1}}{N_{s11}} + \frac{i_{ds2}}{N_{s12}} + \frac{2}{3} \frac{i_{fd}}{N_{s1f}} - i_{mdfe1} \right) \right)
 \end{aligned} \tag{2.3.2.2}$$

The torque generated from the 12V stator winding is shown in equation (2.3.2.3) and the air-gap torque of the 48V stator winding is expressed through equation (2.3.2.4). The iron loss torques of each winding are subtracted from the torque equations without iron losses. The iron loss torque is distributed to each winding taking into account the number of turns of the winding. This is physically motivated, because both windings share the

same stator. The iron loss torque component in the 12V winding is considered when the scaled iron loss q -axis current $\frac{N_{s1}i_{mqfe1}}{N_{s1}+N_{s2}}$ is subtracted from the q -axis current of the 12V side. The iron loss d -axis current is also taken into account and is subtracted from the d -axis stator current weighted with the factor $\frac{N_{s1}}{N_{s1}+N_{s2}}$. The iron losses are considered analogously for the 48V air-gap torque in equation (2.3.2.4).

$$T_{e12V} = \frac{3}{2}p \left((\lambda_{md1} + \lambda_{mag1}) \cdot \left(\frac{i_{qs1}}{N_{s11}} - \frac{N_{s1}i_{mqfe1}}{(N_{s1}+N_{s2})} \right) - \lambda_{mq1} \cdot \left(\frac{i_{ds1}}{N_{s11}} - \frac{N_{s1}i_{mdfe1}}{(N_{s1}+N_{s2})} \right) \right) \quad (2.3.2.3)$$

$$T_{e48V} = \frac{3}{2}p \left((\lambda_{md1} + \lambda_{mag1}) \cdot \left(\frac{i_{qs2}}{N_{s12}} - \frac{N_{s2}i_{mqfe1}}{(N_{s1}+N_{s2})} \right) - \lambda_{mq1} \cdot \left(\frac{i_{ds2}}{N_{s12}} - \frac{N_{s2}i_{mdfe1}}{(N_{s1}+N_{s2})} \right) \right) \quad (2.3.2.4)$$

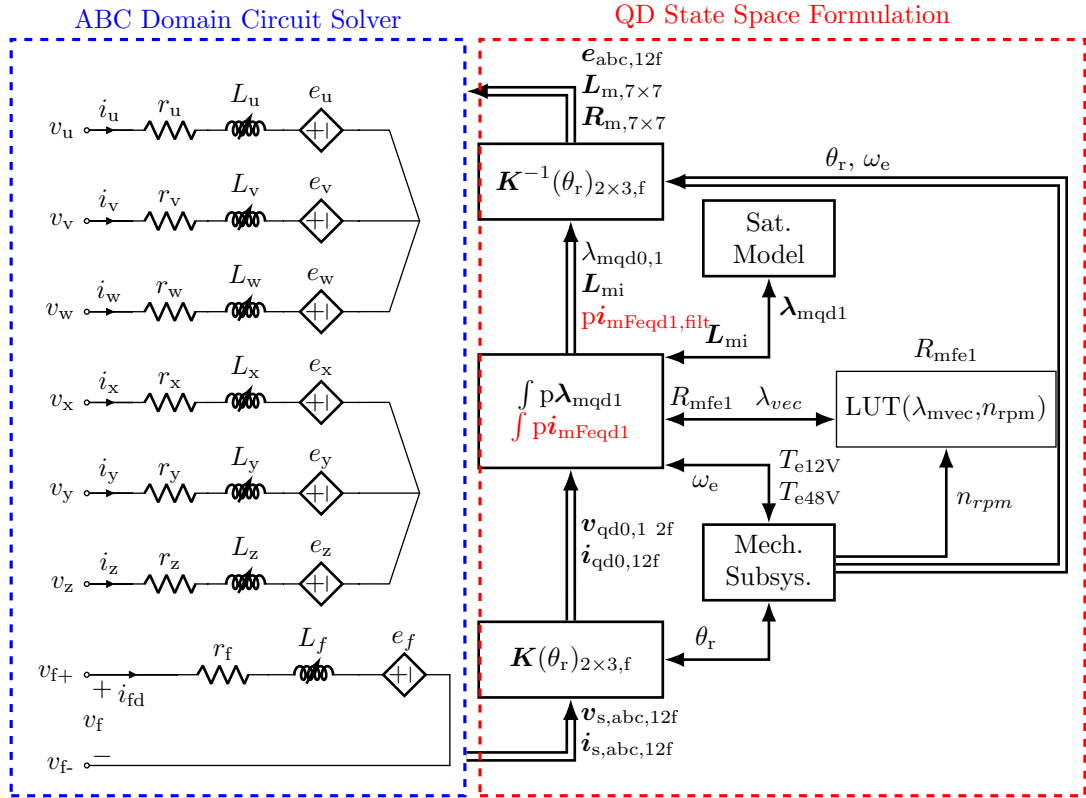


Figure 2.17 – Six-Phase VBR Model Overview with Iron Losses

2.3.3 VBR Formulation with Iron Losses

All required equations for the state space part of the VBR model with iron losses are derived in Subsection 2.3.1. The voltage equations in the d - q reference frame, taking into

account the iron losses, are shown in equation (2.3.1.10). The next step is to convert the equations to their VBR form. The starting point for the VBR model derivation with iron losses is the voltage equations in the d - q reference frame without iron losses as shown in equation (2.2.1.9). The differential magnetizing currents vector $p\mathbf{i}_{mqd0,12f}$ has as entries the magnetizing currents in q -, d - and 0 -direction in reference to both stator systems and the d -axis magnetizing current referred to the rotor. The vector has therefore the following entries: $[i_{mq1}, i_{mq1}, 0, i_{mq2}, i_{md2}, 0, i_{mdf}]$. The magnetizing currents along the q -axis have the corresponding linear dependency: $i_{mq1} = \frac{i_{mq2}}{N_{s12}}$. The magnetizing currents along the d -axis have the linear dependency: $i_{md1} = \frac{i_{md2}}{N_{s12}} = \frac{2i_{mdf}}{3N_{s1f}}$. The magnetizing currents are expressed through the stator, the rotor and the iron loss currents, when Kirchoff's Current Law is applied as shown in equations (2.3.1.3) and (2.3.1.4). A system of equations, expressed in vector-matrix form, is derived this way and represents the explained dependency as shown in equation (2.3.3.1). The matrix \mathbf{N}_{12f} is already known through equation (2.2.1.11). It incorporates the relationship between the magnetizing currents vector $\mathbf{i}_{m,qd0,12f}$ and the stator and rotor currents vector $\mathbf{i}_{s,qd0,12f}$ for the machine model without iron losses. The matrix incorporates the linear dependencies between stator system 1, 2 and the field winding. The magnetizing currents and the stator and rotor currents are related to each-other according Kirchoff's Currents Law. This relationship is also included in the matrix \mathbf{N}_{12f} . The sub-matrix \mathbf{N}_{fe} is included in equation (2.3.3.1) in order to take into account the iron loss currents.

$$p\mathbf{i}_{m,qd0,12f} = \begin{bmatrix} \mathbf{N}_{12f} & \mathbf{N}_{fe} \end{bmatrix} \cdot \begin{bmatrix} p\mathbf{i}_{s,qd0,12f} \\ p\mathbf{i}_{mqd,fe1} \end{bmatrix} \quad (2.3.3.1)$$

$$\mathbf{N}_{fe} = \begin{bmatrix} 0 & 1 & 0 & 0 & \frac{1}{N_{s12}} & 0 & 0 & N_{s1f} \\ 1 & 0 & 0 & \frac{1}{N_{s12}} & 0 & 0 & N_{s1f} & 0 \end{bmatrix}^T$$

The time derivative of the magnetic flux vector $p\boldsymbol{\lambda}_{mqd0,12f}$ can be expressed through the derived expressions from equation (2.3.3.1). The result is shown in equation (2.3.3.2).

$$p\boldsymbol{\lambda}_{mqd0,12f} = \mathbf{L}_{mi,12f} \cdot p\mathbf{i}_{m,qd0,12f} = \begin{bmatrix} \overline{\mathbf{L}_{mi,12f}} & \mathbf{L}'_{mi} \end{bmatrix} \cdot p\mathbf{i}_{sqd0,12f,feq,fed} \quad (2.3.3.2)$$

$$\text{with } \begin{bmatrix} \overline{\mathbf{L}_{mi,12f}} & \mathbf{L}'_{mi} \end{bmatrix} = \mathbf{L}_{mi,12f} \cdot \begin{bmatrix} \mathbf{N}_{12f} & \mathbf{N}_{fe} \end{bmatrix}$$

The result from equation (2.3.3.2) is used to adapt the voltage equations without iron losses, shown in equation (2.2.1.13). The voltage equations with iron losses are shown in equation (2.3.3.3).

$$\mathbf{v}_{s,qd,12f} = [\mathbf{R}_{s,12f} + \omega_e \cdot \mathbf{L}_{ls,12f} \cdot \mathbf{P}_m] \cdot \mathbf{i}_{s,qd,12f} + \mathbf{L}_{ls,12f} \cdot p\mathbf{i}_{s,qd,12f} \quad (2.3.3.3)$$

$$+ \begin{bmatrix} \overline{\mathbf{L}_{mi,12f}} & \mathbf{L}'_{mi} \end{bmatrix} \cdot p\mathbf{i}_{s,qd0,12f,feq,fed} + \omega_e \cdot \mathbf{P}_m \cdot \boldsymbol{\lambda}_{m,qd0,12f}$$

The currents vector with iron losses $\mathbf{p}i_{s,\text{qd}0,12\text{f},\text{feq},\text{fed}}$ is split into two sub-vectors: the currents vector without iron losses $\mathbf{p}i_{s,\text{qd}0,12\text{f}}$ and the iron loss currents represented as a vector $\mathbf{p}i_{\text{mqfe}1}$. Then equation (2.3.3.3) is transformed to equation (2.3.3.4).

$$\begin{aligned} \mathbf{v}_{s,\text{qd}0,12\text{f}} = & [\mathbf{R}_{s,12\text{f}} + \omega_e \cdot \mathbf{L}_{ls,12\text{f}} \cdot \mathbf{P}_m] \cdot \mathbf{i}_{s,\text{qd},12\text{f}} + [\mathbf{L}_{ls,12\text{f}} + \overline{\mathbf{L}_{mi,12\text{f}}}] \cdot \mathbf{p}i_{s,\text{qd},12\text{f}} \\ & + \underbrace{\mathbf{L}'_{mi} \cdot \mathbf{p}i_{\text{mqd},\text{fe}1} + \omega_e \cdot \mathbf{P}_m \cdot \boldsymbol{\lambda}_{m,\text{qd}0,12\text{f}}}_{\text{back-emf with iron losses}} \end{aligned} \quad (2.3.3.4)$$

Equation (2.3.3.4) shows, that the derivatives of the iron loss currents $\mathbf{p}i_{\text{mqfe}1}$ and $\mathbf{p}i_{\text{mdfe}1}$ are part of the back-emf voltage-terms. This introduces an algebraic loop, which has to be resolved via a low-pass filter. The time constant τ_f of the low-pass filter is chosen such, that the simulation speed is fast enough and the accuracy is comparable with the pure DQ model. In this case a value of 1 ms is chosen. The low pass filter is implemented in the time domain within the state space part of the VBR model according to equation (2.3.3.5).

$$\begin{aligned} \mathbf{p}i_{\text{mqfe}1,\text{filt}}^{CD} &= \frac{\mathbf{p}i_{\text{mqfe}1} - \mathbf{p}i_{\text{mqfe}1,\text{filt}}^{CS}}{\tau_f} \\ \mathbf{p}i_{\text{mdfe}1,\text{filt}}^{CD} &= \frac{\mathbf{p}i_{\text{mdfe}1} - \mathbf{p}i_{\text{mdfe}1,\text{filt}}^{CS}}{\tau_f} \end{aligned} \quad (2.3.3.5)$$

The variable with the superscript $_{CS}$ is the continuous state and the variable with the superscript $_{CD}$ is the continuous derivative. The variables with subscript $_{CS}$ are the filtered differential iron loss currents. The VBR form of the model with iron losses is derived when one applies equations (2.2.2.1), (2.2.2.2) and the reverse transformation $\mathbf{K}_{s,2 \times 3}(\theta_r)^{-1}$ from equation (2.2.1.2) to equation (2.3.3.4). This way the final VBR form of the dual-voltage machine with iron losses is derived in equation (2.3.3.6).

$$\begin{aligned} \mathbf{v}_{s,\text{abc},12\text{f}} = & \mathbf{K}_{s,2 \times 3}(\theta_r)^{-1} [\mathbf{R}_{s,12\text{f}} + \omega_e \cdot \mathbf{L}_{ls,12\text{f}} \cdot \mathbf{P}_m] \mathbf{K}_{s,2 \times 3}(\theta_r) \cdot \mathbf{i}_{s,\text{abc},12\text{f}} \\ & + \mathbf{K}_{s,2 \times 3}(\theta_r)^{-1} [\mathbf{L}_{ls,12\text{f}} + \overline{\mathbf{L}_{mi,12\text{f}}}] \cdot (\mathbf{p} \mathbf{K}_{s,2 \times 3}(\theta_r) \cdot \mathbf{i}_{s,\text{abc},12\text{f}} \\ & + \mathbf{K}_{s,2 \times 3}(\theta_r) \cdot \mathbf{p}i_{s,\text{abc},12\text{f}}) \\ & + \mathbf{K}_{s,2 \times 3}(\theta_r)^{-1} \underbrace{\mathbf{L}'_{mi} \cdot \mathbf{p}i_{\text{mqdfe}1}^{filt} + \omega_e \cdot \mathbf{P}_m \cdot \boldsymbol{\lambda}_{m,\text{qd}0,12\text{f}}}_{\text{back-emf with iron losses}} \end{aligned} \quad (2.3.3.6)$$

2.4 Model Parametrization with Measurements

This section explains how to derive the parameters for the presented models and shows simulation results of the programmed models in PLECS. The simulation results are compared against measurements from a test bench to verify the models and their

parametrization. The performed tests in the current section serve only for the model parametrization. The model is verified against the performed measurements at no-load. In Chapters 3 and 4, which handle the current control design and the torque control development, the parametrized model is tested under load conditions.

The required machine parameters for both models, the DQ and the VBR, are the same and can be identified from the d - q equivalent circuit of the machine model shown in Figure 2.15. All parameters are constant except for the main inductances of the machine along the d - and q -axis and the iron loss resistance. The main inductance is represented by an analytic function described in detail in Subsection 2.1.5, which is parametrized by measurements in the current subsection. The iron loss resistance is calculated from measurements and stored as a LUT, which is integrated in the models.

Resistance, Pole Pairs and Displacement Angle

Both stator resistance values are measured with a micro-ohmmeter (Digital Low Resistance Ohmmeter (DLRO)) with a four-wire measurement technique to be able to measure the low resistance values of the machine. The resistance between two phase terminals, for example u - v or x - y , is measured and divided by two to get the stator phase resistances r_{s1} or r_{s2} . This way the resistance r_{s1} is found to be 1,94 m Ω and the stator resistance of the 48V winding, r_{s2} , is equal to 26,61 m Ω . The rotor resistance is also measured with an ohmmeter at the field winding terminals and found to be 7,2 Ω . The machine is known to have 8 pole pairs, which can be also easily measured. For this purpose a certain field winding current and a constant mechanical angular speed are set. The machine phases are detached from the converter and the generated back-emf voltage is measured by an oscilloscope. The ratio between the electrical angular speed of the measured back-emf voltage ω_e and the set mechanical speed by the test bench ω_m corresponds to the pole pairs number p of the machine. The displacement angle α_{12} between both stator systems is derived through variation of the α_{12} parameter in the six-phase transformation matrix from equation (2.2.1.1). The measured phase voltages in the ABC domain are transformed into the d - q domain with the six-phase transformation. The transformed d - q voltages in the 12V and 48V reference frames should have only a voltage component along the q -axis, because the field winding current induces flux only along the d -axis. Therefore, the d -flux component acts through the cross-coupling and the applied transformation only on the q -axis. The parameter α_{12} is varied in the six-phase transformation, such that, when the measured XYZ voltages are transformed into the d - q domain, only a voltage along the q -axis of system 2 is induced. For the prototype machine the measured displacement angle α_{12} is identified to be 30°.

Turns Ratios Identification N_{s12} , N_{s1f} and N_{s2f}

The *turns ratio* N_{s12} between stator 1 and 2 is calculated through the measured voltages at no-load $N_{s12} = \frac{v_{qs1}}{v_{qs2}}$. This is the ratio between the effective number of turns of each winding. The measured q -axis voltages, v_{qs1} and v_{qs2} , are plotted in Fig. 2.18. During the measurement the machine is operated at a constant speed of 1000 rpm. The field winding current is varied from 0 A to 4,5 A in 0,5 A steps. The field winding current is set through a PI controller. The *turns ratio* N_{s12} is found as a mean value over all measured ratios for each excitation current set point. The *turns ratio* $N_{s12} = \frac{N_{s1}}{N_{s2}}$ with a value of 0.245 is calculated. The d -axis magnetizing fluxes, λ_{md1} and λ_{md2} , are calculated according to equations (2.4.0.1) and (2.4.0.2). The magnetizing fluxes are illustrated in Fig. 2.19.

$$\lambda_{md1} = \frac{v_{qs1}}{\omega_e} \quad (2.4.0.1)$$

$$\lambda_{md2} = \frac{v_{qs2}}{\omega_e} \quad (2.4.0.2)$$

The *turns ratio* between stator and rotor, N_{s1f} or N_{s2f} , is more difficult to derive. For this purpose a FOC is employed. The design of the employed current control (FOC) is explained in detail in Chapter 3. In this subsection only the required measurements for the parameter identification are presented. A positive d -axis current at the 48V side is set through the d -axis current controller, while all other currents are controlled to zero. The 48V side is electromagnetically stronger than the 12V side and thus more suitable to magnetize the rotor. The current i_{ds2} is varied from 0 A up to 275 A in 25 A steps at 1000 rpm.

The leakage inductance L_{ls2} plays an important role, when the rotor is magnetized by the stator current. Due to this effect a leakage flux is induced in the stator winding, which results in an additional back-emf voltage due to the rotating flux in the leakage inductance. This voltage term is part of the whole measured voltage along the q -axis v_{qs2} at the machine phase terminals and has to be subtracted from the measured voltage v_{qs2} . Therefore, the magnetizing flux cannot be calculated without the knowledge of L_{ls2} . The relationship between magnetizing flux λ_{md2} and the measured q -axis voltage v_{qs2} taking into account the influence of the leakage inductance L_{ls2} is shown in equation (2.4.0.3). The magnetizing flux referred to the 12V side λ_{md1} can be calculated from the measured q -axis voltage of stator system 1 v_{qs1} . Since no current flows in the stator winding of system 1, the voltage v_{qs1} is only a function of the magnetizing flux λ_{md1} and the electrical angular speed ω_e . Therefore the leakage inductance of stator system 1, L_{ls1} , has no influence on the measured voltage v_{qs1} . The magnetizing flux λ_{md1} is calculated according to equation (2.4.0.4). Equations (2.4.0.3) and (2.4.0.4) form actually a system of equations with the unknown variables λ_{md2} , λ_{md1} and L_{ls2} . Since the magnetizing fluxes λ_{md2} and λ_{md1} are linearly dependent through the already known turn ratio between stator system 1 and stator system 2 N_{s12} , the system of equations can be solved for all three unknown variables λ_{md1} , λ_{md2} and L_{ls2} . The magnetizing flux λ_{md1} calculated according to equation (2.4.0.4) is referred to system 2 with the already found *turns ratio* N_{s12} and is plotted in Fig. 2.23. In Fig. 2.23 the referred flux $\frac{\lambda_{md1}}{N_{s12}}$ is plotted versus the

magnetizing current i_{ds2} . The measurement of λ_{md2} from Fig. 2.19 is plotted also in Fig. 2.21. This time the excitation current is referred to the stator 2 through the *turns ratio* $\frac{2}{3}N_{s2f}$. The factor $\frac{2}{3}$ is used to convert the excitation current to the d - q frame and the *turns ratio* N_{s2f} is adapted such that both curves match as well as possible to each other. Through this procedure the *turns ratio* between stator 2 and rotor is identified. The derived *turns ratio* from stator system 2 to rotor, N_{s2f} , is equal to 0.0076 and respectively from stator system 1 to rotor, N_{s1f} , to 0.0019.

$$\lambda_{md2} = \frac{(v_{qs2} - (\omega_e \cdot L_{ls2} i_{ds2}))}{\omega_e} \quad \lambda_{md1} = \frac{v_{qs1}}{\omega_e} \quad (2.4.0.4)$$

Magnetizing Curve and Main Inductance Parameters: L_{md1} , L_{md1s} , $\lambda_{mT,LV}$ and f_T

The saturation curve is derived as a next step in the parametrization procedure from the measured back-emf voltages in Fig. 2.18. The magnetizing fluxes λ_{md1} and λ_{md2} are calculated according equations (2.4.0.1) and (2.4.0.2) and plotted in Fig. 2.23 and Fig. 2.22 respectively. For the saturation modeling, described in Subsection 2.1.5, four parameters have to be derived from the measured back-emf curve. The parameters describing the saturation curve are the form factor f_T , the unsaturated d -axis inductance $L_{md1,0}$, the saturated d -axis inductance L_{md1s} and the transition flux $\lambda_{mT,LV}$. These have to be varied until they describe a curve, which matches the measured flux from Fig. 2.23. The derived parameters after a fitting procedure are shown in Table 2.1. The same magnetizing flux curve referred to stator 2 (48V) is shown in Fig. 2.22. In order to approximate the measured points of λ_{md2} the found parameters for the stator system 1 (12V) are referred to the system 2. The inductances are referred with $\frac{1}{N_{s12}}^2$ and the transition flux with $\frac{1}{N_{s12}}$. The form factor remains unchanged.

Stator and Rotor Leakage Inductances: L_{ls1} , L_{ls2} and L_{lf}

The leakage inductance of stator system 2 L_{ls2} is derived from equation (2.4.0.3). Equation (2.4.0.3) is solved for L_{ls2} and the magnetizing flux λ_{md2} is substituted with $\frac{\lambda_{md1}}{N_{s12}}$. The magnetizing flux λ_{md1} is derived from equation (2.4.0.4). Thus, the leakage inductance for stator system 2 is calculated according to equation (2.4.0.5). The parameter L_{ls2} is plotted in Fig. 2.24. The leakage inductance varies from 70 μ H down to 28 μ H. This is due to the fact that the 48V side saturates the rotor and stator and therefore also the 48V leakage inductance gets saturated. Further the machine is connected to an external power electronics and the cables connecting the machine and power electronics contribute mainly to the increase of the leakage inductance. In general the leakage inductance of the machine is constant and the saturation behavior is due to the additional cables between the machine and the converter. The machine model with the power electronics model are

integrated in PLECS do not include the inductance of the wiring. Therefore the model is parametrized with a constant leakage inductance. The dual-voltage machine model is parametrized with a mean value over the measured inductances of $L_{ls2} = 38,3 \mu\text{H}$, which is an appropriate value for operating the machine under load conditions.

$$L_{ls2} = \frac{v_{qs2} - \omega_e \frac{\lambda_{md1}}{N_{s12}}}{\omega_e \dot{i}_{ds2}} \quad (2.4.0.5)$$

The current i_{qs1} is varied in order to measure the leakage inductance of stator 1 L_{ls1} . During the test the voltages v_{ds1} and v_{ds2} are recorded. A field winding current of 1,5 A is set in the rotor in order to saturate the main inductance. The rotor current does not have any influence on the d -axis voltages, because the cross-coupling of the field winding current acts on the q -axis voltages. The recorded voltages v_{ds1} and v_{ds2} are plotted in Fig. 2.25. The stator leakage inductance L_{ls1} is calculated according to equation (2.4.0.7) through the calculated magnetizing flux λ_{mq2} from equation (2.4.0.6). Following this measurement procedure a mean value of $L_{ls1} = 12,9 \mu\text{H}$ is found. The leakage inductance of stator system 1 does not show such saturation behavior like L_{ls2} due to the fact the 12V side of the machine is electromagnetically much weaker and does not saturate the stator and rotor iron as much as the 48V side. The rotor leakage inductance L_{lf} is not derived from measurements, but is known to be 119 mH according to some parameters data delivered with the machine prototype. A possible procedure to measure the leakage inductance of the rotor, which can be employed also to measure all other linear parameters of the machine, is explained in [4]. The procedure is complex and involves Standstill Frequency-Response (SSFR) tests. SSFR tests are employed at machine standstill and aim to extract the linear parameters of the machine under various frequencies. The machine is excited with small-signals at different frequencies and its frequency response is measured through a dynamic analyzer. Then a Genetic Algorithm (GA) is employed, which looks for appropriate machine parameters, which describes the measured frequency response curves. This measurement procedure is very tedious and will go out of the scope and focus of the work, if employed. Usually these tests are employed for the parameter identification of higher order models, representing also sub-transient machine behavior [30].

All machine parameters measured through the presented procedure are summed up in Table 2.1.

$$\lambda_{mq2} = \frac{v_{ds2}}{\omega_e} \quad (2.4.0.6) \quad L_{ls1} = \frac{v_{ds1} + \omega_e \lambda_{mq2} \cdot N_{s12}}{-\omega_e \dot{i}_{qs1}} \quad (2.4.0.7)$$

Iron Loss Resistance: R_{mfe1}

For the purpose of measuring the iron loss resistance R_{mfe1} the speed and the flux in the machine have to be varied. Therefore the machine is detached from the converter and

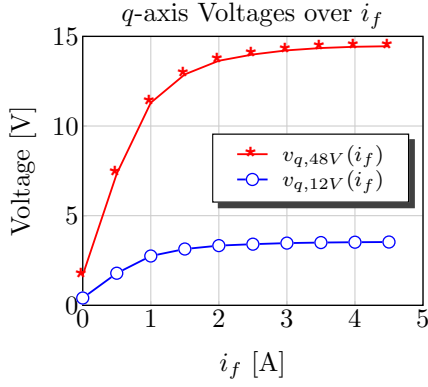


Figure 2.18 – q Voltages over i_{fd}

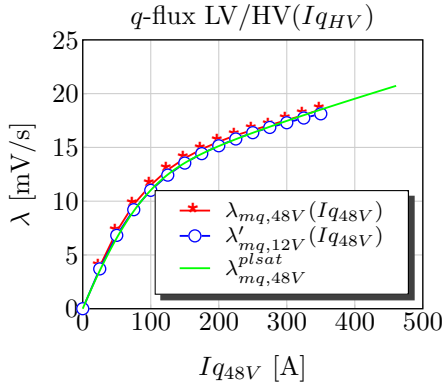


Figure 2.20 – Calc. q -flux

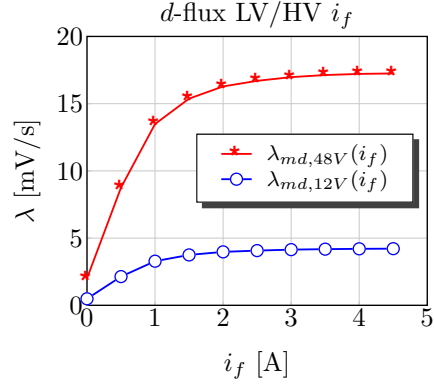


Figure 2.19 – Calc. d -flux

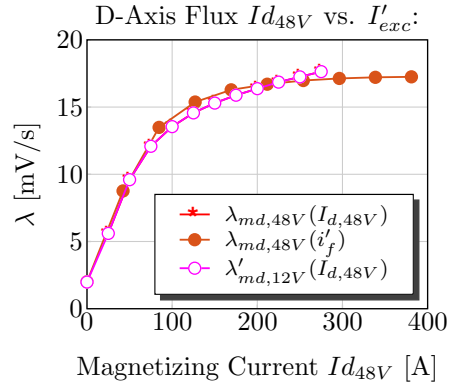


Figure 2.21 – Magn. Flux 12V and 48V over i_{fd}

only the field winding is supplied with current. The field winding is able to magnetize the main inductance up to the maximum rated flux. The field winding current is varied from 0 A up to 3 A in 0,5 A steps. The speed is varied from 1500 rpm to 4000 rpm in 500 rpm steps. The speed of the test bench is limited to around 4000 rpm due to mechanical vibrations of the test stand. During the measurements the generated negative mechanical torque is recorded. The claw-pole dual-voltage machine has permanent magnets integrated in-between the claws of the machine rotor. These ferite magnets cause also a very small amount of iron losses even if the excitation current is zero. These iron losses cannot be separated from the friction losses. Therefore the friction losses are assumed to be equal to the measured mechanical losses at zero excitation current. The power equivalence equation used to derive the iron losses at no-load is shown in equation (2.4.0.8). The iron losses are equal to the measured mechanical losses minus the friction losses at 0 A excitation current. The measured iron losses are plotted in Fig. 2.26 and the measured mechanical torque is illustrated in Fig. 2.27. The recorded voltages used to calculate the magnetizing fluxes as shown in equation (2.4.0.9) are plotted in Fig. 2.28.

$$P_{\text{mech}} = \omega_{\text{mech}} \cdot T_{\text{mech}} = P_{\text{Fe,losses}} + P_{\text{fric}} \quad (2.4.0.8)$$

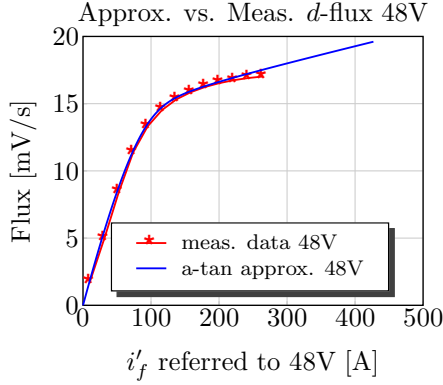


Figure 2.22 – Aprox. vs. Meas. Flux 48V
Leakage Stator Inductance 2 over I_{dHV}

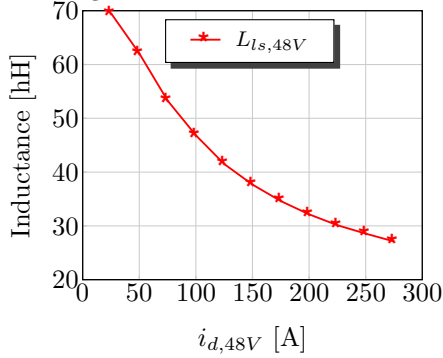


Figure 2.24 – L_{ls2} over i_{ds2}

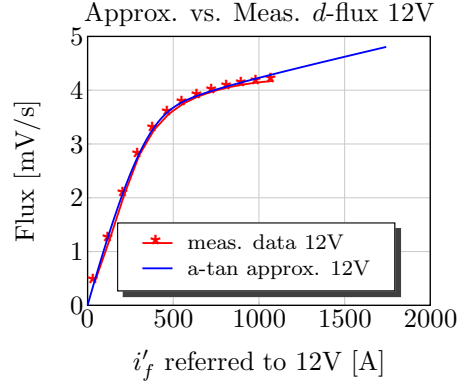


Figure 2.23 – Aprox. vs. Meas. Magn. Flux 12V
 d -axis voltages over I_{qLV}

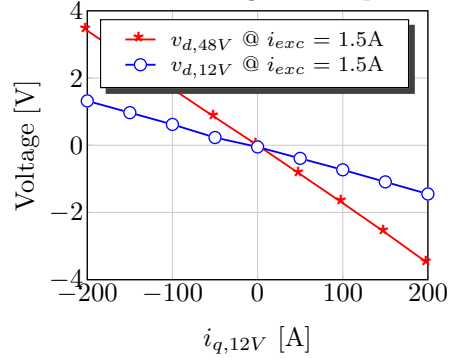


Figure 2.25 – $v_{ds1}(i_{qs1}), v_{ds2}(i_{qs1})$ @ $i_{fd} = 1,5 A$

$$\lambda_{mvec1} = \sqrt{v_{qs1,meas}^2 + v_{qs1,meas}^2} / \overbrace{(n_{rpm,meas} \cdot 2\pi p / 60)}^{\omega_e} \quad (2.4.0.9)$$

The iron loss resistance can be calculated either in reference to stator system 1 or stator system 2. The described model generally refers all quantities to stator system 1 (12V). Equations (2.4.0.10) and (2.4.0.11) show how to calculate the iron loss resistance from the measured back-emf voltages. The measured torques at low excitation currents and speed lower than 2000 rpm show very small values and include a lot of noise. This makes the calculation of the iron loss resistance for low excitation currents and low speeds erroneous, despite the fact that low-pass filters are applied over the measured data. The normal operating range for the excitation current under load is between 1A and 3A. Therefore the inaccurate iron loss resistance for currents under 1A does not represent a hurdle. The measurements show that the iron loss resistance varies significantly with speed and excitation current. Some of the known methods of analytical representation of iron losses as function of frequency and flux, like the Steinmetz or Bertotti equations, are applied to approximate the measured data. The least square algorithm is used to fit the coefficients of the analytical equations to the measurement data. Unfortunately, none of the analytical descriptions of the iron loss phenomena succeeds to represent accurately

Table 2.1 – Machine Model Parameters

param.	value	param.	value	param.	value	param.	value
r_{s1}	1,94 m Ω	N_{s1}	0.98	L_{ls1}	12,90 μ H	L_{md1}	11,83 μ H
r_{s2}	26,61 m Ω	N_{s2}	4.00	L_{ls2}	38,30 μ H	L_{mq1}	9,01 μ H
r_{fd}	7,20 Ω	N_f	508.00	L_{md1s}	0,43 μ H	L_{lf}	119,00 mH
$\lambda_{mT,HV}$	15,84 $\frac{mV}{s}$	L_{md2}	197,10 μ H	L_{md2s}	7,20 μ H	N_{s12}	0.245
$\lambda_{mT,LV}$	3,88 $\frac{mV}{s}$	f_T	1.00	λ_{mag1}	0,44 $\frac{mV}{s}$	λ_{mag2}	1,78 $\frac{mV}{s}$
α	0.96	α_{12}	30.00 $^\circ$	L_{mq2}	150,00 μ H	N_{s1f}	0.0019

the measured iron losses. Therefore, the measured resistance is implemented as a LUT in the model.

$$R_{mfe1} = \frac{(V_{q12V}^2 + V_{d12V}^2)}{\frac{2}{3} \cdot P_{mech}} \quad (2.4.0.10) \quad R_{mfe2} = \frac{(V_{q48V}^2 + V_{d48V}^2)}{\frac{2}{3} \cdot P_{mech}} \quad (2.4.0.11)$$

A matlab script is used to calculate the iron loss resistance and every calculated value is stored in a 2D-LUT in dependence of the excitation current set point i_{fd} and the mechanical speed n_{rpm} . In order to take into account the influence of the stator currents, magnetizing the rotor, the calculated iron loss resistance needs to be stored in dependence of the generated flux λ_{md1} . For this purpose a matlab script is written to interpolate the field winding current based on a current magnetizing flux step $\lambda_{vec,step}$. The magnetizing flux steps are calculated as equivalent flux steps from 0 $\frac{mV}{s}$ up to the maximum measured flux of a 4,2 $\frac{mV}{s}$ according to equation (2.4.0.9) in reference to system 1. The equivalent flux steps are calculated as shown in equation (2.4.0.12). Then for every flux step $\lambda_{vec,step}$ the field winding current is interpolated based on the saturation curve from Fig. 2.23 (or Fig. 2.22 for system 2). Then the iron loss resistance value R_{mfe1} is interpolated based on the found field winding current value corresponding to the flux step $\lambda_{vec,step}$. These values are stored in a 2D-LUT in dependence of λ_{vec} and n_{rpm} . The LUT is integrated in the model. The iron loss resistance is constantly interpolated based on the generated flux λ_{mvec} from the model and the current machine speed. The interpolated value of R_{mfe1} is forwarded to the state space part of the model shown in Fig. 2.17.

$$\lambda_{vec,step} = (\lambda_{vec,max} - \lambda_{vec,min}) / n_{rpm,steps} \quad (2.4.0.12)$$

Simulations are performed with the model, parametrized with the parameters from Table 2.1, and with the derived iron loss resistance LUT. The simulation results are shown in Figures 2.32, 2.33 and 2.31. Figure 2.32 shows the simulated iron losses. The losses are calculated in the same way as these have been measured $P_{Fe,losses} = \omega_{mech} \cdot T_{mech} - P_{fric}$. The simulated mechanical torque is plotted in Fig. 2.33 and the generated back-emf voltages are shown in Fig. 2.31. Both models VBR and Quadrature Direct (QD) deliver the same simulation results. The models are implemented in PLECS and the control of the stator and rotor currents is implemented in Simulink. During the measurements of the iron losses the machine phases are detached from the converter. The same procedure is replicated also in the simulation and only the field winding is supplied with current through the 48V inverter. A schematic of the control, the machine and the power electronics is presented in Fig. 2.34. The machine model is connected to two three-phase mosfet inverters. Each of the inverters consist of six MOSFETs - three high-side mosfets and three low-side MOSFETs. Chapter 3 explains the current control development for the machine.

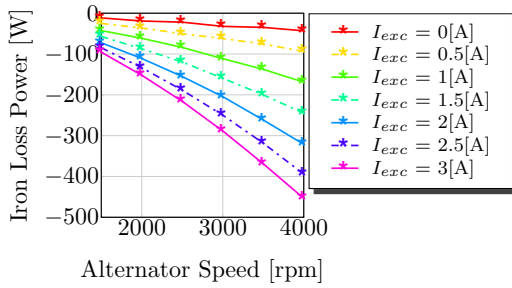


Figure 2.26 – Iron Loss Power at No-Load

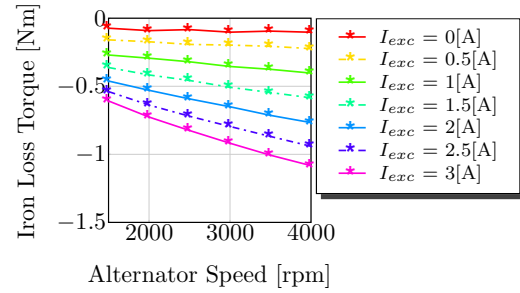


Figure 2.27 – Loss Torque at No-Load

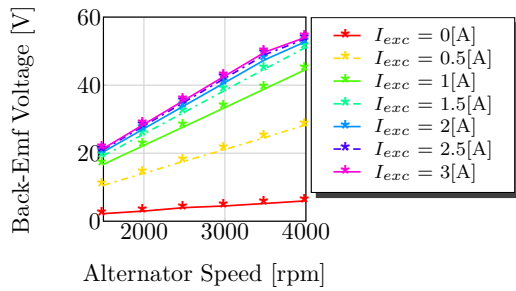


Figure 2.28 – Iron Loss Voltage at No-Load

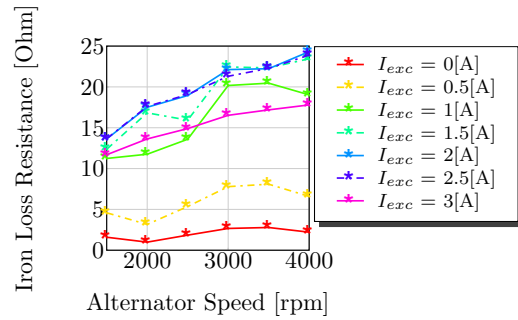


Figure 2.29 – Iron Loss Resistance LUT(i_{fd}, n_{rpm})

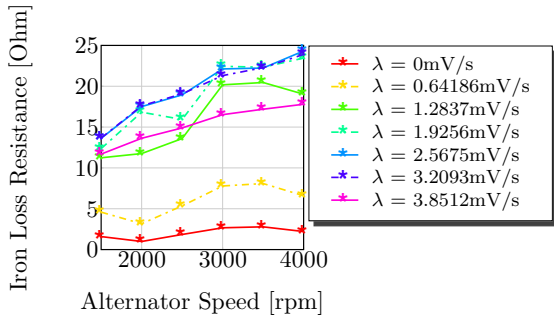


Figure 2.30 – Resistance LUT(λ_{md1}, n_{rpm})

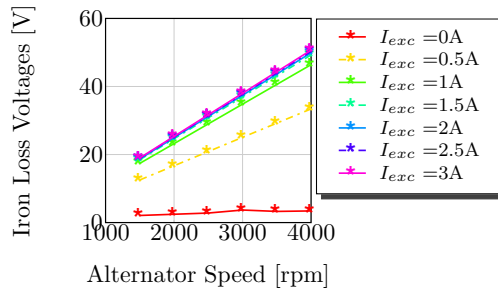


Figure 2.31 – Simulated Back-Emf Voltage

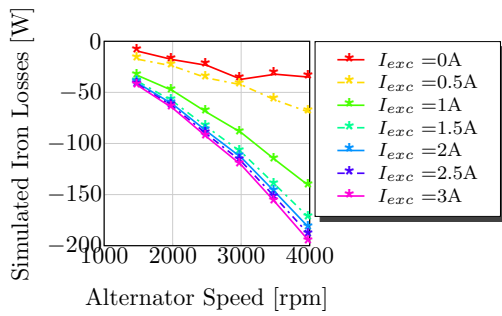


Figure 2.32 – Simulated Iron Losses

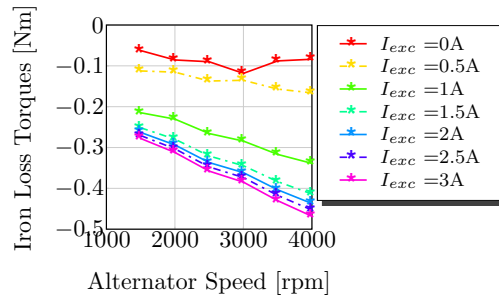


Figure 2.33 – Simulated Iron Loss Torque

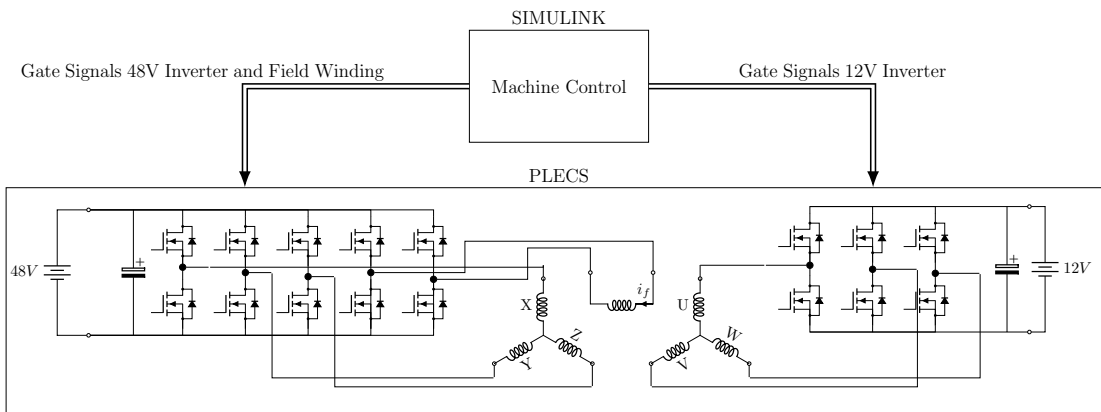


Figure 2.34 – Simulation of the Controlled Dual-Voltage Machine with Power Electronics

3 Current Control Design

This chapter discusses the current control design of the inner control loops for the dual-voltage machine. First, the principles of the feedback control are presented and a short review of various criteria for stability analysis is performed. The state space representation of a physical dynamic system is presented, which is a suitable method of describing a physical model for control design purposes. The loop shaping method as a control design principle for closed loop systems is explained. Then, the MO criterion, which is typically applied to the design of current controllers for electric drives, is presented. For the dual-voltage machine five currents in total (i_{qs1} , i_{ds1} , i_{qs2} , i_{ds2} and i_{fd}) have to be controlled in order to set both torques T_{e12V} and T_{e48V} . For the purpose of control design the machine equations are transformed into their Laplace form. The MO tuning method is applied to the stator and rotor current control loops. Performed simulations show that the performance of the tuned PI controllers deteriorates at speed and therefore a feed-forward action is introduced to counteract the back-emf voltage. The simulations show that the Decoupling Network (DN) and Feedforward Network (FN) both improve the control performance at speed. These decoupling methods counteract the back-emf voltage generated from the machine, but cannot compensate the dynamic coupling between the axis. In order to design a full dynamic decoupling control the dual-voltage machine is considered as a full Multiple-Input Multiple-Output (MIMO) control problem and an approach from the MIMO control theory is applied to counteract the dynamic coupling in the plant. A new Dynamic Decoupling Matrix (DDM) is presented, which compensates the dynamic and static coupling (back-emf). The presented DDM is a pre-compensator matrix used to diagonalize the plant. The new control is verified in a simulation environment and counteracts the dynamic disturbances effectively. The new dynamic decoupling control outperforms conventional static decoupling machine decoupling methods.

The designed PI controllers, tuned after the MO criterion, with a static decoupling action are implemented on a dSpace Rapid Control Prototyping (RCP) system and verified on a test stand. The measurements show very good correlation with the performed simulations. The new dynamic decoupling method with a pre-compensator matrix could not be verified on the test bench due to time limitations. The good correlations between measurements and simulations with the static decoupling method imply that the simulation results performed with the DDM will correlate also well with measurements on a test bench. Unfortunately the DDM could not be tested on the test bench due to time limitations at the end of the project.

3.1 Introduction into Feedback Control

This section explains some basic principles of the feedback control. The section presents some of the state of the art stability criterion and shows, when a control loop gets unstable. The state space representation of a dynamic model is presented as a modeling method. This model representation is often employed for a physical system, when a current control design is pursued. The loop shaping design method is explained in the section. According to this method a controller is designed in such a way that the closed loop system has a certain loop shape in the frequency domain. A special case of the loop shaping design methods is the MO tuning approach, which is employed on current controllers for electric drives. The MO design method is derived based on an example of a plant consisting of an inverter and a machine model.

3.1.1 Stability of a Closed Loop

The purpose of a control loop is to set a certain variable to a pre-specified set point. A control loop consists usually of a transfer function of the plant, a transfer function of the controller and a feedback transfer function enclosed in a feedback loop as illustrated in Fig. 3.1. The most difficult task, when a controller is designed, is to define the transfer

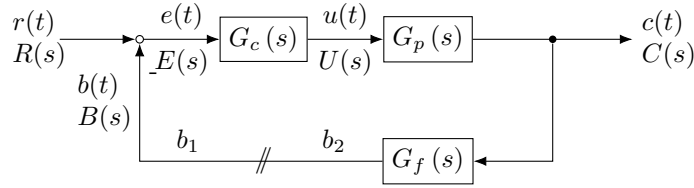


Figure 3.1 – Signal flow diagram of a control loop

function of the controller in a such a way that the target set point is reached in minimum time with a minimum overshoot. At the same time the whole feedback loop has to remain stable regardless of noise in the measured feedback variables or any disturbances acting on the controlled variable and the plant. As an introduction into the stability analysis a simple feedback control loop example, as explained in Reference [63], is discussed with the feedback loop from Fig. 3.1. If the reference signal is set to zero $r(t) = 0$, and b_1 is a signal with sinus excitation $\hat{b}_1 \sin(\omega_1 t)$, then the signal at the split feedback loop b_2 would have a different amplitude and phase: $\hat{b}_2 \sin(\omega_1 t + \phi_0(\omega_1))$. The angle $\phi_0(\omega_1)$ is the phase angle of the split transfer function $-G_0(j\omega)$, which is the ratio between b_2 and b_1 and is given in equation (3.1.1.1).

$$G_0(j\omega) = \frac{b_2(j\omega)}{b_1(j\omega)} = -G_c(j\omega)G_p(j\omega)G_f(j\omega) \quad (3.1.1.1)$$

If the phase shift angle of the split transfer function $-G_0(j\omega)$ becomes at a certain frequency ω_1 180° , then the signal b_2 will have an inverted sign in comparison to b_1 . In case the amplitude ratio of b_1 and b_2 is 1 at this frequency, the feedback loop gets self excited. If the amplitude ratio is greater than one, then the feedback loop will overexcite and get unstable. In case the amplitude is smaller than 1, the self excitation will fade away. The derived conclusions are summarized mathematically as a stability criterion for the feedback loop in equation (3.1.1.2).

$$|G_0(j\omega)|_{|\phi_0=-180^\circ} = \begin{cases} < 1 & \text{stability} \\ = 1 & \text{stability border} \\ > 1 & \text{instability} \end{cases} \quad (3.1.1.2)$$

The magnitude of the transfer function can be calculated according to the absolute value formula of a complex number shown in equation (3.1.1.3) and its phase according to equation (3.1.1.4).

$$|G(j\omega)| = \sqrt{\text{Re}(G_o(j\omega))^2 + \text{Im}(G_o(j\omega))^2} \quad (3.1.1.3)$$

$$|G(j\omega)| = \arctan \frac{\text{Im}(G_o(j\omega))}{\text{Re}(G_o(j\omega))} \quad (3.1.1.4)$$

There are various criteria developed throughout the years, which provide analysis of closed loop transfer functions. The book *Elektrische antriebe-regelung von antriebssystemen [electrical drives- control of drivetrain systems]* by Schröder ; et al. [63] is a good reference regarding analysis of control systems and design of controllers with focus on electrical drives. Another good reference book on general control theory is *Automatic control systems* by Kuo [39]. The book *Multivariable Feedback Control: Analysis and Design* by Skogestad; Postlethwaite provides a good review of stability analysis for Single-Input Single-Output (SISO) and MIMO systems. There are couple of mathematical methods suitable for stability analysis of a closed loop feedback systems, which are developed throughout the years and are enlisted by Reference [39]. The criteria are explained briefly here:

- Routh-Hurwitz stability criterion: This method tests if any roots of the characteristic equation or eigenvalues of the system lie in the right half of the s-plane or on the imaginary axis. The Hurwitz determinant must be positive in order a system to be stable. Routh has developed the so called Routh-table, which provides information on the stability of the system, without calculating the determinant.
- Nyquist stability criterion: This is a graphical method for determining the stability of a dynamic system. The Nyquist plot of the open loop transfer function provides information, if the closed loop transfer function is stable. This method gives information also on the relative stability and is often used for control design.

- Root locus stability criterion: This method is a graphical representation in the complex s-plane of the closed-loop poles, when system parameters (for example a gain) are varied. The change of the pole location's (root locus) of the system depending on the system's gain provides insights on the closed loop stability. The method also gives information on relative stability and can be used for designing controllers.
- Bode diagram criterion: The Bode plot (magnitude and phase) of the transfer function provides information, whether a transfer function is stable or not.
- Lyapunov's stability criterion: This method is used for non-linear systems. The stability of the closed loop system is checked with the Lyapunov function of the system.

Two of the enlisted criteria, the Nyquist stability criterion and the Bode diagram criterion, are explained on a simple example, where the plant is the transfer function from equation (3.1.1.5) and the controller is a proportional one with a gain K_p . The feedback transfer function is set to 1. Thus, the closed loop transfer function from Fig. 3.1 transforms into equation (3.1.1.6). Based on both criteria it is explained how the proportional factor has an effect on the stability of the closed loop system.

$$G_p(s) = \frac{1 - 4s}{s(1 + 2s)(1 + 3s)} \quad G_c(s) = K_p \quad (3.1.1.5)$$

$$\frac{C(s)}{R(s)} = \frac{G_c(s)G_p(s)}{1 + G_c(s)G_p(s)} \quad (3.1.1.6)$$

The Bode graph of the transfer function from equation (3.1.1.5) is shown in Fig. 3.2 with two different proportional factors. The red curve is plotted for a factor of $K_p = 0.3$ and is unstable, because the amplitude of the transfer function at $\varphi_k = 180^\circ$ is greater than 1 and thus the closed loop becomes unstable. If the gain factor is reduced to 0.12 the closed loop gets stabilized, because the amplitude is below 1 and the phase response is independent of K_p . The Bode plot provides also information on the Gain Margin (GM) and Phase Margin (PM) of the stable closed loop system. The GM is defined as the distance between the amplitude of the Bode plot at $\varphi_k = -180^\circ$ and the 0 dB line. The PM is defined as the difference between the angle of instability -180° minus the phase angle of the transfer function, when its magnitude is 0 dB. Both parameters provide information about the relative stability and the robustness of the control loop regarding model uncertainties and measurement noise.

The Nyquist curve of the open loop transfer function is plotted in Fig. 3.3 for the two different gains. For the unstable gain of $K_p = 0.3$, the Nyquist curve encloses the critical point $(-1 + j0)$ and for the stable gain of $K_p = 0.12$ the Nyquist curve encircles the critical point. According to the Nyquist stability criterion a closed loop system is stable, when the number of encirclements of the critical point $(-1 + j0)$ is equal to the number of Right-Half Plane (RHP)-poles (unstable poles) of the open loop system [65]. Further,

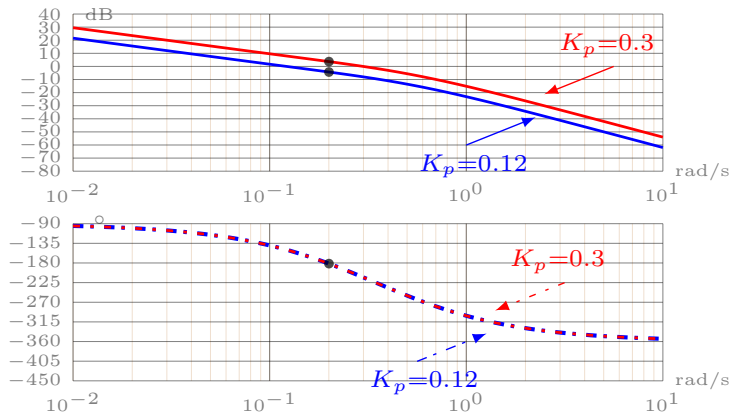


Figure 3.2 – Bode Plot of $G_0(s) = \frac{K_p(1-4s)}{s(1+2s)(1+3s)}$

the Nyquist plot gives information regarding the relative stability of the closed loop. For example, Fig. 3.3 shows the GM and PM of the closed loop. The PM is the angle at which the Nyquist plot of the open loop transfer function crosses the unity circle. The GM is where the Nyquist curve crosses the negative axis between -1 and 0 .

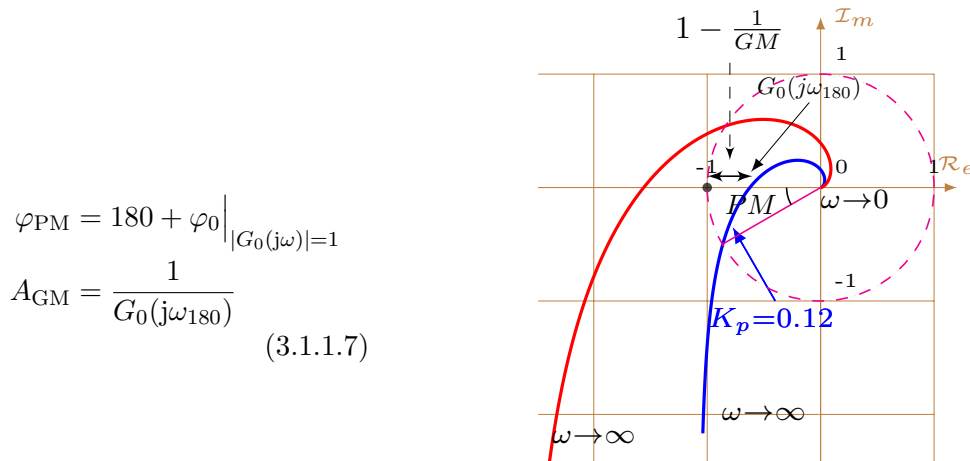


Figure 3.3 – Nyquist Plot of $G_0(s) = \frac{K_p(1-4s)}{s(1+2s)(1+3s)}$

$$\varphi_{PM} = 180 + \varphi_0 \Big|_{|G_0(j\omega)|=1}$$

$$A_{GM} = \frac{1}{G_0(j\omega_{180})} \quad (3.1.1.7)$$

3.1.2 State Space Representation

In the previous section it is shown that for control problems it is convenient to represent the plant and the controller as transfer functions. The transfer functions are defined in the Laplace domain. The connection between a physical dynamic model and the transfer function has to be established. The physical model is brought into a state space form,

which describes the dynamics of the model through linear differential equations. It is assumed that a certain physical model can be described by the two functions (in general a non-linear one), as shown in equation (3.1.2.1) [65].

$$\dot{x} = f(x,y) \qquad y = g(x,u) \text{ with } \dot{x} = \frac{d}{dt}x \qquad (3.1.2.1)$$

If this general model is linearized, then the dynamic model can be represented through equation (3.1.2.2).

$$\begin{aligned} \dot{x}(t) &= Ax(t) + Bu(t) \\ y(t) &= Cx(t) + Du(t) \end{aligned} \qquad \text{with} \qquad \begin{aligned} A &= \frac{\partial f}{\partial x}, & B &= \frac{\partial f}{\partial u} \\ C &= \frac{\partial g}{\partial x}, & D &= \frac{\partial g}{\partial u} \end{aligned} \qquad (3.1.2.2)$$

The state space representation from equation (3.1.2.2) can be transformed into the Laplace domain as shown in equation (3.1.2.3).

$$\begin{aligned} sx(s) &= Ax(s) + Bu(s) \\ y(s) &= Cx(s) + Du(s) \end{aligned} \qquad (3.1.2.3)$$

After some algebraic manipulations an input-output representation from the state-space model can be derived as shown in equation (3.1.2.4).

$$y(s) = \underbrace{\left(C(sI - A)^{-1}B + D \right)}_{G(s)} u(s) \qquad (3.1.2.4)$$

The derived relationship holds also for vector inputs $\mathbf{u}(s)$ and outputs $\mathbf{y}(s)$. The transfer function becomes then a matrix $\mathbf{G}(s)$ consisting of fractional polynomials. This is the case for the transfer function of the dual-voltage machine. Appendix B derives the transfer function of the machine with its state space representation.

3.1.3 Loop Shaping Design

The example shown in Subsection 3.1.1, where the stability of a closed loop system and a simple proportional controller K_p is analyzed, gives already an insight of the loop shaping as a control design method. Generally a loop shaping of open loop systems aims to “shape” the loop such that the magnitude of the transfer function around the loop follows a certain curve $|L(j\omega)|$ ($L = G_c(s)G_p(s)$). The hard requirement for stability has to be always met. The gain of the transfer function $L(j\omega)$ is not allowed to exceed 1 at the *phase crossover* frequency ω_{180} ($\omega_{180} \Leftrightarrow \angle L(j\omega_{180}) = 180^\circ$) in order for the closed loop to remain stable. The *gain crossover* frequency ω_c is the frequency, where the Bode plot crosses 1 from above or where the Nyquist plot crosses the unity circle. This only requirement for a closed loop system to be stable is however not enough for a control design. Goals like a good reference tracking or disturbance rejection are important [65].

Design requirements for the magnitude of $L(j\omega)$ can be identified for three different regions: low frequency region, frequency region around the *phase crossover* frequency ω_{180} and the high frequency region. The desirable shape of the magnitude of the open loop transfer function $|L(j\omega)|$ can be summed up mathematically for the three frequency regions:

- $|L(j\omega)| \gg 1$ for $\omega < \omega_c < \omega_{180}$ at lower frequencies for good reference tracking and disturbance rejection
- $|L(j\omega)| < 1$ at $\omega_{\text{cross}} < \omega < \omega_{180}$ for a stable loop
- $|L(j\omega)| \ll 1$ for $\omega_{\text{cross}} < \omega_{180} \ll \omega$ to attenuate disturbances at high frequencies, e.g. noise

The three statements from above are explained mathematically through an expression of the control error $e(s)$ in the Laplace domain. A controller shall be able to nullify the error between the reference $r(t)$ and the feedback $b(t)$ as good as possible. For this purpose the state space model from equation (3.1.2.3) is extended to include disturbance and noise signals. Therefore the signal flow diagram from Fig. 3.1 of the closed loop system is extended to take into account noise and disturbances as shown in Fig. 3.4 [65]. The signal

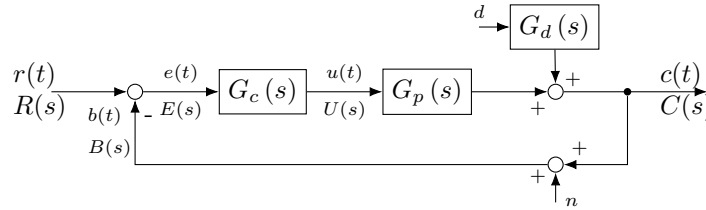


Figure 3.4 – Signal Flow Diagram of a Control Loop with Disturbance and Noise

flow chart from Fig. 3.4 can be described as a transfer function. One can express the control error as a function of the open-loop transfer function L , the disturbance $G_d \cdot d$, and the noise n (3.1.3.1).

$$y - r = e = - \underbrace{(I + L)^{-1}}_S \cdot r + \underbrace{(I + L)^{-1} G_d}_S \cdot d - \underbrace{(I + L)^{-1} L}_T \cdot n \quad (3.1.3.1)$$

From equation (3.1.3.1) it is obvious that a good reference tracking and disturbance rejection require high gain of L . The robustness regarding noise however requires a gain of L close to 0. Further, at frequencies higher than the *phase crossover* frequency ω_{180} , the amplitude has to be smaller than 1 for a stable closed loop. The main requirement for the inner current control loop is good tracking performance [63]. For a good reference tracking, the choice of controller design is often to invert the controlled plant and add an integrator in order to get the steady state error equal to 0. This method is called in the literature *inverse-based controller design* [65] and the controller formula is shown in equation (3.1.3.2). It results from the fact that the output of the closed loop y should

follow the reference r . In a case the reference signal r is a unit step $r(t) = 1, t > 0$, then the Laplace transform is an integrator $r(s) = \frac{1}{s}$. Thus if the controller is designed to invert the plant and to add an integrator to the signal path, a step change in the reference signal should be nullified with no steady state error.

$$K(s) = \frac{\omega_c}{s} G_p(s)^{-1} \quad (3.1.3.2)$$

Modulus Optimum (MO)

A special case of the inverse based controller design and belonging to the loop shaping design criteria is the Modulus Optimum (MO) method. The MO is a method, which aims to shape the closed-loop transfer function such that the magnitude of the closed-loop remains 1 up to the bandwidth frequency ω_b . The method is employed for a good reference tracking performance for the fast inner current control loops in electrical drives [7, 63]. The method is explained briefly here because it is later applied to the control of the dual-voltage machine. For this purpose an example of the PI controller and a plant consisting of two low-pass transfer functions with time constants T_1 and T_σ is illustrated in Fig. 3.5. The gain of the plant is K_s . The gain of the controller is K_r and the time constant of the PI controller is T_n . This method shapes the closed loop transfer function such that its amplitude is close to 1 for frequencies up to the *crossover frequency* without making the plant unstable.

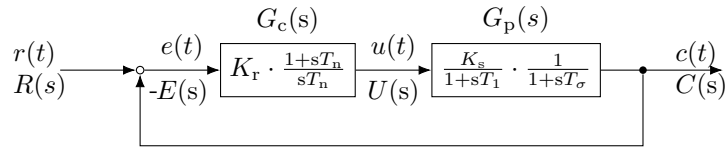


Figure 3.5 – PI-Controller for a Plant with Two First Order Low-Pass Transfer Functions

The closed loop transfer function from Fig. 3.5 is written as output-input relationship $\frac{c(s)}{r(s)}$ in equation (3.1.3.3).

$$\frac{c(s)}{r(s)} = \frac{K_r \cdot \frac{1+sT_n}{sT_n} \cdot \frac{K_s}{1+sT_1} \cdot \frac{1}{1+sT_\sigma}}{1 + K_r \cdot \frac{1+sT_n}{sT_n} \cdot \frac{K_s}{1+sT_1} \cdot \frac{1}{1+sT_\sigma}} \quad (3.1.3.3)$$

The MO tuning method employs the principle of pole-zero-cancellation technique, where the controller compensates the dominant pole in the plant with a zero in the numerator. The time constant of the PI controller T_n is set equal to the biggest time constant of the plant T_1 . Then the transfer function is simplified to the expression shown in equation (3.1.3.4). The other time constant T_σ should be at least 5 times smaller than the biggest time constant T_1 in the plant [63]. This is usually the case for inner current control loops for electric drives. The bigger time constant is a result from the machine resistance

and inductance, $T_1 = \frac{L}{R}$ and the smaller time constant represents inverter dead-time, switching frequency and filters in the measurement [63].

$$\frac{c(s)}{r(s)} = \frac{1}{1 + s \frac{T_1}{K_r K_s} + s^2 \frac{T_1 T_\sigma}{K_r K_s}} \quad (3.1.3.4)$$

The expression of the magnitude of the closed loop transfer function for a given angular frequency $j\omega$ is shown in equation (3.1.3.4).

$$\left| \frac{c(j\omega)}{r(j\omega)} \right|^2 = \frac{1}{\left(1 - \omega^2 \frac{T_1 T_\sigma}{K_p K_s}\right)^2 + \left(\omega \frac{T_1}{K_p K_s}\right)^2} = \frac{1}{1 + \omega^2 \left(\frac{T_1^2}{K_p^2 K_s^2} - \frac{2T_1 T_\sigma}{K_p K_s}\right) + \omega^4 \left(\frac{T_1^2 T_\sigma^2}{K_p^2 K_s^2}\right)} \quad (3.1.3.5)$$

The magnitude of the closed loop transfer function expressed in equation (3.1.3.5) is close to 1 if the second term in front of ω^2 disappears. With this condition the second tuning rule of the MO criteria for the proportional gain of the PI controller is derived in equation (3.1.3.6). The integral factor is calculated through equation (3.1.3.7) as the ratio between the proportional factor K_p and the time constant T_n of the PI controller.

$$K_r = \frac{T_1}{2K_s T_\sigma} \quad (3.1.3.6)$$

$$K_i = \frac{K_p}{T_n} = \frac{1}{2K_s T_\sigma} \quad (3.1.3.7)$$

The bandwidth of the derived closed loop transfer function consisting of controller and plant can be calculated according to equation (3.1.3.8). The angular frequency ω_b is defined as the bandwidth frequency, where the magnitude of the transfer function crosses -3 dB or $\frac{1}{\sqrt{2}}$ [63]. The resulting tuning from equations (3.1.3.6) and (3.1.3.7) is often applied to three phase IPM machines and is noted in this work as the conventional MO tuning method. The tuning is characterized with fast reference tracking and poor disturbance rejection behavior. Due to the strong coupling in the dual-voltage machine between its axis this version of the MO method is not appropriate. Therefore an adapted version of the MO tuning method is explained, which is also applied to the machine.

$$\left| \frac{c(j\omega_b)}{r(j\omega_b)} \right|^2 = \frac{1}{1 + \omega_b^4 \left(\frac{T_1^2 T_\sigma^2}{K_p^2 K_s^2}\right)} = \frac{1}{2} \Leftrightarrow \omega_b = \sqrt{\frac{K_p K_s}{T_1 T_\sigma}} = \sqrt{\frac{1}{2} \frac{1}{T_\sigma}} \quad (3.1.3.8)$$

The controller can be designed also in such a way that the closed loop transfer function has a certain bandwidth. This approach has many practical advantages, because the control performance can be easily adjusted through the bandwidth parameter ω_b . This approach is also more robust against uncertainties in the plant model, additional time delays in the signal chain, noise and low pass filters in the measurement and dead time effect in the inverter. Therefore, it is practical to be able to design a controller, which sets

its reference with a certain bandwidth. The bandwidth influences directly the settling time and overshoot of the PI controller. In order to design a controller after the MO criterion, the time constant of the PI controller is set again equal to the biggest time constant of the plant ($T_n = T_1$). The proportional factor is found when the magnitude of the closed loop transfer function is set equal to -3 dB or $\frac{1}{\sqrt{2}}$. With these premises the magnitude of the closed loop is shown in equation (3.1.3.9) with the possible solutions for the proportional factor K_p .

$$\begin{aligned}
 \left| \frac{c(j\omega_b)}{r(j\omega_b)} \right|^2 &= \frac{1}{\left(1 - \omega_b^2 \frac{T_1 T_\sigma}{K_p K_s}\right)^2 + \left(\omega_b \frac{T_1}{K_p K_s}\right)^2} = \frac{1}{2} \\
 &= -2\omega_b^2 \frac{T_1 T_\sigma}{K_p K_s} + \omega_b^4 \frac{T_1 T_\sigma}{K_p K_s} + \omega_b^2 \frac{T_1}{K_p K_s} = 1 \\
 \Rightarrow K_{p+} &= \frac{T_1 \omega_b \left(\sqrt{(2T_\sigma^2 \omega_b^2 + 1)} - T_\sigma \omega_b\right)}{K_s} \vee K_{p-} = -\frac{T_1 \omega_b \left(\sqrt{(2T_\sigma^2 \omega_b^2 + 1)} + T_\sigma \omega_b\right)}{K_s}
 \end{aligned} \tag{3.1.3.9}$$

Only the positive solution from equation (3.1.3.9) is relevant for the control design. The formulas for calculating the proportional and integral factors for a desired bandwidth ω_b are summarized in equation (3.1.3.10).

$$\begin{aligned}
 K_p^{\omega_b} = K_{p+} &= \frac{T_1 \omega_b \left(\sqrt{2T_\sigma^2 \omega_b^2 + 1} - T_\sigma \omega_b\right)}{K_s} \\
 K_{i\omega_b} &= \frac{K_p^{\omega_b}}{T_n} = \frac{\omega_b \left(\sqrt{2T_\sigma^2 \omega_b^2 + 1} - T_\sigma \omega_b\right)}{K_s}
 \end{aligned} \tag{3.1.3.10}$$

In case the small time constant T_σ is negligible and tends to zero the proportional parameter gets simplified to equation (3.1.3.11). With equation (3.1.3.11) or its full form from equation (3.1.3.9) it is possible to design a controller after the MO criterion with a certain bandwidth of the closed loop transfer function. The reference value is thus being set with the predefined bandwidth ω_b . There is a direct relationship between the *rise time* t_r and bandwidth ω_b of the closed loop as shown in equation (3.1.3.12). The PM of the shaped closed loop is then dependent on the selected controller bandwidth ω_b .

$$K_p = \frac{T_1 \omega_b}{K_s} \tag{3.1.3.11} \qquad t_r = \frac{\pi}{\omega_b} \tag{3.1.3.12}$$

3.2 Current Control for the Dual-Voltage Machine

In this section the presented theory from Section 3.1 is applied to the dual-voltage machine. The non-linear machine model from Chapter 2 is linearized and represented

through a state space form suitable for control design. The inverse-based design method is applied to the dual-voltage machine and the bandwidth MO tuning approach is used to parametrize the PI controllers. The discrete implementation of the PI controllers and the FOC are explained. Simulations of the current controllers in a closed loop with the non-linear machine model from Chapter 2 are performed to verify the tuning. Afterwards, measurements from a test bench with the machine prototype are presented. The measurements confirm the proposed PI tuning and match well to the simulation results. A decoupling network is implemented in the control, which counteracts the back-emf voltage of the machine and improves the control performance at speed.

At the end of the section a new control approach with a dynamic decoupling, called also a pre-compensation of the plant dynamics, is presented and tested in the simulation environment. The results with the new proposed controller are compared with the results from the PI controllers with static back-emf decoupling. The new dynamic decoupling control delivers outstanding results in terms of dynamic response to step changes and disturbance rejection.

3.2.1 Inverse-Based Controller Design

The purpose of a control design for a machine is to be able to control the generated torque or power from the machine. The dual-voltage machine generates two air-gap torques and therefore the aim of the control is to set both electromagnetic torques, T_{e12V} and T_{e48V} , in order to enable an independent power control at each side. Both electromagnetic torques, expressed through equation (2.2.1.17), depend on the currents i_{qs1} , i_{ds1} , i_{qs2} , i_{ds2} and i_{fd} . For this purpose first the current control loops are designed to set the requested reference values. In a current control loop the currents are the reference values \mathbf{r} and the voltages are the manipulated “inputs” \mathbf{u} applied to the plant as shown in Fig 3.5. The machine and the inverter represent the plant to be controlled. The signal flow diagram is drawn with double lines to represent relationship between matrices and vectors. The plant from Fig. 3.5 includes generally also the zero sequence currents. However both zero sequence currents, i_{0s1} and i_{0s2} , do not contribute to the torque generation. In the dual-voltage machine topology the power transfer at standstill is achieved through the control of the i_{0s2} current. The star point current controller is designed in the same way as the other currents and is investigated in detail in reference [66]. Reference [31] optimizes also the Pulse Width Modulation (PWM) technique employed to set the star point voltage in order to reduce the current harmonics of the current. Therefore this chapter sets the focus on the current control design for the torque building currents. In case the reader is interested in the star point current control, Appendix E handles briefly this topic. Further in this work the zero sequence currents are excluded from the plant model considered for the current control design. The plant model of the electric machine can be derived from the voltage equations and is represented symbolically by the matrix $\mathbf{G}_p(s)$. The inverse matrix $\mathbf{G}_p^{-1}(s)$ represents the relationship between currents and voltages transformed into the Laplace form. Equation (3.2.1.1) shows the relationship

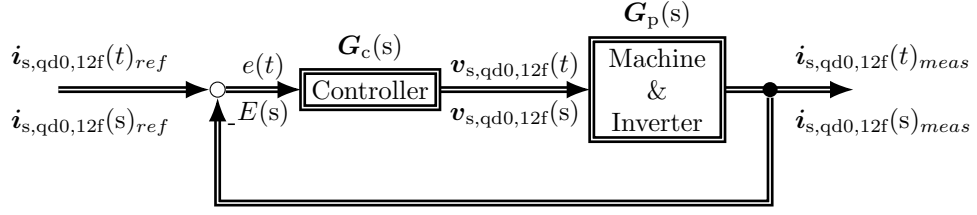


Figure 3.6 – Current Control Loop

between the current vector $\mathbf{i}_{s,qd,12f}$ and the voltage vector $\mathbf{v}_{s,qd,12f}$. The currents are the controlled variables and the voltages are the manipulated ones.

$$\mathbf{v}_{s,qd,12f}(s) = \mathbf{G}_p(s)^{-1} \cdot \mathbf{i}_{s,qd,12f}(s) \quad \rightarrow \quad \underbrace{\mathbf{i}_{s,qd,12f}(s)}_{\text{controlled variables}} = \mathbf{G}_p(s) \cdot \underbrace{\mathbf{v}_{s,qd,12f}(s)}_{\text{manipulated variables}} \quad (3.2.1.1)$$

The plant model $\mathbf{G}_p(s)$ can be obtained as an inversion of the machine voltage equations. For the purpose of current control design the machine equations, derived in Chapter 2, are simplified. The non-linear effects in the machine model are neglected and the main inductance is assumed to be constant. The iron losses in the model are also neglected.

The d - q voltage equations from Subsection 2.2.1 are linearized as shown in equation (2.2.1.13) and afterwards transformed into the s -plane. The linearized differential equations are shown in equations (3.2.1.2) to (3.2.1.6). The Heaviside's operator p represents the differentiation after time $\frac{d}{dt}$ and directly corresponds with the multiplication with the Laplace operator s in the Laplace domain.

$$v_{qs1} = r_{s1}i_{qs1} + (L_{ls1} + L_{qq1})pi_{qs1} + \frac{L_{qq1}}{N_{s12}}pi_{qs2} + \omega_e \left[(L_{ls1} + L_{dd1})i_{ds1} + \frac{L_{dd1}}{N_{s12}}i_{ds2} + \frac{2}{3} \frac{L_{dd1}}{N_{s1f}}i_{fd} \right] \quad (3.2.1.2)$$

$$v_{ds1} = r_{s1}i_{ds1} + (L_{ls1} + L_{dd1})pi_{ds1} + \frac{L_{dd1}}{N_{s12}}pi_{ds2} + \frac{2}{3} \frac{L_{dd1}}{N_{s1f}}pi_{fd} - \omega_e \left[(L_{ls1} + L_{qq1})i_{qs1} + \frac{L_{qq1}}{N_{s12}}i_{qs2} \right] \quad (3.2.1.3)$$

$$v_{qs2} = r_{s2}i_{qs2} + \left(L_{ls2} + \frac{L_{qq1}}{N_{s12}^2} \right) pi_{qs2} + \frac{L_{qq1}}{N_{s12}}pi_{qs1} + \omega_e \left[\left(L_{ls2} + \frac{L_{dd1}}{N_{s12}^2} \right) i_{ds2} + \frac{L_{dd1}}{N_{s12}}i_{ds1} + \frac{2}{3} \frac{L_{dd1}}{N_{s1f}N_{s12}}i_{fd} \right] \quad (3.2.1.4)$$

$$v_{ds2} = r_{s2}i_{ds2} + \left(L_{ls2} + \frac{L_{dd1}}{N_{s12}^2} \right) pi_{ds2} + \frac{L_{dd1}}{N_{s12}}pi_{ds1} + \frac{2}{3} \frac{L_{dd1}}{N_{s1f}N_{s12}}pi_{fd} - \omega_e \left[\left(L_{ls2} + \frac{L_{qq1}}{N_{s12}^2} \right) i_{qs2} + \frac{L_{qq1}}{N_{s12}}i_{qs1} \right] \quad (3.2.1.5)$$

$$v_{fd} = r_f i_{fd} + \left(L_{lf} + \frac{2}{3} \frac{L_{dd1}}{N_{s1f}^2} \right) pi_{fd} + \frac{L_{dd1}}{N_{s1f}}pi_{ds1} + \frac{L_{dd1}}{N_{s12}N_{s1f}}pi_{ds2} \quad (3.2.1.6)$$

The voltage equations can be rewritten in vector-matrix form as shown in equation (3.2.1.1). The matrix $\mathbf{G}_p^{-1}(s)$ is provided in equation (3.2.1.7) and represents the inverted plant matrix of the machine model.

$$\mathbf{G}_p(s)^{-1} = \begin{bmatrix} \boxed{G_{p,11}(s)^{-1}} & \boxed{\omega_e (L_{dd1} + L_{ls1})} & \boxed{s \frac{L_{qq1}}{N_{s12}}} & \boxed{\omega_e \frac{L_{dd1}}{N_{s12}}} & \boxed{\omega_e \frac{2}{3} \frac{L_{dd1}}{N_{s1f}}} \\ \boxed{-\omega_e (L_{ls1} + L_{qq1})} & \boxed{G_{p,22}(s)^{-1}} & \boxed{-\omega_e \frac{L_{qq1}}{N_{s12}}} & \boxed{s \frac{L_{dd1}}{N_{s12}}} & \boxed{s \frac{2}{3} \frac{L_{dd1}}{N_{s1f}}} \\ \boxed{s \frac{L_{qq1}}{N_{s12}}} & \boxed{\omega_e \frac{L_{dd1}}{N_{s12}}} & \boxed{G_{p,33}(s)^{-1}} & \boxed{\omega_e \left(L_{ls2} + \frac{L_{dd1}}{N_{s12}^2} \right)} & \boxed{\omega_e \frac{2}{3} \frac{L_{dd1}}{N_{s12} N_{s1f}}} \\ \boxed{-\omega_e \frac{L_{qq1}}{N_{s12}}} & \boxed{s \frac{L_{dd1}}{N_{s12}}} & \boxed{-\omega_e \left(L_{ls2} + \frac{L_{qq1}}{N_{s12}^2} \right)} & \boxed{G_{p,44}(s)^{-1}} & \boxed{\frac{2}{3} s \frac{L_{dd1}}{N_{s12} N_{s1f}}} \\ 0 & \boxed{s \frac{L_{dd1}}{N_{s1f}}} & 0 & \boxed{s \frac{L_{dd1}}{N_{s12} N_{s1f}}} & \boxed{G_{p,55}(s)^{-1}} \end{bmatrix} \quad (3.2.1.7)$$

The diagonal elements of the transfer matrix are shown in equations (3.2.1.8) to (3.2.1.10) and describe the mathematical relationship between voltages and currents of the same axis. For example the entry $G_{p,11}(s)^{-1}$ describes how the q -axis current i_{qs1} influences the voltage generated along the q -axis of system 1 v_{qs1} .

$$G_{p,11}(s)^{-1} = r_{s1} + s(L_{ls1} + L_{qq1}) \quad (3.2.1.8)$$

$$G_{p,22}(s)^{-1} = r_{s1} + s(L_{dd1} + L_{ls1}) \quad (3.2.1.9)$$

$$G_{p,55}(s)^{-1} = r_f + s \left(L_{lf} + \frac{2}{3} \frac{L_{dd1}}{N_{s1f}^2} \right) \quad (3.2.1.10)$$

$$G_{p,33}(s)^{-1} = r_{s2} + s \left(L_{ls2} + \frac{L_{qq1}}{N_{s12}^2} \right) \quad (3.2.1.11)$$

$$G_{p,44}(s)^{-1} = r_{s2} + s \left(L_{ls2} + \frac{L_{dd1}}{N_{s12}^2} \right) \quad (3.2.1.12)$$

All diagonal elements of the $\mathbf{G}_p^{-1}(s)$ matrix are boxed in blue color and consist of the transfer functions $\mathbf{G}_p(s)_{ii}^{-1}$, $1 \leq i \leq 5$. They link directly the current in the corresponding axis and the resulting output voltage in the same axis. The off-diagonal transfer functions, boxed in yellow, result from the cross-coupling between the d - q axis, when the voltage equations are transformed into the d - q reference frame. These transfer functions are product of the electrical angular speed ω_e , the machine self- and mutual inductances and the currents. These terms are denoted as back-emf static coupling between the axis. There are also transfer functions, boxed in red, which represent the dynamic coupling along one axis. For example a change in the current i_{qs1} results in an induced voltage in q -direction on the 48V side (v_{qs2}). Respectively also a change in the current i_{qs2} (48V) results in an induced voltage along the q -axis of the 12V side (v_{qs1}). The coupling is dynamic because it depends on the Laplace operator s . All dynamic coupling terms are derivatives because they are multiplied with s operator in the Laplace domain. In order to derive the plant matrix of the dual-voltage machine $\mathbf{G}_p(s)$, the matrix $\mathbf{G}_p^{-1}(s)$ needs to be inverted. Alternatively the plant model of the machine $\mathbf{G}_p(s)$ can be derived also

from the state space representation according to equation (3.2.1.13). This mathematical relationship is derived in Subsection 3.1.2 and is also valid for matrices and vectors.

$$\mathbf{y}(s) = \underbrace{\left(\mathbf{C} (s\mathbf{I} - \mathbf{A})^{-1} \mathbf{B} + \mathbf{D} \right)}_{\mathbf{G}_p(s)} \mathbf{u}(s) \quad (3.2.1.13)$$

A detailed derivation of the state space matrices is shown in Appendix B. The matrix of the plant model $\mathbf{G}_p(s)$ is calculated with the Matlab Symbolic Toolbox. The inversion of the matrix $\mathbf{G}_p^{-1}(s)$, which relates currents to voltages, is tedious and takes even a modern computer some minutes to be completed. Despite the fact that the inversion consists of long and complex terms, the matrix does not have singularities and is invertable. The plant model matrix $\mathbf{G}_p(s)$ is however not of an interest for the controller design. As explained in Subsection 3.2.1 the inverse matrix $\mathbf{G}_p^{-1}(s)$ is of interest in order to design a controller. Therefore, the matrix $\mathbf{G}_p(s)$ is not provided here. The inverse matrix is already known through the voltage equations and is shown in equation (3.2.1.7). In Subsection 3.1.3 the idea of designing a controller, which inverts the plant and adds an integrator is already presented. This idea is applied to the dual-voltage machine. *Decoupling* or *feedforward* action is required because of the strong coupling between the axis. The goal of the *feedforward/decoupling* action is to decouple the axis, such that a diagonal controller can be designed. Then, SISO design criteria, such as the presented Modulus Optimum (MO) can be applied during controller design. For this purpose the inverse transfer matrix $\mathbf{G}_p^{-1}(s)$ is decomposed into the dynamic decoupling controller matrix $G_{p,\text{dyn,dcpl}}(s)^{-1}$ as shown in equation (3.2.1.14), a static decoupling controller matrix provided in equation $G_{p,\text{stat,dcpl}}(s)^{-1}$ (3.2.1.15) and the diagonal controller matrix $\mathbf{G}_{p,\text{diag}}(s)^{-1}$ shown in equation (3.2.1.16).

$$G_{p,\text{dyn,dcpl}}(s)^{-1} = \begin{bmatrix} 0 & 0 & s \frac{L_{qq1}}{N_{s12}} & 0 & 0 \\ 0 & 0 & 0 & s \frac{L_{dd1}}{N_{s12}} & s^2 \frac{L_{dd1}}{3 N_{s1f}} \\ s \frac{L_{qq1}}{N_{s12}} & 0 & 0 & 0 & 0 \\ 0 & s \frac{L_{dd1}}{N_{s12}} & 0 & 0 & \frac{2}{3} s \frac{L_{dd1}}{N_{s12} N_{s1f}} \\ 0 & s \frac{L_{dd1}}{N_{s1f}} & 0 & s \frac{L_{dd1}}{N_{s12} N_{s1f}} & 0 \end{bmatrix} \quad (3.2.1.14)$$

$$G_{p,\text{stat,dcpl}}(s)^{-1} = \begin{bmatrix} 0 & \omega_e (L_{dd1} + L_{ls1}) & 0 & \omega_e \frac{L_{dd1}}{N_{s12}} & \omega_e \frac{2}{3} \frac{L_{dd1}}{N_{s1f}} \\ -\omega_e (L_{ls1} + L_{qq1}) & 0 & -\omega_e \frac{L_{qq1}}{N_{s12}} & 0 & 0 \\ 0 & \omega_e \frac{L_{dd1}}{N_{s12}} & 0 & \omega_e \left(L_{ls2} + \frac{L_{dd1}}{N_{s12}^2} \right) & \omega_e \frac{2}{3} \frac{L_{dd1}}{N_{s12} N_{s1f}} \\ -\omega_e \frac{L_{qq1}}{N_{s12}} & 0 & -\omega_e \left(L_{ls2} + \frac{L_{qq1}}{N_{s12}^2} \right) & 0 & 0 \\ 0 & 0 & 0 & 0 & 0 \end{bmatrix} \quad (3.2.1.15)$$

$$\mathbf{G}_{p,\text{diag}}(s)^{-1} = \begin{bmatrix} r_{s1} + s \cdot (L_{ls1} + L_{qq1}) & 0 & 0 \\ 0 & r_{s1} + s \cdot (L_{ls1} + L_{dd1}) & 0 \\ 0 & 0 & r_{s2} + s \cdot \left(L_{ls2} + \frac{L_{qq1}}{N_{s12}^2} \right) \\ 0 & 0 & 0 \\ 0 & 0 & 0 \\ 0 & 0 & 0 \\ 0 & 0 & 0 \\ r_{s2} + s \cdot \left(L_{ls2} + \frac{L_{dd1}}{N_{s12}^2} \right) & 0 & \\ 0 & r_f + s \cdot \left(L_{lf} + \frac{2L_{dd1}}{3N_{s1}f^2} \right) & \end{bmatrix} \quad (3.2.1.16)$$

Designing diagonal controllers for a Multiple-Input Multiple-Output (MIMO) system, which corresponds to the plant of the dual-voltage machine, is known also as the decentralized control approach [65]. The *feedforward* action aims to improve the performance of the decentralized controllers [21]. The multiplication with the Laplace operator s from equation (3.2.1.14) is equivalent to differentiation in time. A derivative control action applied directly on the measured currents is not purposeful, because it brings instability into the control due to its high sensitivity to noise in the measured currents. Therefore, only the static *feed forward* decoupling matrix $G_{p,\text{stat},\text{dcpl}}(s)^{-1}$ is implemented in the control [63, 65]. The diagonal PI controllers take care of the dynamic coupling between the axis. This coupling can be considered as a disturbance and therefore the controllers have to be designed conservatively (detuned). In such dynamically coupled systems, the controllers are often detuned in order to not become unstable, when a step change in the control loop of a neighboring system is applied [21, 65]. An extra detuning parameter is often introduced, which is adjusted after the PI controllers are designed according to a certain SISO design criteria. This detuning parameter is multiplied with the tuning coefficients from each PI controller [37]. The diagonal controllers are designed according to the MO and aim to compensate only the current along its own axis. The MO principle, explained in Subsection 3.1.3, is applied to all five current controllers of the dual-voltage machine. The influence of the inverter is modeled through a low pass filter on each path of the current controllers. This can be represented as a multiplication with the rest of the open loop system by the diagonal transfer function matrix $\mathbf{G}_{p,\text{inv}}(s)$. The matrix, which describes the inverter plant, is shown in equation (3.2.1.17). The matrix includes only diagonal entries. The time constant of the low-pass filter is equal to the switching time period of the inverter. Both three-phase inverters, for the 12V and 48V sides, have a switching time constant of $T_{\text{sw,ph}}$ equal to 100 μsec . The field winding mosfets are operated with a switching period of $T_{\text{sw,f}} = 1 \text{ m sec}$. Given all information presented in

in this subsection the MO tuning criteria can be applied on each of the PI controllers for the dual-voltage machine. The tuning of the controllers is handled in Subsection 3.2.2.

$$\mathbf{G}_{p,inv}(s) = \begin{bmatrix} \frac{1}{1+sT_{sw,ph}} & 0 & 0 & 0 & 0 \\ 0 & \frac{1}{1+sT_{sw,ph}} & 0 & 0 & 0 \\ 0 & 0 & \frac{1}{1+sT_{sw,ph}} & 0 & 0 \\ 0 & 0 & 0 & \frac{1}{1+sT_{sw,ph}} & 0 \\ 0 & 0 & 0 & 0 & \frac{1}{1+sT_{sw,f}} \end{bmatrix} \quad (3.2.1.17)$$

3.2.2 Tuning the PI Controllers

The Modulus Optimum (MO) design criterion is applied to each current axis control loop. The controllers are designed to have a certain bandwidth. This tuning method offers also a practical way to detune the control loops in case of instabilities. The MIMO system is considered as a system of multiple loops, which have to be tuned separately. The loops are illustrated in Fig. 3.9. The coupling is not considered in the tuning. A static decoupling network is added afterwards. The explained MO criterion in Subsection 3.1.3 is applied on the five control loops: i_{qs1} , i_{ds1} , i_{qs2} , i_{ds2} and i_{fd} . With the nomenclature used in Subsection 3.1.3 the time constants and gain factors can be directly substituted with the machine parameters as shown in equation (3.2.2.1).

$$\begin{aligned} K_s = K_{i_{qs1}} = r_{s1}^{-1} & & T_1 = T_{i_{qs1}} = (L_{ls} + L_{qq1}) r_{s1}^{-1} & & T_\sigma = T_{sw,ph} \\ K_s = K_{i_{ds1}} = r_{s1}^{-1} & & T_1 = T_{i_{ds1}} = (L_{ls} + L_{dd1}) r_{s1}^{-1} & & T_\sigma = T_{sw,ph} \\ K_s = K_{i_{qs2}} = r_{s2}^{-1} & & T_1 = T_{i_{qs2}} = \left(L_{ls} + \frac{L_{qq1}}{N_{s12}^2} \right) r_{s2}^{-1} & & T_\sigma = T_{sw,ph} \\ K_s = K_{i_{ds2}} = r_{s2}^{-1} & & T_1 = T_{i_{ds2}} = \left(L_{ls} + \frac{L_{dd1}}{N_{s12}^2} \right) r_{s2}^{-1} & & T_\sigma = T_{sw,ph} \\ K_s = K_{i_{fd}} = r_f^{-1} & & T_1 = T_{i_{fd}} = \left(L_{lf} + \frac{2L_{dd1}}{3N_s 1f^2} \right) r_{s2}^{-1} & & T_\sigma = T_{sw,f} \end{aligned} \quad (3.2.2.1)$$

The derived formulas for calculating the proportional $K_p^{\omega_b}$ and integral $K_i^{\omega_b}$ factors from equation (3.1.3.10) are applied on each current control loop with the substitutions enlisted in equation (3.2.2.1). The proportional and integral factors for the i_{qs1} PI controller are given in equation (3.2.2.2). The rest of the current control loops are tuned in the same way as i_{qs1} and the formulas are provided in Appendix C through equations (C.0.0.6) to (C.0.0.15). In case the small time constant is neglected ($T_{sw,ph} \rightarrow 0$, $T_{sw,f} \rightarrow 0$), the formula for calculating the PI factors is simplified as shown in equation (3.2.2.2).

$$\begin{aligned} T_{n,iqs1} &= (L_{ls1} + L_{qq1}) r_{s1}^{-1} \\ K_{p,iqs1} &= (L_{ls1} + L_{qq1}) \omega_b \left(\sqrt{2T_{sw,ph}^2 \omega_b^2 + 1} - T_{sw,ph} \omega_b \right) \Rightarrow \overset{T_{sw,ph}=0}{=} (L_{ls1} + L_{qq1}) \omega_b \\ K_{i,iqs1} &= \frac{K_{p,iqs1}}{T_{n,iqs1}} = r_{s1} \omega_b \left(\sqrt{2T_{sw,ph}^2 \omega_b^2 + 1} - T_{sw,ph} \omega_b \right) \Rightarrow \overset{T_{sw,ph}=0}{=} r_{s1} \omega_b \end{aligned} \quad (3.2.2.2)$$

The Nyquist stability criterion is applied on each loop in order to check if the closed loop is stable with the applied conventional MO or the adapted Bandwidth MO tuning method. For this purpose the Nyquist plot of the open loop transfer function of i_{qs1} , consisting of a PI controller transfer function and a plant transfer function ($\mathbf{G}_{c,PI}(s)$ and $\mathbf{G}_p(s)$ from Fig. 3.9), is plotted. The derived controller tuning coefficients $K_{p,iqs1}$, $T_{n,iqs1}$ are substituted in the open loop transfer function and the Nyquist plot for i_{qs1} is illustrated in Fig. 3.7. The Nyquist plot for the current control loop of i_{qs1} , tuned after the conventional MO criterion, is plotted in blue. The Phase Margin (PM) in this case is $65,53^\circ$, which matches exactly the PM value provided in the control theory literature for the MO tuning method [63]. Reference [63] provides typical values for a PM, which result in different closed loop behavior.

- Settling behavior without overshoot: $PM \geq 90^\circ$
- Settling behavior with overshoot from 5 % to 10 %: $PM \geq 60^\circ$
- Settling behaviour with considerable overshoot: $PM \geq 30^\circ$

The saturation effect in the machine also plays an important role and has a negative influence on the control performance. The dynamic coupling between the axis acts as a disturbance on each loop. Therefore the conventional MO tuning method, which results in a bandwidth of 1124 Hz, could lead to some instabilities, when applied to the dual-voltage machine. A more appropriate method for the current control of the dual-voltage machine is the bandwidth MO tuning method, which shapes the closed loop transfer function to have a desired bandwidth. Up to this bandwidth the magnitude of the closed loop system is 1. The bandwidth tuning enables direct adjustment of the *rise time* and the settling behavior of each control loop. In case of instabilities each of the loops can be separately detuned to have lower bandwidth and greater PM, which offers flexibility in comparison with the conventional MO tuning with a fixed bandwidth and PM. The stator current control loops are tuned to have a bandwidth of 200 Hz and the field winding current control loop is tuned to have a bandwidth of 8 Hz. A 200 Hz bandwidth of the closed system results in a PM of $83,66^\circ$, which, in a perfectly decoupled system, should lead to almost no overshoot [63]. In Fig. 3.7 the Nyquist plot of the open loop transfer function is shown for the current i_{qs1} . The Nyquist plots for the other stator current control loops look identical because each one is tuned with a bandwidth of $f_b=200$ Hz. The stability criteria is fulfilled, because the curve does not encircle the critical point of $(-1 + j0)$. The Nyquist plot of the closed loop transfer function is illustrated in Fig. 3.8 and shows the typical plot of a low pass filter. The PM of the open loop transfer function of the field winding current is with a tuning of $f_b = 8$ Hz equal to $87,26^\circ$. From the shaped closed loops with a desired bandwidth, the expected *rise times* t_r can be calculated from the relationship between *bandwidth* and *rise time* shown in equation (3.1.3.12). The shaped closed loop for the stator currents results in a rise time t_r of 2,5 m sec. For the field winding current the expected *rise time* t_r is equal to 62,5 m sec. Its Nyquist plots are provided in Figures C.7 and C.8 in Appendix C. All controller parameters used to tune the current control loops are summarized in Table 3.1. The parameters are

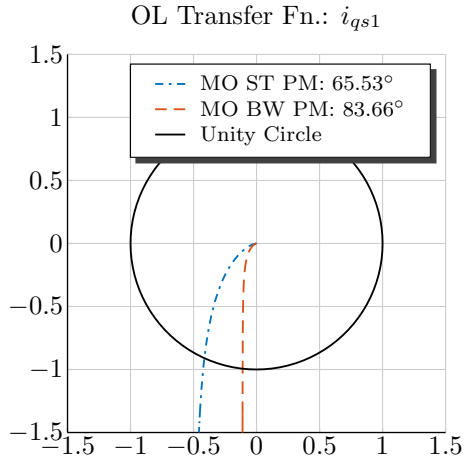


Figure 3.7 – Nyquist Plot of the OL Transfer Function i_{qs1}

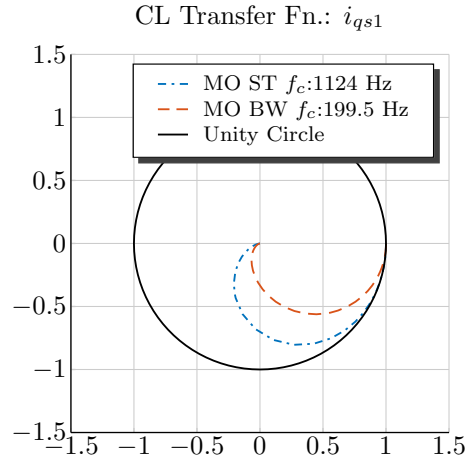


Figure 3.8 – Nyquist Plot of the CL Transfer Function i_{qs1}

calculated according to the formulas provided in equations (C.0.0.3) to (C.0.0.15) with the unsaturated main inductance values.

The controller parameters have to be adapted depending on the machine operating point due to the strong saturation of the main inductance. Otherwise the control may become unstable, when the machine is operated in highly saturated regions. This is due to the fact that the saturated inductance is much smaller than the unsaturated one. Therefore the PI control parameters are calculated in the software in real-time with the inductance values depending on the target current $L(I^*)$. This approach makes the controller tuning robust against the saturation effect in the machine. Subsection 3.2.3 handles in detail the digital implementation of the PI controllers and verifies the controller tuning in a simulation.

Table 3.1 – Controller Parameters

$K_{p,iqs1}$	$K_{p,ids1}$	$K_{p,iqs2}$	$K_{p,ids2}$	$K_{p,ifd}$
0.034571	0.025802	0.37836	0.23229	99.085
$K_{i,iqs1}$	$K_{i,ids1}$	$K_{i,iqs2}$	$K_{i,ids2}$	$K_{i,ifd}$
2.1686	2.1686	29.7575	29.7575	344.4278

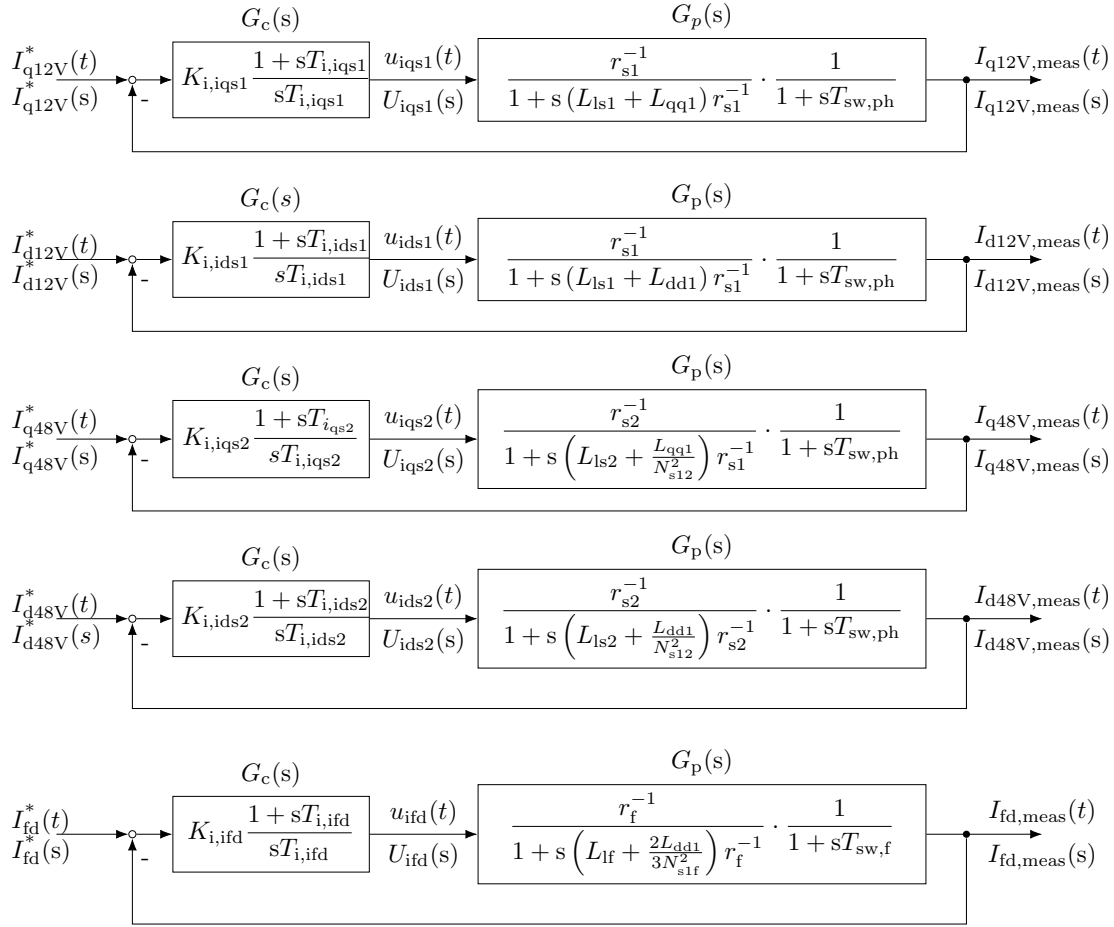


Figure 3.9 – Tuning the Decentralized PI Controllers

3.2.3 PI Control Implementation

This subsection handles the discrete implementation of the FOC in general and the digital implementation of the PI controllers. The machine model from Subsection 2.4 is implemented in the PLECS Blockset and simulated with a continuous solver. The implemented control in Simulink is however discrete and is scheduled analog a digital implementation on a micro-controller. This is helpful, because the same control software is implemented afterwards on an Autobox (RCP). Therefore, the side effects resulting from the digital implementation can be foreseen already in the simulation and the stability of the digital control verified.

Currents and Rotor Position Sensing

The digital FOC requires the currents and angle position to be sensed synchronously. The high frequent switching of the MOSFETs causes ripple on the phase currents. Therefore, the currents are sensed always in the middle of the switching period. This ensures a ripple free measurement of the currents. The sensing in the middle of the switching period "catches" only the mean value of the current during the switching period. The currents are sensed in reality with LEM transducers [43] and the rotor position with an encoder from Renishaw [59]. The current transducers deliver a voltage from 0 V to 5 V, which corresponds to a certain current range suitable for the chosen transducer. In the simulation environment the sensors are also modeled in the continuous time domain and their signal is sampled in the middle of the switching period. The sampled voltage is mapped to the corresponding physical current value in the software based on the sensor data sheets. This approach has the advantage that the control software from the simulation can be directly executed later on the Autobox and the data acquisition blocks can be tested already in the simulation. This saves time because the test bench is only used to test the current controllers and not the bug-fix data acquisition blocks. The field winding current is also sensed through a LEM transducer with a smaller range (± 20 A) than the phase current sensors (± 800 A). The field winding current i_{fd} is sampled in the middle of the switching period of the slow control loop (1 m sec).

Forward DQ Transformation

After the rotor position and phase currents are sensed, the six-phase transformation matrix from equation (2.2.1.1) is applied in the control software to calculate the actual d - q currents. A simple angle compensation, based on the actual angular electrical speed of the rotor $\omega_{e,act}$ and the switching period $T_{sw,ph}$, is employed to consider the rotor movement during the discrete control period. This ensures a correct transformation into the d - q frame (forwards) and the correct employment of the d - q control voltages (backwards), which is especially important later for the torque control at higher speeds. The calculated compensation angle from equation (3.2.3.1) is subtracted in the forwards transformation, because the currents and rotor position are measured in the "past" in respect to the beginning of the next control period and added during the backwards transformation, because the d - q control voltages need to be projected into the middle of the next switching period.

$$\theta_{comp} = 0.5 \cdot \omega_{e,act} \cdot T_{sw,ph} \quad (3.2.3.1)$$

The low pass filter behavior of the current and rotor position sensors are also compensated based on manufacturer's datasheets. The measured d - q currents are used in the current control loops to calculate the error between set point and actual value as shown in Fig. 3.10.

Discrete PI Control Implementation

In order to verify the proposed MO tuning, simulations with the derived tuning from Subsection 3.2.2 and the machine model presented in Chapter 2 are performed. Since the model and the prototype machine show significant saturation of the main inductance, the PI controller parameters are calculated online in the control based on the requested currents and the machine model inductances stored in a LUT. This makes the tuning of the PI controllers more robust against changes in the main inductance. For this purpose only the resistance and inductance independent terms from equation (3.2.2.2) are calculated offline and the multiplication with the inductances for the proportional gain K_p and with the resistance for the integral gain K_i is performed in the software. In reality also the resistances change their values depending of of the temperature. Therefore this calculation method for the integral factors K_i has advantage when the controllers are applied to the machine prototype.

The digital implementation of the PI controllers requires a transformation from the s -domain into the z -domain. This can be done through various approximation methods. For example, the *Backward Euler* method, the *Forward Euler* method or the *Trapezoidal* method are commonly found in the literature [7]. In this case the trapezoidal method is chosen, because this method ensures that the proven stability in the continuous domain is transferred also into the discrete time domain. This is not always the case for the other methods [7]. The formula for the z -transformation used in the discrete implementation form of the PI controllers is provided in equation (3.2.3.2), where T_s is the sample time¹. The same digital form of the PI controller is used in the simulation as well as on the RCP platform.

$$y[k] = y[k - 1] + \frac{u[k] + u[k-1]}{2} \cdot T_s \quad \circ \curvearrowright \bullet \quad \frac{Y(z)}{U(z)} = \frac{T_s}{2} \frac{z+1}{z-1} \quad (3.2.3.2)$$

Backwards DQ Transformation and Modulation Technique

The calculated control voltages are transformed back to the ABC domain through the backwards transformation from equation (2.1.3.10). after the control voltages are transformed back into the ABC frame, they have to be applied to the inverter through some modulation technique. The employed modulation technique, which transforms the ABC control voltages into PWM pulses, used to turn on and off the MOSFETs, is a standard Space Vector Modulation (SVM) technique with an injected third harmonic. A detailed explanation of the modulation technique is omitted at this stage, as this can be comprehended in the scientific literature for control of electrical drives [16].

¹ T_s is equivalent to $T_{sw,ph}$ for the fast control loop (stator currents control) and to $T_{sw,f}$ for the slow control loop (excitation current control)

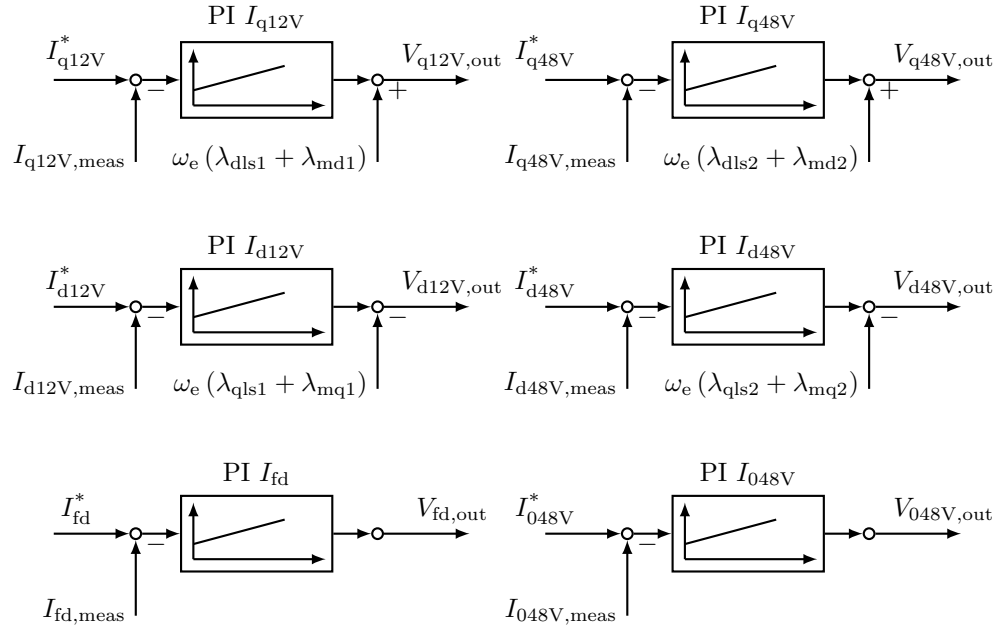


Figure 3.10 – PI Controllers with Decoupling

Dead-Time

The inverter and the machine model are implemented in PLECS and therefore only the PWM gate signals for inverters are sent to the PLECS model. A dead time of $1,5 \mu\text{sec}$, resulting from the imperfect switching of the mosfets, is also considered in the PWM generation. This ensures, that no short circuit occurs, when the High-Side (HS)-mosfet is turned off and the Low-Side (LS)-mosfet turned on or the other way around.

Anti-Windup

In real systems the actuator is not unlimited and saturates to its minimum and maximum values. In the case of the machine control the limiting factor is the DC link voltage of the battery or the electrical power source. Therefore, an anti-windup is implemented in all PI controllers in order to deactivate the integrator, when the commanded voltage is greater or equal to the maximum available voltage of the source. For the PI controllers of the stator currents the DC link voltage limits the maximum voltage vector, which can be constructed from its d and q components. For the 48V side these are v_{qs2} and v_{ds2} . For the 12V side the vector sum of v_{qs1} and v_{ds1} is limited. The limit is the maximum possible voltage vector, which can be applied to the machine based on the employed modulation technique (SVM). With the applied SVM the maximum voltage vector is equal to $\frac{V_{DC}}{\sqrt{3}}$. If the vector limit of the d - and q -axis components exceeds this limit, the integration of both, d - and q -axis, PI controllers is held for each stator system.

3.2.4 Simulation Results

After the discrete implementation of the FOC and the digital implementation of the PI controllers were briefly explained, simulation results from a closed loop control with all five current controllers are presented. The predicted control behavior from the proposed MO tuning in terms of dynamic performance is verified in the simulation environment. Usually a controller is tested through a set point change and its settling behavior is observed. The inclusion of the simulation results with each of the five current controller tests will however overload the current subsection with too many figures. Therefore only some arbitrary single controller tests are analyzed here. All other results from the controller tests are included in Appendix D.

The control performance is tested at zero speed and at 1000 rpm to demonstrate the influence of the back-emf (static) coupling in the machine. The speed of 1000 rpm is chosen such that it is high enough but below the corner speed of the machine, where the field weakening region starts. A decoupling network is added to counteract the back-emf (static) coupling in order to improve the control performance at speed.

Combined tests for some of the PI controllers with simultaneous set point changes are performed. In the author's point of view these cases are characteristic, because the strong coupling between the axis is demonstrated. The simultaneous set point changes are also relevant for the machine exploitation later during the torque control. Therefore the following tests are included in this subsection and their control behavior is analyzed:

- A set point change is performed at the 12V stator currents. The field winding current and the 48V stator currents (i_{qs2} , i_{ds2}) are controlled to zero. This case generates electromagnetic torque of the 12V winding T_{e12V} , while the electromagnetic torque at the 48V side, T_{e48V} , remains zero.
- A set point change is performed at the 48V stator currents. The field winding and the 12V stator currents (i_{qs1} , i_{ds1}) are controlled to zero. This case generates electromagnetic torque of the 48V winding T_{e48V} , while the electromagnetic torque at the 12V side, T_{e12V} , remains zero.
- A set point change is performed at both stator windings, 12V and 48V, in the same direction (both positive or negative). A set point change of the field winding is performed also. This case generates two electromagnetic torques in motoring or generative mode, T_{e12V} and T_{e48V} , and a resulting motoring or generative mechanical torque T_{mech} .
- A set point change at both stator windings, 12V and 48V, in opposite directions and a set point change at the field winding is performed. This setting generates two electromagnetic torques in opposite direction: for example T_{e12V} generative and T_{e48V} motoring. The resulting mechanical torque T_{mech} is either generative or motoring depending on the sum of the air-gap torques $T_{e12V} + T_{e48V}$.

Simulation Results with the MO Tuning at a Speed of 0 rpm

First, a very simple controller test is performed at a 0 rpm, which implies that no back-emf (static) coupling is present in the plant. The static coupling matrix from equation (3.2.1.15) becomes zero. In this case the signal flow diagram from Fig. 3.9 is valid, except for the dynamic coupling, which is still present in the plant but not illustrated in the signal flow diagram. The controller tuning can be tested and the results should be close to the predicted behavior during tuning. The dynamic coupling is considered as a disturbance along the path. Only one controller set point is changed at a time. This way the controller interactions are minimized.

Figure 3.11 shows a simulation at 0 rpm with a set point change for current $i_{qs1} = 100$ A and all other currents are controlled to 0. The predicted *rise time* t_r from Subsection 3.2.2 of 2,5 m sec matches with the simulation, which shows a rise time of 2,5 m sec. The rise time is calculated from the simulation trace and marked with an annotation in the first plot of Fig. 3.11. The dynamic coupling from 12V to 48V is evident in the middle plot of Fig. 3.11 . The induced q current at the 48V side i_{qs2} is very small and increases up to -5 A. The field winding current is not disturbed by the step changed because it acts along the orthogonal d -axis.

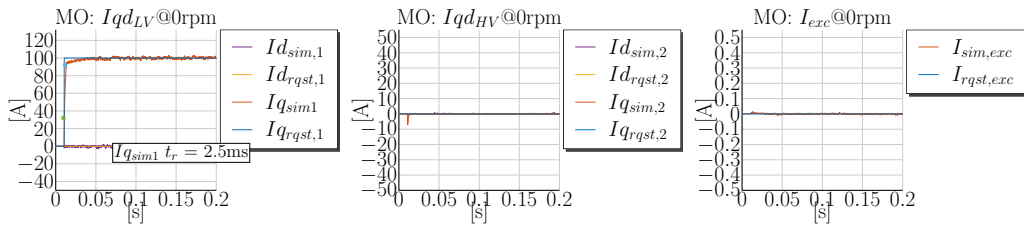


Figure 3.11 – Simulation @0rpm: $i_{qs1} = 100$ A, $i_{ds1} = 0$ A, $i_{qs2} = 0$ A, $i_{ds2} = 0$ A and $i_{fd} = 0$ A MO Tuning

The dynamic coupling is evident also during the step change of the 48V q -axis current from Fig. 3.12. The 48V q -axis current set point is changed from 0 A to 100A and an induced q -axis current at the 12V side of up to -65 A is visible. The 48V stator winding has 4-times more number of turns than the 12V winding and thus the disturbance effect at 12V is much greater. The control performance of the 48V q -axis controller is very good and has a *rise time* t_r of 2,63 m sec. The saturation of the main inductance has also an effect at the control performance and the generated disturbance at the other controllers. Therefore the induced currents are not exactly in the ratio 1:4. A change of 100 A at the 48V q -axis current saturates the q -axis inductance 4-times more than the same test at 12V for $i_{qs1} = 100$ A. The operating point of the machine is different in this case and the inductance is much smaller according to the saturation curve of the q -axis illustrated in Fig. 2.20 from Chapter 2. Since the machine model includes the saturation of the main inductance, the *rise times* t_r calculated in the simulation and the predicted rise times during the control design may differ. The calculated *rise times*

from Subsection 3.2.2 are calculated based on the linear machine model and no dynamic coupling between the axis. Both effects, saturation and dynamic coupling, are replicated in the model and do influence the control performance. Further the control calculates the PI parameters based on the MO formulas and the inductance values at the reference points. The listed effects are the reason that there is slight deviation from expected control behavior and simulated one. Nevertheless, the simulated responses correlate very well with the expected control behavior. The field winding current from the right-most plot in Fig. 3.12. is slightly disturbed during the 48V q -axis step change due to the cross-magnetization effect included in the model. The cross-magnetization is included in the model together with the saturation modeling of the main inductance and is a result of the non-zero term L_{qd1} from equation (2.2.1.12).

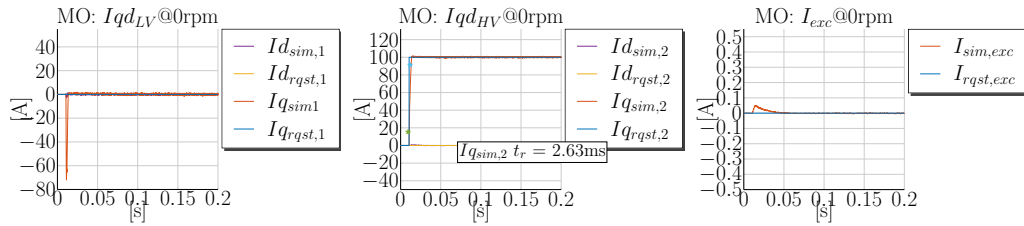


Figure 3.12 – Simulation @0rpm: $i_{qs1} = 0$ A, $i_{ds1} = 0$ A, $i_{qs2} = 100$ A, $i_{ds2} = 0$ A and $i_{fd} = 0$ A MO Tuning

In the right-most plot of Fig. 3.13 a step change for the field winding current of 2 A is performed. The simulated *rise time* of 49 msec is different from the predicted one in Subsection 3.2.2 of 62,5 msec because the main inductance along the d -axis is highly saturated at 2 A excitation current and its value much smaller than the unsaturated one. This can be verified from the measurement of the flux over the excitation current in Fig. 2.19. From the simulation result it is obvious that the field winding current needs much more time to settle than the stator currents. It's performance can be improved if a feed-forward term is added. The feed-forward term for the field winding current is shown in equation (3.2.4.1). The resistance value of the field winding r_{fd} is used to calculate the feed-forward voltage, which is required for the requested field winding current I_{fd}^* to be settled. The improvement due to the *feed-forward* action is evident in the simulations performed in the Subsection 3.2.5, which handles in general the back-emf *decoupling* of the stator current controllers.

$$v_{fd,ff} = I_{fd}^* \cdot r_{fd} \quad (3.2.4.1)$$

The maximum possible dynamic performance of the field winding remains physically limited due to the high number of turns of the rotor and the DC voltage source limitation at the 48V side. A similar dynamic in the field winding as in the stator current controllers can be achieved only if the DC voltage source, used to supply the field winding, is scaled to at least the rotor to stator turns ratio $\frac{1}{N_{s2f}}$. For the investigated prototype machine according to the stator to rotor turns ratio from Table 2.1 this would result in a scaled nominal voltage of $V_f' = 48 \frac{N_f}{N_{s2}} = 48 \text{ V} \frac{508}{4} = 6,096 \text{ kV}$.

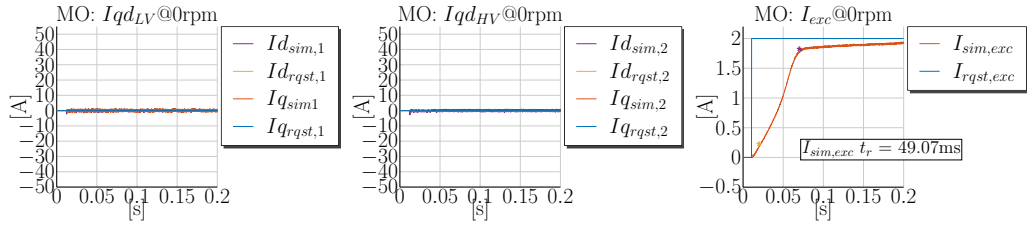


Figure 3.13 – Simulation @0rpm: $i_{qs1} = 0$ A, $i_{ds1} = 0$ A, $i_{qs2} = 0$ A, $i_{ds2} = 0$ A and $i_{fd} = 2$ A MO Tuning

In summary, the observations, made during the controller tests performed at 0 rpm, verify the proposed controller tuning and also the presented model from Chapter 2. When only one current set point is changed at a time the dynamic control loop interactions are minimized. The observed dynamic coupling between the axis is evident during the controller tests but does not lead to any instabilities thanks to the conservative tuning of the PI controllers. The influence of the 48V controller to the 12V current controller is strong and therefore causes induced currents at the 12V side, which are non-negligible. The 12V controller is nevertheless able to counteract the disturbance and no instabilities are observed. The observed slight deviation from the predicted settling behavior is explained and results from the non-linearity in the machine model used during the tests. In general, the controllers perform very well and are able to control the current set points without an overshoot in the predicted time.

The signal flow diagram from Fig. 3.9 is valid only for the speed of 0 rpm. The back-emf coupling in the machine has a strong influence on the control performance at speed, which will be demonstrated as next.

Simulation Results without a Decoupling Action at 1000 rpm

The back-emf coupling in the plant is a generated voltage due to the flux rotating in rotor and stator. Thanks to the d - q transformation this coupling is usually not dynamic in the d - q frame and does not depend on the Laplace operator, when a linear machine model is considered. Despite its static character the coupling has strong negative influence on the control performance. This is demonstrated through simulations with the proposed tuning at a speed of 1000 rpm without any compensation of this effect in the control. The speed of 1000 rpm is in the base speed region of the machine. The same set point changes on the stator and rotor currents are performed again for a better comparison with the previous tests.

Figure 3.14 shows a step change for i_{qs1} of 100 A. It is noticeable that the current controllers need more time to settle due to the back-emf voltage generated in the machine. The *rise time* of 12,6 m sec is higher than the same test at 0 rpm. The 12V d -axis current controller exhibits a disturbance through the reference change of the q -axis current. The

root cause of this disturbance is due to the non-linearity of the main inductance and the cross-magnetization effect. The cross-magnetization effect is a change of the inductance value of one axis depending on the current in the cross-coupling axis. The employed machine model for the controller test also includes a dynamic cross-magnetization in the main inductance [46], which is a further change of the inductance due to a current change in the orthogonal current axis. The effect of the dynamic coupling is also amplified due to the rotating flux. The induced currents at the 48V side, i_{qs2} and i_{ds2} , are greater than the induced ones during the same test at 0rpm. The induced positive d -axis currents are also dynamically coupled to the field winding, which is also disturbed. The induced positive currents in the d -axis induce in turn a negative current in the field winding of up to $-0,2$ A. The induced field winding current compensates for the flux resulting from the dynamic coupling along the d -axis as described with equation (3.2.1.6).

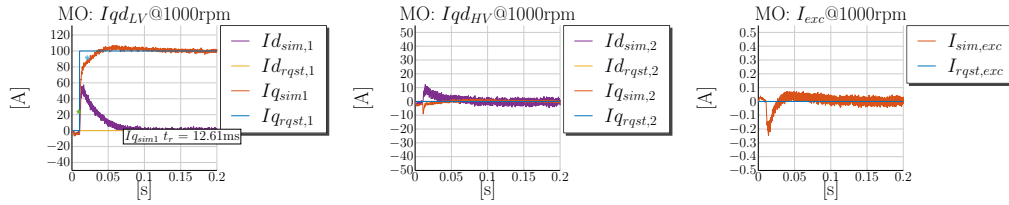


Figure 3.14 – Simulation @1000rpm: $i_{qs1} = 100$ A, $i_{ds1} = 0$ A, $i_{qs2} = 0$ A, $i_{ds2} = 0$ A and $i_{fd} = 0$ A MO Tuning

A step change at the 48V side for $i_{qs2} = 100$ A results in a stronger coupling to the 12V side at 1000 rpm than at 0 rpm. The 48V current controller manages to rise the i_{qs2} current to 90 % of its reference in 4,77 m sec. The first plot of Fig. 3.15 shows the induced currents at the 12V side of up to 100 A for the i_{ds1} current and up to -80 A for the i_{qs1} . The induced i_{ds1} current is a result of the induced i_{ds2} current during the set point change of up to 60 A from the middle plot of Fig. 3.15. The cross-magnetization effect in the model amplifies the coupling between all axis. The field winding current is also disturbed up to $-0,7$ A. The 12V current controllers is still able to nullify the disturbance, however the control performance is strongly deteriorated. The simulation results during the step change of the 48V axis current controller at the speed of 1000 rpm show that the control loop interactions get amplified at speed and the disturbances are stronger.

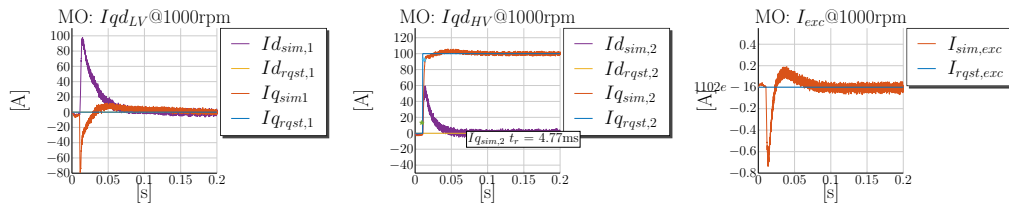


Figure 3.15 – Simulation @1000rpm: $i_{qs1} = 0$ A, $i_{ds1} = 0$ A, $i_{qs2} = 100$ A, $i_{ds2} = 0$ A and $i_{fd} = 0$ A MO Tuning

Also the step change of the field winding current causes induced currents visible in both stator systems. Figure 3.16 shows the results of a step point change of the field winding for $i_{fd} = 2$ A at 1000 rpm. The induced currents at the 12V stator winding are up to -30 A for the q -axis current (i_{qs1}) and up to 15 A for the d -axis current (i_{ds1}). The 48V axis currents are induced of up to ± 10 A. Because the dynamic of the field winding current is much slower, both stator current controllers can easily counteract the disturbance. The field winding current is set in a similar time as the experiment at 0 rpm. The settling time is 54 ms and close to the one simulated at 0 rpm because the rotor reference frame is stationary in reference to the field winding controller.

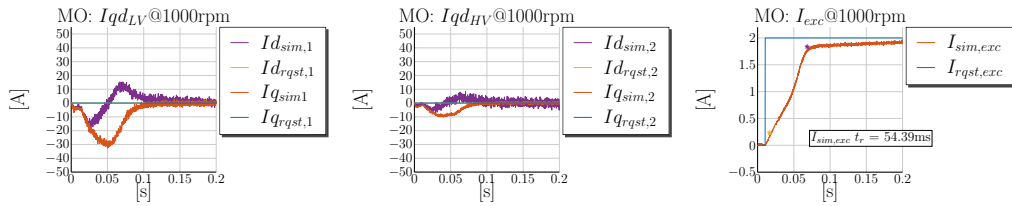


Figure 3.16 – Simulation @1000rpm: $i_{qs1} = 0$ A, $i_{ds1} = 0$ A, $i_{qs2} = 0$ A, $i_{ds2} = 0$ A and $i_{fd} = 2$ A MO Tuning

The performed simulations prove that the control performance is highly deteriorated at speed due to the back-emf voltage generated from the machine. The predicted control performance during the PI controller tuning in terms of settling time cannot be achieved. The dynamic coupling effect between the axis is also amplified at higher speed. The non-linearity of the main inductance contributes further to the deterioration of the control. All these side effects summed together lead to poor control performance.

The static back-emf coupling between the axis can be canceled out with a suitable decoupling network. Decoupling networks are usually applied in three-phase motor control for IPM machines to improve the performance at speed [16, 63, 70]. The decoupling network for the dual-voltage machine depends on all five currents and includes the mutual coupling between the axis. The employed decoupling network is described in Subsection 3.2.5.

3.2.5 Static Decoupling Action

The PI controllers tuned after the MO tuning method, with a desired closed loop bandwidth, compensate the machine time constants of the plant. The tuning method does not consider any coupling between the axis. The controller matrix from equation (3.2.1.7) includes dynamic and static decoupling terms. The dynamic decoupling terms involve differentiation of the measured d - q currents, which brings instability in the control due to the noise in the measurements and is not a suitable approach. Therefore these terms are not included in the decoupling control.

The controller matrix also includes static coupling² terms resulting from the speed voltage terms. Therefore, the static decoupling matrix $G_{p,stat,dcpl}(s)^{-1}$ from equation (3.2.1.15) can be added to the control action of the PI controllers. The control structure with speed decoupling terms is shown in Fig. 3.10. The decoupling network consist of the back-emf voltage terms added to the PI controller outputs. In Fig. 3.10 the back-emf voltage is expressed through the leakage and main fluxes for better legibility. The fluxes can be calculated through the inductances and currents as shown in equations (3.2.1.2) to (3.2.1.6). In the control software, the decoupling voltages are calculated based on the inductances, the currents and the electrical angular speed. The leakage and the main inductances are forwarded from the outer, slower control loop - calculated in 1 msec task, to the fast control loop - calculated in a 100 μ sec task. The main inductance values are constantly interpolated based either on the currently requested currents or on the measured ones. The decoupling can be based on the actual or the requested currents. If the voltages for the decoupling terms are calculated based on the actual currents, this is known as a Decoupling Network (DN). In case the decoupling voltages are based on the requested currents, then the method is a *feed-forward* one and the applied network is called a Feedforward Network (FN). The FN has a predictive action and the DN has a post-factum action. Both methods have their advantages and disadvantages.

The FN network has the advantage that the decoupling voltage does not depend on any measurement quantity and thus is not sensitive to noise in the measurements. However the method has also the disadvantage that in a case of a step point jump the inductance at the target current value is used and thus deviates from the actual inductance during the time the current is settled.

The DN on the other hand interpolates the actual inductance during the set point changes and thus should perform better at least in a simulation environment, where no noise in the signal chain is evident.

Simulations are performed with both methods to verify the improvement of the control performance. Here only the simulation results with the DN are included due to these considerations. The DN delivers slightly better results than the FN and therefore are presented in the subsection. The simulations with the FN network are included in Appendix D.

Figure 3.17 shows the step point change for the 12V q current controller at 1000 rpm with an applied DN and all other currents controlled to 0 A. The current is settled very fast with a *rise time* of 1,6 msec. The induced currents at the 48V stator are also reduced in comparison with Fig. 3.14. The decoupling is beneficial also for the field winding current control, which is not affected during the set point change.

Figure 3.18 shows a step point change at the 48V q -axis current, i_{qs2} , with an applied DN to counteract the back-emf coupling. The *rise time* is around 2,1 msec. Though the control performance of the 48V side is improved, there is still a disturbance at the 12V

²static, because the matrix is not dependent of the Laplace operator s

3 Current Control Design

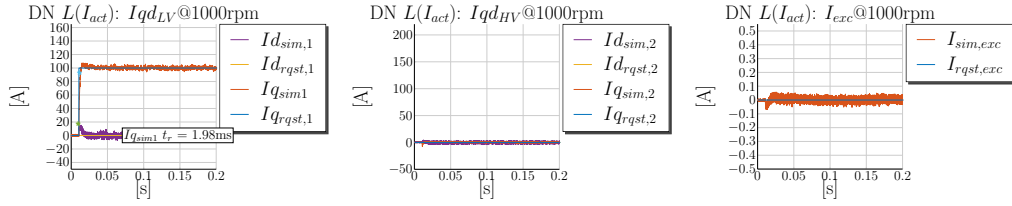


Figure 3.17 – Simulation @1000rpm: $i_{qs1} = 100$ A, $i_{ds1} = 0$ A, $i_{qs2} = 0$ A, $i_{ds2} = 0$ A and $i_{fd} = 0$ A MO with a DN $L(I_{act})$

side visible. The induced q -axis current i_{qs1} rises up to -80 A and the induced d current i_{ds1} is up to 30 A. The induced currents are mainly a result from the dynamic coupling between the axis. When the induced currents are compared with the same test without a decoupling action, then the improvement is of around 30%. The field winding current shown in the right most plot of Fig. 3.18 is slightly disturbed and the induced current is up to $-0,2$ A. During the same test without a decoupling action, shown in Fig. 3.15, a field winding current of up to $-0,7$ A is induced. The DN improves clearly the control performance although there is still disturbance left, caused by the dynamic coupling of the axis.

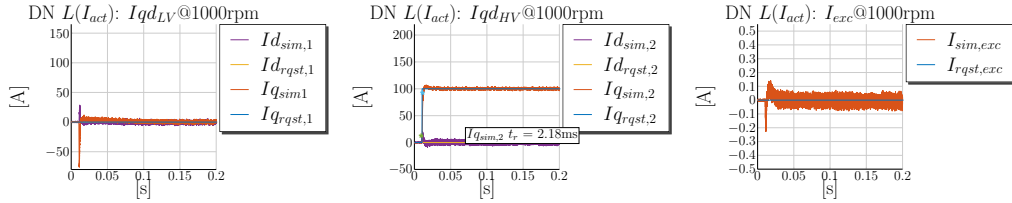


Figure 3.18 – Simulation @1000rpm: $i_{qs1} = 0$ A, $i_{ds1} = 0$ A, $i_{qs2} = 100$ A, $i_{ds2} = 0$ A and $i_{fd} = 0$ A MO with a DN $L(I_{act})$

Finally, a reference change for the field winding current is tested. Again the field winding current is controlled to 2 A with an applied feed-forward action to the field winding controller itself. The feed forward action reduces the *rise time* to 40 m sec. The induced q -axis current at the 12V side is up to 55 A, as shown in Fig. 3.19 and the 48V q -axis current of up to 20 A.

The made observations during the controller tests with the DN prove that the added DN improves the control performance at speed. However the dynamic coupling between the axis is still evident in the plant and cannot be counteracted with the back-emf decoupling method. The dynamic coupling effect is amplified through the speed rotation due to the cross-magnetization in the main inductance modeling. Though the dynamic coupling cannot be compensated, the tuned PI controllers do not get unstable and are able to cancel in a short time the disturbance.

The performed single controller tests are useful to verify the proposed controller tuning. However in reality the requested currents are changed simultaneously to set a specific

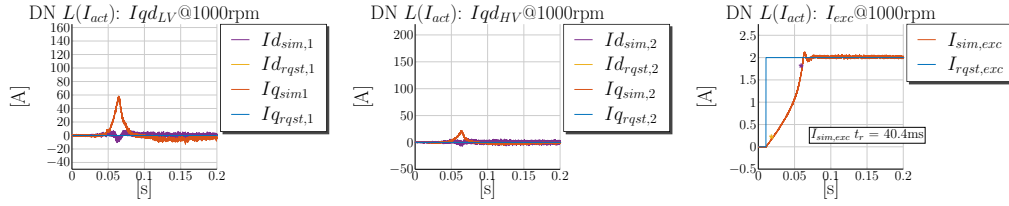


Figure 3.19 – Simulation @1000rpm: $i_{qs1} = 0$ A, $i_{ds1} = 0$ A, $i_{qs2} = 0$ A, $i_{ds2} = 0$ A and $i_{fd} = 2$ A MO with a DN $L(I_{act})$

torque value. Therefore a combined test, during which more than one current set point is changed, are performed to check the full control behavior of the system. Due to legibility reasons not all combinations of simultaneous set point changes will be covered. Rather the set point changes, which are used to generate both torques, T_{e12V} and T_{e48V} , are tested in the simulation environment.

Generating a 12V Torque and Controlling the 48V Torque to Zero at 1000 rpm

The dual-voltage machine is able to generate two air-gap torques. The machine control should be able to set one of the air-gap torques and control the other one to zero. First, simulations are performed to generate a 12V torque and control the 48V torque to zero. For this purpose the field winding current is set to a certain value and the 12V stator currents are set to certain reference values. In general the employed salient-pole machine generates an electromagnetic torque, which consists of a synchronous torque component and a reluctance torque component. The synchronous torque results from the interaction of the rotating electromagnetic field generated by the field winding and the generated rotating electromagnetic field by the stator. The reluctance torque component is a result of the difference between the d - and q -axis inductances. The reluctance torque is generated, because the rotating magnetic flux by the stator winding follows a path of minimum reluctance, which results in turn of a rotor movement. The reluctance torque component is however much smaller in magnitude in comparison to the synchronous torque in the employed salient-pole machine. The synchronous torque is generated through the interaction of the q -axis current and the flux produced by the field winding current. The reluctance torque is produced because of the stator current vector built by i_{qs1} and i_{ds1} . In this case the L_{qq} inductance is smaller than L_{dd} (refer to Table 2.1) and therefore a positive reluctance torque is generated by a positive i_{ds1} and a positive i_{qs1} .

The combined controller tests are performed for a better comparison to the previous tests again at 1000 rpm. The static decoupling is included in the control.

In order to set up the case, where a 12V torque is generated and the 48V torque is controlled to zero, the field winding current is set arbitrary to 2 A, the q -axis current i_{qs1} to 100 A, the d -axis current i_{ds1} to -50 A and the 48V currents to 0 A. In this test a motoring 12V torque is generated. Figure 3.20 shows the corresponding simulation results.

The disturbances at the 48V side are greater in comparison to the single controller tests of the 12V q -axis stator current. The induced 48V d -axis current rises up to 45 A and the 12V d -axis current is also disturbed into the positive direction due to the negative step change of the 12V d -axis current i_{ds1} to -50 A. The field winding current rises also into the negative region of up to $-0,5$ A due to the induced positive stator d axis currents at the very beginning of the set point change. The settling time is approximately $100 \mu\text{sec}$ greater than the single controller tests. Both controllers, i_{qs1} and i_{ds1} , show an overshoot of around 50 %. The overshoot is significant despite the conservative MO tuning of the PI controlers. It is a result mainly due to the dynamic coupling between the axis. The right-most plot of Fig. 3.20 shows the generated electromagnetic torques of the 12V and 48V windings. The machine model generates as expected no electromagnetic torque at the 48V winding T_{e48V} and a 12V electromagnetic torque, T_{e12V} , of around 5 Nm.

In general, the controllers perform worse in comparison to the single controller tests. This is conceivable, because the dynamic and static control loop interactions are augmented when the set points for multiple controllers are changed at once. Even though the performance deteriorates and the overshoots are greater the controllers can still nullify the disturbances and do not become unstable.

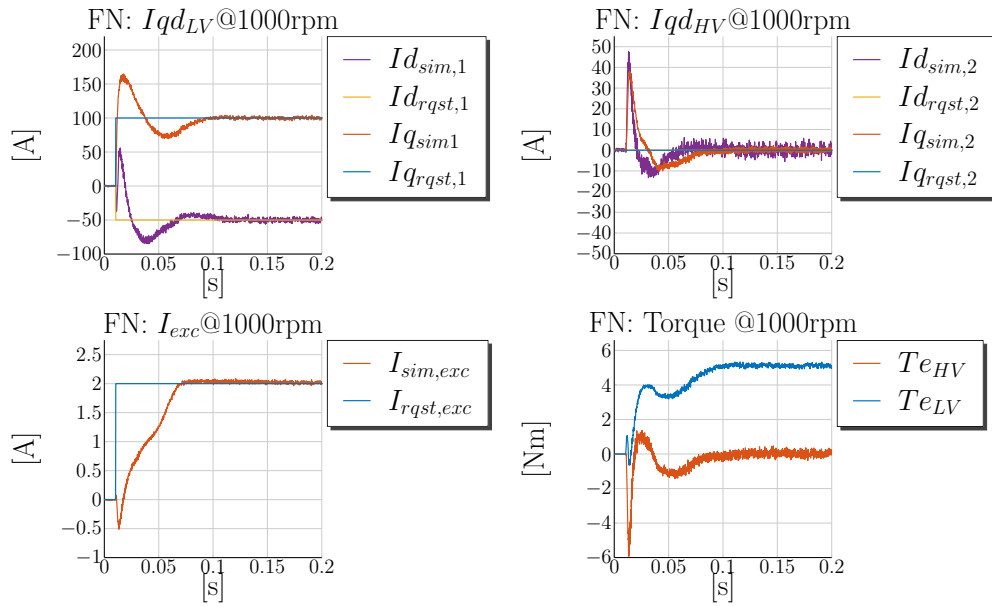


Figure 3.20 – Simulation @1000rpm: $i_{qs1} = 100$ A, $i_{ds1} = -50$ A, $i_{qs2} = 0$ A, $i_{ds2} = 0$ A and $i_{fd} = 2$ A MO-FN $L(I_{rqst})$

The generation of a negative 12V torque is achieved through the control of the q -axis current at -100 A. The dynamic responses of the currents are analogous and therefore the results are omitted here. The simulation results are included in Appendix D.

Generating a 48V Torque and Controlling the 12V Torque to Zero

Another characteristic case for the dual-voltage machine is the generation of a 48V torque and controlling the 12V torque to zero. For this case the same set points are commanded at the 48V side and the 12V currents are controlled to zero. The simulation results are shown in Fig. 3.21. Due to the q -axis set point step of the 48V side, positive d -current, i_{ds1} , is induced up to 75 A. The q -axis current of the 12V side, i_{qs1} , is disturbed up to 60 A. The field winding current in this case is almost not disturbed because the 12V d -axis current, i_{ds1} , rises to 75 A, which compensates the negative step change at the 48V d -axis current to -50 A. Both fluxes due to the changes in the d -axis currents get mostly compensated and therefore the disturbance in the field winding is smaller. The 48V q -axis current shows an overshoot of around 40 %. The 48V d -axis current shows no overshoot because the induced positive d -axis current counteracts the change of the 48V current. The generated 12V and 48V torques are plotted in the right-most plot of Fig. 3.21. The generated torque at the 12V side is as expected 0 Nm and the generated 48V torque is around 24 Nm.

In summary, the simultaneous change of the 48V axis currents and the field winding produce complex interactions between all five current control loops. The 48V current controllers are less influenced by the 12V side currents and show smaller overshoots than the same test at the 12V side. The 12V current controllers encounter greater disturbance than the 48V ones during the equivalent test in the previous experiment. The dynamic current responses of the machine are plausible and can be comprehended through the analysis of the machine voltage equations from (3.2.1.2) to (3.2.1.6). The simulations also prove that the controllers react differently on each side and are dependent on the current set point change. Therefore no reproducible control reaction can be achieved. This is a result of the fact that the dynamic coupling in the machine and the control loop interactions depend on the selected current set points and also on that, which side, the 12V or the 48V, is being tested. The observations made during the controller tests are due to the electromagnetic asymmetry of the machine. The electromagnetic asymmetry fulfills the requirement to the machine to produce different voltage levels at each three-phase stator system.

The analogous test for a negative 48V torque is also omitted here and included in Appendix D.

Generating Simultaneous 12V and 48V Torques in the Same Mode

The next controller test represents a simultaneous change of all current set points. The current set points are changed such that the 12V and 48V torques are generated in the same mode. In Fig. 3.22 the motoring modes of both windings are demonstrated. Appendix D includes simulation results of both windings in generator mode. In Fig. 3.22 the 12V and 48V q -axis currents are changed to 100 A and the d -axis currents to -50 A. The overshoots in the d -axis currents are negligible. The overshoot in the 48V q -axis

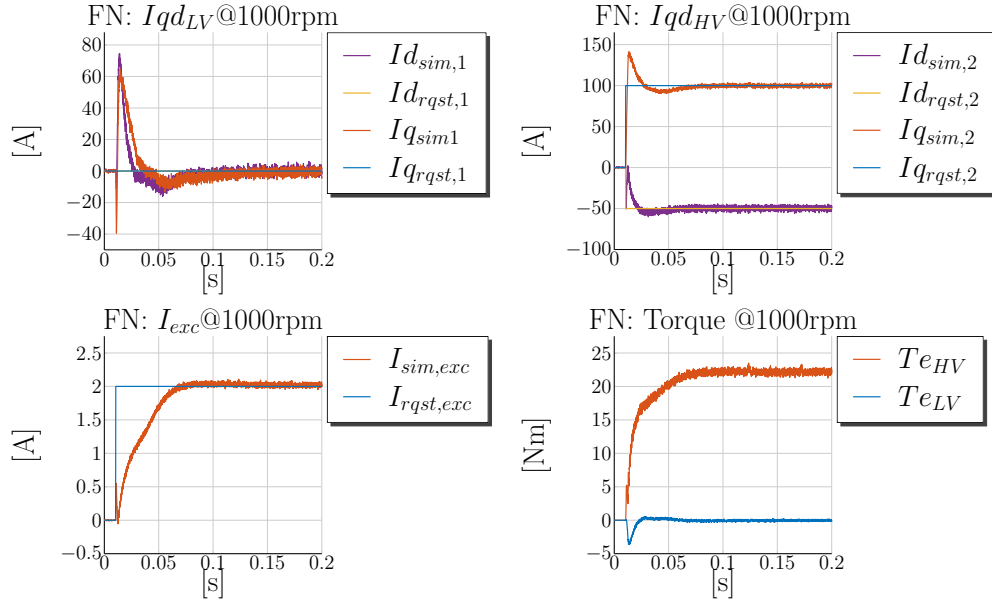


Figure 3.21 – Simulation @1000rpm: $i_{qs1} = 0$ A, $i_{ds1} = 0$ A, $i_{qs2} = 100$ A, $i_{ds2} = -50$ A and $i_{fd} = 2$ A MO-FN $L(I_{rqst})$

current, i_{qs2} , is of about 30 % and the overshoot in the 12V q -axis current, i_{qs1} , is around 50 %. The stator current controllers perform well, because both q -axis reference currents are in the same direction and therefore both controllers act in the same direction. The overshoots are greater than during the single controller tests, which is plausible, because the produced disturbance during the set point change contribute to the control action and result in a faster *settling* and *rise* times. The same logic holds for the set point change of the d -axis currents.

The field winding current shows a similar dynamic behavior as during the single controller test. Small disturbance is visible at the very beginning of the set point change mainly due to the negative d axis currents. The settling of the negative d -axis currents results in a positive current induced in the field winding and thus contributes to the faster settling of the field winding current.

The performed simulations during the combined tests show, that the proposed PI tuning is robust enough to handle simultaneous set point changes of all current controllers.

Generating 12V and 48V Torques in Opposite Modes

During rotation the air-gap of the dual-voltage machine can be employed to transfer power from 12V to 48V side and vice versa. Depending on the sign of the sum of both torques, $T_{e12V} + T_{e48V}$, the mechanical torque is either motoring or generative. In order

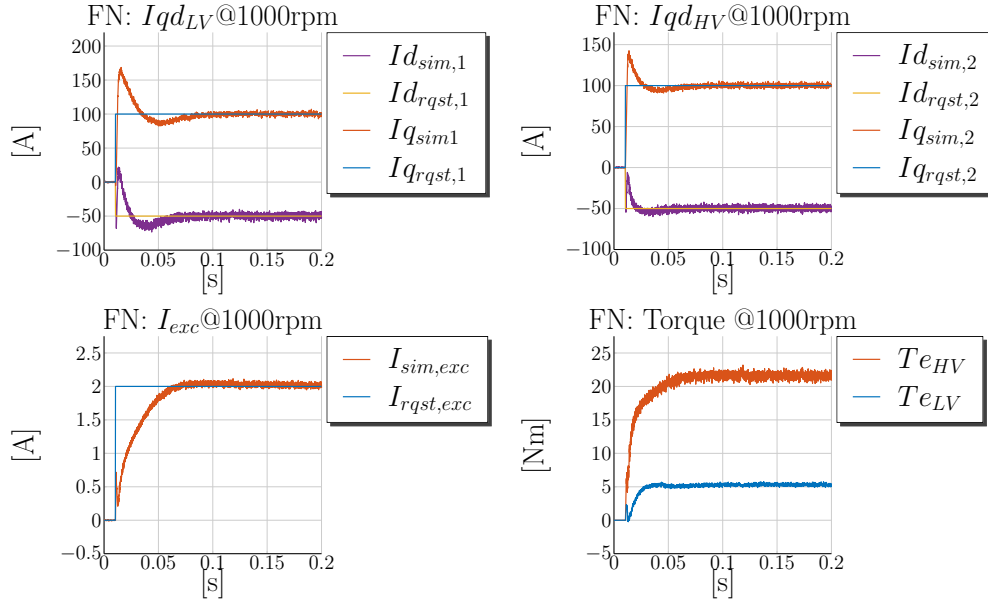


Figure 3.22 – Simulation @1000rpm: $i_{qs1} = 100$ A, $i_{ds1} = -50$ A, $i_{qs2} = 100$ A, $i_{ds2} = -50$ A and $i_{fd} = 2$ A MO-FN $L(I_{rqst})$

to set up this case the q -axis current of one side has to have different sign than the q -axis current of the other side. The 48V winding is set in a motoring mode with $i_{qs2} = 100$ A and the 12V winding in a generating mode with $i_{qs1} = -100$ A. The simulation results of the complementary experiment are included in Appendix D.

It is obvious that in Fig. 3.23 the q - and d -axis currents of the 12V side are distorted at the beginning of the set point change. The d -axis current rises up to 30 A before the controller can compensate the disturbance. The 48V controller performs well and is able to set the d -axis current without an overshoot and the q axis current with an overshoot of 30%. The field winding is almost not disturbed.

In this case it is evident that the 48V controller influences the dynamic behavior of the 12V currents a lot. The currents even rise first into the opposite direction until the controller can compensate the disturbance. This is due to the fact that the employed feed-forward decoupling network uses the requested 48V, 12V and field winding currents to calculate the back-emf voltage, which is added to the PI controller outputs.

3.2.6 Simulation Results Summary of the Controller Tests

In the previous subsections a tuning for the five PI current controllers for the dual-voltage machine is derived. The MO design criterion, a loop shaping design method, is applied to the current control loops, such that the closed loops show a certain bandwidth. The stator loops are tuned to have a bandwidth of 200 Hz and the field winding loop is tuned

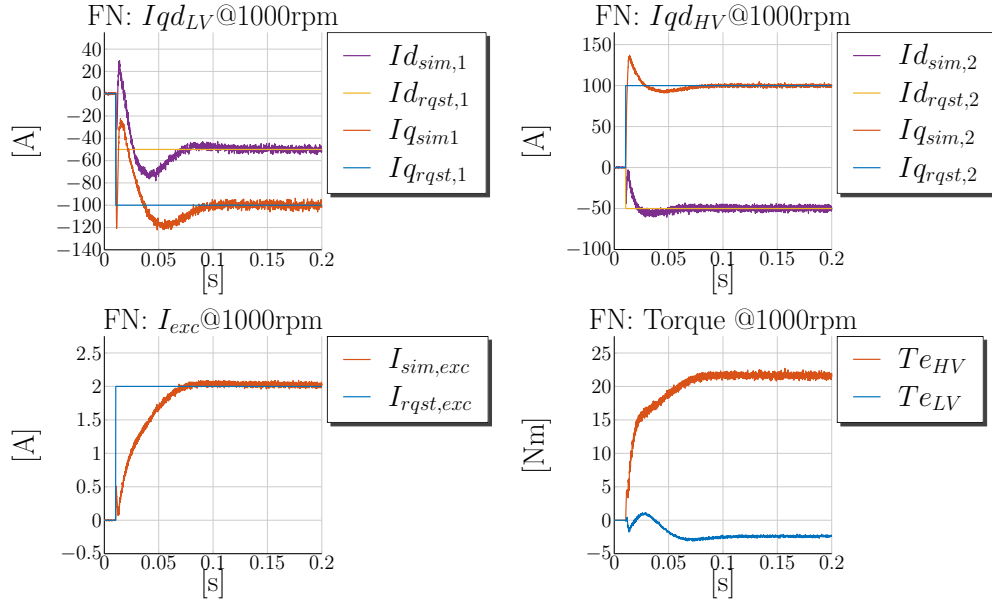


Figure 3.23 – Simulation @1000rpm: $i_{qs1} = -100$ A, $i_{ds1} = -50$ A, $i_{qs2} = 100$ A, $i_{ds2} = -50$ A and $i_{fd} = 2$ A MO-FN $L(I_{rqst})$

to have a bandwidth of 8 Hz. The current control loops are tuned conservatively, in order to react to a set point change without an overshoot. The conservative tuning is of an advantage because of the evident control loop interactions in the plant. The control loop interactions are due to the coupling between each axis. A sharp tuning may lead in certain edge regions to instabilities in the control.

The closed loops are tested with the presented dual-voltage machine model from Chapter 2. First, controller tests of each control loop are performed individually, while the other set points are not changed. This way only the controller tuning of a single control loop is verified and the influence of the control loop interactions is minimized. The expected control performance correlates good with the tests in the simulation environment. Specifically, the expected *rise times*, resulting from the chosen PI control parameters, are compared with the simulated ones. The *rise times* during the single controller tests show very good correlation with the calculations. The current references are set without an overshoot, which correlates with the chosen PM of the controllers. The small deviations identified in the simulation in comparison with the predicted control behavior are because the machine model includes saturation and cross-magnetization. The controller tuning is based on the other side merely on a simplified linear machine model. The saturation effect is considered as a “continuous” gain scheduling, because the PI control parameters are calculated in real time based on the saturation behavior of the machine in the outer control loop. This is not a pure non-linear control, but rather makes the PI controllers robust in their behavior against changes in the main inductance values.

Further, it is shown that the back-emf voltage terms have a negative effect on the control at speed. If no decoupling or feed-forward action is added to the control the control performance deteriorates and the *rise times* increase more than 5 times for the 12V side and is doubled for the 48V side at 1000 rpm in comparison to the same tests performed at 0 rpm. Both techniques, feed-forward and decoupling network, improve the controller performance at higher speed and reduce the *rise time* to similar values as those at 0 rpm. These decoupling techniques are static ones, because both do not depend on the Laplace operator s . Therefore the dynamic coupling is evident during the controller tests. The dynamic coupling causes induced currents into the other systems when the reference of one control loop is changed. These induced currents, during a controller test of one system, are considered as a disturbance in the other systems and the rest of the PI controllers are able to counteract this disturbance. The aforementioned drawback is also the main disadvantage in the applied decoupling action.

Combined controller tests with simultaneous set point changes of multiple controllers are performed in order to prove the stability of the controller tuning during some typical cases for the dual-voltage machine. Four relevant cases are identified and replicated in the simulation:

- Generating 12V torque and controlling the 48V winding to zero torque
- Generating 48V torque and controlling the 12V winding to zero torque
- Generating torque in both windings in the same mode
- Generating torque in both windings in opposite modes

The performed tests in all four cases prove the stability of the controllers but show also the disadvantages of the static decoupling. The simultaneous set point changes result in strong control loop interactions and higher disturbances on each control loop. The expected control loop behavior from the MO tuning cannot be observed during the simulation because of these strong dynamic control loop interactions. The settling behavior of the currents depends on the modes, motor or generator, in which each winding is brought.

After verifying the stability of the controllers and their performance in the simulation environment, these have to be tested on a test bench with a machine prototype. Subsection 3.2.7 explains briefly the measurement setup used during the tests and Subsection 3.2.8 shows the experimental results and compares these with the simulations.

3.2.7 Measurement Setup

In Subsection 3.2.4 the described PI controller tuning is successfully tested in a simulation environment and a static decoupling method is added to improve the control performance at speed. The control is implemented in a Model in the Loop (MIL) environment. The machine model is programmed in PLECS and the control in Simulink. This enables an

easy transition of the control software from the MIL environment to the Hardware in the Loop (HIL) test bench. The verified control software in the simulation also includes the data acquisition blocks from the sensors and thus can be directly compiled for the RCP system without the need for any further adjustments. Before presenting the performed measurements for the controller tests the employed hardware setup for the real-time machine control is briefly explained.

Computing Platform

The discrete PI control of all five currents and the computation of the six-phase backwards and forwards transformations require the employment of a powerful processor, which can calculate the control signals every 100 μ sec. For this purpose a 1 GHz DS1005 PowerPC [17] is employed. The real-time fast data acquisition is performed with a Field-Programmable Gate Array (FPGA) board DS5203 [19]. The FPGA board handles the data acquisition from the encoder for the rotor position measurement and the data acquisition from all current sensors. These have to be performed simultaneously and in the middle of the switching period. The PWM generation is also performed on the FPGA board. The measurement of all other non-real time quantities, for example the DC link voltages and the temperature sensors, is handled through the IO board DS2202 [18]. All boards and the PowerPC communicate through a Peripheral High Speed (PHS) bus. More details about the computing platforms can be found in the corresponding datasheets [17–19].

Current and Voltage Measurement

The current measurement is performed with LEM [43] transducers suitable for automotive motor control applications. The phase current measurements are performed with six HC5F800-S [41] transducers, able to measure currents up to ± 800 A. The star point current is measured using the current transducer of type HC5F400-A [40], which is able to measure currents in the range of ± 400 A. The excitation current is measured with a LTS15-NP current transducer [42], which measures currents in-between ± 15 A. The measurement of the DC link voltages is achieved through passive voltage dividers integrated into the power electronics control board, which are sensed by the DS2202 IO board through a 50-pin sub-d electrical connector.

Rotor Position Measurement

The rotor position is sensed through a rotary encoder from Renishaw [60]. Specifically the model RE36IC0611B40F2A00 [59] is used. It is an incremental encoder with 2048 positions per revolution, a maximum speed of 10 000 rpm and an mechanical accuracy of $\pm 0,3^\circ$. The generated pulses from the rotary encoder are sensed and processed by

the FPGA board. The code implemented on the FPGA converts the pulses to a rotor position, which is stored in a register and read out through the PHS bus by the PowerPC. The implemented control on the PowerPC uses then the rotor position for the machine control.

Test Bench Setup

The test bench, including the RCP system, is schematically illustrated in Fig. 3.24. For the controller tests and all other tests done during this work a control desk experiment is set up. Through the control desk software all internal control signals can be viewed, plotted and recorded. The following quantities are for example monitored with control desk: the measured and requested d - q currents, the electrical angular speed ω_e , the measured DC link voltages, $V_{12V,meas}$ and $V_{48V,meas}$, and others. All important internal signals are transmitted via a Control Area Network (CAN) bus to the Dewetron data acquisition system. The DS2202 IO board has support for transmitting CAN messages, which are sent through the sub-d connector to the power electronics control board and read out through a CAN DE-9 connector by the Dewetron system. Dewesoft records the received CAN messages on a desktop computer. Further, Dewesoft records also all other physical variables measured by the installed sensors on the test bench and transmitted through the Dewetron data acquisition hardware. Figure 3.24 shows the LEM current and voltage transducers placed at the machine phase terminals between the power electronics and the machine prototype. These sensors are used to calibrate the other sensors employed for the machine control and integrated into the power electronics. LEM transducers are used also to measure the DC link currents and voltages at the 12V and 48V side. A second encoder is installed between the load machine and the torque transducer, which measures the rotor position redundantly to the one mounted at the machine rotor. Only the encoder mounted in the machine is used for the real-time control. The torque transducer senses the mechanical torque, whose signal is acquired by the Dewetron system and recorded in Dewesoft. The torque transducer measures torques in the range of ± 100 Nm. The 12V and 48V loads and sources are also illustrated in Fig. 3.24 with its main specifications. The load machine is an IM from Bosch Rexroth with a maximum speed of 10 000 rpm, a maximum power of 64,4 kW and maximum torque of 341 Nm and is commanded by a Bosch Rexroth software running at the desktop computer. The inverter employed for the load machine is an external inverter by Siemens not included in the figure. In Fig. 3.24 the electrical cable connection between the components is illustrated with orange double lines. The load machine, the encoder, the torque transducer and the test machine are on one shaft. The test machine is connected through a coupling, which is omitted in the figure for better legibility. The mechanical connection between the components is represented by a black double line. The signal path of all transducers mounted on the test bench and the internal quantities of the control software transmitted via CAN bus to the data acquisition software Dewesoft is illustrated with blue dashed double lines. The control commands ensuring the real-time control of the machine are transmitted by sub-d connectors from the Autobox to the power electronics. This signal path is drawn in red

solid double line. The control desk runs on a notebook and is used to perform changes in the software application parameters running on the Autobox. Set point changes in the reference currents are performed through the control desk experiment. This control path is non-real-time and is drawn in red double dashed line.

After the review of the employed test bench, measurements for the current control are performed and the results analyzed in the next subsection. The measured quantities are visualized with graphics and compared with the previously performed simulations. Through the performed measurements both the controller tuning and the programmed machine model from Chapter 2 are verified. The measured dynamic current responses are compared to the simulated ones.

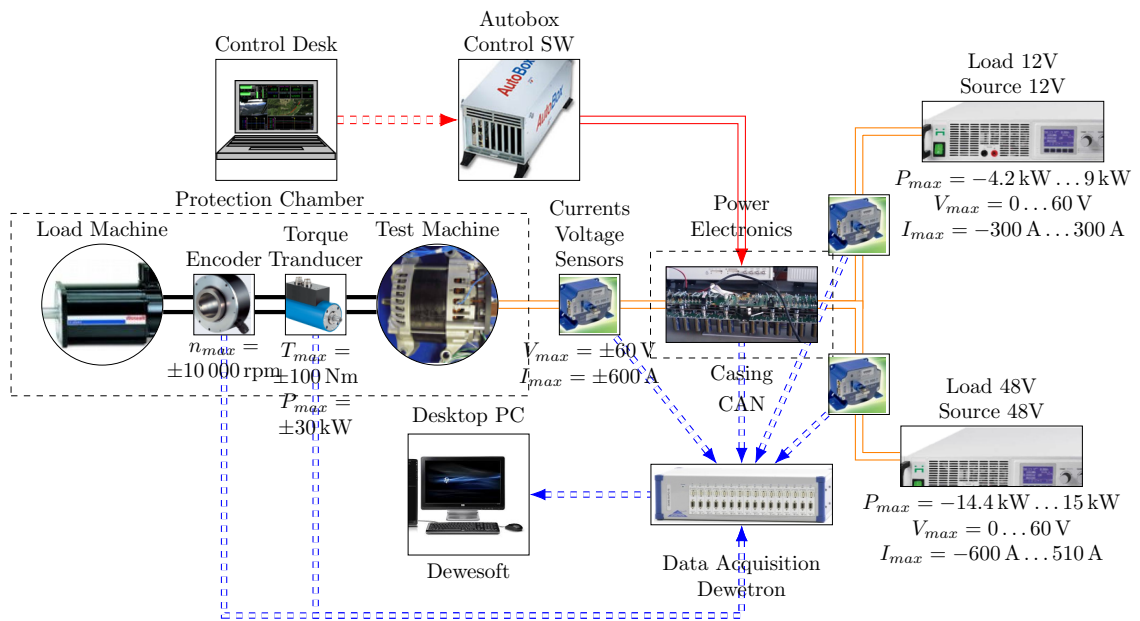


Figure 3.24 – Test Bench Schematic

3.2.8 Measurements in a Current Control Loop

In this subsection measurements of the combined controller tests, corresponding to the simulations performed in Subsection 3.2.4, are presented. The performed simulations prove that the combined controller test are more challenging for the current controllers than the single controller tests. Furthermore the combined tests verify better the machine model dynamics. The interactions between the current controllers are more evident when multiple reference points are changed at once. The combined tests prove also as a worst case example the stability of the current controllers. In the next paragraphs measurements of the cases with torque generation at both sides are presented. For better comparison

the very same cases with the same reference currents are replicated at the test bench as in the performed simulation before.

Generating 12V Torque and controlling 48V at Zero Torque

The first case shown in Figure 3.25 shows measurement results with torque generation at the 12V winding and controlling the 48V torque to zero. For this case the same reference currents are set as in the simulation from Subsection 3.2.5. The q -axis 12V current is set to 100 A, the d -axis current to -50 A and the field winding current to 2 A. The induced d -axis current i_{ds2} at the 48V side rises up to 50 A and the q -axis current i_{qs2} increases up to 40 A. The measured currents at the 48V side correlate very good with the simulation from Fig. 3.20, where the induced d -current, i_{ds2} , is up to 55 A and the q -current, i_{qs2} , up to 35 A. The machine model reproduces very good the dynamics of the 48V currents. The overshoot for the i_{qs1} current is around 75 % of the reference value with a maximum of 175 A. The simulated overshoot is 150 A and lies very close to the measurement. The measured d -axis current overshoot for i_{ds1} is -75 A and corresponds good with the simulated one. The measured field winding current response in the third plot shows a similar course as the the simulated one. One difference is visible at the beginning of the step point change, where in the simulation environment the field winding current is disturbed first in the negative direction before settling to the 2 A reference current. In general, the measured dynamic responses correlate very good with the simulated dynamic responses of the current controllers. The observed disturbances at the 48V side during the performed simulations are confirmed also through the measurement on the test bench.

The measured mechanical torque is plotted in the right-most plot of Fig. 3.25. The measured torque is around 4 Nm, while the simulated one from Fig. 3.20 is around 4,5 Nm. The simulated torque lies close to the measured one. The deviation is explained with the fact that the iron losses are not included in the machine model used for the simulations during the current control verification. Focus on the predicted torque accuracy from the model is put on in the next chapter, where the torque control is handled and the torque control simulations are performed. The dynamic model without iron losses simulates faster and is therefore preferred for the current control tests.

Generating 48V Torque and Controlling the 12V Torque to Zero

Generating a 48V torque, while controlling the 12V winding to zero torque, is even a more challenging task because of the strong electromagnetic influence of the 48V side to the 12V one. Figure 3.26 shows measurement results of set point changes for the 48V side and the field winding, while the 12V side currents are controlled to zero. The q -axis current, i_{qs2} , is controlled to 100 A and the d -axis current, i_{ds2} , to -50 A and the field winding to 2 A. These set points generate a mechanical torque of 17 Nm.

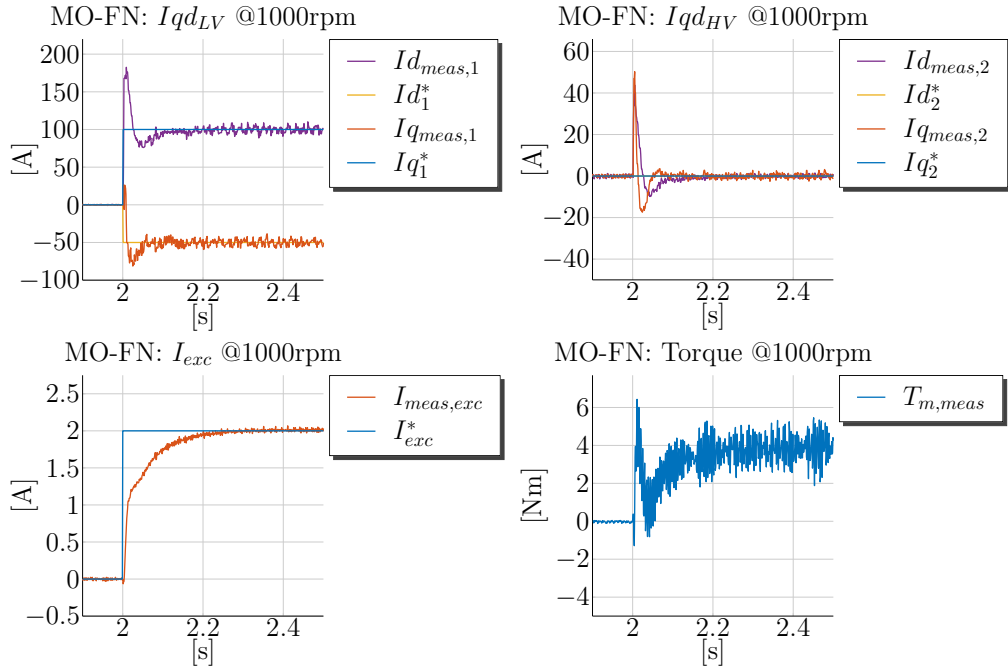


Figure 3.25 – Measurements @1000rpm: $i_{qs1} = 100$ A, $i_{ds1} = -50$ A, $i_{qs2} = 0$ A, $i_{ds2} = 0$ A and $i_{fd} = 2$ A MO with a FN

The current overshoot for i_{qs2} is 50 % and the d -axis current, i_{ds2} , is settled with almost no overshoot. The simulation from Fig. 3.21 with the same set points shows an overshoot of around 40 % for the q -axis current, i_{qs2} , and almost no overshoot for i_{ds2} . The settling behavior predicted from the simulation results corresponds to the measured dynamic currents responses.

The induced 12V d -axis current, i_{ds1} , increases up to 40 A and the q -axis current, i_{qs1} , up to 130 A. The simulation shows also similar results with an induced d -axis current i_{ds1} of up to 50 A and an induced i_{qs1} of up to 100 A. Though the exact peak values do not perfectly match the main characteristics of the dynamic disturbance is correctly predicted from the machine model. The measured settling behavior of the field winding correlates well with the simulated one besides of the disturbance in the field winding at the beginning of the set point change not evident in the measurement.

It is noted in the test bench measurement description from Subsection 3.2.7 that due to bandwidth limitation of the employed CAN bus not every single measured currents value is recorded. This can lead to some inaccuracies in the measured currents dynamics and may be the reason that the discussed field winding disturbance is not captured. However, the general form of the current dynamics is recorded and relates with a good accuracy to the simulated currents.

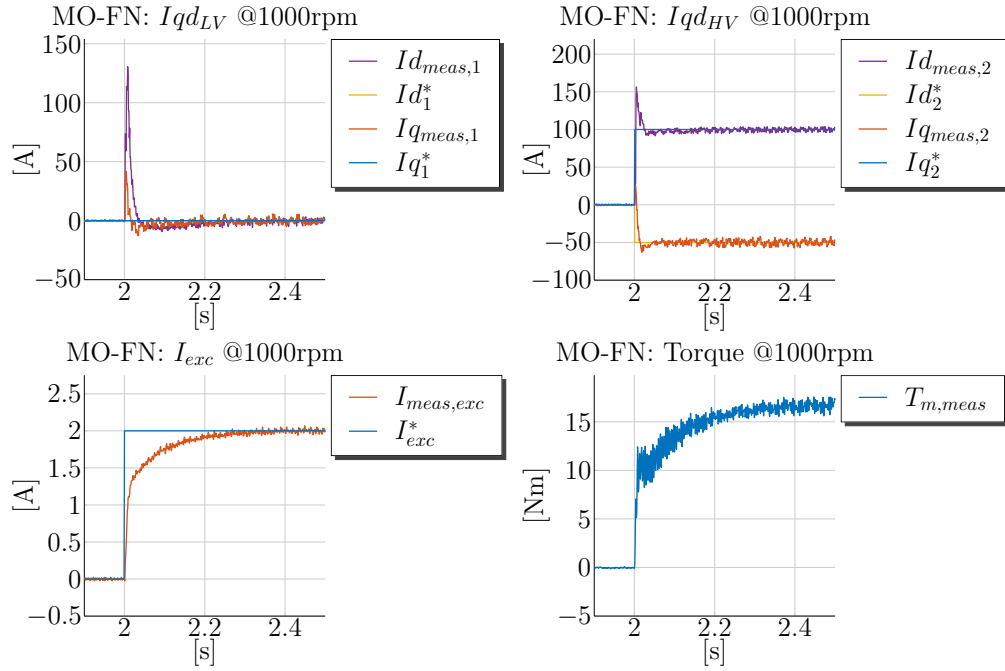


Figure 3.26 – Measurements @1000rpm: $i_{qs1} = 0$ A, $i_{ds1} = 0$ A, $i_{qs2} = 100$ A, $i_{ds2} = -50$ A and $i_{fd} = 2$ A MO with a FN

In a summary, the measured dynamics during both tests, generating torque at a single winding and controlling the other to zero, correlate very well with the simulated currents. During both tests the induced currents at the idle side are into the positive direction in the measurement as well as in the simulation, which is explained through the machine voltage equations. The magnitudes of the induced currents correspond very well between measurement and simulation. The presented measurements prove the stability of the current controllers and also verify the implemented machine model with a comparison of the currents' dynamics between simulation and measurement.

Generating 12V and 48V Torques in the Same Mode

The dual-voltage machine is able to generate a positive mechanical torque with both windings energized in a motoring mode. For this purpose the current set points of all five currents are simultaneously changed. The 12V and 48V q -axis currents are set to 100 A and the field winding is set to 2 A in order to produce the synchronous torque component. The d -axis currents are set to -50 A. The measured dynamic current responses from Fig. 3.27 show overshoots in the settling of the q -axis currents and no overshoot in the settling of the d -axis currents.

The overshoot of i_{qs1} is up to 200 A and around 100 % of the reference and the overshoot for i_{qs2} is up to 150 A and around 50 %. In the simulation from Fig. 3.22 the q -axis

current overshoot is 60 % for the 12V side and 30 % for the 48V side. Although the overshoot magnitudes are not accurately predicted in the simulation, the machine model predicts well the tendency of having greater overshoot when both controllers act in the same direction. No overshoot is present in the settling of the d -axis currents because the positive change of the field winding current interacts with the d -axis currents. The positive field winding change induces a positive d -axis flux in the stator windings and thus acts against the stator d -axis controllers. The measured field winding curve shows a similar trajectory as in the previous experiments.

The observed overshoots for i_{qs1} and i_{qs2} in the measurement are higher than the simulated ones which indicates that the real inductances may be smaller than the parametrized ones in the model. Despite the 100 % overshoot the 12V current controller does not become unstable and controls the reference value as requested.

It is evident that the measured mechanical torque represents the sum of both electromagnetic torques, $T_{e12V} + T_{e48V}$, from the last two experiments. The case from Fig.3.25 generates a mechanical torque of 4 Nm and the one from Fig.3.26 produces a mechanical torque of 17 Nm. In Fig. 3.27 both windings contribute to the torque production and therefore the sum is equal to 21 Nm. The same torque superposition effect is replicated also in the performed simulation from Fig. 3.22.

In summary, the measured dynamic current responses correlate well with the performed simulations for the combined motoring torque production. The simulation predicts the tendency for the q -axis currents to overshoot during the settling of the q -axis reference currents. The current controllers are stable during the combined experiment and verify the robust tuning.

Generating 12V and 48V Torques in Opposite Modes

The most important feature of the dual-voltage machine is to be able to control both windings to generate torques with different signs and this way to transfer power between both power supply networks at rotation. The 48V winding generates a positive torque and the 12V winding a negative one or vice versa. For legibility purposes only one of these cases is presented here. The 48V currents are controlled to generate a motoring torque and the 12V currents are adjusted to generate a torque in a generator mode. This case is possibly one of the most frequent ones during the machine exploitation in a vehicle as the 12V side is generally always in generator mode to supply the 12V loads and the 48V side is depending on driver's request either in generating mode during a recuperation or motoring mode during a boost.

Figure 3.28 presents the measurement results of this case. The 12V q -axis current, i_{qs1} , is controlled to -100 A and the 48V q -axis current, i_{qs2} , is set to 100 A. The rest of the currents are set as in the previous experiment. The 12V winding generates a torque of -4 Nm in a generator mode and supplies the 12V side with power and the 48V winding generates a motoring torque of 17 Nm and draws positive current from the 48V source.

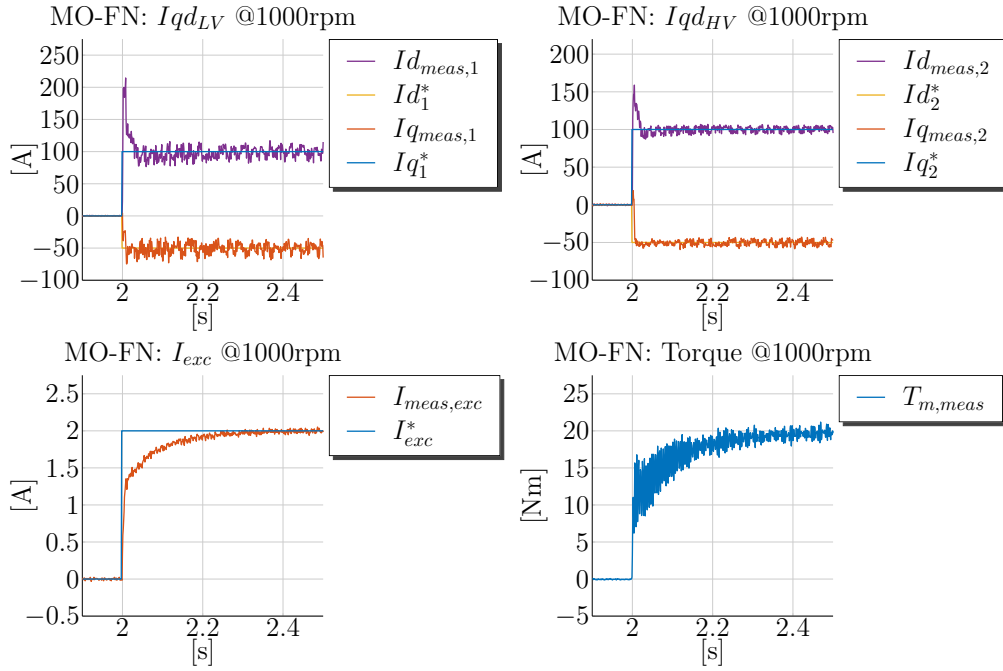


Figure 3.27 – Measurements @1000rpm: $i_{qs1} = 100$ A, $i_{ds1} = -50$ A, $i_{qs2} = 100$ A, $i_{ds2} = -50$ A and $i_{fd} = 2$ A MO with a FN

Both electromagnetic torques cannot be measured as only the mechanical torque produced at the shaft is sensed. The measured mechanical torque is included in the right-most plot of Fig. 3.28 and is expected to be 13 Nm.

In the measurement from Fig. 3.28 is evident that the q -axis 12V current, i_{qs1} , shows a smaller overshoot during its settling in comparison to the previous experiment. This is due to the fact that the 48V q -axis current controller acts in the opposite direction to set the positive reference of 100 A and thus counteracts the dynamics of the 12V current controller. The overshoot of the 48V q -axis controller is slightly below 150 A and thus a bit less in comparison to the previous case. The simulation for the same case from Fig. 3.23 shows also reduced overshoots for both current controllers with 20% for the 12V side and 30% for the 48V side. The 12V d -axis current controller is settled with a higher overshoot of around 30% as well in the simulation as in the measurement. The dynamic current loop interactions in this case are the most complex ones because both windings are controlled in an opposite mode and induce fluxes in opposite directions at least in the q -axis. The d -axis current controllers are also disturbed due to the dynamic cross-coupling between d - and q -axis.

The right-most plot shows the measured mechanical torque, which is around 13 Nm. As expected the mechanical torque is less in comparison with the previous cases because the 12V winding generates a negative torque and counteracts the 48V winding, which is in a motor mode. The same effect is predicted from the simulation results in Fig. 3.23, where

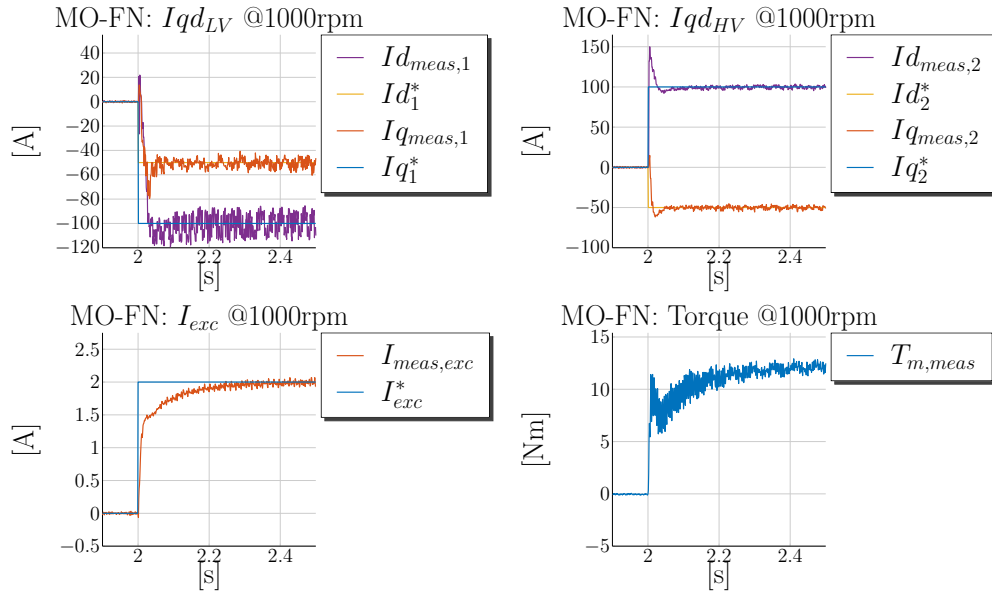


Figure 3.28 – Measurements @1000rpm: $i_{qs1} = -100$ A, $i_{ds1} = -50$ A, $i_{qs2} = 100$ A, $i_{ds2} = -50$ A and $i_{fd} = 2$ A MO with a FN

both sub-torque T_{e12V} and T_{e48V} are plotted. As the iron losses are not included in the model employed for the current controller tests, the simulated torques from Fig. 3.23 are overestimated. Inaccuracies in the torque prediction may be due to inaccuracies in the parametrization of the machine's main inductance. The physical principle for the energy transfer between both windings is however well described in the simulation thus thanks to the developed machine model.

A noticeable observation, evident from the presented measurements is, that the 12V q - and d -axis currents show significant noise in this case in comparison to the ones, where the 48V currents are controlled to zero. When both windings are energized and generate torque the electromagnetic interaction between the 48V and the 12V side is higher and additional high harmonic currents are induced into the 12V side.

3.2.9 Conclusion from the Simulation and Measurement Results

The presented simulations and measurements verify as well the presented model from Chapter 2 as the proposed controller tuning with the decoupling network from this chapter. The simulations correlate good with the measured dynamic responses and prove that the model includes the complex machine dynamics, which are characteristic for the dual-voltage machine.

Generally, the controllers behave as designed, which has been proven through the single control loop tests performed at 0rpm. During these tests, the control loop interactions

are minimized, the back-emf influence is eliminated and the settling behavior of the current controllers is as predicted by the MO tuning theory. The pre-calculated *rise times* and settling behavior are achieved and no overshoots are observed.

The control behavior deteriorates at speed and without any decoupling method the controllers need much more time to set the current reference. The performed simulations prove that the added back-emf static decoupling network improves the performance of the controllers such that the controllers achieve similar performance as during the same tests at 0 rpm. Although only one current reference is changed at a time the dynamic coupling is evident as a disturbance on the other current controllers.

Besides the single control loop tests also combined controller tests are performed as well in the simulation as on a test bench in order to check the control performance in different cases. During the combined controller tests the current references are changed simultaneously such that air-gap torques are generated by each of the windings. The combined controller tests demonstrate the complex machine dynamics, which are characterized by the interactions between both stator systems and the rotor. The performed tests are selected such, that the dual-voltage machine is operated in variations of its modes. For example, a torque production at one of the windings is recreated while the other is controlled to zero. The torque generation by both windings simultaneously is tested when they are operated in the same mode and in opposite modes.

The measured dynamic current responses during the combined controller tests correlate well with the simulations. Both prove that the 12V current controllers are less robust against disturbances caused by the 48V controllers. The 48V controller reaction to the set point changes at the 48V side cause non-negligible currents of the 12V side. This is confirmed through both simulations and measurements. The 12V current controllers are however still able to nullify the disturbances and no instability is caused. When both windings generate a motoring torque, the observed overshoots at the 12V side can be up to 100 %, because the control action from both q -axis controllers sums up and induces positive q -axis currents. On the other side, when both windings are operated in opposite modes, the controllers act against each other and the overshoots are minimized. The field winding current controller has much slower dynamics due to the high number of turns in the rotor. This results in settling times of around 30 m sec. In case the field winding is not pre-energized this is a limiting factor in the dynamics of the torque control generated by the machine.

Despite the fact that the current controllers influence each other and are highly coupled through the machine dynamics, the chosen tuning is robust enough to control the requested set points and the controllers do not become unstable. Besides the shown measurements and simulations in this chapter, many more were performed in an automated manner on a test bench, which proves further the stability of the controllers also during the combined tests. The proposed MO tuning with the decoupling network is this way verified and can be used further in the torque control development of the machine. Generally during the torque control the set points are not changed abruptly but rather ramped with a

pre-specified torque gradient. The torque gradient has to take into account the maximum possible dynamics that can be achieved by the underlying current control loops.

This subsection proved the robustness of the proposed tuning against control loop interaction caused due to the plant dynamics. However the measurement and simulation results showed also the drawbacks of conventional decoupling methods employed in the motor control despite their adaption to the dual-voltage machine. For this reason, the author introduces in Subsection 3.2.10 a new decoupling control method, which aims to decouple dynamically and statically the current controllers from each other taking into account the machine voltage equations.

Unfortunately the test bench was not available at this time of the project to verify this method on the machine prototype. In the authors' point of view the already presented simulations and measurements with the conventional decoupling show very well correlation and therefore it is naturally to assume that, if the new decoupling method shows promising results in the simulation environment, these are likely to correlate with measurements performed eventually in the future. The new decoupling method is derived based on the machine theory and verified in the simulation environment in Subsection 3.2.10.

3.2.10 Dynamic Decoupling

Despite the fact that the proposed MO tuning is proven to be robust enough during the combined controller tests, also the drawbacks of the conventional decoupling methods are obvious. It has to be noted, that an externally-excited salient-pole machine is employed as a dual-voltage machine, which makes the control loop interactions even stronger. The rotor flux is varied through the field winding current, which represents one more degree of freedom in the machine control. It is however also an additional winding, which is coupled with both stator systems. In contrast to that this is not the case for an IPM machine and an IM. Therefore the control of the dual-voltage externally-excited machine is a multi-variable control design problem.

Consequently, in order to counteract adequately the complex dynamic and static coupling between the current axis, a more general approach in the control design has to be sought. For this purpose the literature for multivariable control is studied and some of the practices are applied to the dual-voltage machine. Reference [65] offers a detailed and thorough presentation of the various design methods for multivariable control. A full literature review on this topic will go out of the scope of the current work. However a brief presentation of the theory behind the multivariable decoupling is presented before the control for the dual-voltage machine is derived. Reference “*Multiple input, multiple output process*” [53] presents a short review of MIMO control strategies and suggests the following approaches to deal with control loop interactions:

1. “Detune” one or more feedback controllers
2. select different manipulated or controlled variables

3. use decoupling or feed-forward control
4. design a full multivariable control

Point 1 has been already applied because the chosen bandwidth of the current controllers from Subsection 3.2.2 is conservative. The resulting PM from the MO tuning is above 80° and thus with enough phase reserve. Overshoots are caused only during the combined controller tests at speed, because the control loop interactions are not handled. Point 2 is at least for the torque control in the base speed range not an option because the currents are the controlled variables and are directly linked to the torque production. The voltages are also the only available variables, which can be manipulated. Point 3 is tested in Subsection 3.2.5 and shows good results in terms of improving the control performance at higher speeds during single controller tests. The strong dynamic coupling between the axis however cannot be decoupled with a DN or a FN and is evident in the performed simulations and measurements.

Point 4 is considered in this subsection. The idea is to design an additional controller, which “diagonalizes” the plant, such that the PI controllers “encounter” only transfer functions dependent on the variables to be controlled. Reference “*Decoupling of multiple-input-multiple-output systems*” [21] suggests the introduction of a plant pre-compensator matrix which decouples the plant. This subsection handles a new approach on decoupling of the stator current controllers with the aim to achieve dynamic and static decoupling between the stator current controllers.

The idea to add a **pre-compensator matrix** with additional controllers, which decouples the plant, is pursued. Such approaches for a full-decoupling of the plant are applied in chemical, flight and vehicle dynamics control engineering [65]. The interested reader is referred to reference “*Multivariable Feedback Control: Analysis and Design*” [65], which handles in detail the topic of multivariable control. The principle of the pre-compensator decoupling matrix is explained first on a simple Two-Input Two-Output (TITO) plant with a TITO controller, which is presented also in reference [21].

TITO Decoupling Example

The controllers and the plant are schematically illustrated in Fig. 3.29 for the case of a Two-Input Two-Output (TITO) system. The controllers and the plants are symbolically illustrated through transfer functions, such that the derivation of the decoupling control is held general. The plant is coupled between its paths through the transfer functions $G_{p,12}(s)$ and $G_{p,21}(s)$. Two decoupling controllers $D_{c,12}(s)$ and $D_{c,21}(s)$ are required to counteract the coupling in the plant. Analytic formulas for both decouplers are derived. For example, the decoupler $D_{c,21}(s)$ attempts to counteract the control loop interactions

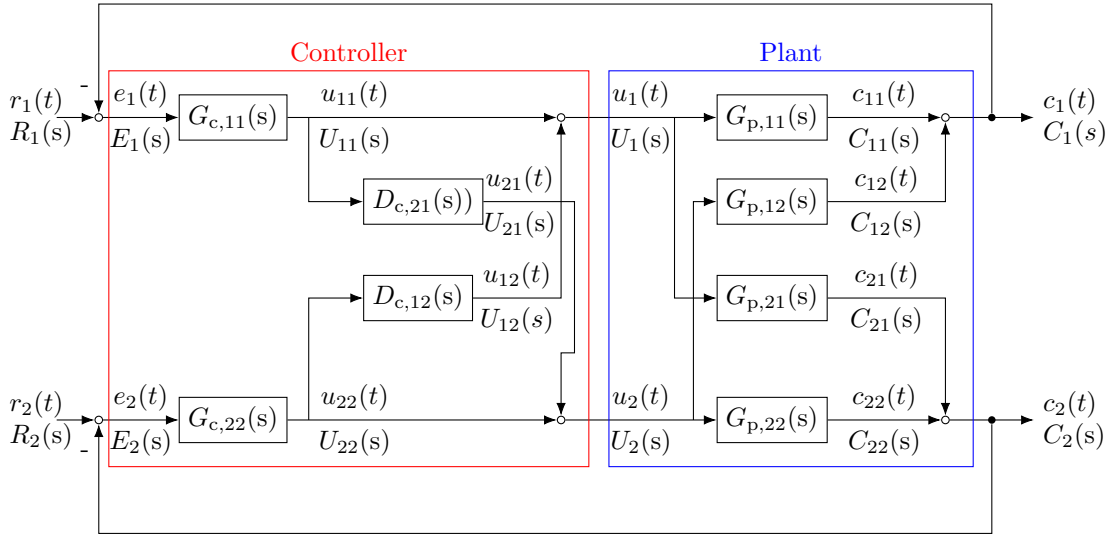


Figure 3.29 – Example a TITO Plant with Decoupling Controller

of $C_2(s)$ and $U_1(s)$ through the transfer function $G_{p,21}(s)$ at $G_{c,22}(s)$. The cancellation occurs at $U_2(t)$, if the condition in equation (3.2.10.1) is satisfied [21].

$$G_{p,21}(s)U_{11}(s) + G_{p,22}(s)D_{c,21}(s)U_{11}(s) = 0 \quad \rightarrow \quad D_{c,21}(s) = -\frac{G_{p,21}(s)}{G_{p,22}(s)} \quad (3.2.10.1)$$

Equation (3.2.10.1) defines the transfer function of the ideal decoupler $D_{c,21}(s)$. In an analogous way the formula for $D_{c,12}(s)$ is calculated and provided in equation (3.2.10.2).

$$D_{c,12}(s) = -\frac{G_{p,12}(s)}{G_{p,11}(s)} \quad (3.2.10.2)$$

Equations (3.2.10.1) and (3.2.10.2) prove that the decouplers can be designed, such that the plant is transformed into its diagonal form, before the diagonal controllers act on the manipulated variable. The decouplers can be arranged into a matrix, which is called a pre-compensator matrix. The term pre-compensator matrix is common in the literature about the MIMO control design. The name indicates that this matrix compensates the couplings in the plant before the controller acts on the manipulated variable.

The shown example of a TITO control system is illustrated through its single control loop interaction paths and the corresponding transfer functions in Fig. 3.29. From Fig. 3.29 is obvious that the diagram becomes hardly readable, when each connection and transfer function is separately drawn. This representation issue becomes even greater for a 5×5 multivariable system, which is the case of the dual-voltage machine. Therefore the matrix and vector representation in signal flow diagrams is used further for the derivation of the decoupling control for the dual-voltage machine.

The diagonal controllers are symbolically represented in a matrix named $\mathbf{G}_{c,\text{diag}}(s)$ and have the goal to control only one variable, for which they are designed for. The decoupling

controllers are arranged in another **pre-compensator matrix** named $\mathbf{P}_{\text{dyn}}(s)$. The arrangement of both controller matrices and the plant are schematically illustrated in Fig. 3.30. The full controller then consists of a multiplication by the diagonal controller $\mathbf{G}_{c,\text{diag}}(s)$ and the dynamic pre-compensator $\mathbf{P}_{\text{dyn}}(s)$. For matrices and vectors the multiplication sequence is very important and has to be performed from right to left referring the visualization in a signal flow diagram. The double lines in the figure denote a vector flow signal diagram. The matrices and vectors are drawn consistently in **bold** and can represent any $n \times n$ matrix or $n \times 1$ vector.

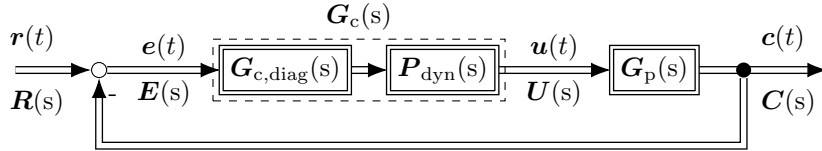


Figure 3.30 – Signal Flow Diagram of a Controller with a Pre-Compensator

Dynamic Decoupler for the Dual-Voltage Machine

The general control schematic from Fig. 3.30 is adapted to the dual-voltage machine and is redrawn in Fig. 3.31. In Fig. 3.31 the controller $\mathbf{G}_{c,\text{diag}}(s)$ stands for a matrix representing the PI controllers in a diagonal form and the decoupler $\mathbf{P}_{\text{dyn}}(s)$ is the **pre-compensator matrix**, which diagonalizes the plant. The controller matrix $\mathbf{G}_{c,\text{diag}}(s)$ consists of the transfer functions of the PI controllers. Its outputs are the voltage commands generated by the PI controllers denoted in the figure through the vector $\mathbf{v}_{s,\text{qd},12\text{f}}(t)_{\text{PI}}$. Then the PI voltage vector is multiplied by the pre-compensator matrix to calculate the final voltage commands required to set the reference currents.

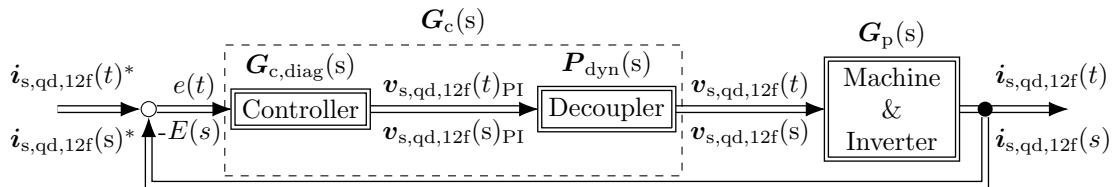


Figure 3.31 – Current Control Signal Flow Diagram with a Pre-Compensator

If a perfect decoupling can be applied to the dual-voltage machine, the plant becomes purely diagonal and each controlled variable depends only on its corresponding manipulated variable. For example the output from the PI controller for i_{qs1} should be able to adjust only the i_{qs1} current through its output voltage and should not influence the other currents. A decoupler for the plant model $\mathbf{G}_p(s)$, representing the dual-voltage machine, is searched, which transforms the plant into the diagonal matrix from equation (3.2.10.3). The diagonal matrix is assumed to be the plant model. The MO tuning in the

previous subsection is designed according this plant model. This is also the state of the art assumption in the electric drive control theory books [16, 63]. All other couplings between the axis are handled usually through decoupling networks. The searched matrix $\mathbf{P}_{\text{dyn}}(s)$ is multiplied with the full plant model represented by the matrix $\mathbf{G}_p(s)$, such that the diagonal $\mathbf{G}_{p,\text{diag}}(s)$ matrix from equation (3.2.10.3) is derived. Equation (3.2.10.4) is valid for the relationship between $\mathbf{G}_p(s)$ and $\mathbf{G}_{p,\text{diag}}(s)$. In order to find the **pre-compensator matrix** the equation is multiplied by the inverse plant matrix $\mathbf{G}_p^{-1}(s)$ from its left side. Then the **pre-compensator matrix** is equal to the multiplication of the diagonal plant model matrix $\mathbf{G}_{p,\text{diag}}(s)$ with the inverse plant model matrix $\mathbf{G}_p^{-1}(s)$. The inverse plant matrix $\mathbf{G}_p^{-1}(s)$ is already known from equation (3.2.1.7).

$$\mathbf{G}_{p,\text{diag}}(s) = \text{diag} \left[\left(r_{s1} + s(L_{ls1} + L_{qq1}) \right)^{-1}, \left(r_{s1} + s(L_{ls1} + L_{dd1}) \right)^{-1}, \right. \\ \left. \left(r_{s2} + s \left(L_{ls2} + \frac{L_{qq1}}{N_{s12}^2} \right) \right)^{-1}, \left(r_{s2} + s \left(L_{ls2} + \frac{L_{dd1}}{N_{s12}^2} \right) \right)^{-1}, \left(r_f + s \left(L_{lf} + \frac{2L_{dd1}}{3N_{s1f}^2} \right) \right)^{-1} \right] \quad (3.2.10.3)$$

$$\mathbf{G}_{p,\text{diag}}(s) = \mathbf{G}_p(s) \cdot \mathbf{P}_{c,\text{dyn}}(s) \Rightarrow \mathbf{P}_{c,\text{dyn}}(s) = \mathbf{G}_p^{-1}(s) \cdot \mathbf{G}_{p,\text{diag}}(s) \quad (3.2.10.4)$$

Because the multiplication of both matrices, $\mathbf{G}_p^{-1}(s)$ and $\mathbf{G}_{p,\text{diag}}(s)$, is tedious, it is performed with the Matlab Symbolic Toolbox and the result is provided in equation (3.2.10.5).

$$\mathbf{P}_{c,\text{dyn}}(s) = \begin{bmatrix} 1 & \frac{\omega_e(L_{dd1} + L_{ls1})}{(R_{s1} + sL_{dd1} + sL_{ls1})} & \frac{L_{qq1}N_{s12}s}{sL_{qq1} + N_s 12^2 R_{s2} + sL_{ls2}N_{s12}^2} \\ \frac{-\omega_e(L_{ls1} + L_{qq1})}{R_{s1} + L_{ls1}s + L_{qq1}s} & 1 & \frac{-L_{qq1}N_{s12}\omega_e}{L_{qq1}s + N_{s12}^2 R_{s2} + L_{ls2}N_{s12}^2 s} \\ \frac{L_{qq1}s}{N_{s12}(R_{s1} + L_{ls1}s + L_{qq1}s)} & \frac{L_{dd1}\omega_e}{N_{s12}(R_{s1} + L_{dd1}s + L_{ls1}s)} & 1 \\ \frac{-L_{qq1}\omega_e}{N_{s12}(R_{s1} + L_{ls1}s + L_{qq1}s)} & \frac{L_{dd1}s}{N_{s12}(R_{s1} + L_{dd1}s + L_{ls1}s)} & \frac{-\omega_e(L_{ls2}N_{s12}^2 + L_{qq1})}{L_{qq1}s + N_{s12}^2 R_{s2} + L_{ls2}N_{s12}^2 s} \\ 0 & \frac{L_{dd1}s}{N_{s1f}(R_{s1} + L_{dd1}s + L_{ls1}s)} & 0 \\ \frac{L_{dd1}N_{s12}\omega_e}{N_{s12}^2 R_{s2} + L_{dd1}s + L_{ls2}N_{s12}^2 s} & \frac{2L_{dd1}N_{s1f}\omega_e}{2L_{dd1}s + 3N_{s1f}^2 R_f + 3L_{lf}N_{s1f}^2 s} & \\ \frac{L_{dd1}N_{s12}s}{L_{dd1}s + N_{s12}^2 R_{s2} + L_{ls2}N_{s12}^2 s} & \frac{2L_{dd1}N_{s1f}s}{2L_{dd1}s + 3N_{s1f}^2 R_f + 3L_{lf}N_{s1f}^2 s} & \\ \frac{\omega_e(L_{ls2}N_{s12}^2 + L_{dd1})}{L_{dd1}s + N_{s12}^2 R_{s2} + L_{ls2}N_{s12}^2 s} & \frac{2L_{dd1}N_{s1f}\omega_e}{N_{s12}(2L_{dd1}s + 3N_{s1f}^2 R_f + 3L_{lf}N_{s1f}^2 s)} & \\ 1 & \frac{2L_{dd1}N_{s1f}s}{N_{s12}(2L_{dd1}s + 3N_{s1f}^2 R_f + 3L_{lf}N_{s1f}^2 s)} & \\ \frac{L_{dd1}N_{s12}s}{N_{s1f}(L_{dd1}s + N_{s12}^2 R_{s2} + L_{ls2}N_{s12}^2 s)} & 1 & \end{bmatrix} \quad (3.2.10.5)$$

The matrix from equation (3.2.10.5) is characteristic through its diagonal elements equal to 1. This means that the outputs from the PI controllers act straight to their own axis and the off-diagonal elements describe how the other PI controllers contribute to the control of the specific current. For example, for the control of current i_{qs1} the output of the PI current controller i_{qs1} acts straight to the output voltage, v_{qs1} , which is denoted by

the 1 at the very first position $(1,1)$ in the matrix $\mathbf{P}_{\text{dyn}}(s)$. The other PI current controller outputs for the remaining currents, $i_{\text{ds}1} \dots i_{\text{fd}}$, act to the output voltage $v_{\text{qs}1}$ through the off-diagonal terms in the first row of the matrix $\mathbf{P}_{\text{dyn}}(s)$ $(1,2)\dots(1,5)$. The remaining PI controller outputs are each multiplied by the corresponding matrix entry from $\mathbf{P}_{\text{dyn}}(s)$ and then summed up with the output from the PI controller for $i_{\text{qs}1}$ to generate the final control voltage $v_{\text{qs}1}$. This way the control action of each PI controller acts not only on its own axis but also through the off-diagonal terms to the other axis to eliminate the possible coupling, which would result from change of the PI controller output.

Then, the full control matrix consists of the diagonal PI controllers matrix $\mathbf{G}_{\text{c,diag}}(s)$ multiplied by the DDM **pre-compensator matrix** $\mathbf{P}_{\text{dyn}}(s)$ as shown in equation (3.2.10.6).

$$\mathbf{G}_{\text{c}}(s) = \mathbf{P}_{\text{dyn}}(s) \cdot \overbrace{\frac{\omega_{\text{b}}}{s} \cdot \mathbf{G}_{\text{p,diag}}(s)^{-1}}^{\mathbf{G}_{\text{c,diag}}(s)=\text{PI Controllers}} \quad (3.2.10.6)$$

The **pre-compensator matrix** consists of machine specific parameters. The off-diagonal terms depend on the machine inductances, the resistances and the turn ratios. Further, some of the terms depend on the speed and the Laplace operator s and represent a machine parameter and speed dependent low pass filter. One example for this type of decoupling terms is the second term in the first row of the matrix $\mathbf{P}_{\text{dyn}}(s)_{(1 \times 2)}$, where a speed and machine parameter dependent low pass filter is formed. This type of decoupling element counteracts the static back-emf coupling in the plant. Another filter type, noticeable in the transfer functions of the **pre-compensator matrix**, is the high pass filter, which is used to counteract the dynamic coupling between the current axis and does not include speed dependent terms. An example for this filter type is the third entry in the first row of the matrix $\mathbf{P}_{\text{dyn}}(s)_{(1 \times 3)}$. The described transfer function is a high pass filter with a certain gain. Both, the corner frequency and the gain, depend on the machine parameters. This filter type counteracts the dynamic coupling between the current axis. Both filter types are evident along the whole **pre-compensator matrix**. From these observations it can be concluded, that the performance of the presented decoupling matrix depends on the accuracy of the machine parameters. This is not surprising, because the MO tuning does also depend on the machine parameters and in case of inaccuracies in the inductance measurement the control performance is negatively influenced.

With the derivation of the dynamic decoupler from equation (3.2.10.4) the pre-compensator matrix for the dual-voltage machine is derived in theory. The next step is to verify the new controller in a simulation environment. For this purpose the decoupling matrix has to be brought into a discrete form and implemented in the Simulink control software. The basic components of the matrix are low-pass filters and differentiators in time, because the high-pass filter can be represented as a differentiator multiplied by a low-pass filter. The discrete form of the low pass filter is shown in equation (3.2.10.7) and the discrete differentiator is shown in equation (3.2.10.8).

$$y(t) = \frac{1}{\frac{T}{T_s} + 1} \left[K u(t) + \frac{T}{T_s} y(t-1) \right] \quad (3.2.10.7)$$

$$y(t) = \frac{u(t) - u(t-1)}{T_s} \quad (3.2.10.8)$$

The factor K from equation (3.2.10.7) is the filter gain, T is the filter time constant and T_s is the filter sample time. Further details about the discrete implementation of the decoupling matrix from equation (3.2.10.5) are omitted at this stage. The work behind the implementation is laborious but straight forward and can be recreated with the already provided information. Therefore the next paragraph focuses on the simulation results with the new controller.

Simulation Results with the Dynamic Decoupling

The combined controller tests performed in the simulation environment in Subsection 3.2.4 and verified with the measurements presented in Subsection 3.2.8 are reproduced in this subsection to test the new decoupling control.

First, the set point changes at the 12V current controllers are performed and the 48V currents are controlled to zero. The current i_{qs1} is set to 100 A, the current i_{ds1} is controlled to -50 A and the field winding current is adjusted to 2 A at a speed of 1000 rpm. Figure 3.32 shows the simulation results. The settling of the q - and d -axis 12V currents is very neat with an overshoot of around 5 to 10 %, which corresponds to the MO tuning of the PI controllers. There are no induced currents at the 48V side noticeable and the field winding is also set properly. A note should be made at this stage, that the decoupling of the stator to rotor winding is not included in the simulation. This means that the last row of the **pre-compensator matrix** from equation (3.2.10.5) is set to zero, except for the diagonal element (5×5) , which represents the feed-through of the field winding PI controller. This means that the dynamic d -axis coupling from the 12V and 48V stator to rotor is not counteracted. The reason for this is clarified later on. The rotor to stator decoupling, represented through the right-most column of the matrix $\mathbf{P}_{\text{dyn}}(s)$, is however included.

In contrast to this result, the performed simulation with the back-emf decoupling for this case, illustrated in Fig. 3.20, showed 60 % overshoot for the q -axis controller and a 25 % for the d -axis controller. The induced currents at the 48V side show a magnitude of around 45 A. The corresponding measurement from Fig. 3.25 shows an overshoot of 75 % for the q -axis controller, 25 % for the d -axis controller and induced currents at the 48V side of up to 50 A. The new controller clearly surpasses the performance of the conventional decoupling method.

3.2 Current Control for the Dual-Voltage Machine

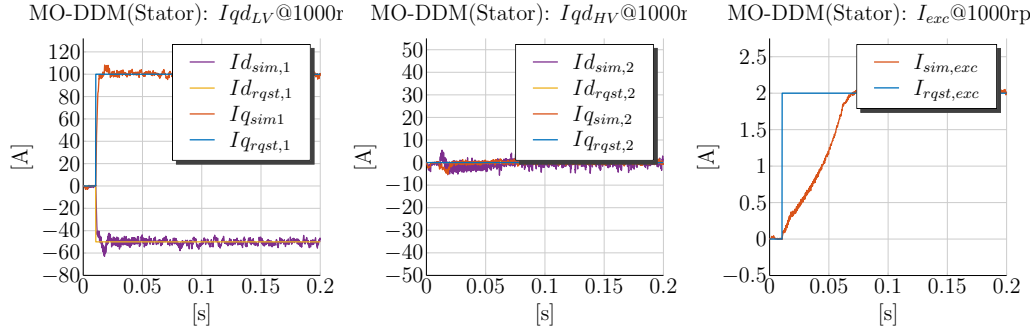


Figure 3.32 – Simulation @1000rpm: $i_{qs1} = 100$ A, $i_{ds1} = -50$ A, $i_{qs2} = 0$ A, $i_{ds2} = 0$ A and $i_{fd} = 2$ A MO with a DDM (Stator) $L(I_{rqst})$

The next simulated case is a torque production through the 48V winding and a zero current control at the 12V winding. The currents i_{qs2} , i_{ds2} and i_{fd} are set to 100 A, -50 A and 2 A respectively. Figure 3.33 shows the simulation results. The q - and d -axis 48V currents are controlled properly with slight overshoots around 5 to 10%. The 12V current controllers remain undisturbed during the set point change. The field winding current is controlled in a similar manner as in the previous case. It is noticeable at the beginning of the set point change that the field winding current rises faster than in the previous experiment because the 48V d -axis stator current is changed to the negative and the dynamic decoupling is not included in the control of the field winding.

On the other side, the simulations performed with the conventional decoupling method from Fig. 3.21 show an 40% overshoot for the q -axis controller and induced currents of up to 75 A at the 12V side. Figure 3.26 shows the measurement results from this case. The overshoot in the q -axis 48V current is around 50% and the induced currents at the 12V side are up to 125 A for the q -axis and 40 A for the d -axis. Also in this case the dynamic decoupling method outpaces in its performance the back-emf decoupling.

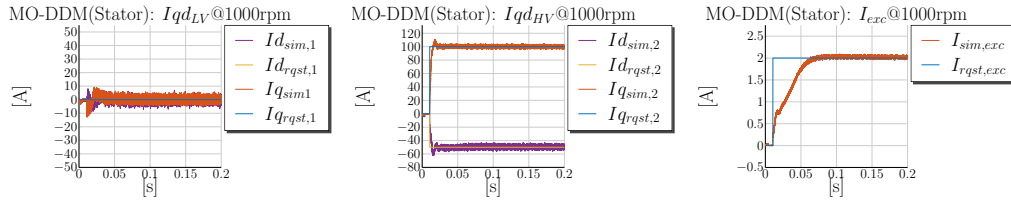


Figure 3.33 – Simulation @1000rpm: $i_{qs1} = 0$ A, $i_{ds1} = 0$ A, $i_{qs2} = 100$ A, $i_{ds2} = -50$ A and $i_{fd} = 2$ A MO with a DDM (Stator) $L(I_{rqst})$

The next simulated case is a motoring torque production through both stator windings. The q -axis currents are set to 100 A, the d -axis currents to -50 A and the field winding to 2 A. Figure 3.34 shows the simulation results. All four stator current controllers set fast the requested reference values. The overshoot of the 12V current controllers is around 20% and the overshoot of the 48V current controllers is 10%. It seems that the 12V

current controller is still affected through the step point changes at the 48V side. This could lie in the fact that the new decoupling control is solely based on the linearized voltage equations of the machine and the machine model also includes the cross-coupling between L_{dd} and L_{dq} inductances and the saturation of the main inductance. Despite this very small deviation the 12V controller performs very well and the dynamic decoupling contributes to the fast settling time without big overshoots.

The contribution of the dynamic decoupling is made obvious, when this result is compared to the results from Fig. 3.22, where a back-emf decoupling is employed. The overshoot for the 12V q -axis current controller is 60% and the one for the 48V q -axis controller is 40%. The measurements from this case are illustrated in Fig. 3.27. The overshoot for the q -axis 12V controller is 100% and for the q -axis 48V controller 60%.

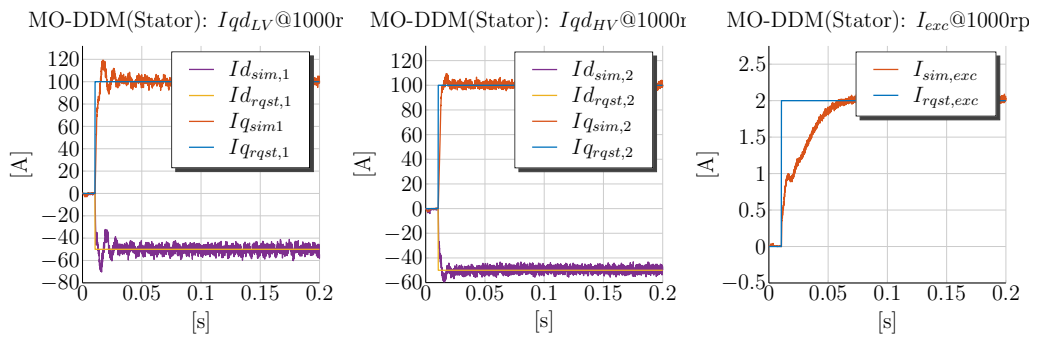


Figure 3.34 – Simulation @1000rpm: $i_{qs1} = 100$ A, $i_{ds1} = -50$ A, $i_{qs2} = 100$ A, $i_{ds2} = -50$ A and $i_{fd} = 2$ A MO with a DDM (Stator) $L(I_{rqst})$

The last case, tested with the dynamic decoupling, is a negative torque production at the 12V winding and a positive torque at the 48V winding. The 12V currents are set to $i_{qs1} = -100$ A and $i_{ds1} = -50$ A. The 48V currents are set to $i_{qs2} = 100$ A and $i_{ds2} = -50$ A and the field winding to 2 A. Figure 3.35 shows the simulation results. The results are identical to the ones from the previous experiment. The 12V current controllers show overshoots of around 20% and the 48V ones of around 10%. The pre-compensator matrix together with the diagonal controller achieves very good performance also in this combined mode.

Figure 3.23 shows the corresponding simulation results with the back-emf decoupling and Fig. 3.28 shows the corresponding measurements. Also in this case the new decoupling method excels the conventional decoupling. In the author's point of view, further comparison and analyses between the dynamic decoupler and the back-emf decoupling are surplus. The dynamic decoupling shows promising results in the simulation and the same is expected for eventual test bench measurements. This expectation is justified, because the machine model is already verified through the comparison between simulation and measurements from Subsections 3.2.4 and 3.2.8.

At last, the reason for not including the dynamic decoupling from both stators to the rotor is explained. Simulations with this decoupling has been also performed, however

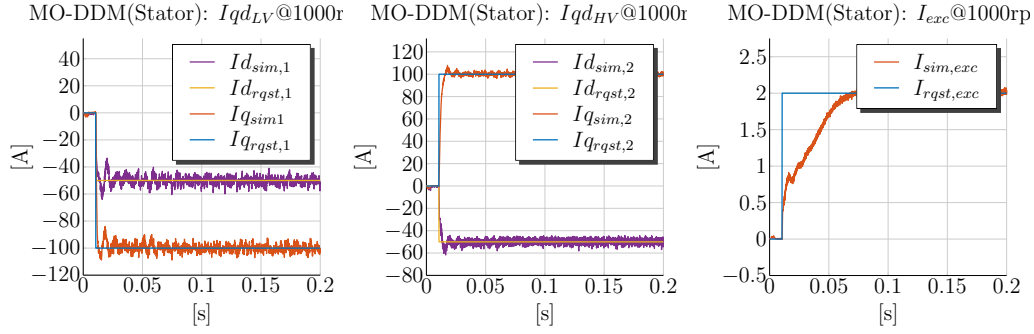


Figure 3.35 – Simulation @1000rpm: $i_{qs1} = -100$ A, $i_{ds1} = -50$ A, $i_{qs2} = 100$ A, $i_{ds2} = -50$ A and $i_{fd} = 2$ A MO with a DDM (Stator) $L(I_{rqst})$

high distortion in the field winding current and also no cancellation effect of the dynamic coupling from stator to rotor are observed. This is due to the fact, that the decoupling voltage terms $P_{c,dyn}(s)_{(5,2)}$ and $P_{c,dyn}(s)_{(5,4)}$ from equation (3.2.10.5) exceed the limit of the voltage source used to supply the field winding. The voltage source is the same source as for the 48V winding. In order to demonstrate this, the decoupling voltages from the last studied case, corresponding to the plotted currents from Fig. 3.35, are shown in Fig. 3.36.

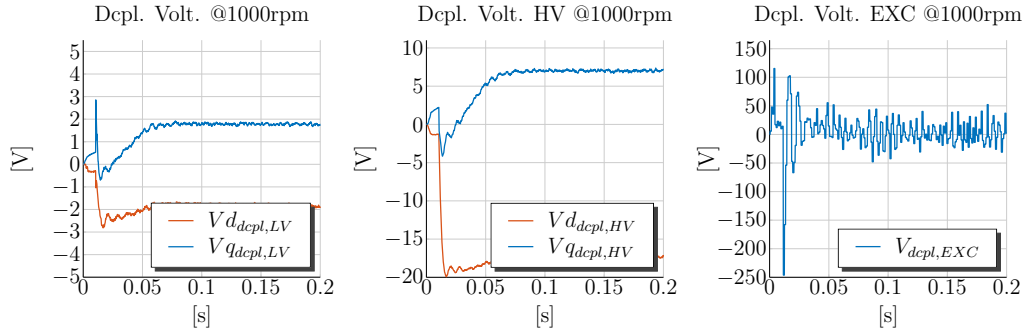


Figure 3.36 – Simulation @1000rpm: $i_{qs1} = -100$ A, $i_{ds1} = -50$ A, $i_{qs2} = 100$ A, $i_{ds2} = -50$ A and $i_{fd} = 2$ A MO with a DDM (Stator) $L(I_{rqst})$

In the first plot from Fig. 3.36 the decoupling voltages for the 12V stator are shown. It is evident how the dynamic decoupling takes place at the set point change of both stator currents, while the back-emf (static) decoupling is compensated afterwards with the rising field winding current. The same holds also for the decoupling voltages for the 48V stator plotted in the middle. The right-most plot from Fig. 3.36 shows the calculated decoupling voltage for the field winding current. The decoupling voltage, which is required to counteract the disturbance from the stator PI controllers, exceeds the maximum possible DC link voltage by couple of magnitudes. The dynamic decoupling could succeed if the employed voltage source for the field winding is much greater than 48V. In fact, the voltage source needs to be scaled according to the rotor to stator effective

number of turns N_{sf1} , so that the proposed decoupling could counteract the coupling from stator to rotor. This statement can be proven through a simple calculation presented through equation (3.2.10.9). For example a change in the 12V d -axis current i_{ds1} of 200 A within 5 msec results in a voltage change of approx. 150 V at the field winding. The calculation is held simple and only unsaturated inductance values are used. This coupling voltage cannot be compensated through the source, which is limited through the maximum available DC link voltage at the 48V side.

$$\Delta v_{ind,f} = \frac{\Delta i_{ds1}}{\Delta t} \frac{2}{3} L_{dd1} N_{sf1} = \frac{\Delta 200}{\Delta 0.005} \cdot \frac{2}{3} \cdot 1.016 \cdot 10^{-5} \cdot 570 = 154 \text{ V} \quad (3.2.10.9)$$

However, since the 12V and 48V side both have suitable voltage sources for their operating ranges the decoupling in both stator systems works very well. From the other plots of the decoupling voltages is visible how the decoupling consists of a dynamic part and a back-emf part.

Conclusions for the Dynamic Decoupling Control

The performed simulations verify the proposed new decoupling method. The decoupling method is derived from the linear dual-voltage machine model and is verified in the simulation with a model, which includes saturation and cross-coupling. The dynamic decoupler shows outstanding results in comparison to the state of the art decoupling methods with feedback (post-active) action. No overshoots are present during the combined controller tests with the new pre-compensator dynamic decoupling matrix, which lies in contrast to the results achieved with the back-emf decoupling.

One drawback is observed during the tests. The field winding is supplied with the same voltage source as the 48V side and therefore a full decoupling control in the field winding control cannot be achieved. This issue is however not a drawback of the presented dynamic decoupling method, but a peculiarity in the field winding supply of the dual-voltage machine topology in order to make the machine topology cost effective.

As mentioned before at this time of the project the test bench was not available to confirm the proposed new decoupling control with the machine prototype. The fact, that the performed simulations and measurements from Subsections 3.2.4 and 3.2.8, show good correlation to each other, leaves no doubt that measurements performed in the future are expected to show the same good correlation with the performed simulations in the current subsection.

4 Torque and Power Control Development

This chapter discusses the outer control loop of the cascade control for the dual-voltage machine. The outer control loop has the task to control the torque or the power of both windings of the machine.

First, the state of the art torque control principle for the Externally-Excited Synchronous Machine (EESM) with one voltage level is explained. The control for an EESM is not well documented in literature. On the other hand the control for an IPM machine has good research records. Therefore, the principles from the torque control for an IPM machine are adopted and extended to the specifics of the EESM. Some of the common control strategies in the BS range and in the field weakening area are reviewed and briefly explained. The Maximum Torque-per-Ampere (MTPA) control principle is a state of the art torque control method employed in the BS range of an IPM. The MTPA strategy is well documented in the scientific literature. The MTPA control method is adapted to the EESM and the rotor losses are taken also into account. Then, a new optimal current trajectory, described with a new abbreviation, Maximum Torque-per-Copper Losses (MTPCL), is derived through mathematical formulas and visualized in the 2D (i_{ds}, i_{qs})- and 3D (i_{ds}, i_{qs}, i_{fd})-planes. The MTPCL method is adapted for the dual-voltage machine and implemented in the second part of this chapter. The Maximum Torque-per-Voltage (MTPV) method is also briefly presented as a torque control principle in the field weakening area. The MTPV control considers the voltage limits and achieves a torque control in the field weakening area.

The operation of the dual-voltage machine requires the control of both air-gap torques. For this purpose a non-linear optimization problem, which minimizes the machine losses, is set and solved numerically. The torque control is developed for the BS range based on the offline calculated operating points. The developed torque control is verified based on the developed machine model in the simulation environment. Afterwards the torque control is verified also on the test bench. The measurement results are compared against the simulation results. The measurements show that ignoring the iron-losses for the claw-pole dual-voltage machine during the calculation of the operating points leads to significant deviations between predicted torque and measured one. This is in contrast to an IPM machine. For IPM machines the iron losses are often not included in the working points calculation.

In the FW mode a new Voltage Angle Control (VAC) is developed. A transition mechanism for switching between both control regions, the FOC and the VAC, is developed based on the modulation indices at the 12V and 48V sides. The new VAC and the switching

mechanism are verified in the simulation environment with the machine model. The FW control is tested also on the test bench.

4.1 Torque Control - State of the Art

The employed torque control strategies are generally different for two characteristic control areas of the machine. The first control region is characterized with the fact that the maximum available DC current is the only limiting factor for the torque production of the machine and is denoted as the Base Speed (BS) range. The employed control strategies in this region attempt to minimize the machine losses considering the requested torque as a boundary **equality** condition and the maximum available DC current as a boundary **inequality** condition. For most of the torque reference points the maximum available DC current is not a binding condition in the optimization problem and thus is often excluded from the problem formulation. The torque **equality** condition is always binding and thus included in the optimization. One of the most well known torque control strategies is the MTPA control. The machine copper losses make up around 70 to 80 % of the whole machine losses, hence a certain torque request generation with minimum possible stator current is considered to be optimal and efficient. Therefore this strategy in the BS range of the machine is called the Maximum Torque-per-Ampere (MTPA) method [63].

The second control region starts at higher speed and is characterized through the fact that the maximum available DC voltage is the main limiting factor for the torque production of the machine. The maximum available DC current limit has to be also considered in this region, but is for the majority of the working points not the binding factor and thus often eliminated in the problem formulation. This machine operating region is called the Field Weakening (FW) area. In this region, the back-emf voltage generated through the rotor flux has to be counteracted through a negative d -axis current in a PM machine. This way the machine's air-gap flux is weakened. This is required, because the generated back-emf voltage has to be reduced below the DC limit. Through this action enough voltage margin for the settling of the q -axis current is left, which is the main torque building current component. The speed, at which the transition from BS to FW region occurs, is called the machine's *corner speed* ¹.

In the following two subsections a brief literature review for the outlined control strategies in the BS and FW area is conducted. The MTPA control method, applied to the IPM machines, is explained and the MTPCL control for an EESM with one voltage level is

¹The *corner speed* is fixed for the IPM machines. The EESM can actually have multiple corner speeds, because the rotor flux is generated through the varying field winding current and thus the DC link voltage is exceeded at different speeds, when the field winding current is not constant. However, also for this machine type the *corner speed* is characterized as the speed, where the generated back-emf voltage exceeds the rated DC voltage source limit, when field winding is supplied with maximum continuous current.

afterwards derived. In Subsection 4.1.1 the MTPA and MTPCL torque control methods for the BS range are explained as an introduction into the optimal control problem formulation for the dual-voltage machine. In Subsection 4.1.2 the MTPV as a FW control method is explained for the EESM machine.

4.1.1 Torque Control in the Base Speed Range for an Externally-Excited Synchronous Machine

A certain torque of an IPM or an EESM machine can be set through a variety of possible operating points. Despite the fact that the EESM has one more Degree-of-Freedom (DOF) in comparison to the IPM machine, the torque control of the EESM is in its basic principles very similar to the one of the IPM machine. Both have a synchronous torque component and a reluctance torque component, which contribute to the whole torque generation. The goal of the employment of a rotor winding is to be able to magnetize fully the rotor with relatively low currents and thus low losses. Therefore it is desirable to magnetize the rotor through the field winding due to the high number of turns in the rotor. In some cases of small requested torque values in the BS range it is more efficient to reduce the field winding current and not fully saturate the rotor. The field winding current reference has to be considered in the optimal choice of the working points. This makes the selection of the optimal current points a three-dimensional search problem and therefore difficult to visualize. On the other hand the torque control of the IPM machine is achieved through only two currents, i_{qs} and i_{ds} , and is appropriate to exemplify the torque control derivation based on a graphic.

In order to define the torque control problem in the BS range, the torque equation of the EESM is considered as shown in equation (4.1.1.1). Depending on the machine inductances, L_d and L_q , a certain torque can be set through various combination of i_{qs} , i_{ds} and i_{fd} . The claw-pole externally-excited machine has a synchronous torque component, which results from the interaction of the flux produced by the field winding current and the q -axis stator current. The reluctance torque component results from the difference between the reluctance paths along the d - and q -axis and thus from the difference in the L_d and L_q inductances. The field winding current is referred from the rotor to the stator with the winding ratio $N_{sf2} = 139$ scaled with the factor of $\frac{2}{3}$ due to the d - q transformation. The referred d -axis inductance L'_{fd} from equation (4.1.1.1) is equal to the d -axis inductance L_d .

$$T_e = \frac{3}{2} \cdot p \cdot (L'_{fd} \cdot i'_{fd} \cdot i_q + (L_d - L_q) \cdot i_d \cdot i_q) \quad (4.1.1.1)$$

The optimal torque control for an IPM machine requires the selection of the stator currents i_{qs} and i_{ds} such that the losses are minimized [10, 16]. In order to explain the MTPA control based on the EESM torque equation, the field winding current i_{fd} is assumed to be fixed at 2 A. This way the torque control for the EESM is transformed into an optimal control problem for an IPM machine because the rotor flux is fixed. Two

constant torque curves are plotted in Fig. 4.1 based on equation (4.1.1.1) for a fixed field winding current of 2 A. As an example values for the d - and q -axis inductances the unsaturated values from Table 2.1 are used. The inductances are parametrized with the values: $L_{md2} = 197,1 \mu\text{H}$ and $L_{mq2} = 150 \mu\text{H}$. The inductances, L_d and L_q , are set for the sense of example to $\frac{2}{3}$ of their unsaturated values, so that the plotted curves do consider some effect of the saturation. The saturation behavior of the inductances results from the interaction of all three currents, i_{ds} , i_{qs} and i_{fd} , and therefore this simplified assumption is not true for a real machine. This assumption is used only for the purposes of explaining the torque control method. Besides the constant torque curves also two constant current vector lines are plotted in Fig. 4.1. It is evident that the optimal current vector is found when both curves, the constant torque curve and the current vector circle, are tangent to each other. Then the condition, that a certain torque value is set through minimum current, is met. This automatically leads to the minimization of the stator copper losses for the machine, which are shown in equation (4.1.1.2).

$$P_{\text{co}} = \frac{3}{2} \cdot r_s \cdot (i_{\text{qs}}^2 + i_{\text{ds}}^2) \quad (4.1.1.2)$$

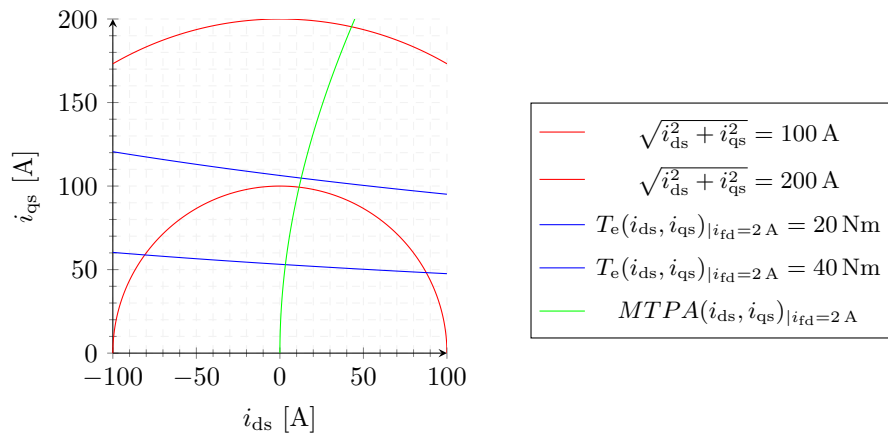


Figure 4.1 – Constant Torque Curves and Constant Current Curves

The illustrated condition that both curves, the torque curve and the current vector circle from Fig. 4.1, have to be tangent to each other can be mathematically formulated. The optimal torque control problem is set up through equation (4.1.1.3). The stator current losses have to be minimized with respect to the torque boundary condition shown in equation (4.1.1.3). The requested torque according to the optimal problem from equation (4.1.1.3) is always set with minimum possible DC current. In the practice the optimal control problem is solved numerically and the optimal currents are stored in a LUT. The found working points are afterwards filtered out such that the torques, which exceed the

maximum possible current limit, are not allowed. Therefore this condition is omitted in the further considerations for the optimal control problem formulation.

$$\begin{aligned}
 & \text{minimize} && P_{\text{co}}(i_{\text{ds}}, i_{\text{qs}}) = \frac{3}{2} \cdot r_{\text{s}} \cdot (i_{\text{qs}}^2 + i_{\text{ds}}^2) \\
 & \text{subject to} && T_{\text{e}}(i_{\text{ds}}, i_{\text{qs}})_{|T_{\text{e}}^*} = \frac{3}{2} \cdot p \cdot (L'_{\text{fd}} \cdot i'_{\text{fd}} \cdot i_{\text{q}} + (L_{\text{d}} - L_{\text{q}}) \cdot i_{\text{d}} \cdot i_{\text{q}}) - T_{\text{e}}^* = 0
 \end{aligned} \tag{4.1.1.3}$$

The optimization problem from equation (4.1.1.3) can be solved through the Lagrangian method. For this purpose the Lagrange function is set up in equation (4.1.1.4) [56].

$$\mathcal{L}(i_{\text{ds}}, i_{\text{qs}}, \lambda) = P_{\text{co}}(i_{\text{ds}}, i_{\text{qs}}) + \lambda \cdot T_{\text{e}}(i_{\text{ds}}, i_{\text{qs}})_{|T_{\text{e}}^*} \tag{4.1.1.4}$$

The new variable λ is called the Lagrange multiplier. In the optimization problem, a point is searched, described by the triplet $(i_{\text{ds}0}, i_{\text{qs}0}, \lambda_0)$, for which the gradients of both functions are parallel to each other and the boundary condition is still fulfilled. The Lagrange multiplier is required, because the gradients of both functions have to be parallel to each other but can have different lengths. This is equivalent to the condition that the contours of both functions, $P_{\text{co}}(i_{\text{ds}}, i_{\text{qs}})$ and $T_{\text{e}}(i_{\text{ds}}, i_{\text{qs}})$, are tangent to each other and the torque is equal to the searched reference value. This is represented mathematically through the solution of the system of equations defined in equation (4.1.1.5) [56].

$$-\nabla_{i_{\text{ds}}, i_{\text{qs}}, \lambda} \mathcal{L}(i_{\text{ds}}, i_{\text{qs}}, \lambda) = 0 \quad \Leftrightarrow \quad \begin{cases} \nabla_{i_{\text{ds}}, i_{\text{qs}}} P_{\text{co}}(i_{\text{ds}}, i_{\text{qs}}) = \lambda \cdot \nabla_{i_{\text{ds}}, i_{\text{qs}}} T_{\text{e}}(i_{\text{ds}}, i_{\text{qs}})_{|T_{\text{e}}^*} \\ T_{\text{e}}(i_{\text{ds}}, i_{\text{qs}})_{|T_{\text{e}}^*} = 0 \end{cases} \tag{4.1.1.5}$$

The gradient of the Lagrange function is calculated based on the stator copper losses and the torque from equation (4.1.1.3). The result is shown in equation (4.1.1.6).

$$\nabla_{i_{\text{ds}}, i_{\text{qs}}, \lambda} \mathcal{L}(i_{\text{ds}}, i_{\text{qs}}, \lambda) = \begin{cases} 3r_{\text{s}}i_{\text{ds}} + \lambda \frac{3}{2}p(L_{\text{d}} - L_{\text{q}})i_{\text{qs}} & = 0 \\ 3r_{\text{s}}i_{\text{qs}} + \lambda \frac{3}{2}p(L'_{\text{fd}}i'_{\text{fd}} + (L_{\text{d}} - L_{\text{q}})i_{\text{ds}}) & = 0 \\ \frac{3}{2}p(L'_{\text{fd}} \cdot i'_{\text{fd}} \cdot i_{\text{qs}} + (L_{\text{d}} - L_{\text{q}}) \cdot i_{\text{ds}} \cdot i_{\text{qs}}) - T_{\text{e}}^* & = 0 \end{cases} \tag{4.1.1.6}$$

The system of equations shown in (4.1.1.6) consists of three non-linear equations and three independent variables. The optimal control problem is fully defined and can be solved after the unknown variables i_{ds} , i_{qs} and λ for a certain torque reference T_{e}^* . In order to derive only the Maximum Torque-per-Ampere (MTPA) curve from Fig. 4.1 it is enough to eliminate the Lagrange multiplier λ from the first two equations and find an implicit expression for the MTPA curve depending only on i_{qs} and i_{ds} . This is done based on the first two equations shown in (4.1.1.6). The expression for the MTPA curve is shown in equation (4.1.1.7). In Fig. 4.1 the MTPA curve is plotted for $i_{\text{fd}} = 2$ A. The MTPA curve for a certain field winding current is identical to the MTPA curves calculated for IPM motors [10, 12], because the magnetic flux is always a fixed value for

the IPM machine. The curve can be visualized in the d - q current plane and is used to illustrate the optimal torque trajectory.

$$MTPA(i_{ds}, i_{qs}) = i_{ds} \cdot (L_d \cdot i_{ds} + L'_{fd} \cdot i'_{fd} - L_q i_{ds}) - i_{qs}^2 \cdot (L_d - L_q) \quad (4.1.1.7)$$

In order to illustrate the field winding current dependency of the MTPA curve, the optimal curves are plotted in Fig. 4.2 as a family of curves with the field winding as an adjustable parameter. The MTPA curves and the corresponding constant torque curves are plotted for three different values: $i_{fd} = 1$ A, 2 A and 3 A. The more the rotor is magnetized with the field winding current, the more the salient-pole machine behaves like a synchronous machine with a very small amount of reluctance torque. The less the magnetization of the rotor results from the field winding current, the more stator current is required to set a certain torque, which is generated due to the difference between L_d and L_q . A new optimal curve can be found based on a compromise between the stator and the rotor copper losses. The less the rotor copper losses are in comparison to the stator copper losses the more cost effective is to magnetize fully the rotor and the optimal d - q current trajectory relates to the one of an IPM motor.

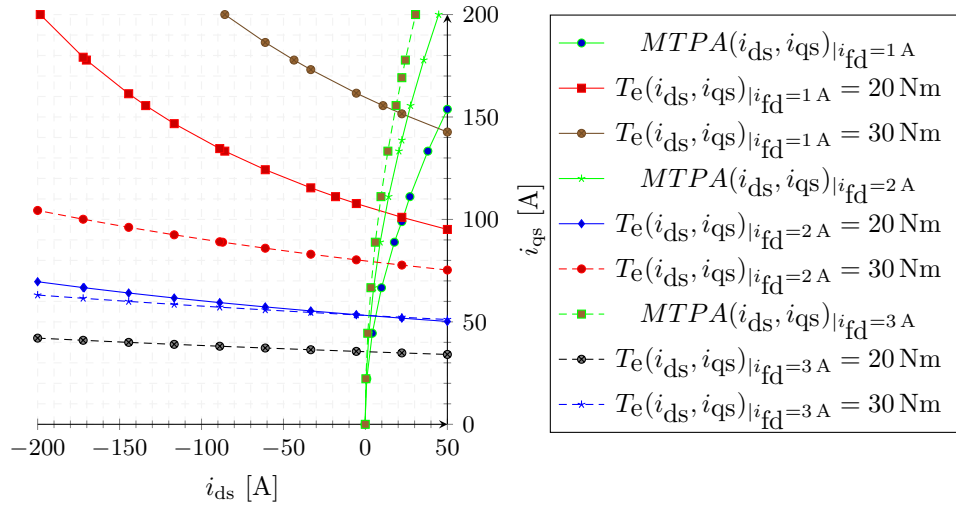


Figure 4.2 – Constant Torque Curves and MTPA Curves with i_{fd} as a Parameter

The optimal torque control for an EESM machine is not well documented in the literature. Reference [47] discusses briefly the control of an EESM machine. However, only a schematic of the control is presented and some of the challenges resulting from the one additional DOF in the control of an EESM are addressed. The optimal current control curves are not presented to the reader and the torque control is generally not discussed in detail.

The torque control of an EESM is not well researched according to the performed literature research. Therefore, the optimal torque control is derived first for the three-phase case,

before the focus is set on the torque control of the six-phase dual-voltage machine. The optimal current trajectory for the EESM machine has to be derived. The MTPA trajectory is not the optimal curve for the EESM. The optimal control trajectory of the EESM in the BS range is defined with a new abbreviation called Maximum Torque-per-Copper Losses (MTPCL), which describes better the optimization problem. The optimal torque control problem is mathematically formulated through equation (4.1.1.8). The copper losses of the stator and the rotor are minimized with respect to the torque equation constraint. The MTPCL curve is searched through the solution of the system of equations defined through the gradient of the Lagrange function as it has been done for the MTPA curve. The values for the stator resistance r_s and the rotor resistance r_{fd} are set for the sense of an example to the values of r_{s2} and r_{fd} from the machine parameters provided in Table 2.1.

$$\begin{aligned} \text{minimize} \quad & P_{Co}(i_{ds}, i_{qs}, i_{fd}) = \frac{3}{2} \cdot r_s \cdot (i_{qs}^2 + i_{ds}^2) + r_f \cdot i_{fd}^2 \\ \text{subject to} \quad & T_e(i_{ds}, i_{qs}, i_{fd})|_{T_e^*} = \frac{3}{2} \cdot p \cdot (L_d \cdot \frac{2N_f}{3N_s} \cdot i_{fd} \cdot i_q + (L_d - L_q) \cdot i_d \cdot i_q) - T_e^* = 0 \end{aligned} \quad (4.1.1.8)$$

The gradient of the Lagrange function is calculated in equation (4.1.1.9) based on the optimization problem from equation (4.1.1.8). The system of equations is fully defined with 4 equations and 4 independent variables: i_{ds} , i_{qs} , i_{fd} and λ . The optimal current trajectory is independent of the torque reference and can be only derived from the first three equations. The Lagrange multiplier is eliminated, when the third equation from (4.1.1.8) is solved after λ . The result is shown in equation (4.1.1.10).

$$\nabla_{i_{ds}, i_{qs}, i_{fd}, \lambda} \mathcal{L}(i_{ds}, i_{qs}, i_{fd}, \lambda) = \begin{cases} 3r_s i_{ds} + \lambda \frac{3}{2} p (L_d - L_q) i_{qs} & = 0 \\ 3r_s i_{qs} + \lambda \frac{3}{2} p (L_d \frac{2N_f}{3N_s} i_{fd} + (L_d - L_q) i_{ds}) & = 0 \\ 2r_f i_{fd} + \lambda \frac{3}{2} p L_d \frac{2N_f}{3N_s} i_{qs} & = 0 \\ \frac{3}{2} p (L_d \cdot \frac{2N_f}{3N_s} i_{fd} \cdot i_{qs} + (L_d - L_q) \cdot i_{ds} \cdot i_{qs}) - T_e^* & = 0 \end{cases} \quad (4.1.1.9)$$

$$\lambda = \frac{2N_s i_{fd} r_f}{L_d N_f i_{qs} p} \quad (4.1.1.10)$$

The solution for λ from equation (4.1.1.10) is substituted in the first two equations from equation (4.1.1.9). The result after the substitutions is provided in equation (4.1.1.11).

$$\begin{aligned} \frac{\partial \mathcal{L}(i_{ds}, i_{qs}, i_{fd}, \lambda)}{\partial i_{ds}} &= 3i_{ds} r_s - \frac{3N_s i_{fd} r_f \cdot (L_d - L_q)}{L_d N_f} \stackrel{!}{=} 0 \\ \frac{\partial \mathcal{L}(i_{ds}, i_{qs}, i_{fd}, \lambda)}{\partial i_{qs}} &= 3i_{qs} r_s - \frac{3N_s i_{fd} r_f (i_{ds} \cdot (L_d - L_q) + \frac{2L_d N_f i_{fd}}{3N_s})}{L_d N_f i_{qs}} \stackrel{!}{=} 0 \end{aligned} \quad (4.1.1.11)$$

The first equation from the system of equations (4.1.1.11) is easier to solve after i_{fd} or i_{ds} than the second equation. In order to derive the MTPCL curve in the (i_{ds}, i_{qs}) -plane, one has to solve the equation with respect to the field winding current i_{fd} to eliminate the field winding current dependency. This way the expression for the field winding current from equation (4.1.1.12) is derived. The expression, describing the field winding current, is substituted in the second equation from (4.1.1.11) and the implicit description of the MTPCL curve in the (i_{ds}, i_{qs}) -plane is derived in equation (4.1.1.13). It is noticeable that the implicit equation for the MTPCL curve does depend also on the field winding and stator resistances in contrast to equation (4.1.1.7), which depends only on the d - and q -axis inductances. The optimal trajectory, which minimizes the copper losses for the machine, is plotted in the (i_{ds}, i_{qs}) -plane in Fig. 4.3.

$$i_{fd} = \frac{L_d N_f i_{ds} r_s}{L_d N_s r_f - L_q N_s r_f} \quad (4.1.1.12)$$

$$\begin{aligned} MTPCL(i_{ds}, i_{qs}) &= i_{ds}^2 \left(2r_s L_d^2 N_f^2 + 3r_f L_d^2 N_s^2 - 6r_f L_d L_q N_s^2 + 3r_f L_q^2 N_s^2 \right) \\ &\stackrel{!}{=} 3N_s^2 i_{qs}^2 r_f (L_d - L_q)^2 \end{aligned} \quad (4.1.1.13)$$

A curve in the (i_{ds}, i_{fd}) -plane is plotted in Fig. 4.3 based on equation (4.1.1.12), which

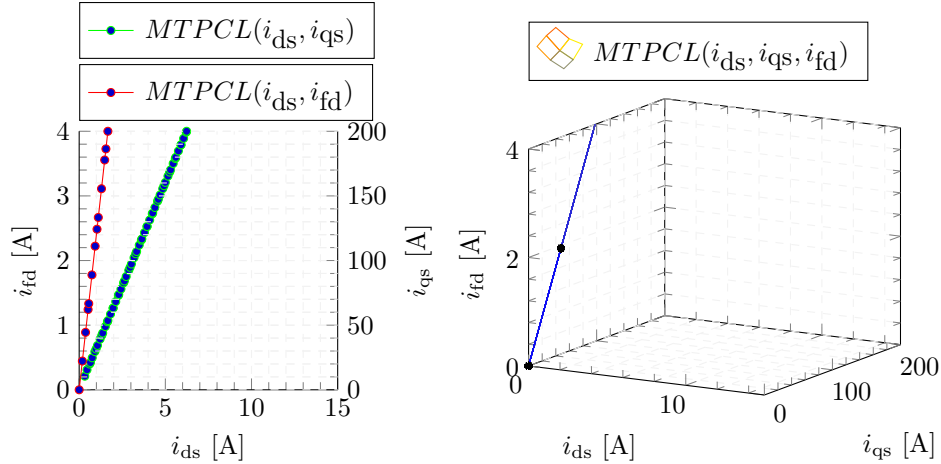


Figure 4.3 – Illustration of the MTPCL Curve in 2-D and 3-D

includes the dependency of the field winding current i_{fd} from the i_{ds} current. The MTPCL curve can be represented also in a 3D plot spanned by the three independent variables: i_{ds} , i_{qs} and i_{fd} as x , y and z Cartesian coordinates. The curve is illustrated in the second plot of Fig. 4.3.

The constant torque curves for a fixed field winding current or for an IPM motor are illustrated only in 2D in the (i_{ds}, i_{qs}) -plane. In Figure 4.2 the constant torque curves are plotted as a family of curves for three different field winding currents. When the field

winding current is considered as continuous, the constant curves become constant torque surfaces in the 3D-plane spanned by the coordinate system defined through the currents (i_{ds}, i_{qs}, i_{fd}) . Two of the surfaces are plotted in Fig. 4.4 for 20 Nm and 40 Nm torque references. The visualization in 3D is though possibly hard to comprehend for the reader. For better readability two views at the 3D plot are provided. The MTPCL line is also plotted in the 3D graph to illustrate how it intersects the constant torque surfaces. The surfaces with constant torques and the optimal MTPCL line can significantly change their shape depending on the saturation behavior of the main inductance. The curves are plotted with the assumption of constant inductances and therefore the phase angle between i_{ds} and i_{qs} is very small. If the saturation behavior is considered in the plots this angle is expected to increase, because the field winding current saturates much more the d -axis inductance. In reality the d -axis inductance L_d is far more saturated than the q -axis inductance L_q because of the strong magnetization caused by the field winding current. Due to this behavior the reluctance torque component can even inverse its sign because of the expression $L_d - L_q$.

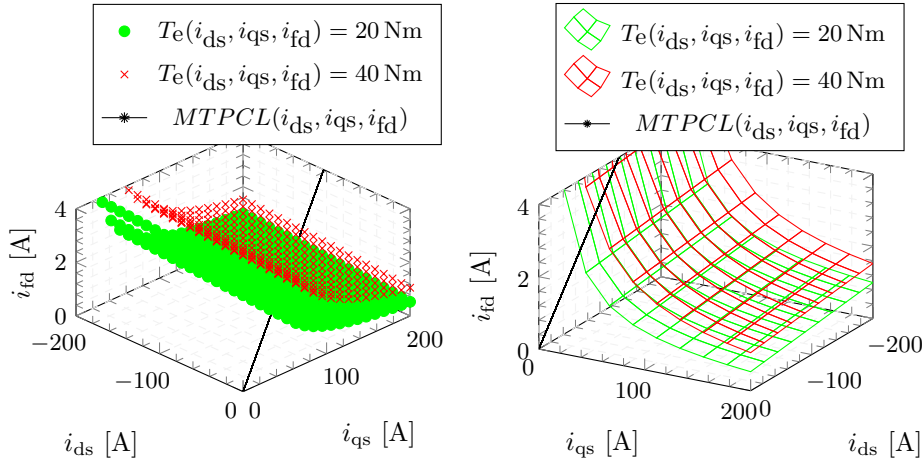


Figure 4.4 – Constant Torque Surfaces in 3-D

The optimal control problem can be solved analytically as long as the inductances L_d and L_q are assumed to be linear. The problems arise in the practice, when the data for the L_d and L_q inductances is provided as LUTs. Therefore numerical methods have to be employed to look for the optimal operating points for the machine. This problem is discussed later, when the optimal torque control is derived for the dual-voltage machine, where the inductances are available as LUT. The saturation of the inductances can be described through the parametrized implicit arcustangens function from Subsection 2.1.5. Unfortunately this function is not easy to differentiate due to its implicit formulation. Therefore, there's no way around the use of numerical differentiation methods and numerical search algorithms.

The theory provided in the current subsection alludes the complexity behind the torque control of the EESM. This comes from the additional DOF in the torque control in

comparison to the IPM machine. The optimization problem for the dual-voltage machine involves a non-linear search for 5 independent variables: i_{qs1} , i_{ds1} , i_{qs2} , i_{ds2} and i_{fd} . Though the five dimensional optimization problem cannot be visualized, the presented theory in the current subsection for the torque control in the BS range is equally applicable also to the dual-voltage machine. The Lagrangian method for a non-linear search is applicable for n -dimensional problems.

Before the optimal control problem for the dual-voltage machine in the BS range is set up and discussed in detail, the torque control in the second important region for the machine operation, the FW range, is explained for an EESM machine with one voltage level in Subsection 4.1.2.

4.1.2 Torque Control in the Field-Weakening Range for an Externally-Excited Synchronous Machine

The generated back-emf voltage becomes greater than the maximum available DC link voltage above the *corner speed* of the machine. If no countermeasures are undertaken a passive rectification would occur through the body diodes of the MOSFETs. In order to prevent this and to be able to control actively the power either in motor or generator mode, the resulting flux from the rotor has to be weakened such that the voltage caused by the rotating air-gap flux is reduced below the DC limit. The flux weakening has to be achieved in a such a way, that a voltage margin for the control of the main torque building current component, i_{qs} , is left. In order to weaken the air-gap flux a negative i_{ds} current is required, which counteracts the generated flux from the field winding.

A lot of research activities are ongoing in the field of FW control for IPM machines [10, 22, 23]. The electric drives are highly employed by the industry nowadays and the control methods in the FW area are researched in detail. However, most of the FW methods are applied to the high-voltage machines operating at voltage ranges above 350-400 V and less research activities are performed on machines operating below 60 V. Typical for the high-voltage machines is that the voltage drops across the stator resistances are negligible in comparison to the generated back-emf voltage. Therefore the employed control methods are based on a strategy, which has the goal to achieve a Maximum Torque-per-Flux (MTPF) control [10]. The application of the dual-voltage machine is however intended for voltages below 60 V. The voltage drop across the stator resistance is therefore non-negligible along the d -axis and has to be considered, when the optimal current trajectory is derived. The reason for this is exemplified and explained graphically in the current subsection. The optimal current trajectory considering the maximum DC voltage limit is called correctly in the FW mode a Maximum Torque-per-Voltage (MTPV) control. The terms MTPV and MTPF are often used interchangeably in the literature, because their application for high voltage machines makes them practically the same. Both abbreviations stand for the optimal current trajectory in the FW range of the machine.

The maximum available voltage can be described in the (v_{ds}, v_{qs}) -plane as a circle or in the (i_{ds}, i_{qs}) -plane as an ellipse. The voltage ellipse is described through equation (4.1.2.1). The factor $\frac{\sqrt{3}}{3}$ in front of the DC voltage results from the employed modulation technique. The employed modulation technique is a state of the art Space Vector Modulation (SVM) with an injected third harmonic. This modulation technique is able to reproduce a maximum rotating voltage vector with the length of $\frac{\sqrt{3}}{3}$ of the magnitude of the DC voltage.

$$\sqrt{\underbrace{(r_s \cdot i_{qs} + \omega_e \cdot (L'_{fd} i'_{fd} + L_d i_{ds}))^2}_{v_{qs}} + \underbrace{(r_s \cdot i_{ds} - \omega_e \cdot L_q i_{qs})^2}_{v_{ds}}} \leq \frac{\sqrt{3}}{3} \cdot V_{DC} \quad (4.1.2.1)$$

Equation (4.1.2.1) is plotted for different speeds in Fig. 4.5 and a constant voltage source of 48 V. The same torque lines from Fig. 4.1 and the MTPA curve are included in the plot in order to illustrate how the DC link voltage limits the maximum possible torque and the employment of the optimal MTPA trajectory. The field winding current is kept constant at 2 A. The voltage ellipse is plotted in a dashed black line for a speed of 1500 rpm and in a solid black line for a speed of 3000 rpm. In order to illustrate the influence of the stator resistance to the shape of the voltage ellipse for 48 V applications another voltage ellipse is plotted in dashed magenta lines for the same speeds with $r_s = 0 \Omega$. The speed of 1500 rpm is around the corner speed of the machine. The stator resistance has a non-negligible influence on the radius of the voltage ellipse. If the resistance is neglected, the allowed requested torque would be greater than is in reality possible. In this case the current controllers may go into the saturation. If the speed is doubled at 3000 rpm, the voltage ellipse shrinks towards its center and the allowed maximum torque is only of around half of the maximum torque possible at 1500 rpm. The angle spanned by the current vector along the MTPA curve has to increase with an increasing speed in order to weaken the magnetic field produced by the field winding current and still be able to set a certain torque reference. The torque setting is not anymore loss optimal due to the limitation imposed by the shrinking voltage ellipse.

The FW action is explained based on Fig. 4.5 for one torque reference. The constant torque line for a certain torque reference, which has to be set, is plotted in a dashed blue line in Fig. 4.5 and intersects the MTPA curve and the voltage ellipse at 2000 rpm. The voltage ellipse for the speed of 2000 rpm is plotted also with a dashed blue line in Fig. 4.5. If the requested torque at point **A** has to be further maintained despite the increasing speed beyond 1500 rpm, the constant torque curve is followed along the **A-B** path. At point **B** the constant torque curve intersects the voltage ellipse calculated for the speed of 2000 rpm. The current vectors plotted from the origin to point **A** and from the origin to point **B** show how the FW angle β increases in order to maintain the torque above 1500 rpm. The length of the vector for point **B** is longer than the one for point **A**. The differences in the vector lengths are comprehensible, because the MTPA curve represents torque points, which are set with least possible current. The q -axis current component is slightly reduced in the FW area in order to maintain the torque reference.

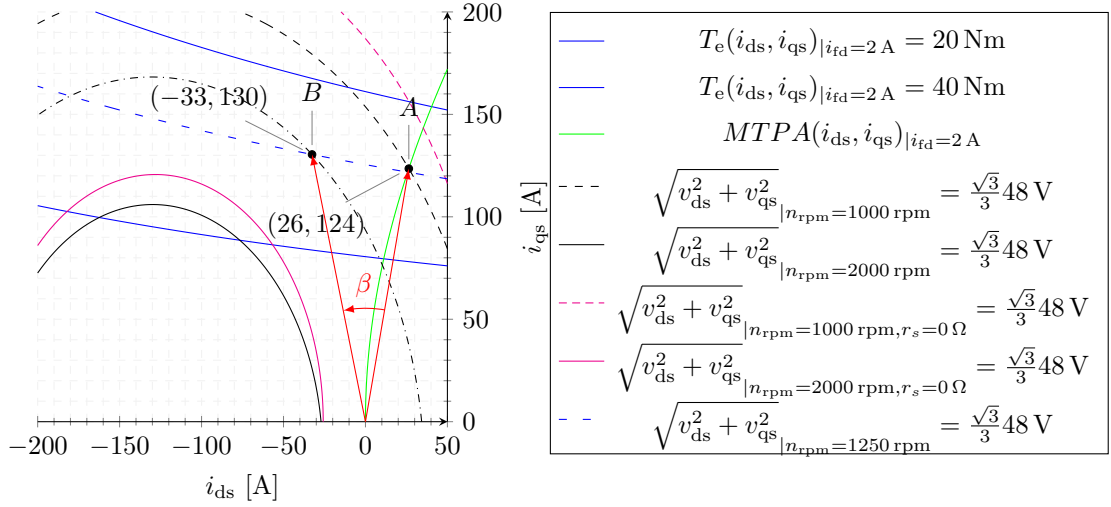


Figure 4.5 – Constant Torque Curves and Voltage Ellipses for $i_{fd}=2\text{ A}$

If the speed increases up to 3000 rpm the constant torque reference cannot be maintained anymore. The constant torque, plotted with the dashed blue line, and the voltage ellipse illustrated in a solid black line do not have any crossing points. At a speed of 3000 rpm the torque has to be reduced below 20 Nm because the physical limits of the machine and the DC source are reached. In this last section of the FW path the generated torque is the maximum possible one, bounded by the DC voltage source limit and the speed. The last section of the FW path is known as a MTPV curve.

The optimal FW trajectory can be mathematically derived for any torque reference, if an optimization problem for this purpose is defined. Besides the torque equation as a boundary condition, the voltage boundary from equation (4.1.2.1) has to be added as an additional **inequality** condition to the previously formulated optimization problem set up through equation (4.1.1.3). The new optimization problem is defined through the system of equations shown in (4.1.2.2). This optimization problem is valid also in the BS region. The voltage ellipse has an infinite radius at a speed of 0 rpm and shrinks with increasing speed. When the speed remains below the corner speed, the **inequality** condition from equation (4.1.2.2) is not binding and thus can be omitted.

$$\begin{aligned}
 \min. \quad & P_{co}(i_{ds}, i_{qs}) = \frac{3}{2} \cdot r_s \cdot (i_{qs}^2 + i_{ds}^2) \\
 \text{subj. to} \quad & T_e(i_{ds}, i_{qs}) = \frac{3}{2} \cdot p \cdot (L'_{fd} \cdot i'_{fd} \cdot i_q + (L_d - L_q) \cdot i_d \cdot i_q) - T_e^* = 0 \\
 & V_{vec}(i_{ds}, i_{qs}) = \sqrt{\underbrace{(r_s i_{qs} + \omega_e (L'_{fd} i'_{fd} + L_d i_{ds}))^2}_{v_{qs}} + \underbrace{(r_s i_{ds} - \omega_e L_q i_{qs})^2}_{v_{ds}}} \leq \frac{\sqrt{3}}{3} V_{DC}
 \end{aligned} \tag{4.1.2.2}$$

An optimization problem with inequality conditions is solved in a similar way as an optimization problem with solely equality constraints. When the inequality constraint is binding (active), the optimization problem can be reformulated to a one that includes only equality conditions. An **inequality** condition can be transformed into an **equality** condition, when a **slack** variable s_i is introduced [9, 56]. The slack variable is a variable that is added to an inequality in order to transform it into an equality. The slack variable has to be non-negative in order not to change the originally defined problem. This way, the inequality condition from equation (4.1.2.1) can be transformed to the equality from equation (4.1.2.3).

$$\sqrt{\underbrace{(r_s \cdot i_{qs} + \omega_e \cdot (L'_{fd} i'_{fd} + L_d i_{ds}))^2}_{v_{qs}} + \underbrace{(r_s \cdot i_{ds} - \omega_e \cdot L_q i_{qs})^2}_{v_{ds}}} + s_i = \frac{\sqrt{3}}{3} V_{DC} \quad , s_i \geq 0 \quad (4.1.2.3)$$

The Lagrange method employed for solving optimization problems with equality constraints is generalized by Karush-Kuhn-Tucker (KKT) for problems including also inequalities [9]. In order to solve the optimization problem the auxiliary Lagrangian function is defined in equation (4.1.2.4). The Lagrangian function is extended to include the voltage vector limits in the same way as an equality condition. A new multiplier μ is defined for the inequality conditions. Additional restrictions are required for the multiplier μ in contrast to λ .

$$\mathcal{L}(i_{ds}, i_{qs}, \lambda, \mu) = P_{co}(i_{ds}, i_{qs}) + \lambda \cdot T_e(i_{ds}, i_{qs})|_{T_e^*} + \mu \cdot V_{vec}(i_{ds}, i_{qs})|_{V_{DC}} \quad (4.1.2.4)$$

Based on the optimization problem from equation (4.1.2.2) and the Lagrangian function from equation (4.1.2.4), the KKT conditions for this problem are derived in equation (4.1.2.5). The KKT conditions define the necessary conditions [25], which have to be met, in order for a certain point (i_{ds}, i_{qs}) to be an extremum with respect to the boundary conditions set by the requested torque reference and the maximum available DC voltage.

$$\begin{aligned} -\nabla P_{co}(i_{ds}, i_{qs}) &= \mu \nabla V_{vec}(i_{ds}, i_{qs}) + \lambda \nabla T_e(i_{ds}, i_{qs})|_{T_e^*} && \text{(stationary condition)} \\ \mu \cdot \underbrace{\left(V_{vec}(i_{ds}, i_{qs}) - \frac{\sqrt{3}}{3} V_{DC} \right)}_{V_{vec}(i_{ds}, i_{qs})|_{V_{DC}}} &= 0 && \text{(complementary slackness)} \\ T_e(i_{ds}, i_{qs})|_{T_e^*} &= 0 \quad , \quad V_{vec}(i_{ds}, i_{qs})|_{V_{DC}} \leq 0 && \text{(primal feasibility)} \\ \mu &\geq 0 && \text{(dual feasibility)} \end{aligned} \quad (4.1.2.5)$$

The first condition is called a *stationary condition*, which means that the gradient of the function, which has to be minimized, has to be parallel to a scaled sum of the gradients of both constraints. The points described by the stationary condition are the extrema of the Lagrange function from equation (4.1.2.4). The variables μ and λ are called KKT

multipliers. Equation (4.1.2.6) shows the calculated gradients of the Lagrangian function with respect to i_{ds} , i_{qs} , λ and μ . The system of equations consists of 4 equations and 4 variables and is therefore fully defined. The system of equations fulfills the KKT condition from equation (4.1.2.5) besides the non-negative condition for μ . After the system of equations from (4.1.2.6) is solved, candidate points, i_{ds}^* , i_{qs}^* , λ^* and μ^* , are found. The calculated points of extrema can be filtered out after $\mu \geq 0$. The Second-Order-Sufficient Condition (SOSC) has to be fulfilled in order to check if a point minimizes the losses under the constraints. For this purpose the matrix $\nabla^2 \mathcal{L}(i_{ds}^*, i_{qs}^*, \lambda^*, \mu^*)$ has to be positive-definite². A further deepening into the theory of mathematical optimization will go out of the scope of the work. The interested reader in mathematical optimization is referred to reference [9].

$$\nabla \mathcal{L}(i_{ds}, i_{qs}, \lambda, \mu) = \begin{cases} 3r_s i_{ds} + \lambda \frac{3}{2} p (L_d - L_q) i_{qs} \\ \quad + 2\mu r_s (i_{ds} r_s - L_q i_{qs} \omega_e) & = 0 \\ + 2\mu L_d \omega_e (i_{qs} r_s + \omega_e (L_d i_{ds} + L'_{fd} i'_{fd})) \\ 3r_s i_{qs} + \lambda \frac{3}{2} p (L'_{fd} + i'_{fd} + (L_d - L_q) i_{ds}) \\ \quad + \mu (2r_s (i_{qs} r_s + \omega_e (L_d i_{ds} + L'_{fd} i'_{fd})) & = 0 \\ \quad - 2L_q \omega_e (i_{ds} r_s - L_q i_{qs} \omega_e)) \\ \frac{3}{2} p (L'_{fd} \cdot i'_{fd} \cdot i_{qs} + (L_d - L_q) \cdot i_{ds} \cdot i_{qs}) - T_e^* & = 0 \\ (i_{qs} r_s + \omega_e (L_d i_{ds} + L'_{fd} i'_{fd}))^2 + (i_{ds} r_s - L_q i_{qs} \omega_e)^2 - \frac{V_{DC}^2}{3} & = 0 \end{cases} \quad (4.1.2.6)$$

From the system of equations from (4.1.2.6) is evident that, when the speed and torque are fixed, just one point can be found as optimal in the (i_{ds}, i_{qs}) -plane. A mathematical description of the optimal current curve cannot be analytically calculated in the (i_{ds}, i_{qs}) -plane based on the defined problem. This is so, because the first two equations depend on two KKT multipliers, λ and μ . If, for example, the second equation is solved after μ and substituted in the first equation, there will still be the dependency based on λ . This dependency on λ cannot be eliminated because either the 3rd nor the 4th equation depend on λ . Nevertheless the system of equations is fully defined and can be solved numerically for a certain combination of torque reference, DC voltage and speed. A Matlab optimization script is set later in the thesis for this purpose to solve the optimization problem in the FW area for the dual-voltage machine. The numerical optimization algorithms in Matlab are based on the theory of the KKT conditions explained in the current section.

The MTPV curves for IPM machines are often provided in the (i_{ds}, i_{qs}) -plane in the scientific literature [10, 22, 23, 32]. The approach to calculate the MTPV trajectory is different than the one to calculate the optimal working points based on the optimization problem defined in equation (4.1.2.6). The MTPV or MTPF curves are trajectories in the (i_{ds}, i_{qs}) -plane, which generate a maximum torque considering the physical limits set

²A matrix \mathbf{A} is positive-definite, if the product $\mathbf{x}^T \cdot \mathbf{A} \cdot \mathbf{x}$ is a positive scalar value, for any vector of $\mathbf{x} \neq \vec{0}$

through a given DC link voltage and a given speed. A different optimization problem is formulated in equation (4.1.2.7) in order to derive the MTPV curve and to illustrate the optimal current trajectory in the FW area.

$$\begin{aligned} \max. \quad & T_e(i_{ds}, i_{qs}) = \frac{3}{2} \cdot p \cdot (L'_{fd} \cdot i'_{fd} \cdot i_q + (L_d - L_q) \cdot i_d \cdot i_q) \\ \text{subj. to} \quad & V_{vec}(i_{ds}, i_{qs}) = \sqrt{\underbrace{(r_s i_{qs} + \omega_e (L'_{fd} i'_{fd} + L_d i_{ds}))^2}_{v_{qs}} + \underbrace{(r_s i_{ds} - \omega_e L_q i_{qs})^2}_{v_{ds}}} \leq \frac{\sqrt{3}}{3} V_{DC} \end{aligned} \quad (4.1.2.7)$$

The new formulation attempts to maximize the torque under the restriction, that the maximum available voltage has to be considered. For this problem a Lagrangian function can be set up. This step is omitted here as it is straightforward. The gradients of both curves, the constant voltage ellipses and the constant torque curves, have to be parallel to each other in order to calculate the steady state points. Then the optimization problem can be solved in an analogous manner as the one for the MTPA curve from equation (4.1.1.8). The derivation of the MTPV curve is concluded exactly the same way with elimination of the Lagrange multiplier through the first two equations: the partial derivatives after i_{ds} and i_{qs} . Only the solution is presented here. An implicit representation of the MTPV curve is provided in equation (4.1.2.8). From the derived equation is evident that the resistance r_s and the speed ω_e are still included in the mathematical description of the curve. This is due to the fact that the voltage drops over the stator resistances are considered in the MTPV curve.

$$\begin{aligned} MTPV(i_{ds}, i_{qs}) = & \frac{3}{2} p (L'_{fd} i'_{fd} + i_{ds} (L_d - L_q)) \\ & - \frac{3 i_{qs} p (L_d - L_q) (2 r_s (i_{qs} r_s + \omega_e (L_d i_{ds} + L'_{fd} i'_{fd})) - 2 L_q \omega_e (i_{ds} r_s - L_q i_{qs} \omega_e))}{2 (2 r_s (i_{ds} r_s - L_q i_{qs} \omega_e) + 2 L_d \omega_e (i_{qs} r_s + \omega_e (L_d i_{ds} + L'_{fd} i'_{fd})))} \end{aligned} \quad (4.1.2.8)$$

In case the stator resistances are neglected and set to 0Ω , the MTPV curve transforms to the MTPF curve. Equation (4.1.2.9) describes the MTPF curve and has a much simpler form, because it does not include any dependency on the speed and the resistance.

$$MTPF(i_{ds}, i_{qs}) = \frac{3}{2} \cdot 8 \cdot (L'_{fd} i'_{fd} + i_{ds} \cdot (L_d - L_q)) - \frac{3 L_q^2 8 i_{qs}^2 (L_d - L_q)}{2 L_d (L'_{fd} i'_{fd} + L_d i_{ds})} \quad (4.1.2.9)$$

Both curves are plotted in Fig. 4.6. The MTPF curve is plotted in an orange dashed line. The MTPV curve is plotted for three different speeds: one at 1500 rpm, one at 3000 rpm and one at 9000 rpm. It is apparent, that with an increasing speed, the MTPV curve coincides with the MTPF curve. Only the curve at 1500 rpm is visually distinguishable from the MTPF trajectory. Though the mathematical description of the MTPV curve is much more complicated than the MTPF curve, at higher speeds there is practically no difference. The difference is mainly around the corner speed of the machine.

The optimal trajectory in the FW area, where the torque is limited by the voltage, is denoted by the points **B** and **C**. Point **B** is left from point **A**. Both points set the same

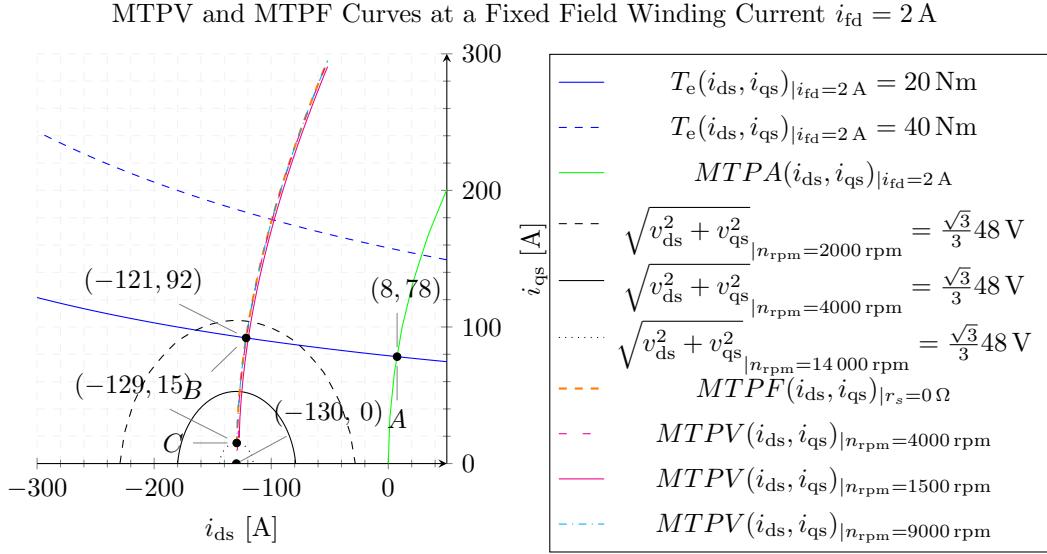


Figure 4.6 – Maximum Torque-per-Voltage (MTPV) for a Fixed Field Winding Current

torque reference of 20 Nm. Point **A** represents the optimal current vector according to the MTPA curve in the BS range and point **B** is the crossing point between the constant torque line at 20 Nm and the MTPF curve. When the speed is increased from 3000 rpm up to 16 000 rpm, the optimal current trajectory follows the path described by **B-C**. Point **C** represents the maximum possible torque at 16 000 rpm. The voltage ellipse shrinks substantially. The voltage ellipse at 16000rpm is plotted with a black dotted line. If the speed continues to increase it will shrink to the point at the i_{ds} -axis defined by $(-i'_{fd}, 0)$.

The FW principle is visually explained for a fixed field winding current of 2 A in Fig. 4.6. This is equivalent to the FW action applied to IPM machines, where the rotor magnetic flux cannot be varied. In order to illustrate how the field winding current influences the optimal trajectories in the FW range, the voltage ellipses and MTPV curves are plotted for two other field winding currents, 1 A and 3 A, in Fig. 4.7. From Fig. 4.7 is clear that with an increasing field winding current the center of the voltage ellipses migrates towards increasing negative d -axis currents. This is owing to the fact that the center of the voltage ellipses is defined through the magnetizing rotor current i_{fd} referred to the stator: i'_{fd} . The more the magnetizing current is increased, the more the torque lines get flatter and the reluctance torque component is reduced. For example, the second plot of Fig. 4.7 is characterized through flat constant torque lines and high negative d -axis currents, which are required to weaken the flux produced by the field winding current. It is obvious, that the greater field winding current, in this case 3 A, enables the setting of the torque reference of 20 Nm at 3000 rpm. This is not valid for the first plot of Fig. 4.7, where both torque references, for 20 Nm and 40 Nm, are not physically feasible. This leads automatically to the conclusion, that feasible working points in the FW area are accompanied with higher field winding currents. This observation is interesting,

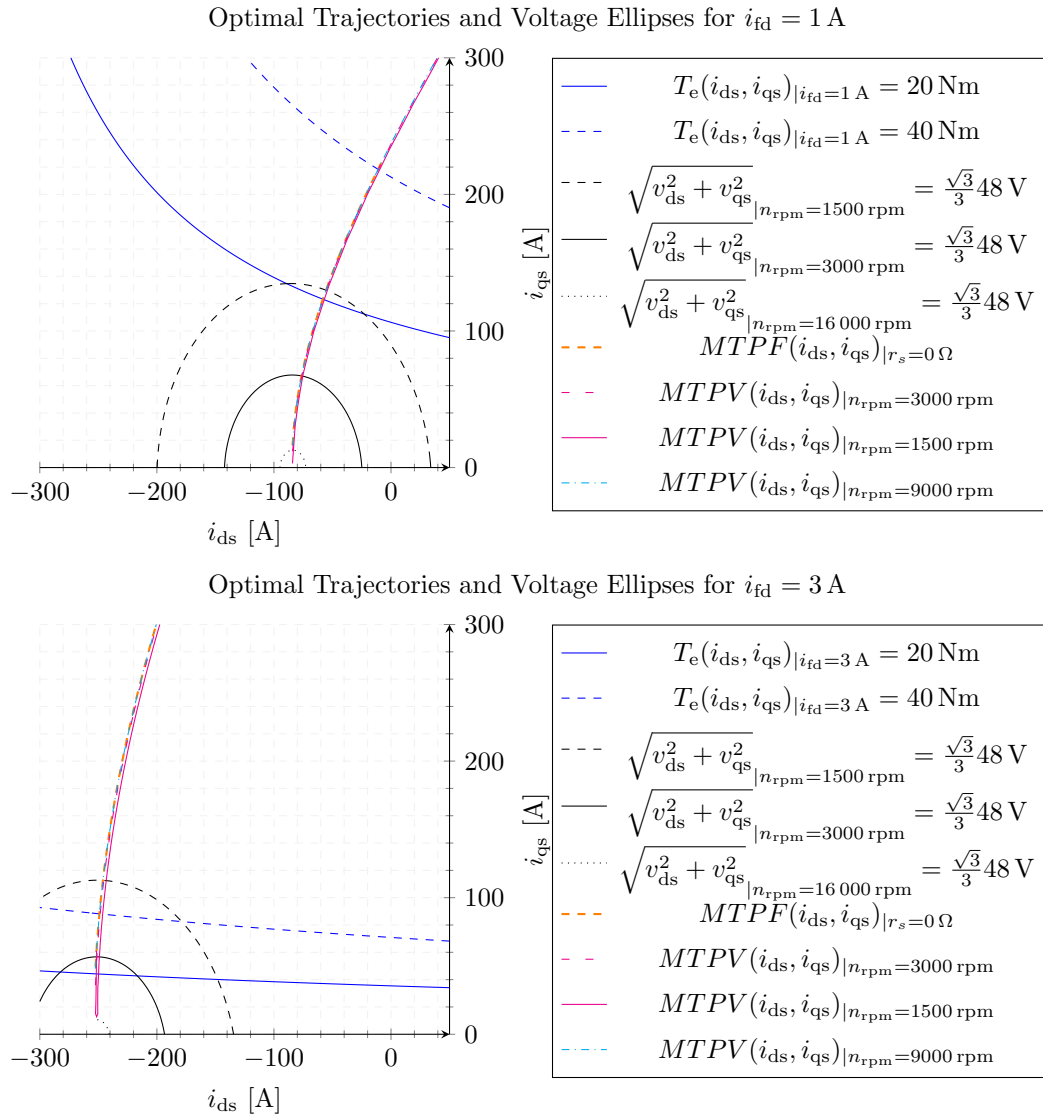


Figure 4.7 – MTPV Curves for Two Different Field Winding Currents, $i_{fd} = 1$ A and 3 A

because another assumption for the torque control in FW mode seems natural. Instead of weakening the magnetic field with negative d -axis current, one may assume that it may be more cost effective to reduce the field winding current and thus lower the stator and rotor losses in the FW area. The presented graphics from Fig. 4.7 clearly refute this thesis and proves that maximal torque references for the EESM in the FW area can only be set with high field winding currents. This observation can be interpreted also from another point of view. In order to exploit fully the electric machine and generate maximum power, the machine inductances have to be saturated fully as this enables maximal usage of the machine iron.

The MTPV curves are illustrated in Fig. 4.7 also for both field winding currents, 1 A and 3 A. It is characteristic for the MTPV curve with field winding current of 3 A that the tilt towards the negative d -axis currents is steeper than the tilt for the curve with $i_{fd} = 1$ A. The optimal MTPV curve for $i_{fd} = 1$ A is more curved towards negative d -axis currents. Therefore the torque curves at $i_{fd} = 1$ A comprise of greater reluctance torque component and have a parabolic shape. The illustrated cases lead to the conclusion that for higher torque references, which exploit fully the electric machine, the optimal currents trajectory is closer to the one from the second plot of Fig. 4.7 and for small torque references, not requesting maximum power, the optimal curve is closer to the one at 1 A.

The optimal MTPV trajectory can be derived also in the 3D-plane, where all three currents, i_{ds} , i_{qs} and i_{fd} , are variable. For this purpose the problem defined in equation (4.1.2.7) is extended to consider also the field winding current as an optimization variable. The extension of the problem is straightforward and omitted at this place. The gradients of the Lagrange function are extended to include the partial derivative after i_{fd} . The gradients of the Lagrange function are provided in equation (4.1.2.10) and set to zero to find the steady state points.

$$\begin{aligned}
 \frac{\partial \mathcal{L}(i_{ds}, i_{qs}, i_{fd}, \mu)}{\partial i_{ds}} &= 2\mu r_s (i_{ds} r_s - L_q i_{qs} \omega_e) + 2\mu L_d \omega_e \left(i_{qs} r_s + \omega_e \left(L_d i_{ds} + \frac{2L_d N_f i_{fd}}{3N_s} \right) \right) \\
 &\quad + \frac{3}{2} i_{qs} p (L_d - L_q) = 0 \\
 \frac{\partial \mathcal{L}(i_{ds}, i_{qs}, i_{fd}, \mu)}{\partial i_{qs}} &= \mu 2r_s \left(i_{qs} r_s + \omega_e \left(L_d i_{ds} + \frac{2L_d N_f i_{fd}}{3N_s} \right) \right) - \mu 2L_q \omega_e (i_{ds} r_s - L_q i_{qs} \omega_e) \\
 &\quad + \frac{3p}{2} \left(i_{ds} (L_d - L_q) + \frac{2L_d N_f i_{fd}}{3N_s} \right) = 0 \\
 \frac{\partial \mathcal{L}(i_{ds}, i_{qs}, i_{fd}, \mu)}{\partial i_{fd}} &= \frac{L_d N_f i_{qs} p}{N_s} + L_d \frac{4N_f}{3N_s} \mu \omega_e (i_{qs} r_s + \omega_e (L_d i_{ds} + 2L_d N_f i_{fd})) = 0 \\
 \frac{\partial \mathcal{L}(i_{ds}, i_{qs}, i_{fd}, \mu)}{\partial \mu} &= \left(i_{qs} r_s + \omega_e \left(L_d i_{ds} + \frac{2L_d N_f i_{fd}}{3N_s} \right) \right)^2 + (i_{ds} r_s - L_q i_{qs} \omega_e)^2 - \frac{V_{DC}^2}{3} = 0
 \end{aligned} \tag{4.1.2.10}$$

The MTPV curve can be calculated based on the solution of the first 3 equations. When the Lagrange multiplier μ is eliminated, an implicit equation for the MTPV curve is derived in equation (4.1.2.11). The MTPV curves from equation (4.1.2.11) are plotted in the (i_{ds}, i_{qs}) - and (i_{ds}, i_{fd}) -planes and in the 3D- (i_{ds}, i_{qs}, i_{fd}) -plane in Fig. 4.8. The curves are dependent on the speed and the stator resistance. The optimal curves are plotted as an example for 1500 rpm, 3000 rpm and 4500 rpm in the 3D-plot to show the different trajectories as a function of the speed. It is evident from the first plot in Fig. 4.8 that the shape of the curves for MTPV(i_{ds}, i_{fd}) is almost independent of the speed and overlap visually over each other. The curves for MTPV(i_{ds}, i_{qs}) show a greater dependency on

the speed. The FW angle between i_{qs} and i_{ds} is increased with increasing speed and the i_{qs} current is reduced in contrast to the negative i_{ds} current.

$$MTPV(i_{ds}, i_{qs}) = \frac{-3p(L_q^2\omega_e^2 + r_s^2)(i_{ds}r_s + L_q i_{qs}\omega_e)}{2L_q r_s \omega_e^2} \quad (4.1.2.11)$$

$$MTPV(i_{ds}, i_{fd}) = -\frac{3N_s i_{ds} r_s^2 + 3L_d L_q N_s i_{ds} \omega_e^2}{2L_d L_q N_f \omega_e^2}$$

The plotted MTPV curves in the 3D- (i_{ds}, i_{qs}, i_{fd}) -plane illustrate the gradients between the surfaces described by the voltage equation from (4.1.2.3) and the constant torque surfaces described through equation (4.1.1.1). The plotting of the constant torque surfaces and voltage ellipsoids in the 3D-plane are omitted here.

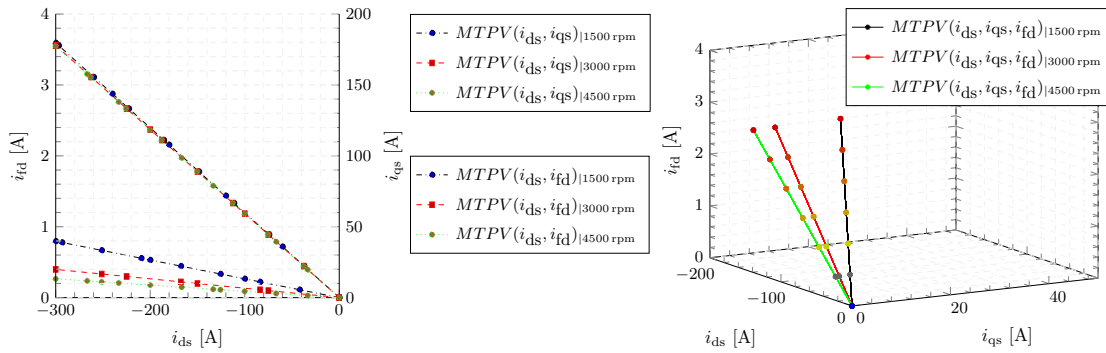


Figure 4.8 – MTPV Trajectory with a Variable Field Winding Current i_{fd}

The presented torque control theory for the EESM exemplifies the fact that the complexity in the optimization problems for the BS and the FW range increases in comparison to the IPM machines due to the additional degree of freedom caused by the field winding current. The presented theory in this subsection is simplified with the assumption of linear inductances used in the torque and voltage equations. Despite the simplifications it is evident from the calculated optimal current trajectories that the defined optimization problems are hard to solve. Even the system of equations from (4.1.2.6), which defines the Lagrangian gradients, is non-linear and has to be numerically solved, even though the inductances are linear. In reality, the inductances have a non-linear dependency on the currents, which complicates the search for the optimal working points. Therefore, numerical optimization methods are employed to search for the optimal torque control points as well in the BS as in the FW region. Further, measurements show later in the thesis, that the iron losses constitute a non-negligible part of the main machine losses and have to be considered for the claw-pole machine in contrast to IPM machines [6, 10, 12]. This loss effect makes further the use of numerical optimization for the dual-voltage machine inevitable.

The presented theory in the current subsection is extended and applied to the torque control of the dual-voltage six-phase machine in Section 4.2 for the BS range.

4.2 Torque Control in the BS Range for the Dual-Voltage Machine

The MTPCL torque control principle for the EESM presented in Subsection 4.1.1 for the BS range is extended for the dual-voltage machine to include two air-gap torque references: T_{e12V}^* and T_{e48V}^* . The minimization of the copper losses has to be achieved for both stator windings and the rotor field winding. For this purpose the problem set up in equation (4.1.1.8) is extended to include the copper losses of both stator windings and the two equations for both air-gap torques from equation (2.2.1.16) derived in Chapter 2. The torque equations shown in (2.2.1.16) are expressed through magnetizing fluxes and currents. This is a convenient representation of the torque generated by a machine's winding as far as the machine modeling is considered. The torque equation in this form is simple and is derived based on its basic form from the Lorentz force law. It is useful to be able to decompose the whole torque into *synchronous* and *reluctance* torque components, when the torque control development is discussed. Through a torque decomposition the coupling between both stator systems and the field winding becomes evident. For the purpose of analysis the torque equations are transformed from a flux-currents form into a inductances-currents form. This way the generated torque from each winding can be divided into the different torque components. The *synchronous torque*, caused by the interaction of the field winding current and the stator currents, is separated from the *reluctance torque*, caused by the differences in the magnetic reluctance paths along the d - and q -axis of the machine. The equations for the 12V and 48V air-gap torques from (2.2.1.16) are rewritten, so that the fluxes are substituted through inductances and currents. The transformation of the torque equations is derived in equations (4.2.0.1) and (4.2.0.2). The air-gap torques, T_{e12V} and T_{e48V} , comprise of a *synchronous torque* component, a *reluctance torque* component and a *cross-reluctance torque* component. In contrast to the conventional three-phase equation from (4.1.1.1), both air-gap torques include also the interaction between the stator systems expressed through the *cross-reluctance torque* component. This is a result of the interaction between the mutual magnetic flux produced by the second stator system and the stator currents vector from the first stator system.

$$\begin{aligned}
T_{e12V} &= \frac{3}{2} \cdot p \cdot \left((\lambda_{md1} + \lambda_{mag1}) \cdot \frac{i_{qs1}}{N_{s11}} - \lambda_{mq1} \cdot \frac{i_{ds1}}{N_{s11}} \right) \\
&= \frac{3}{2} \cdot p \cdot \left(\left(L_{dd1} \frac{2N_f}{3N_{s1}} i_{fd} + L_{dd1} \frac{N_{s2}}{N_{s1}} i_{ds2} + L_{dd1} i_{ds1} + \lambda_{mag1} \right) i_{qs1} \right. \\
&\quad \left. - \left(L_{qq1} \frac{N_{s2}}{N_{s1}} i_{qs2} + L_{qq1} i_{qs1} \right) i_{ds1} \right) \\
&= \frac{3}{2} \cdot p \cdot \left(\underbrace{\left(L_{dd1} \frac{2N_f}{3N_{s1}} i_{fd} + \lambda_{mag1} \right) i_{qs1}}_{\text{synch. Torque}} + \underbrace{\left(L_{dd1} - L_{qq1} \right) i_{ds1} i_{qs1}}_{\text{reluctance Torque}} \right. \\
&\quad \left. + \underbrace{\left(L_{dd1} - L_{qq1} \right) \frac{N_{s2}}{N_{s1}} i_{ds2} i_{qs1}}_{\text{cross-rel. Torque}} \right)
\end{aligned} \tag{4.2.0.1}$$

$$\begin{aligned}
 T_{e48V} &= \frac{3}{2} \cdot p \cdot \left((\lambda_{md1} + \lambda_{mag1}) \cdot \frac{i_{qs2}}{N_{s12}} - \lambda_{mq1} \cdot \frac{i_{ds2}}{N_{s12}} \right) \\
 &= \frac{3}{2} \cdot p \cdot \left(\underbrace{\left(L_{dd1} \frac{2N_f}{3N_{s1}} i_{fd} + \lambda_{mag1} \right) \frac{i_{qs2}}{N_{s12}}}_{\text{synch. Torque}} + \underbrace{(L_{dd1} - L_{qq1}) \frac{i_{ds2}}{N_{s12}} \frac{i_{qs2}}{N_{s12}}}_{\text{reluctance Torque}} \right) \\
 &\quad + \underbrace{(L_{dd1} - L_{qq1}) \frac{N_{s2}}{N_{s1}} i_{ds1} i_{qs2}}_{\text{cross-rel. Torque}}
 \end{aligned} \tag{4.2.0.2}$$

The 12V torque equation (4.2.0.1) is analyzed in order to explain the mathematical derivation. The whole magnetic flux along the d -axis, $\lambda_{md1} + \lambda_{mag1}$, is substituted with the product of the currents generating the d -axis flux and the inductance along the d -axis. The currents have to be referred to the stator system 1, so that the 12V torque equation can be calculated in one reference stator system. The field winding current is scaled with the turns ratio $\frac{N_f}{N_{s1}}$ and with a factor of $\frac{2}{3}$ because the d -axis inductance L_{dd1} is defined in the d - q system. The d -axis current of the 48V side is referred to the stator system 1 with the ratio $\frac{N_{s2}}{N_{s1}}$. The 12V d -axis current is considered in the multiplication without any scaling and the permanent magnet's flux is finally added. The q -axis flux is decomposed in an analogous manner. The 48V q -axis current is scaled with the stator 2 to stator 1 turns ratio $\frac{N_{s2}}{N_{s1}}$ and multiplied by the inductance along the q -axis L_{qq1} . The 12V q -axis current contributes also to the generation of the q -axis flux and is multiplied without any scaling with the inductance L_{dd1} . After mathematical reformulation the torque equation from (4.2.0.1) is rewritten and decomposed into three torque components: a *synchronous torque* component, a *reluctance torque* component and a *cross-reluctance torque* component. The synchronous torque component results from the interaction of the magnetic flux produced by the field winding current and the permanent magnet's flux and the q -axis current of the 12V stator, i_{qs1} . The reluctance torque is a result of the differences in the reluctance paths along the d - and q -axis: $L_{dd1} - L_{qq1}$. The third term represents the cross-reluctance torque component as an expression of the coupling between both stator systems. The 12V cross-reluctance torque is generated due to the negative 48V d -axis current, the 12V q -axis current and due to the different inductances along the d and q -axis. This new torque component, specific for the dual-voltage machine, is denoted in this work by the term *cross-reluctance torque*. The torque component is not influenced by the field winding current, because it is caused by the differences in the reluctance paths along the d - and q -axis: $L_{dd} - L_{qq}$.

Equations (4.2.0.1) and (4.2.0.2) show both air-gap torques in an inductance form, which are used to set up the optimization problem for the dual-voltage machine as shown in

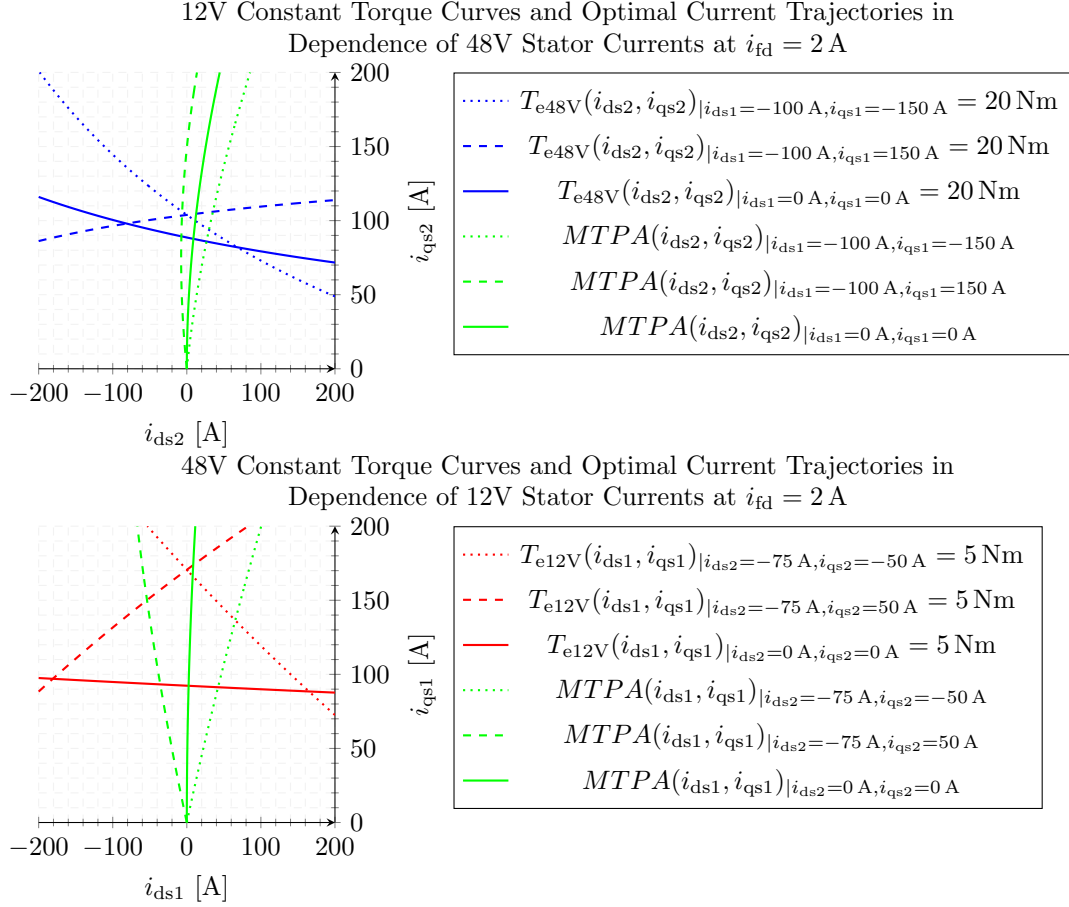
equation (4.2.0.3). The goal is to find optimal current references, which set both air-gap torques at the requested values, T_{e12V}^* and T_{e48V}^* , and minimize the losses.

$$\begin{aligned}
 \min. \quad & P_{\text{co}}(i_{\text{ds1}} \dots i_{\text{fd}}) = \frac{3}{2}r_{\text{s1}} \left(i_{\text{qs1}}^2 + i_{\text{ds1}}^2 \right) + \frac{3}{2}r_{\text{s2}} \left(i_{\text{qs2}}^2 + i_{\text{ds2}}^2 \right) + r_{\text{f}}i_{\text{fd}}^2 \\
 \text{subj. to} \quad & T_{\text{e}}(i_{\text{ds1}} \dots i_{\text{fd}})|_{T_{e12V}^*} = \frac{3}{2}p \left(L_{\text{dd1}} \frac{2N_{\text{f}}}{3N_{\text{s1}}} i_{\text{fd}} i_{\text{qs1}} + (L_{\text{dd1}} - L_{\text{qq1}}) i_{\text{ds1}} i_{\text{qs1}} \right. \\
 & \quad \left. + (L_{\text{dd1}} - L_{\text{qq1}}) \frac{N_{\text{s2}}}{N_{\text{s1}}} i_{\text{ds2}} i_{\text{qs1}} \right) - T_{e12V}^* = 0 \quad (4.2.0.3) \\
 & T_{\text{e}}(i_{\text{ds1}} \dots i_{\text{fd}})|_{T_{e48V}^*} = \frac{3}{2}p \left(\frac{L_{\text{dd1}}}{N_{\text{s12}}^2} \frac{2N_{\text{f}}}{3N_{\text{s2}}} i_{\text{fd}} i_{\text{qs2}} + \left(\frac{L_{\text{dd1}}}{N_{\text{s12}}^2} - \frac{L_{\text{qq1}}}{N_{\text{s12}}^2} \right) i_{\text{ds2}} i_{\text{qs2}} \right. \\
 & \quad \left. + (L_{\text{dd1}} - L_{\text{qq1}}) \frac{N_{\text{s2}}}{N_{\text{s1}}} i_{\text{ds1}} i_{\text{qs2}} \right) - T_{e48V}^* = 0
 \end{aligned}$$

The problem defined in equation (4.2.0.3) consists of five unknown currents and is difficult to solve. The optimal trajectories depend, on all five currents. One way to visually represent how both systems influence each others working points is to plot the torque equations in separate planes and set the currents of the neighboring stator system and the rotor current to fixed values. Both torque equations from (4.2.0.3) can be plotted in two different coordiante systems and the currents of the other stator system are considered as parameters. The 12V torque, T_{e12V} , is visualized in the $(i_{\text{ds1}}, i_{\text{qs1}})$ -plane and the 48V torque, T_{e48V} , in the $(i_{\text{ds2}}, i_{\text{qs2}})$ -plane. The currents of the other system are set as an example to different working points in order to illustrate visually the influence of the other system to the torque generation of the first one.

The 48V torque curves are plotted in the upper part of Fig. 4.9 and the 12V torque curves are included below. The torque curves are illustrated in blue and the MTPA curves in green. The inductance values are assumed to be linear in the plotted torque curves. The very same values are used as in the plots from Subsection 4.1.1. The 12V side inductances are referred with the square of the winding ratio, $\frac{N_{\text{s1}}^2}{N_{\text{s2}}^2} = 0.25^2$, from the 48V side. The torque equations at the 48V side are plotted as an example for a 20 Nm reference and at the 12V side for a 5 Nm reference. The field winding current is set to 2 A for better analogy with the previous plots.

The influence of the *cross-reluctance torque* to the torque lines is visualized in Fig. 4.9. The torque lines are plotted, when the neighboring stator system is operated in generator, idle or motor mode. The 48V torque equation for a reference of 20 Nm is plotted in a solid blue line for the 12V stator currents set to 0 A: $i_{\text{ds1}} = 0$ A and $i_{\text{qs1}} = 0$ A. The constant torque line for the same reference is plotted with a dashed blue line for 12V stator winding operated in motor mode. The currents are set as an example to $i_{\text{ds1}} = 50$ A and $i_{\text{qs1}} = 150$ A. The positive 12V d -axis current, $i_{\text{ds1}} = 50$ A, shifts the torque curve for $i_{\text{ds2}} = 0$ A on the q -axis downwards. This means that less i_{qs2} current is required to set the same torque reference. This is a result of the d -axis mutual flux of the 12V side interacting with the q -axis current of the 48V side. This interaction is described through the term $L_{\text{dd1}} \frac{N_{\text{s2}}}{N_{\text{s1}}} i_{\text{ds1}} i_{\text{qs2}}$ in equation (4.2.0.1). The positive value of the current i_{ds1} adds an additional torque component. The optimal current point for a torque reference of



20 Nm is denoted by the intersection of the constant torque line in a dashed blue color and the MTPA curve plotted with a dashed green line. The MTPA curve line denotes the optimal current trajectory in the case, when the 12V winding is operated in motor mode at the currents: $i_{ds1} = 50$ A and $i_{qs1} = 150$ A. The constant torque line in a dashed blue color has a different tilt than the constant torque line in solid blue because of the term $-L_{qq1} \frac{N_{s2}}{N_{s1}} i_{qs1} i_{ds2}$ from the torque equation. The current i_{qs1} is set to a positive value of 150 A, which leads to an increase of the term $-L_{qq1} \frac{N_{s2}}{N_{s1}} i_{qs1} i_{ds2}$, when the d -axis current i_{ds2} increases into the negative values. The 48V q -axis current is decreased, when the i_{ds2} current increases maximal to the negative d -axis, to compensate this effect.

In contrast to the torque curve for $i_{qs1} = 0$ A and $i_{ds1} = 0$ A plotted with a solid blue line, the torque reference in a dashed blue line has a cross-reluctance torque component, which increases the reluctance torque of the 48V winding. Though the torque lines look much different, the optimal current points in both cases do not lie much further from each other. The crossing point of the dashed green MTPA curve and the dashed blue

torque curve lies left from the crossing point of the solid green MTPA curve and the solid blue torque curve.

The 48V torque equation is plotted for the case, when the 12V winding is in generator mode, $i_{qs1} = -150$ A and $i_{ds1} = 50$ A, in a blue dotted line in Fig. 4.9. The generated *cross-reluctance torque* counteracts the 48V reluctance torque due to the increasing negative 48V d -axis currents. The more the 48V d -axis current i_{ds2} is increased towards negative values the greater the term $-L_{qq1} \frac{N_{s2}}{N_{s1}} i_{qs1} i_{ds2}$ becomes with respect to negative values. Therefore this term has to be compensated through the synchronous torque component. A positive q -axis current of the 48V side generates a synchronous torque component with the field winding flux and compensates the negative reluctance torque.

Similar analysis can be performed based on the bottom plot of Fig. 4.9. The 12V torque curve is plotted for a reference of 5 Nm in a solid red line, when the 48V system is operated at $i_{qs2} = 0$ A and $i_{ds2} = 0$ A. The 5 Nm torque curve is plotted when the 48V winding is in a motor or generator mode. The curve in a dashed red line is plotted for 48V currents in motor mode: $i_{qs2} = 50$ A and $i_{ds2} = 50$ A. The torque curve in a dotted red line is plotted for 48V currents in generator mode: $i_{qs2} = -50$ A and $i_{ds2} = 50$ A. The 12V torque curves follow the same trend as the 48V torques in the top plot of Fig. 4.9. The 12V torque curve in dotted red line increases with an increasing negative 12V d -axis currents due to the term $-L_{qq1} \frac{N_{s2}}{N_{s1}} i_{qs2} i_{ds1}$ from equation (4.2.0.1). The 48V q -axis current is set to the negative value of -50 A. When multiplied with an increasing negative value of i_{ds1} and the inductance term $-L_{qq1} \frac{N_{s2}}{N_{s1}}$, the cross-reluctance torque component increases into the negative values. Therefore a positive q -axis current is required to compensate the cross-reluctance torque component and set the torque reference of 5 Nm. As a result the torque curve increases with an increasing negative d -axis current values. The course of the torque curve in a dashed red line for the 48V current references of $i_{ds2} = 50$ Nm and $i_{qs2} = 50$ A can be explained following a similar logic³.

From Fig. 4.9 becomes evident that the optimal MTPA curve tilts left or right with respect to the operation of the other stator system. When the other stator system is operated in motor mode its q -axis current is positive and therefore the optimal MTPA curve tilts left in relation to the MTPA curve, when the other system is idle. The optimal curve tilts left, because a negative d -axis current is required to set the positive torque reference with optimal currents. The opposite behavior is observable, when the other system is operated in generator mode. Then the MTPA curve tilts right. In this case a positive d -axis current is required in order to minimize the losses and contribute to the motoring torque generation of the winding.

The performed graphical analysis for both torque equations prove that the interaction of both systems is strong, when the d -axis currents are increased either in the positive or negative directions. The resulting *cross-reluctance torque* component influences the

³This behavior is explained with the following terms from the cross-reluctance torque equations: $L_{dd1} \frac{N_{s2}}{N_{s1}} i_{ds1} i_{qs2}$ or $L_{dd1} \frac{N_{s2}}{N_{s1}} i_{ds2} i_{qs1}$

torque production of each stator system. Therefore the current references have to be adapted when the other system changes its reference torque.

In the BS range the d -axis currents are small in comparison with the employed negative d -axis currents in the FW area. Figure 4.9 includes the optimal current trajectories for the BS range. The 12V MTPA curve is calculated in the (i_{ds1}, i_{qs1}) -plane with the assumption of the field and 48V stator currents being fixed. The 48V MTPA trajectory is plotted in the (i_{ds2}, i_{qs2}) -plane with fixed values for the field winding current and the 12V stator currents. The equations for the MTPA curves as a function of the currents, flowing in the second stator system, are derived based on the optimization problem in equation (4.2.0.3). The corresponding Lagrange functions are provided in equations (4.2.0.4) and (4.2.0.5).

$$\mathcal{L}(i_{ds1}, i_{qs1}, \lambda_1)_{|i_{ds2}, i_{qs2}, i_{fd}=const} = P_{co}(i_{ds1}, i_{qs1}) + \lambda_1 \cdot T_e(i_{ds1}, i_{qs1})_{|T_{e12V}^*} \quad (4.2.0.4)$$

$$\mathcal{L}(i_{ds2}, i_{qs2}, \lambda_2)_{|i_{ds1}, i_{qs1}, i_{fd}=const} = P_{co}(i_{ds2}, i_{qs2}) + \lambda_2 \cdot T_e(i_{ds2}, i_{qs2})_{|T_{e48V}^*} \quad (4.2.0.5)$$

The Lagrange multiplier is eliminated, when the gradients of the Lagrange function are calculated and the MTPA curves are derived. The expression for the 12V MTPA curve is provided in equation (4.2.0.6) and the expression of the 48V MTPA curve is shown in equation (4.2.0.7). The calculation of the gradients and the derivation of the MTPA curves are straightforward and omitted here.

$$MTPA(i_{ds1}, i_{qs1}) = 3i_{ds1}r_{s1} - \frac{9N_{s1}i_{qs1}r_{s1} \left(i_{qs1} (L_{dd1} - L_{qq1}) - \frac{L_{qq1}N_{s2}i_{qs2}}{N_{s1}} \right)}{2L_{dd1}N_f i_{fd} + 3L_{dd1}N_{s1}i_{ds1} + 3L_{dd1}N_{s2}i_{ds2} - 3L_{qq1}N_{s1}i_{ds1}} \quad (4.2.0.6)$$

$$MTPA(i_{ds2}, i_{qs2}) = 3i_{ds2}r_{s2} - \frac{3i_{qs2}r_{s2} \left(i_{qs2} \left(\frac{L_{dd1}}{N_{s12}^2} - \frac{L_{qq1}}{N_{s12}^2} \right) - \frac{L_{qq1}N_{s2}i_{qs1}}{N_{s1}} \right)}{i_{ds2} \left(\frac{L_{dd1}}{N_{s12}^2} - \frac{L_{qq1}}{N_{s12}^2} \right) + \frac{2L_{dd1}N_f i_{fd}}{3N_{s2}} + \frac{L_{dd1}N_{s2}i_{ds1}}{N_{s1}}} \quad (4.2.0.7)$$

The 12V and 48V MTPCL curves can be derived in an analogous way. In this case the field winding current is variable and therefore one more Lagrange gradient⁴ after the field winding current i_{fd} is added. When the Lagrange multipliers λ_1 and λ_2 are eliminated, the equations for the MTPCL curves are derived as shown in equations (4.2.0.8) and (4.2.0.9).

⁴The additional Lagrange gradient is the partial derivative of the Lagrangian Function with respect to the field winding current i_{fd} .

$$\begin{aligned}
 MTPCL(i_{ds1}, i_{qs1}) = 3i_{qs1}r_{s1} &+ \frac{3N_{s1}i_{ds1}r_{s1} (i_{ds1} (L_{dd1} - L_{qq1})) + \frac{L_{dd1}N_{s2}i_{ds2}}{N_{s1}}}{L_{qq1}N_{s1}i_{qs1} - L_{dd1}N_{s1}i_{qs1} + L_{qq1}N_{s2}i_{qs2}} \\
 &- \frac{2L_{dd1}^2N_f^2i_{ds1}i_{qs1}r_{s1}}{3N_{s1}r_f} \quad (4.2.0.8)
 \end{aligned}$$

$$\begin{aligned}
 MTPCL(i_{ds2}, i_{qs2}) = 3i_{qs2}r_{s2} &+ \frac{3N_{s1}i_{ds2}r_{s2} \left(i_{ds2} \left(\frac{L_{dd1}}{N_{s12}^2} - \frac{L_{qq1}}{N_{s12}^2} \right) + \frac{L_{dd1}N_{s2}i_{ds1}}{N_{s1}} \right)}{L_{qq1}N_{s2}i_{qs1} - \frac{L_{dd1}}{N_{s12}^2}N_{s1}i_{qs2} + \frac{L_{qq1}}{N_{s12}^2}N_{s1}i_{qs2}} \\
 &- \frac{2\frac{L_{dd1}}{N_{s12}^2}^2N_f^2N_{s1}i_{ds2}i_{qs2}r_{s2}}{3N_{s2}r_f} \quad (4.2.0.9)
 \end{aligned}$$

In a conclusion, both stator systems interfere with each through the *cross-reluctance torque*, which influences the choice of the optimal operating points. When both stator windings are operated in the same mode the reluctance torque component is increased. When the windings operate in opposite modes, the *cross-reluctance torque* component counteracts the reluctance torque generated by the winding. Therefore the whole reluctance torque component is decreased. Therefore the operation of the machine in a mixed-mode is less efficient than the operation of both windings in the same mode.

Though the illustrated torque curves in Fig. 4.9 are based on linear inductances and thus no influence of all five currents on the saturation of the inductances is considered, it is evident that both torque equations are dependent on each other mainly due to the common rotor magnetic flux produced by the field winding and to some extent due to the *cross-reluctance torque*. In the search of the optimal current operating points a compromise has to be made between both systems in terms of the minimization of the whole copper losses and maintaining the torque references. The plotted torque references, 20 Nm and 5 Nm, are exactly in the ratio 1 to 4, which is in favor of the whole losses minimization. The optimal field winding current for these torque references is similar because the torque references are in the ratio 1 to 4. In this case the second torque reference does not influence much the choice of the optimal current references for the first system.

This is however not valid for a lot of other operating points, where, for example, one winding has to be operated at lower power outcome and the other winding has to deliver its maximum possible power. Then, the efficiency of the whole system is expected to drop and the optimal current references have to be chosen such, that the torque references are maintained. The winding, which is operated at maximum power, determines the field winding current reference. The other one, which has to operate at lower power, can regulate its power outcome through reduction of the stator currents. In this case, the choice of the stator current reference points has to be accurate in order not to generate any unwanted torque.

The presented analysis on the optimal choice of the current references presume, that the optimal control of the dual-voltage machine is a compromise between how both sides are operated. The control can be influenced a lot, in terms of whole efficiency, from the upper control strategy, which selects the torque references.

In this work the scope is limited to the choice of the optimal current references bounded by both torque requests from the higher control strategy. For this purpose the optimization problem in equation (4.2.0.3) is solved numerically with a Matlab script, which looks for the optimal current references. Before the numerical optimization is handled, the torque control in the FW mode for the dual-voltage machine is discussed based on the linear machine model in Section 4.3.

4.3 Torque Control in the Field-Weakening Region for the Dual-Voltage Machine

4.3.1 Torque Control with Linear Parameters

The optimal control problem set up in equation (4.2.0.3) is bounded by both torque references. The DC voltage limits do not restrict the choice of the optimal current references in the BS range. In the case of the dual-voltage machine each three-phase winding is connected to a separate DC voltage source and thus has its own power limitations in terms of maximum available DC current and voltage. The limitation by the DC link voltage is a challenging task in the FW area, because the voltage limits are expressed as ellipses in the (i_{ds1}, i_{qs1}) - and (i_{ds2}, i_{qs2}) -planes. Both torque equations, (4.2.0.1) and (4.2.0.2), are coupled through the field winding current and through the stator currents due to the *cross-reluctance torque*. In the voltage equations the dependence of both three-phase systems on each other is even more complicated. The field winding current and the d -axis current from the other system define the position of the voltage ellipse's center along the d -axis. In contrast to the conventional EESM the voltage ellipses of the dual-voltage machine can be shifted also along the q -axis. This is due to the influence of the q -axis current to the other sub-system. In order to analyze how the control of the dual-voltage machine is restricted by the DC link voltages at the 12V and 48V sides, the voltage equations for both sides are written out based on the linearized machine model from Chapter 3 defined through equations (3.2.1.2) to (3.2.1.5). The dynamic terms are not relevant for the optimization problems and are omitted from the voltage equations. The steady state voltage equations, limited by the maximum DC link voltages, are shown in equations (4.3.1.1) and (4.3.1.2).

$$v_{qs1}^2 + v_{ds1}^2 = \left(r_{s1} i_{qs1} + \omega_e \left[(L_{ls1} + L_{dd1}) i_{ds1} + \frac{L_{dd1}}{N_{s12}} i_{ds2} + \frac{2}{3} \frac{L_{dd1}}{N_{s1f}} i_{fd} + \lambda_{mag1} \right] \right)^2 + \left(r_{s1} i_{ds1} - \omega_e \left[(L_{ls1} + L_{qq1}) i_{qs1} + \frac{L_{qq1}}{N_{s12}} i_{qs2} \right] \right)^2 \leq \frac{V_{12V,DC}^2}{3} \quad (4.3.1.1)$$

$$v_{qs2}^2 + v_{ds2}^2 = \left(r_{s2} i_{qs2} + \omega_e \left[(L_{ls2} + \frac{L_{dd1}}{N_{s12}^2}) i_{ds2} + \frac{L_{dd1}}{N_{s12}} i_{ds1} + \frac{2}{3} \frac{L_{dd1}}{N_{s1f} N_{s12}} i_{fd} + \lambda_{mag2} \right] \right)^2 + \left(r_{s2} i_{ds2} - \omega_e \left[(L_{ls2} + \frac{L_{qq1}}{N_{s12}^2}) i_{qs2} + \frac{L_{qq1}}{N_{s12}} i_{qs1} \right] \right)^2 \leq \frac{V_{48V,DC}^2}{3} \quad (4.3.1.2)$$

Equations (4.3.1.1) and (4.3.1.2) show that, besides the field winding current also the d -axis current of the other winding defines the center of the voltage ellipse along the d -axis. The q -axis current of the other system also influences the voltage ellipse's center with respect to the q -axis in a similar manner. In order to analyze how the currents of the other stator system influence the optimal choice of working points in the FW area, the centers of the voltage ellipses are calculated. Equations (4.3.1.1) and (4.3.1.2) are

compared to the general equation of a shifted ellipse provided in (4.3.1.3) in order to identify a formula for the centers of the voltage ellipses⁵.

$$\frac{(x - c_1)^2}{a^2} + \frac{(y - c_2)^2}{b^2} = 1 \quad (4.3.1.3)$$

The centers of the voltage ellipses, denoted by the points c_{12V} and c_{48V} in the x-y Cartesian coordinate system, are identified for each of the voltage equations after a mathematical reformulation. The centers are described by equations (4.3.1.4) and (4.3.1.5)⁶. The centers of the voltage ellipses depend on the d - and q -axis inductances and the currents of the other system. It is important to visualize this dependency in order to comprehend how both windings limit each others operating points in the FW area.

$$c_{12v}(i_{ds1}, i_{qs1}) = (c_1, c_2) = \left(-\frac{\frac{L_{dd1}}{N_{s12}} \cdot i_{ds2} + \frac{2}{3} \frac{L_{dd1}}{N_{s1f}} i_{fd}}{L_{ls1} + L_{dd1}}, -\frac{\frac{L_{qq1}}{N_{s12}} i_{qs2}}{L_{ls1} + L_{qq1}} \right) \quad (4.3.1.4)$$

$$c_{48v}(i_{ds2}, i_{qs2}) = (c_1, c_2) = \left(-\frac{\frac{L_{dd1}}{N_{s12}} \cdot i_{ds1} + \frac{2}{3} \frac{L_{dd1}}{N_{s1f} N_{s12}} i_{fd}}{L_{ls2} + \frac{L_{dd1}}{N_{s12}^2}}, -\frac{\frac{L_{qq1}}{N_{s12}}}{L_{ls2} + \frac{L_{qq1}}{N_{s12}^2}} \right) \quad (4.3.1.5)$$

In order to analyze how the feasible working points are limited in the field weakening area by the voltage ellipses, three different cases are plotted for the 12V and 48V sides. In all three cases the speed is kept constant at 4500 rpm and the DC voltages at both sides are also set to constant values: $V_{DCLV} = 12 \text{ V}$ and $V_{DCHV} = 48 \text{ V}$. The first case is illustrated for torque references at both sides of 0 Nm: $T_{e12V}^* = 0 \text{ Nm}$ and $T_{e48V}^* = 0 \text{ Nm}$. The second case illustrates torque references in generator mode with torque references of $T_{e12V}^* = -2 \text{ Nm}$ and $T_{e48V}^* = -8 \text{ Nm}$. The third case represents constant torque curves in motor mode with torque references of $T_{e12V}^* = 6 \text{ Nm}$ and $T_{e48V}^* = 2 \text{ Nm}$. In all three cases the other side is operated at a certain constant field weakening d -axis current and three different q -axis currents: a positive q -axis current, a zero q -axis current and a negative q -axis current. The q -axis current is the torque building current component and is used to control the active power of the winding. Through the variation of the q -axis current of the other side the influence on the voltage ellipses is visualized. This way the feasible working points as a function of the currents in the other stator system are visualized. All parameters used for the plotting of the voltage ellipses and torque curves are provided already in Table 2.1. The main inductances are set to $\frac{2}{3}$ of their unsaturated values. The analyses are performed based on the linearized voltage and torque equations. The

⁵The voltage drops over the stator resistances are omitted in this comparison because they do not fit to the ellipses equation. This simplification is tolerable at higher speeds, which is conformed by the next graphical plots.

⁶The voltage equations do not represent exactly ellipses, because the voltage drops over the resistances do not fit to the pure form of an ellipse equation. However, the equations are very close to the form of an ellipse and are therefore denoted in this work as voltage ellipses. This is also a common practice in the state of the art literature.

4 Torque and Power Control Development

saturation of the main inductance has to be taken into account in the calculation of the working points for the dual-voltage machine in order to predict accurately the generated torque.

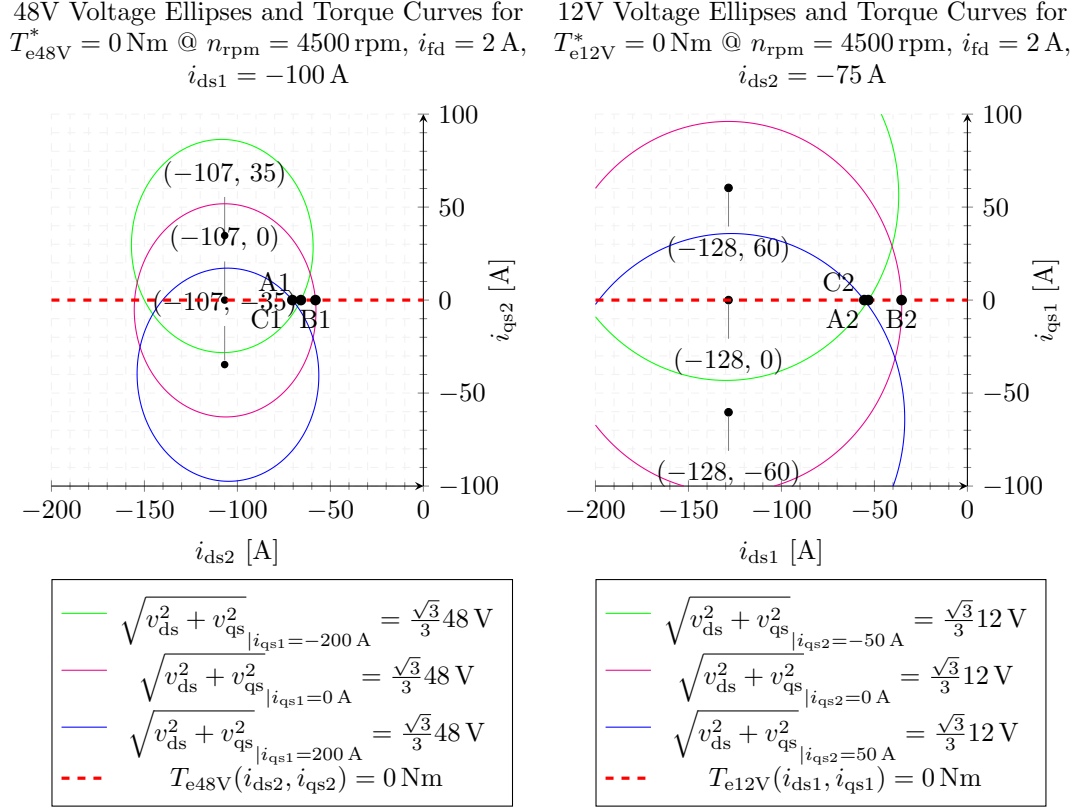


Figure 4.10 – Voltage Ellipses for the Dual-Voltage Machine, $i_{fd} = 2 \text{ A}$ and $n_{rpm} = 4500 \text{ rpm}$ and zero torque control

The voltage ellipses are plotted in both planes for the 12V and the 48V side in Fig. 4.10 along with the constant torque curve for 0Nm torque reference. The left plot in Fig. 4.10 shows the voltage ellipses for the 48V side, while the 12V side is set through the q -axis current in generator, idle and motor mode. The 48V torque curve is plotted also according to equation (4.2.0.2). The field weakening d -axis current i_{ds1} is set to -100 A in all three cases. The 48V voltage ellipse is plotted in a solid magenta line for a 12V q -axis current of 0 A. The constant torque curve matches with the negative 48V d -axis. In order to control the 48V side to zero torque, a certain negative 48V d -axis current is required. The negative d -axis current weakens the magnetic field generated by the field winding. The optimal current vector is the crossing point of the constant torque line for 0Nm and the corresponding voltage ellipse. The optimal point for this case is marked in the plot with **B1**. The optimal point in this case is similar to a machine with only one stator system, because the q -axis current of the 12V side does not influence the voltage

ellipses. The voltage ellipse is plotted with a solid green line for a negative 12V q -axis current of -200 A. The voltage ellipse is shifted towards positive q -axis current values, according to equation (4.3.1.5), which describes the center of the 48V voltage ellipses. Therefore the optimal point **A1** in the left plot of Fig. 4.10 marks the optimal current vector for the 48V side under these conditions. The point **A1** lies left in respect to the point **B1**. The 48V voltage ellipse are plotted also for a motoring 12V q -axis current of 200 A in blue. The optimal operating point in the (i_{ds2}, i_{qs2}) -plane is marked with **C1**, which is close to the point **A1**. This is due to the fact that the voltage ellipse for the q -current of 200 A is almost symmetrical in respect to the d -axis with the voltage ellipse plotted in green.

The 12V voltage ellipses and torque curve for a reference of 0 Nm are plotted in the right plot of Fig. 4.10. The 48V q -axis current is adjusted to set the 48V winding in generator, idle and motor mode through the following reference currents: -50 A, 0 A and 50 A. The results are similar to the ones for the 48V side. The optimal points are marked with **A2**, **B2** and **C2**.

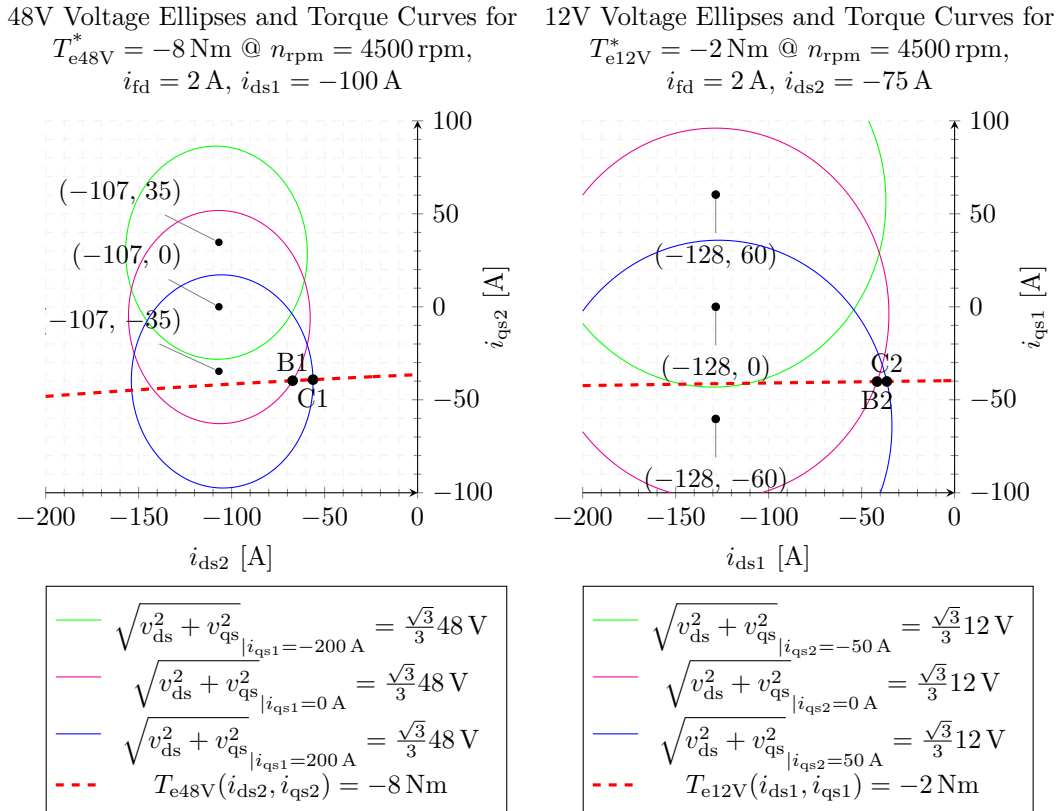


Figure 4.11 – Voltage Ellipses for the Dual-Voltage Machine, $i_{fd} = 2$ A and $n_{rpm} = 4500$ rpm and generative torque control

Figure 4.11 illustrates the voltage ellipses and the torque curves for negative 12V and 48V torque references. The left plot shows the 48V torque curve for a reference of -8 Nm and three different voltage ellipses. The voltage ellipse is plotted in a solid magenta line for a q -axis current of a 0 A . The torque curve intersects the voltage ellipse at point **B1**. Point **B1** represents the optimal current vector in the FW area. The voltage ellipse is plotted for a negative 12V q -axis current of -200 A in a solid green line. The negative q -axis current shifts the center of the voltage ellipse towards positive 48V q -axis currents. The torque curve does not intersect the green voltage ellipse and therefore the torque reference of -8 Nm is not feasible, when the 12V side is operated in generator mode with a current of -200 A . The voltage ellipse is plotted for a positive 12V q -axis current of 200 A in solid blue line. The ellipse is shifted towards negative 48V d -axis currents. Under these boundaries the torque reference of -8 Nm is feasible. The optimal current vector is marked with point **C1**, where the torque reference intersects the voltage ellipse. The field weakening angle at point **C1** is smaller than the field weakening angle at point **B1**.

The analogous cases for the 12V side are plotted in the right plot of Fig. 4.11. The 12V torque curve is plotted for a reference of -2 Nm . The same trend is evident also for the 12V side. The voltage ellipses are plotted for 48V q -axis currents of 50 A , 0 A and -50 A . The analysis for the 12V side are omitted here due to their analogy with the already performed analysis for the 48V side.

The last case, which is analyzed, is the setting of a motoring torque by each of the windings in the FW mode. Figure 4.12 shows the voltage ellipses and torque curves in the FW area for motoring 12V and 48V torque references. The left plot shows the 48V torque reference of 6 Nm and the voltage ellipses for 12V q -axis currents of -200 A , 0 A and 200 A . A negative 12V q -axis current shifts the 48V voltage ellipse towards positive 48V q -axis currents. When the 12V q -axis current is positive, the ellipse is shifted towards the negative 48V q -axis currents. If the 12V q -axis current is set to 200 A the torque reference is not anymore feasible. The voltage ellipse in blue with the torque reference in dashed red line do not have any intersection point. The points **A1** and **B1** mark the optimal current vectors for the negative q -axis current of -200 A and the q -axis current of 0 A respectively. The 12V torque curve in motor mode and the voltage ellipses are included on the right for the sake of completeness and follow the same trend.

The selection of the negative 48V d -axis current i_{ds2} is crucial for the operation of the 12V side in the FW region. The 12V side cannot weaken fully the magnetic flux produced by the rotor and the weakening is achieved mainly thanks to the 48V current. The fact that the 12V leakage inductance, $L_{ls1} \approx 10\text{ }\mu\text{H}$, is non-negligible in comparison to the 12V d -axis main inductance, $L_{dd1} \approx 14\text{ }\mu\text{H}$, is beneficial for the operation of the 12V winding in the FW area. The field weakening effect of the negative 12V d -axis current is increased this way according to equation (4.3.1.1) due to the sum of both inductances: $L_{ls1} + L_{dd1}$.

The performed brief analysis in the FW area for the dual-voltage machine show the implicit dependency of each side on the other in terms of feasible operating points. The

4.3 Torque Control in the FW Range for the Dual-Voltage Machine

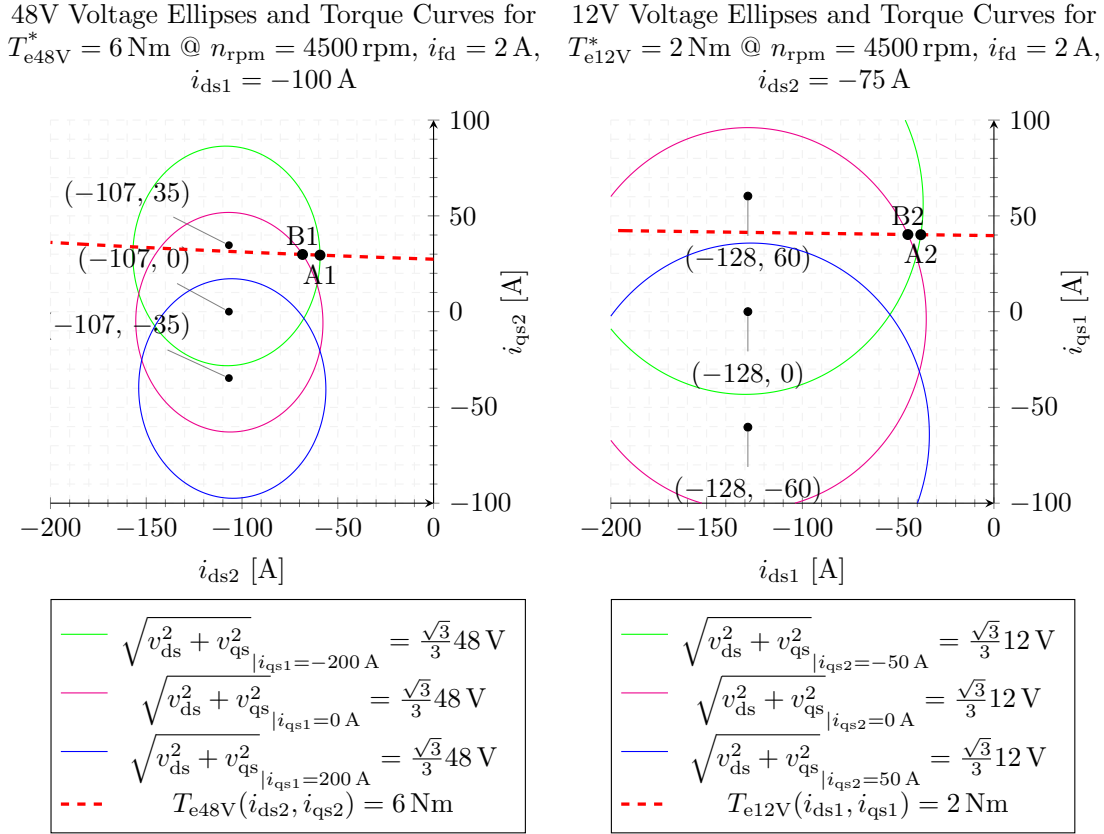


Figure 4.12 – Voltage Ellipses for the Dual-Voltage Machine, $i_{fd} = 2 \text{ A}$ and $n_{rpm} = 4500 \text{ rpm}$ and motoring torque control

optimal torque control problem is a five dimensional one and therefore impossible to be visualized in one graph. In order to make visual analysis possible, the voltage ellipses and torque curves are plotted for each side separately, while the other stator winding is operated in three different operating modes: a generator, an idle and a motor mode. This way the dependency of each side on the operation of the other can be illustrated. The analysis do not include any saturation effects of the main inductance and therefore only serve as a qualitative statement. The conclusions made based on the linearized machine equations show the general dependency of the stator windings on each other. Similar trends should be observed also when the optimal working points are calculated based on a saturation data. The derived conclusions are checked for plausibility later with the performed simulations and measurements. The saturation of the main inductance is taken into account during the calculation of the optimal currents references. The working points for the dual-voltage machine are calculated offline through a Matlab optimization script based on non-linear data for the main inductance. The areas of feasible working points are expected to behave in the same way for the offline calculated points as the linear analysis indicates.

In a summary it can be concluded that, when both sides operate in the same modes a greater field weakening angle is required. When both sides operate in opposite modes the field weakening angle is less due to the shifting of the voltage ellipses along the q -axis. When one of the sides is operated at load in generator mode and the other side has to maintain a zero torque reference a positive q -axis current is required in the FW area. This effect is specific to the dual-voltage machine due to the *cross-reluctance* torque generated between both stator systems. In case one side is operated in a motor mode and the other winding has to be controlled to a zero torque reference, then a negative q -axis current is required in the other winding in order to compensate the *cross-reluctance* torque.

4.3.2 Torque Control with Non-Linear Parameters

The presented linear analysis for the torque control problem provides an insight into the feasible working point areas in the d - q plane. In order to accurately calculate the generated torque from the machine, the saturation behavior has to be considered. The saturation of the main inductance is highly non-linear and often provided as data in form of a LUT. Therefore the employment of non-linear optimization methods is inevitable. The non-linear programming algorithm has to search for the optimal current references under the non-linear boundaries. The optimization problem, which describes the optimal torque control problem, is formulated through equation (4.3.2.1). The losses of the machine have to be minimized and the voltage and torque conditions satisfied.

min.:

$$P_{\text{co}} = \frac{3}{2} \cdot r_{s1} \cdot (i_{qs1}^2 + i_{ds1}^2) + \frac{3}{2} \cdot r_{s2} \cdot (i_{qs2}^2 + i_{ds2}^2) + r_f i_{fd}^2$$

subj. to :

$$T_{e12V} = \frac{3}{2} \cdot p \cdot \left(\left(L_{dd1} \frac{2N_f}{3N_{s1}} i_{fd} + L_{dd1} i_{\text{mag}12V} \right) i_{qs1} + (L_{dd1} - L_{qq1}) i_{ds1} i_{qs1} \right. \\ \left. + (L_{dd1} - L_{qq1}) \frac{N_{s2}}{N_{s1}} i_{ds2} i_{qs1} \right) - T_{e12V}^* = 0$$

$$T_{e48V} = \frac{3}{2} \cdot p \cdot \left(\left(\frac{L_{dd1}}{N_{s12}^2} \frac{2N_f}{3N_{s2}} i_{fd} + \frac{L_{dd1}}{N_{s12}^2} i_{\text{mag}48V} \right) i_{qs2} + \left(\frac{L_{dd1}}{N_{s12}^2} - \frac{L_{qq1}}{N_{s12}^2} \right) i_{ds2} i_{qs2} \right. \\ \left. + (L_{dd1} - L_{qq1}) \frac{N_{s2}}{N_{s1}} i_{ds1} i_{qs2} \right) - T_{e48V}^* = 0$$

$$v_{qs1}^2 + v_{ds1}^2 = \left(r_{s1} i_{qs1} + \omega_e \left[(L_{ls1} + L_{dd1}) i_{ds1} + \frac{L_{dd1}}{N_{s12}} i_{ds2} + \frac{2}{3} \frac{L_{dd1}}{N_{s1f}} i_{fd} + L_{dd1} i_{\text{mag}12V} \right] \right)^2 \\ + \left(r_{s1} i_{ds1} - \omega_e \left[(L_{ls1} + L_{qq1}) i_{qs1} + \frac{L_{qq1}}{N_{s12}} i_{qs2} \right] \right)^2 \leq \frac{V_{12V,DC}^2}{3}$$

$$\begin{aligned}
 v_{qs2}^2 + v_{ds2}^2 = & \left(r_{s2} i_{qs2} + \omega_e \left[\left(L_{ls2} + \frac{L_{dd1}}{N_{s12}^2} \right) i_{ds2} + \frac{L_{dd1}}{N_{s12}} i_{ds1} + \frac{2}{3} \frac{L_{dd1}}{N_{s1f} N_{s12}} i_{fd} + \frac{L_{dd1}}{N_{s12}^2} i_{mag48V} \right] \right)^2 \\
 & + \left(r_{s2} i_{ds2} - \omega_e \left[\left(L_{ls2} + \frac{L_{qq1}}{N_{s12}^2} \right) i_{qs2} + \frac{L_{qq1}}{N_{s12}} i_{qs1} \right] \right)^2 \leq \frac{V_{48V,DC}^2}{3} \quad (4.3.2.1)
 \end{aligned}$$

The main inductances, L_{dd1} and L_{qq1} , depend on all five currents. The saturation behavior of the main inductances has been measured in Section 2.4 from Chapter 2. The same data is used to calculate the working points for the machine through a Matlab optimization script. It has to be noted that the saturation curves are measured only at no-load conditions and a simplification has been made to account for the cross-saturation effect occurring at load conditions. The anisotropic factor $\alpha = \sqrt{\frac{L_{qq1}}{L_{dd1}}}$ is assumed to be constant for all current values, which creates a prerequisite for inaccuracies in the torque calculation. Since no 3D-FEA inductance data is available for the machine, the measured saturation curve from Section 2.4 is used for the non-linear optimization.

The employed minimization function is called *fmincon* provided by Mathworks [48] and is able to search for optimal values under non-linear constraints. The function can handle non-linear inequality and equality constraints, which are even based on LUT data. A brief explanation of how the *fmincon* function is employed inside the Matlab script is helpful, because the function requires certain settings in order to succeed in the search for optimal working points. The provided Matlab documentation for the function describes the influence of each parameter on the search.

The *fmincon* function is mathematically described by equation (4.3.2.2) [48]. The first case $c(x)$ represents the non-linear inequality condition and accepts also a vector form. In our case this condition includes both voltage inequality conditions. This case is also extended to include the maximum possible current limits at 12V and 48V side and the maximum field winding current. The second case, $ceq(x) = 0$, handles the equality constraints and can also handle multiple equalities as a vector. Both torque references are formulated in the second case. Through the third and fourth case, $A \cdot x \leq b$ and $Aeq \cdot x = beq$, linear constraints can be included. These cases are not required, because no linear constraints are present in the optimization problem. Through the last case it is possible to limit the area for the variables to be searched over. This case is not used, because the search area for the currents is limited by the first case.

$$\min_x f(x) \text{ such that } \begin{cases} c(x) \leq 0 \\ ceq(x) = 0 \\ A \cdot x \leq b \\ Aeq \cdot x = beq \\ lb \leq x \leq ub \end{cases} \quad (4.3.2.2)$$

A short matlab code snippet is included in Listing 4.1 to demonstrate how the *fmincon* function is employed inside the optimization script.

Listing 4.1 – Settings for fmincon

```

pm = [p ue1f ue12 Rs_48V Rf Rs_12V Lls_12V Lls_48V Imag ... 1
      Te_LV Te_HV w_rpm u_max_12V u_max_48V ... 2
      mod_index_LV mod_index_HV Imax_48V Imax_12V Ierr_max ]; 3
fun = @(x) minimize_losses(x,pm); 4
A = []; b = []; 5
Aeq = []; beq = []; 6
lb = []; ub = []; 7
nonlcon = @(x) nonlin_cond_MTPF_plsaturation(x,pm,Im_arr , 8
      Psim_arr , Aniso);
options = optimset('Algorithm','interior-point','TolFun',1.0e 9
      -3,'TolX',1.0e-8,'TolCon',1e-2,'MaxIter',30000,'MaxFunEvals
      ',30000);
[x, fval, exitflag] = fmincon(fun,x0,A,b,Aeq,beq,lb,ub,nonlcon, 10
      options);

```

The vector pm contains the linear parameters used during the optimization. These are for example the constant machine parameters: the pole pairs number p , the winding ratios from stator 1 to rotor N_{s1f} and from stator 1 to stator 2 N_{s12} , the stator and rotor resistances r_{s1} , r_{s2} and r_{fd} , the leakage inductances L_{ls1} and L_{ls2} and the current offset due to the machine's permanent magnets flux i_{mag} . The torque references T_{e12V}^* and T_{e48V}^* and the maximum DC voltages $V_{12V,DC,max}$ and $V_{48V,DC,max}$ are also included in the parameter vector. New torque references and different speeds are passed through the pm vector to the optimization functions each time a new iteration of the for-loops is started. During the nonlinear search these parameters remain constant. The maximum possible modulation indices are included as parameters $M_{12V,idx}$ and $M_{48V,idx}$, which are set based on the employed modulation technique. In this case these values are set to $\frac{\sqrt{3}}{3}$, which is the maximum possible modulation index for a SVM with a third harmonic injection. The maximum possible DC current limits, $I_{12V,DC,max}$ and $I_{48V,DC,max}$, are included in the parameters vector as constant limits as well. The last entry of pm is the maximum allowed field winding current. There are two ways of handling the current limits. The current limits can be included in the optimization problem as inequality conditions, as it is done hereby, or also can be left open. After the working points are calculated, these can be filtered out to include only current references inside the maximum possible DC current limits.

The saturation data is provided in the form of an one dimensional LUT based on the measured saturation curves from Section 2.4 from Chapter 2. The saturation data are included not as inductances but as a magnetizing flux λ_{md} over magnetization current i_{md} . This representation is easier to integrate in the optimization problem because the voltage and torque equations are written out with magnetizing fluxes in a simpler form.

$$\begin{aligned}
 \min.: \quad P_{co} &= \frac{3}{2} \cdot r_{s1} \cdot (i_{qs1}^2 + i_{ds1}^2) + \frac{3}{2} \cdot r_{s2} \cdot (i_{qs2}^2 + i_{ds2}^2) + r_f i_{fd}^2 \\
 \text{subj. to: } T_{e12V} &= \frac{3}{2} \cdot p \cdot (\lambda_{md1} i_{qs1} - \lambda_{mq1} i_{ds1}) - T_{e12V}^* = 0 \\
 T_{e48V} &= \frac{3}{2} \cdot p \cdot (\lambda_{md2} i_{qs2} - \lambda_{mq2} i_{ds2}) - T_{e48V}^* = 0 \\
 v_{qs1}^2 + v_{ds1}^2 &= (r_{s1} i_{qs1} + \omega_e [L_{ls1} i_{ds1} + \lambda_{md1}])^2 \\
 &\quad + (r_{s1} i_{ds1} - \omega_e [L_{ls1} i_{qs1} + \lambda_{mq1}])^2 \leq \frac{V_{12V,DC}^2}{3} \\
 v_{qs2}^2 + v_{ds2}^2 &= (r_{s2} i_{qs2} + \omega_e [L_{ls2} i_{ds2} + \lambda_{md2}])^2 \\
 &\quad + (r_{s2} i_{ds2} - \omega_e [L_{ls2} i_{qs2} + \lambda_{mq2}])^2 \leq \frac{V_{48V,DC}^2}{3}
 \end{aligned} \tag{4.3.2.3}$$

Equation (4.3.2.3) shows the optimization problem rewritten with fluxes instead of inductances, which is equivalent to the optimization problem defined in equation (4.3.2.1). The d - and q -axis magnetizing fluxes depend on all five currents and have to be calculated based on the saturation curves. The saturation data is included as a magnetizing current array $I_{m,arr}$ and magnetizing flux array $\lambda_{m,arr}$ in reference to stator 1 (12V) aligned to the d -axis. A way is required to determine the d - and q -axis magnetizing fluxes based on all five currents. In order to use these arrays, the d - and q -axis currents are converted into one magnetizing currents vector. First, an effective d -axis current in reference to the 12V side is calculated I_{dLV}^{eff} . The 12V current i_{ds1} is summed to the effective current without any scaling. The field winding current i_{fd} and the 48V d -axis current, i_{ds2} , are scaled through the corresponding winding ratios and summed to the effective d -axis current as shown in equation (4.3.2.4). A current offset i_{mag} is added also to account for the small amount of permanent magnetic flux produced by the magnets placed inbetween the claws of the rotor. The effective q -axis current is calculated in a similar way. Along the q -axis only two currents influence the generated flux: i_{qs1} and i_{qs2} . The current i_{qs1} is summed without scaling to I_{qLV}^{eff} and the q -axis current of the 48V side, i_{qs2} , is scaled with the winding ratio $N_{s21} = \frac{1}{N_{s12}}$ as shown in equation (4.3.2.4). The anisotropic factor from equation (4.3.2.4) is defined as $\alpha = \sqrt{L_{mq}/L_{md}}$. It is used to calculate the scaled effective q -axis current referred to the 12V side. This principle is described as the conversion of a machine from an anisotropic one to an isotropic one without saliency [44]. Based on the calculated magnetizing current vector, $I_{LV,vec}^{eff,scaled}$, which includes the influence of all currents, the magnetizing flux vector $\lambda_{m,vecLV}$ is interpolated from the measurement data.

$$\begin{aligned}
 I_{dLV}^{eff} &= \frac{1}{N_{s1f}} \cdot \frac{2}{3} \cdot i_{fd} + i_{ds1} + \frac{1}{N_{s12}} i_{ds2} + i_{mag} & I_{qLV}^{eff} &= i_{qs1} + \frac{1}{N_{s12}} \cdot i_{qs2} \\
 I_{qLV}^{eff,scaled} &= I_{qLV}^{eff} \cdot \alpha & I_{LV,vec}^{eff,scaled} &= \sqrt{I_{dLV}^{eff\ 2} + I_{qLV}^{eff,scaled\ 2}}
 \end{aligned} \tag{4.3.2.4}$$

The voltage and torque equations require nonetheless the absolute magnetizing fluxes along the d - and q -axis. Therefore the flux vector, $\lambda_{m,vecLV}$, has to be decomposed along both orthogonal axis. The magnetizing fluxes in q - and d -direction, λ_{mq1} and λ_{md1} , are calculated from the magnetizing flux vector $\lambda_{m,vecLV}$ and the angle between the d - and q -axis effective currents, φ_{eff} , according to the Pythagoras' formula. In order to derive the real value of the q -axis flux λ_{mq1} , the q -axis component of the magnetizing flux vector has to be scaled with the anisotropic coefficient α . The formulas, used to decompose the magnetizing flux vector $\lambda_{m,vecLV}$ into d - and q -axis fluxes, are summarized in equation (4.3.2.5).

$$\varphi_{eff} = \arctan\left(\frac{I_{qLV}^{eff}}{I_{dLV}^{eff}}\right) \quad \lambda_{mq1} = \alpha \cdot \sin(\varphi_{eff}) \cdot \lambda_{mvec} \quad \lambda_{md1} = \cos \varphi_{eff} \cdot \lambda_{mvec} \quad (4.3.2.5)$$

It is obvious that the so defined optimization problem relies highly on the parameters of the machine model. Therefore it is very important to determine as accurately as possible all parameters describing the saturation behavior. For example, the turn ratio from stator to rotor N_{s1f} can dramatically influence the choice of the optimal field winding current and thus impact on the torque accuracy. Also the other parameters, which describe the saturation curve: the unsaturated inductance, L_{md0} , the transition flux λ_T , the saturated inductance L_{mds} and the form factor f_T , have to be selected carefully during the characterization of the model. All parameters are crucial in order to predict the generated torque as close as possible to the measured one in the whole operating range. Further, even if the parameters are derived accurately, one simplification is made in the model. The saturation modeling presumes that the anisotropic factor is constant throughout all saturation levels. It is interesting to examine later, how this simplification impacts on the accuracy of the torque prediction observed during the measurements.

The presented equations, used to calculate the saturated fluxes, are integrated in the function *nonlin_cond_MTPF_plsaturation* from Listing 4.1, which calculates the torque and voltage equations based on the nonlinear flux data. The function *minimize_losses* from Listing 4.1 calculates the copper losses, which have to be minimized. The copper losses are provided in equation (4.3.2.1).

The *fmincon* function requires certain settings to be adjusted in order to deliver useful results. The options for the *fmincon* function, which contains the non-linear programming solver, are set through the *optimset* function. The selected options are very important and should be chosen appropriately for the defined optimization problem and based on the knowledge about the non-linear constraints. The settings defined through *optimset* are crucial for the solver in order to succeed and find the optimal current references. The selected algorithm is *interior-point*, because it can handle piece-wise differentiable functions. This is true for the defined optimization problem, because the magnetizing flux data is stored as a LUT and interpolated with a *spline* function. The *spline* interpolation method is used to interpolate the flux between the measured data points. The used

interpolation method is also crucial for the optimization algorithm in order to succeed because only the cubic *spline* method is twice continuously differentiable. This is a necessary condition for the solver of *fmincon* in order to calculate the required gradients for the search and to find local minima. The parameter *TolFun* sets the required accuracy for the minimization function, which in this case is 0,1 %. If the required accuracy is too fine, the nonlinear optimization may not succeed to find an optimum. This parameter has to be chosen according to the application requirements. The parameter *TolX* sets the step size over the currents vector \vec{x} , until which the algorithm continues to search. If the settings for the non-linear optimization are adequately chosen, the algorithm stops far from the minimum possible step size. In general, if all settings are appropriate, an optimal point is found in a couple of iterations. The parameter *TolCon* has the same meaning as *TolFun* but is applied to the nonlinear constraints. In this case these are the maximum possible voltage limits and the requested torque references. This parameter is set also to 1 %, which means that the boundaries are met within 1 % tolerance. The rest of the settings are self explaining.

The parameter *x0* in the *fmincon* function call denotes the initial starting point for the search. The script works well with the zero vector $\vec{0}$ as a starting point. The optimization script performs faster if the starting point is iteratively chosen close to previous solution in nearby torque references. The outputs of *fmincon* include the optimal values in the vector \vec{x} . The value of the copper losses at the optimal currents vector in *fval* and an *exitflag*, which denotes if the optimization has succeeded. A value of 1 denotes that an optimum is found.

Though the presented numerical optimization is able to find the optimal working points in the BS range, there are some issues in the FW range, which have to be solved in order the numerical optimization to succeed in a reasonable time span. Above the *corner speed* for the machine the FW region starts and the maximum torques of each winding are not anymore feasible. Above this speed the constant power region for the machine begins and both windings are limited by the maximum power outcome they can provide. Therefore it is meaningless to force the optimization algorithm to search for working points, which are physically not possible. This issue can be solved in two ways. The first way is to store the optimal values of the minimum and maximum feasible torque references from the last speed loop and start in the next iteration of the speed loop from these values⁷. The second way to deal with this issue is to convert the maximum possible power of the machine for each speed in equivalent torque references and limit the search for the optimal working points between these minimum and maximum torque references. The maximum possible torque references are then stored over the speed range for the 12V and 48V side as an array in an one dimensional LUT.

The structure of the implemented torque control based on offline calculated working points is schematically presented in Fig. 4.13. The requested torque references are limited

⁷Even if the initial guess is not fulfilling the boundaries, for example it lies outside the feasible voltage limits in the FW area, but is close to the optimal point the *interior-point* algorithm is able to find the optimal point in a couple of iterations

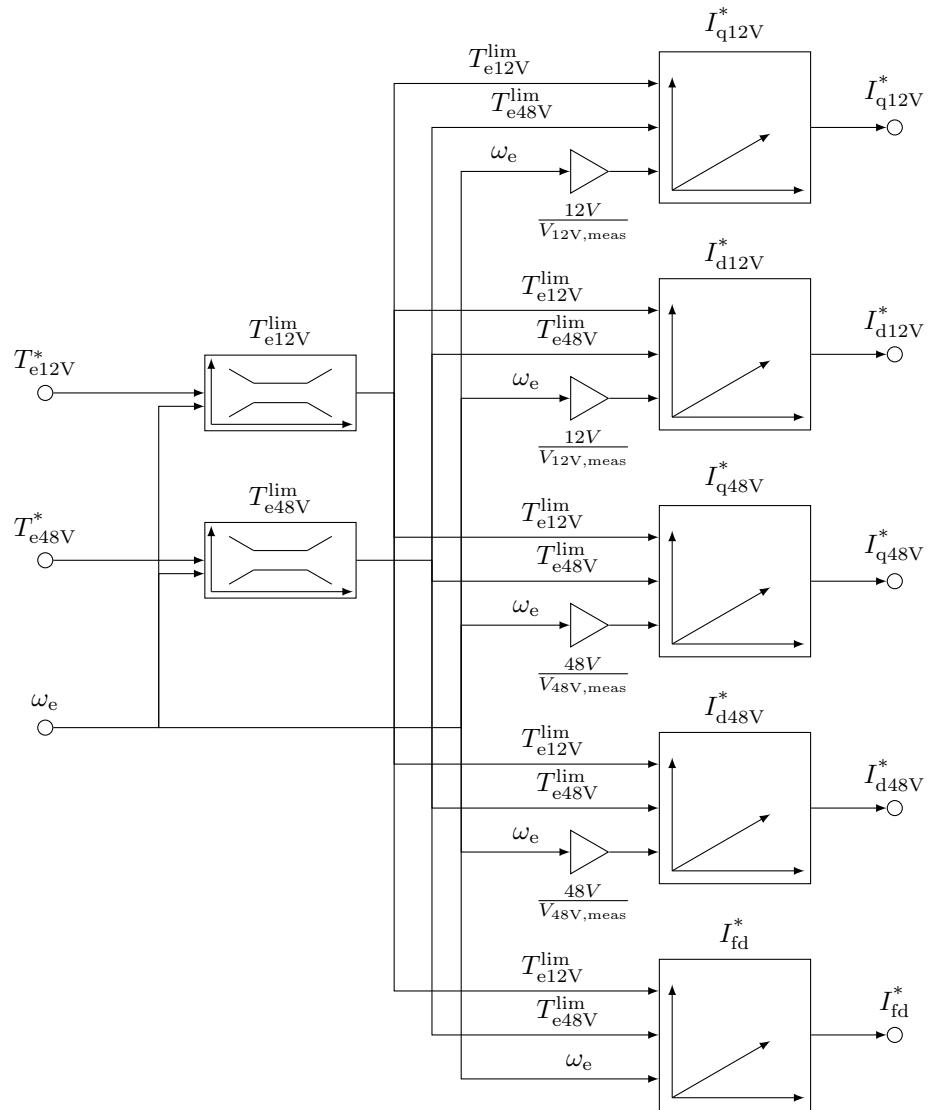


Figure 4.13 – Working Points

by the maximum feasible torques in correspondence to the currently measured speed. The limited torque references are then forwarded to the LUTs, which select the optimal current references calculated offline with *fmincon*. This way only feasible working points are requested from the inner current control loop. The right side of Fig. 4.13 shows the LUTs, where the offline calculated current references, I_{q12V}^* , I_{d12V}^* , I_{q48V}^* , I_{d48V}^* and I_{fd}^* , are stored. These current references are adjusted as a function of both torque references, T_{e12V}^* and T_{e48V}^* , and the actual electrical speed ω_e . The script calculates working points only for constant DC link voltages. For the 12V side the used voltage source is set fixed at 12 V and for the 48V side at 48 V. In reality a battery voltage can vary from 36 V

4.3 Torque Control in the FW Range for the Dual-Voltage Machine

to 54 V for the 48V side and from 10 V to 15 V for the 12V side ⁸. Therefore the actual electrical speed ω_e is scaled with the ratio of the constant DC link voltage, for which the working points have been calculated, and the measured DC link voltage: $ratio_{48V} = \frac{48V}{V_{DCHV}}$ and $ratio_{12V} = \frac{12V}{V_{DCLV}}$. This workaround is required because a LUT with more than 3 dimensions cannot be implemented on a RCP system and is also too extensive in terms of used processor memory.

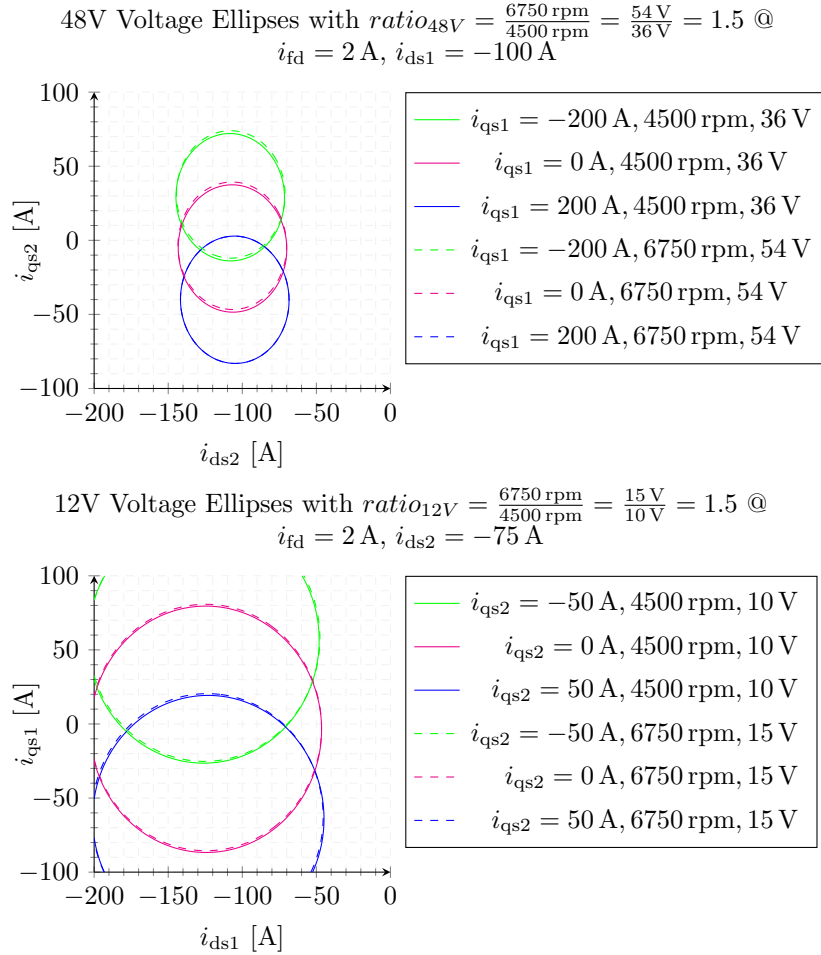


Figure 4.14 – Voltage Ellipses at variable DC Link Voltages

In order to demonstrate that this method correctly handles the variable DC link voltage, the voltage ellipses are plotted for two different speeds and DC link voltages, which are exactly in the same ratio. Figure 4.14 illustrates the 12V and 48V voltage ellipses. The voltage ellipses in the top plot of Fig. 4.14 are plotted for the 48V side. The voltage

⁸The voltage range depends on the employed battery technology and the State of Charge (SOC) of the battery and can vary for each application. Typical values for the 48V and 12V side are assumed in this work.

ellipses are plotted once with a solid line for a DC link voltage of 36 V and a speed of 4500 rpm and once with a dashed line for a DC link voltage of 54 V and a speed of 6750 rpm. The voltages and speeds are exactly in the ratio of 1,5. It becomes evident from the graphs that all three ellipses coincide with each other and therefore the feasible operating areas in the FW range for both cases are the same. The same is valid for the 12V side voltage ellipses, which are plotted in the bottom plot. The voltage at the 12V side is once set to 10 V for a speed of 4500 rpm and once to 15 V for a speed of 6750 rpm. The dashed and solid lines coincide with each other, which means that in both cases the feasible operating area at the 12V side is the same.

The current section explains the implemented torque control for the dual-voltage machine. As a next step the implemented control is tested in a simulation environment.

4.4 Simulations and Measurements in the BS Range

The implemented torque control with two torque references, T_{e12V}^* and T_{e48V}^* , is tested first in the simulation environment and afterwards on a test bench. The torque control tests are performed first in the BS range. The DC link voltages do not restrict the current controllers and they are always able to set the requested current references regardless of their values. The tests in the BS range are performed at 1000 rpm, which is below the corner speed of 1500 rpm.

The analysis of the optimal working points becomes a very challenging task because of the interaction of all five currents. The torque equations shall be analyzed first in order to understand how each current influences the torque generation. Both torque equations are written out in equations (4.4.0.1) and (4.4.0.2) through their inductance form. The torque equations are integrated in the optimization algorithm through their flux form, because this way of representation is more convenient for the non-linear search. However this form of the torque equations, though simple, does not give any insight of how all currents interact with each other. A more beneficial representation for the analysis is the inductance form of the torque equations. The inductance form shows how each current influences the generated torque. Equations (4.4.0.1) and (4.4.0.2) are derived when both magnetizing fluxes are substituted with the product of their inductance values along the d - or q -axis and all currents contributing to the magnetizing currents along the d - or q -axis. The derivation is already explained through equations (4.2.0.1) and (4.2.0.2).

$$\begin{aligned}
 T_{e12V}^* = \frac{3}{2}p \left(\underbrace{\left(L_{dd1} \frac{2N_f}{3N_{s1}} i_{fd} + \lambda_{mag1} \right) i_{qs1}}_{\text{synch. torque}} + \underbrace{(L_{dd1} - L_{qq1}) i_{ds1} i_{qs1}}_{\text{reluctance torque}} \right. \\
 \left. + \underbrace{(L_{dd1} - L_{qq1}) \frac{i_{ds2}}{N_{s12}} i_{qs1}}_{\text{cross-rel. torque}} \right)
 \end{aligned} \tag{4.4.0.1}$$

$$\begin{aligned}
 T_{e48V}^* = \frac{3}{2}p \left(\underbrace{\left(\frac{L_{dd1}}{N_{s12}} \frac{2N_f}{3N_{s1}} i_{fd} + \frac{\lambda_{mag1}}{N_{s12}} \right) i_{qs2}}_{\text{synch. torque}} + \underbrace{\left(\frac{L_{dd1}}{N_{s12}^2} - \frac{L_{qq1}}{N_{s12}^2} \right) i_{ds2} i_{qs2}}_{\text{reluctance torque}} \right) \\
 + \underbrace{\left(L_{dd1} - L_{qq1} \right) \frac{i_{ds1}}{N_{s12}} i_{qs2}}_{\text{cross-rel. torque}}
 \end{aligned} \tag{4.4.0.2}$$

Both torque equations consist of a *synchronous component*, a *reluctance* component and a *cross-reluctance* component. The *reluctance* and *cross-reluctance* torque components are of the same physical nature and generate a torque component due to the difference in the reluctance paths along the *d*- and *q*-axis. Here these parts are separated in order to distinguish better between the torque generated due to the cross-interaction of the stator currents of both windings and the torque generated due to the stator currents of only one winding. The *synchronous torque* is a result of the interaction of the magnetic flux generated by the rotor and the *q*-axis current of the specific winding. The synchronous torque component plays the most important role in the torque generation for the claw-pole machine. This is so because the rotor to stator ratios, $\frac{N_f}{N_{s1}}$ or $\frac{N_f}{N_{s2}}$, are large numbers and generate a significant magnetic flux with small rotor currents. The ratio between L_{dd} and L_{qq} for this machine is around $\frac{L_{dd}}{L_{qq}} = 1.33$, which is small in comparison to pure synchronous reluctance machines. Synchronous reluctance machines can have a much greater ratio in the range of 2.5 to 5 [33, 34, 64]. Therefore the reluctance torque does not contribute a lot to the torque production. With this prior knowledge one can expect, that the offline calculated current references should favor the generation of a *synchronous torque* component against the *reluctance* and *cross-reluctance* torque. Nevertheless the machine does show some reluctance due to the difference between L_{dd} and L_{qq} . Therefore the stator current references have to be chosen such that a small amount of reluctance torque contributes to the whole torque equations of both windings. The *cross-reluctance* torque is especially interesting, as it is a result of the interaction of the *d*-axis flux produced by one winding with the *q*-axis current of the other winding. The *cross-reluctance* torque may not play as an important role in the torque generation for the claw-pole machine as the *synchronous torque*, however it does influence the torque of each winding and represents the coupling between both stator systems. In a case, where a torque control for a *synchronous reluctance machine* with two voltage levels has to be developed the *cross-reluctance* torque component would play the most important role in the torque generation and would highly influence the optimal stator currents. As a next step analysis of the pre-calculated optimal current references are performed. These analyses are a first verification, if the Matlab optimization script delivers plausible results.

The operating points for all five current references are plotted in graphs in order to check the plausibility of the pre-calculated working points and perform analysis. Each current reference is read out as a function of both torque references, T_{e12V} and T_{e48V} , and therefore can be represented in a 3-D graph. However, a representation in a 3D-plot is not very useful to understand the graphs, as a 3-D plot is hardly readable. For this reason 2D plots are plotted with a family of curves to represent the working points as a

function of both torque references. This way the 3D data can be represented through a varying parameter in the legend. Each current reference is plotted once in a plot as a function of the 12V torque reference and a crosswise dependency of the 48V torque reference as a parameter. A second plot represents each current reference as a function of the 48V torque reference and a crosswise dependency of the 12V torque reference. For example, Fig. 4.15 shows the optimal d - and q -axis currents of the 12V side. The x -axis of the left plots is always the 12V torque reference T_{e12V}^* . The right plots on the other hand have as x -axis the 48V torque reference. This way of illustration is kept the same for all graphs, which illustrate the pre-calculated current references. The curves of all current references have to be analyzed at once and interpreted with respect to both torque equations in order to comprehend entirely the course of the plotted current references.

4.4.1 Optimal Currents for a 12V Torque Reference

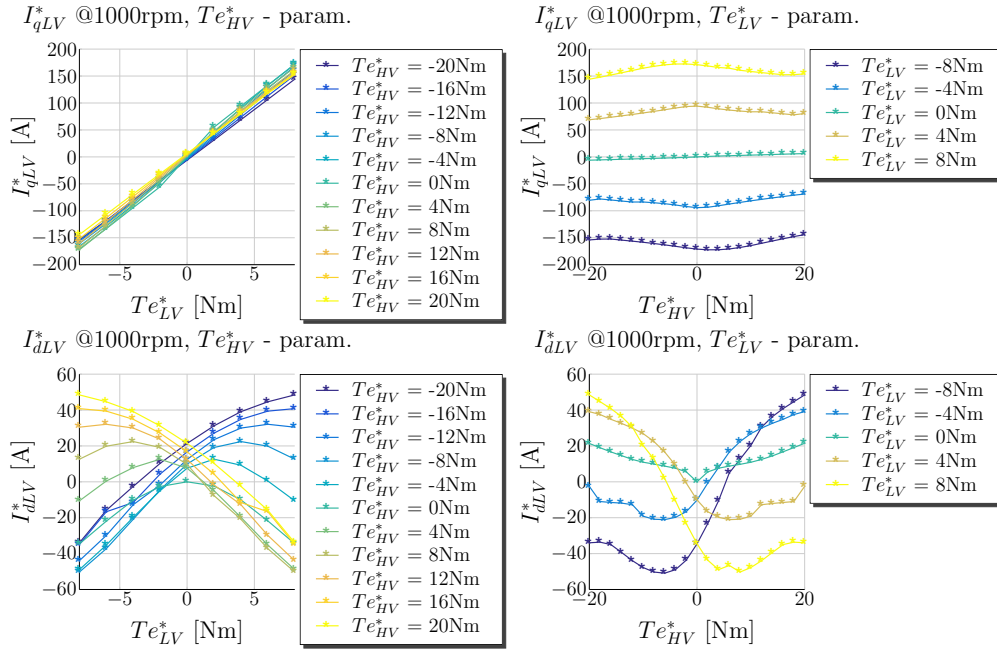


Figure 4.15 – Working Points for MTPCL: 12V Currents

Figure 4.15 shows the current references for the 12V stator system. Both top plots of Fig. 4.15 show the q -axis current references of the 12V system and both bottom plots the d -axis current references. The top left plot shows the 12V q -axis current, i_{qs1} , as a function of the 12V torque reference, T_{e12V}^* , and a crosswise dependency of the 48V torque reference T_{e48V}^* . The curves for the q -axis current look plausible and increase almost linearly with higher torque references. The greater the 12V torque in motoring mode is, the greater is also the positive q -axis current. When the requested 12V torque

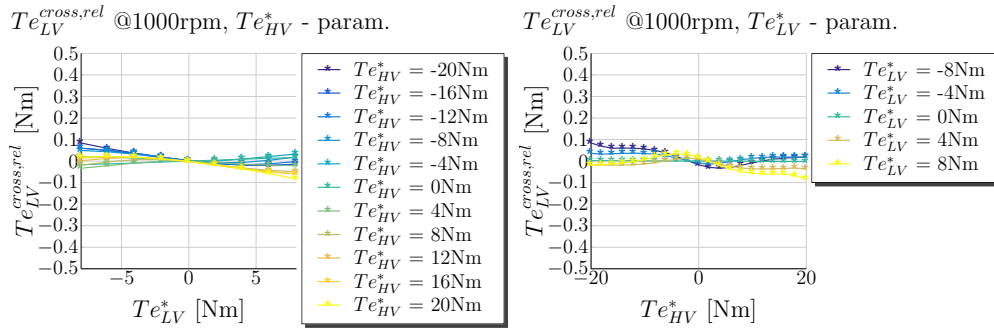


Figure 4.16 – MTPCL: 12V Cross Reluctance Torque

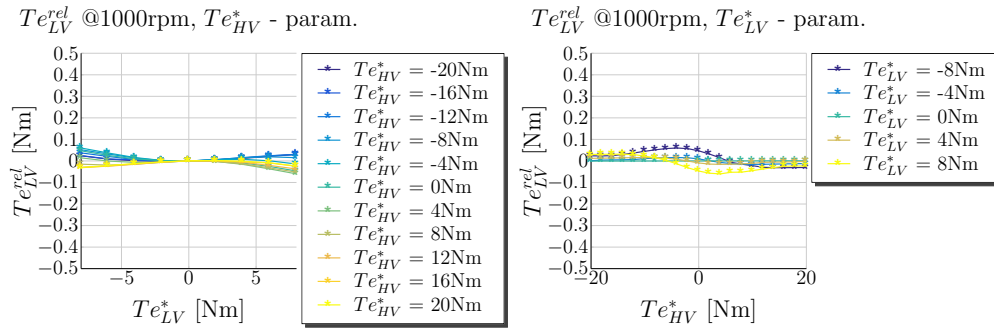


Figure 4.17 – MTPCL: 12V Reluctance Torque

is in generator mode, the q -axis current is increased towards its negative values. The remaining three plots in the figure do not look so trivial and require a deeper analysis in order to understand why the curves behave like this.

The right top plot of Fig. 4.15 shows the q -axis current dependency of the 48V torque reference. From the curves is evident that the q -axis current is adjusted because the *cross-reluctance* and the *reluctance* torque components influence the generated torque. In support of this statement the 12V *cross-reluctance* torque is plotted in Fig. 4.16 and the 12V *reluctance* torque is plotted in Fig. 4.17. The figures show clearly that the 12V *cross-reluctance* torque prevails over the 12V *reluctance* torque. This is comprehensible, because the generated flux by the 48V currents in the *cross-reluctance* torque is four times greater than by the 12V currents. When the *cross-reluctance* torque component from equation (4.4.0.1) is compared to the *reluctance torque* component, it is clear that the mutual inductances $\frac{L_{dd1}}{N_{s12}}$ and $\frac{L_{qq1}}{N_{s12}}$ are four times greater than L_{dd1} and L_{qq1} . Due to the *synchronous torque* the q -axis currents are generally much greater than the d -axis currents for a certain torque reference. The *reluctance torque* component is only caused on the other hand by the interaction of one q -axis current. Therefore both q -axis currents contribute to a greater *cross-reluctance* torque in comparison to the reluctance one.

Fig. 4.16 shows the 12V *cross-reluctance* torque as a function of both torque references. The 12V *cross-reluctance* torque is calculated according to equation (4.4.1.1). As expected, the *cross-reluctance* torque does not contribute a lot to the torque generation in comparison to the *synchronous torque* component. The same holds also for the 12V *reluctance torque* component shown in Fig. 4.17.

$$T_{e12V}^{cross-rel.} = \underbrace{\frac{3}{2} \cdot p (L_{dd1} - L_{qq1}) \frac{i_{ds2}}{N_{s12}} i_{qs1}}_{cross. rel. Torque} \quad (4.4.1.1)$$

Despite this influence of the 48V winding to the 12V torque, the 12V winding has to be able to maintain the requested torque reference and compensate this effect through its synchronous torque component. For this purpose the excitation current is adjusted to higher values. Figure 4.18 shows in the left plot how the field winding current is adjusted when the 12V torque is varied from generator to motor mode. For example, one can take a look at the optimal field winding curve when the 48V winding is operated at -20 Nm. The optimal field winding current is gradually reduced, when the 12V winding is changed from -8 Nm to 8 Nm. A higher field winding current is required when both windings are operated in generator mode, because the whole reluctance torque created at 12V side is positive and impacts negatively the 12V torque. On the other hand when the 12V torque reference is adjusted towards the positive values, the generated positive *cross-reluctance* torque contributes to the whole 12V torque and therefore the field winding current is reduced. Figure 4.18 shows also that the field winding current is mostly determined due to the 48V torque reference. The left plot of Fig. 4.18 shows the field winding currents as a function of the 12V torque reference and the right plot shows the optimal field winding currents as a function of the 48V torque reference. It is evident that the higher the 48V torque is, the greater is also the requested field winding current. If the 48V torque is 0 Nm, the 8 Nm torque reference of the 12V side can be achieved also with a field winding current of around $1,7$ A. However, if a reference torque of 20 Nm is requested at the 48V side, the field winding currents are increased of up to $3,5$ A: the upper right corner of the left plot of Fig. 4.18.

4.4.2 Optimal Currents for a 48V Torque Reference

Figure 4.19 shows the calculated optimal 48V current references. The left top plot shows the 48V q -axis current as a function of the 12V torque T_{e12V}^* and a crosswise function of the 48V torque references. In contrast to the corresponding plot of Fig. 4.15, which illustrates the 12V q -axis current in dependency of the 48V torque reference, the optimal q -axis current of the 48V side is not influenced a lot by the 12V torque reference. The 48V q -axis current i_{qs2} increases almost linearly with the 48V torque reference as illustrated in the top right plot of Fig. 4.19. This observation corresponds to the previously made assumption, that the *synchronous reluctance torque* component plays the most important

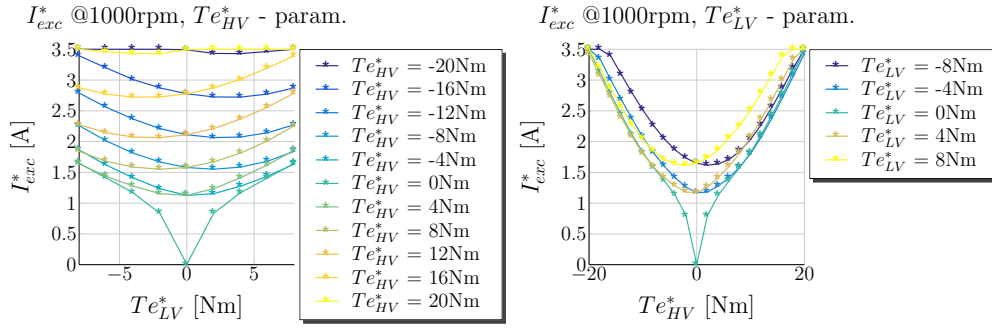
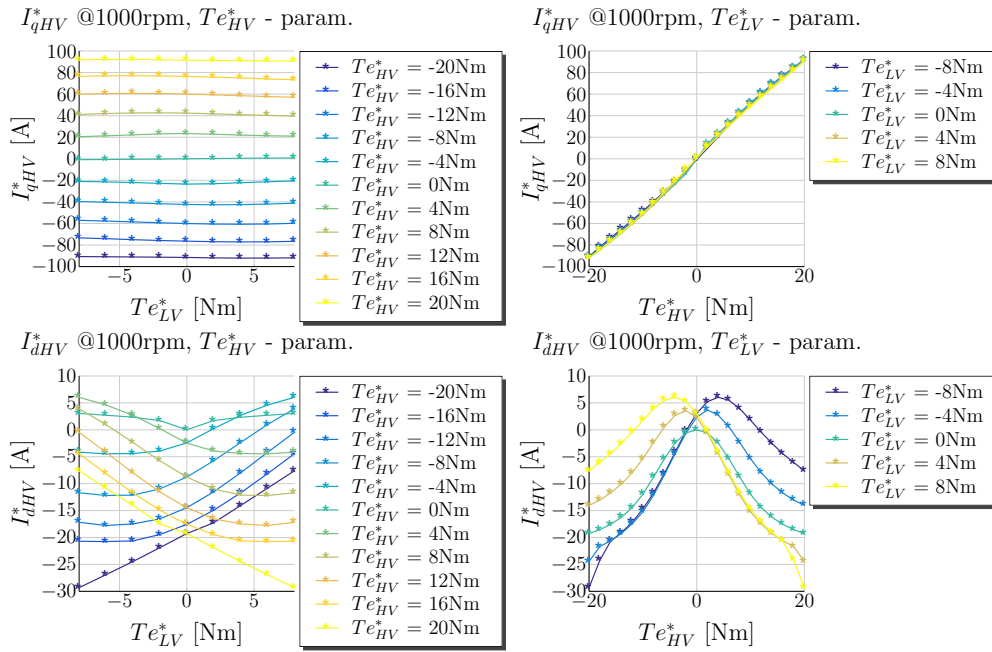

 Figure 4.18 – Working Points for MTPCL: I_{exc}


Figure 4.19 – Working Points for MTPCL: 48V Currents

role in the torque generation of the claw-pole machine. Both bottom plots show the optimal d -axis currents as a function of both torques. The 48V d -axis currents look very different in comparison to the 12V d -axis currents. The 12V d -axis currents do change their sign in accordance to the 12V torque reference to make use of the *cross-reluctance* torque component. In contrast to the 12V d -axis current, the 48V d -axis currents are in most of their parts negative. Both, the 48V *cross-reluctance* and the 48V *reluctance* torques, are illustrated in Figures 4.20 and 4.21. The 48V *cross reluctance* torque component is calculated according equation (4.4.2.1). As expected the *cross reluctance* torque and the *reluctance* torque components do not contribute a lot to the torque generation of the claw-pole machine because the difference between L_{dd1} and L_{qq1} is small.

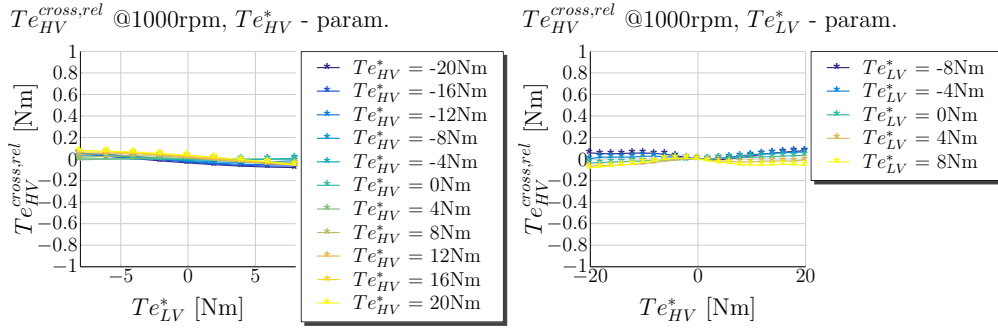


Figure 4.20 – MTPCL: 48V Cross Reluctance Torque

$$T_{e48V}^{cross-rel.} = \underbrace{\frac{3}{2} \cdot p \cdot (L_{dd1} - L_{qq1}) \frac{i_{ds1}}{N_{s12}} i_{qs2}}_{cross. rel. Torque} \quad (4.4.2.1)$$

When the 48V winding has to set a positive torque reference, the 48V q -axis current i_{qs2} increases to a certain positive value to generate a *synchronous* torque. The 48V q -axis current i_{qs2} interacts with the d -axis flux produced by the 12V d -axis current i_{ds1} and generates a torque according to the left part of equation (4.4.2.1). The behavior of the 12V d -axis current is more complex and the optimal current values change their sign. The 12V d -axis curves are plotted in Fig. 4.15. As an example the curve for a positive 48V torque reference at 20 Nm can be considered. When the 12V torque reference is in motoring mode, for example 8 Nm, the the d -axis currents are negative up to -60 A. When the 12V torque is in the opposite mode, generator mode, the 12V d -axis currents increase up to 55 A. Therefore the left part of equation (4.4.2.1) becomes positive and reaches its maximum when the 48V torque reference is at 20 Nm and the 12V torque reference at -8 Nm. This way the left part of the equation contributes to the positive torque reference of the 48V side. The right part of equation (4.4.2.1) is a results of the interaction between the q -axis flux produced by the 12V winding and the d -axis current of the 48V winding. In the case of a negative 12V torque reference, e.g. -8 Nm, the q -axis current of the 12V side is negative. This way the product of $-\frac{L_{qq1}}{N_{s12}}$ and i_{qs1} is positive. Therefore the sign of the right part of the equation depends on the value of i_{ds2} . For this case, a positive 48V torque reference of 20 Nm and a negative 12V torque reference of -8 Nm, the value of i_{ds2} is around -10 A and can be read out from the right bottom plot of Fig. 4.19. Therefore the right part of the equation is negative and reduces the 48V *cross-reluctance* torque.

Based on the performed analysis it can be concluded, that the value of the 48V d -axis current is a compromise between the *reluctance torque*, the *cross-reluctance* torque and the *synchronous* torque component.

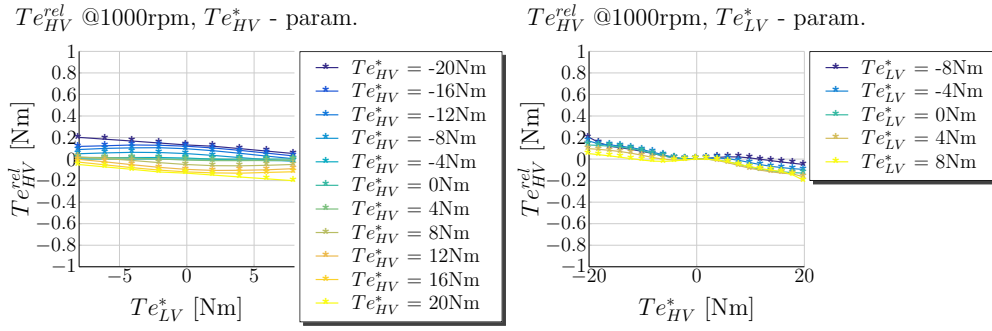


Figure 4.21 – MTPCL: 48V Reluctance Torque

In summary, it can be concluded for the torque control of the 48V side, that the *synchronous* torque component plays the most important role in the torque generation. From the optimal current curves of the 48V side, it is observed, that the ratio between L_{dd1} and L_{qq1} can invert due to different saturation levels of both inductances. The reluctance ratio $\frac{L_{dd1}}{L_{qq1}}$ is very small in comparison to pure reluctance machines and therefore the L_{qq1} inductance can become greater than the L_{dd1} inductance depending on the operating point.

4.4.3 Analysis Summary of the Optimal Current References

Based on the performed analysis for the claw-pole machine it can be concluded, that the torque of the claw-pole machine depends on a lot of factors and is very complex in terms of the observed interactions between all currents. The air-gap torque of the claw-pole machine consists of a *synchronous* torque, a *reluctance* torque and a *cross-reluctance* torque component. The machine is operated efficiently, when an optimum between all three torque components is found. In contrast to this, a pure reluctance machine does not have any *synchronous* torque component and the generated torque depends only on the difference in the reluctance paths. On the other hand, a non-salient-pole synchronous machine, which does not show any difference between L_{dd} and L_{qq} , has also a simplified torque equation consisting of only a *synchronous* torque. The IPM machine generates a torque, which consists of a *synchronous* torque component and a *reluctance* torque component. The choice of the optimal current references for the IPM machine is simpler, because the rotor flux is fixed and determined only by the permanent magnets flux. Though the claw-pole machine does not show high reluctance torque components, all torque components have to be considered in order to achieve better torque accuracy. The torque of the claw-pole machine is mostly determined by the *synchronous* torque. This torque component is determined through the choice of the field winding current and the q -axis current of each winding. The 48V *synchronous* torque component is almost not influenced by the changes in the references of the 12V side. The choice of the optimal 48V d -axis currents adjusts the generated *cross-reluctance* and *reluctance* torque components. The 12V torque is more impacted by the changes in the current references of the 48V

side. Through the stator currents interaction a *cross-reluctance* torque component is generated between both windings. The 12V winding has to be able to maintain a certain reference despite the changes of the 48V side.

In the next paragraph simulation results in a closed loop with the developed model are presented. The machine torque control is tested for some characteristic cases.

4.4.4 Torque Control Simulations in the BS Range

Due to the dual-voltage operation of the machine, the possible operating modes of the machine are literally overwhelming and simulation results for each possible operating mode would negatively impact the readability of the thesis. Therefore only some characteristic test cases are illustrated here to demonstrate that the proposed torque control is suitable to regulate both torques of the machine. The simulations are performed to demonstrate that the decoupling through the adjustment of the current references is working as expected. Through the adjustment of the current references, each side is able to maintain its own torque reference.

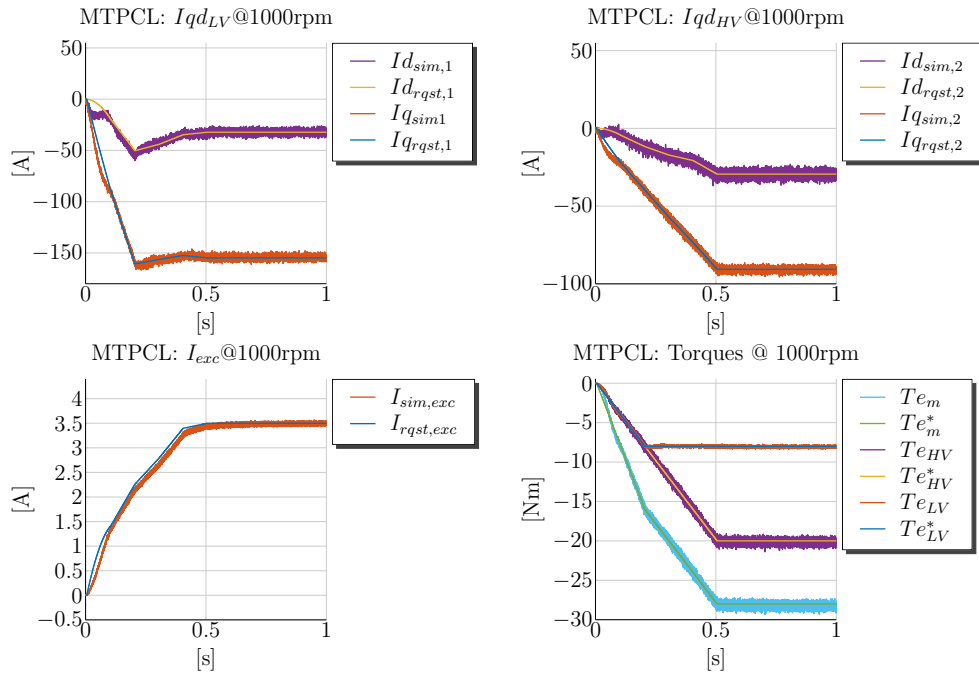


Figure 4.22 – MTPCL Simulation @1000rpm: $T_{e_{12V}} = -8 \text{ Nm}$, $T_{e_{48V}} = -20 \text{ Nm}$

Figure 4.22 shows a simulated case, where both windings are controlled in generator mode. The 12V winding is controlled to set a -8 Nm reference and the 48V winding is controlled to a -20 Nm reference. The simulation is performed at 1000 rpm. The first plot of Fig. 4.22 shows the 12V d - and q -axis current references and the second plot

the 48V d -axis and q -axis currents. The requested working points correspond to the illustrated optimal curves from Figures 4.15 and 4.19. The 12V d -axis current is set to around -30 A and the 48V d -axis current to -25 A. The q -axis current of the 12V side is set to around -150 A and the 48V q -axis current to around -85 A. The field winding current is set to 3,5 A. This is the maximum allowed current limit set during the offline optimization⁹. The torque references are plotted in the bottom right plot of Fig. 4.22. It is evident from the graph that linear torque ramps on both torque references are applied in the simulation. This results however in non-linear ramps for the current references. Because the saturation of the main inductance is highly non-linear, also the current references need to be adapted in a non-linear manner in order to follow the ramped torque references. From all three current plots is clear that the current controllers can track the current references. The machine model calculates also the generated 12V and 48V air-gap torques. The last plot of Fig. 4.22 shows also the simulated torques. The simulated torques correspond to the requested torque references. The mechanical torque is represented in a simplified manner as the sum of both torque references.

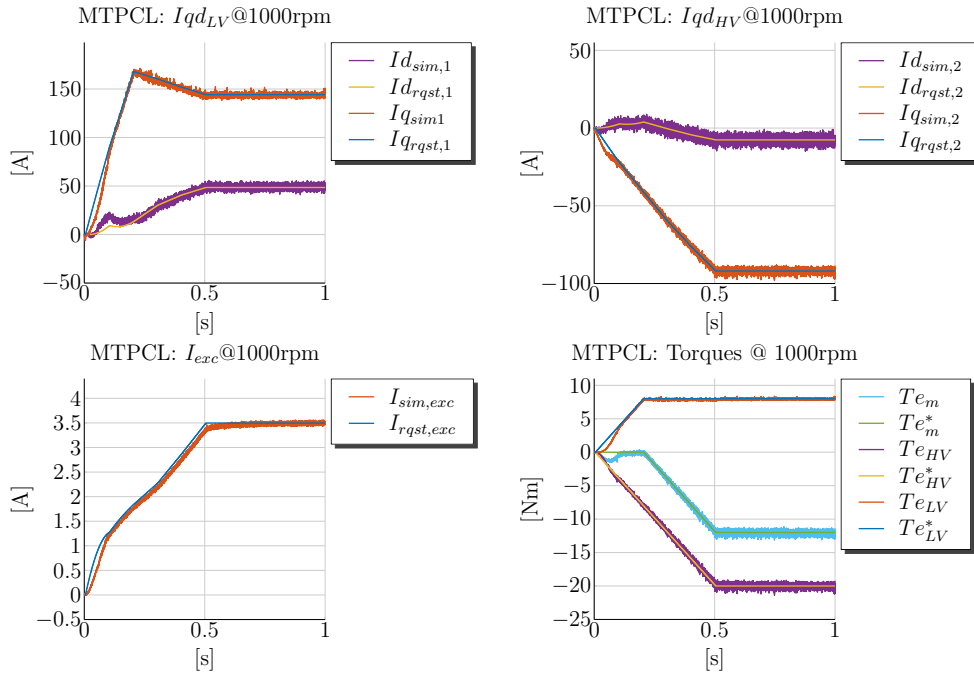


Figure 4.23 – MTPCL Simulation @1000rpm: $T_{e_{12V}} = 8$ Nm, $T_{e_{48V}} = -20$ Nm

In the next studied case, the 48V torque reference is kept at -20 Nm and the 12V torque reference is changed to a positive value of 8 Nm. Figure 4.23 shows the simulation of the combined mode. In comparison to the previous simulation, illustrated in Fig. 4.22, the 12V d -axis current is increased to a positive value of around 50 A and the 48V d -axis current

⁹Since no data is available on the maximum operating machine current limits, the maximum allowable field winding current is chosen conservatively in order not to damage the machine prototype.

is decreased to -10 A. This way the *cross-reluctance torque* is exploited. The last plot of Fig. 4.23 shows the torque references. The simulated mechanical torque is 12 Nm, which is the sum of the 12V and 48V torque references. It becomes clear from the simulation, that the 48V winding is able to maintain its torque reference through the adjustment of the 48V d -axis current. The 48V winding is not impacted a lot by the reference change of the 12V winding. The 12V winding sets a positive value of around 50 A in order to generate a *cross-reluctance torque*. In this case a positive *cross-reluctance torque* at the 12V side is generated according to the plots from Fig. 4.16. The *cross-reluctance torque* component of around 0,5 Nm contributes to the torque generation for the reference of 8 Nm.

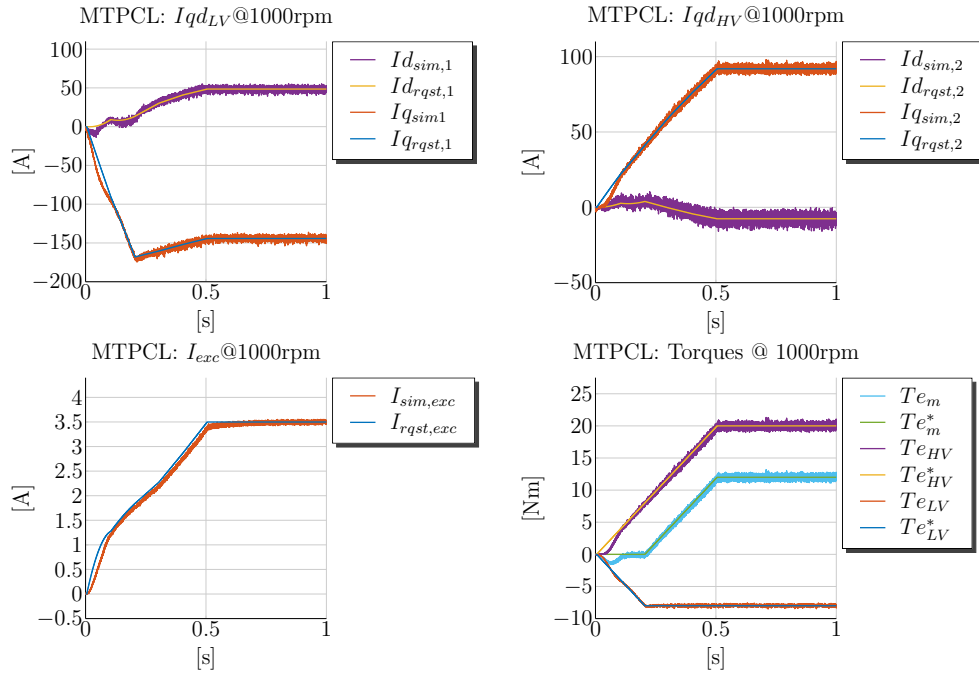


Figure 4.24 – MTPCL Simulation @1000rpm: $T_{e12V} = -8$ Nm, $T_{e48V} = 20$ Nm

The next illustrated case shows how the 12V winding maintains its reference value through adjustment of its stator currents despite the change of the 48V reference. Figure 4.24 shows simulation results of a torque control with 12V reference of -8 Nm and a 48V reference of 20 Nm. In comparison to Fig. 4.22 the 48V winding is operated in exactly the opposite mode. Figure 4.24 shows in its top left plot that the 12V stator currents are adjusted. In contrast to the simulated case from Fig. 4.22, the d -axis current is changed from a negative value of -35 A to 50 A. In this case both windings operate in opposite modes and therefore the generated 12V *cross-reluctance torque* is negative according to the plots from Fig. 4.16. It contributes to the 12V torque reference of -8 Nm. The simulated torques from the last plot of Fig. 4.24 show clearly that through the adjustments of the stator current references the 12V winding is able to maintain its

8 Nm reference despite the fact that the 48V winding is operated at the positive torque reference of 20 Nm.

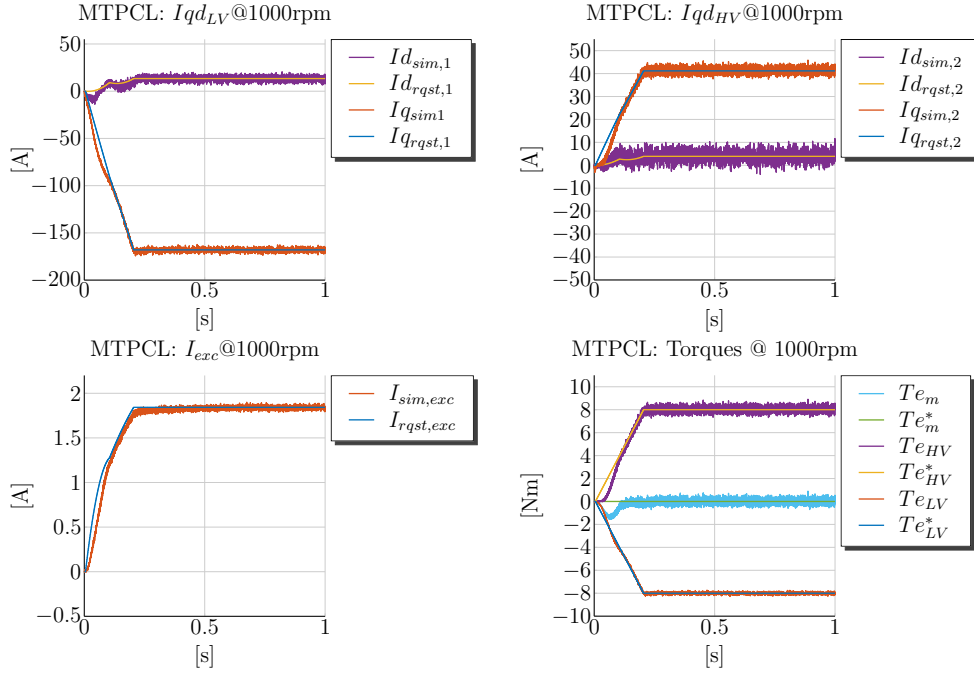


Figure 4.25 – MTPCL Simulation @1000rpm: $T_{e12V} = -8\text{ Nm}$, $T_{e48V} = 8\text{ Nm}$

The last simulated case is the operation of both stator windings at the same torque reference but with opposite signs. This way a power transfer can be achieved from the 12V to the 48V side or vice versa. In this combined operating mode a zero mechanical torque is generated. The electrical power transfer happens in the air-gap of the machine. Figure 4.25 shows the simulation results of this case. The 12V winding is operated in generator mode and the 48V winding in motor mode. The 12V q -axis current is set to -164 A and the 48V q -axis current is controlled to 41 A . The d -axis current of the 12V side is set to 16 A and the 48V d -axis current is adjusted to 4 A . This way a small amount of *cross-reluctance* torque is generated at both sides. The field winding current is set to a value of $1,8\text{ A}$. The last plot shows the torque references. The simulated 12V and 48V air-gap torques match exactly their references and therefore no mechanical torque is generated. This mode can be employed, when the 12V side has to be charged, but no mechanical torque has to be applied to the rotor shaft.

The simulation results show how the decoupling action in the torque control for the dual-voltage machine works. It becomes evident that though the 12V winding is more influenced by the operation of the 48V side, through an adequate adjustment of the current references it is possible to maintain the requested torque. The simulations are performed for all possible combinations of torque settings at the speed of 1000 rpm . The torque reference is varied from -8 Nm to 8 Nm in 4 Nm torque steps and the 48V winding

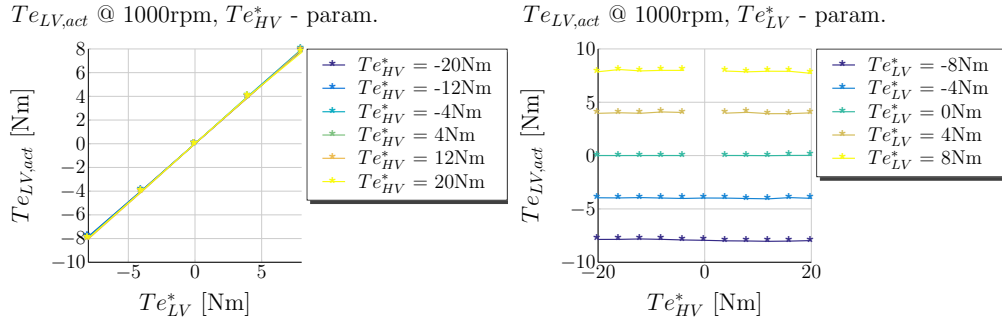


Figure 4.26 – Simulations for MTPCL: $T_{LV,act}$

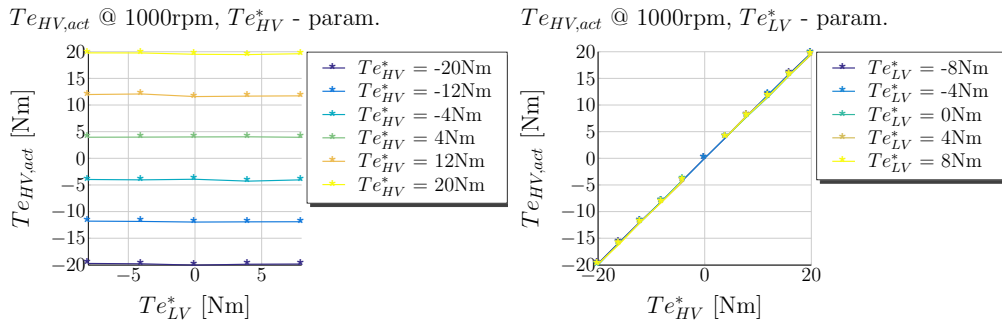


Figure 4.27 – Simulations for MTPCL: $T_{HV,act}$

from -20 Nm to 20 Nm in 4 Nm steps. The results from the simulations are processed through a Matlab script and the mean values are plotted in Figures 4.26 and 4.27. Figure 4.26 shows on the left the 12 V torque reference as a function of itself. The right plot of the figure shows the 12 V torque reference as a function of the 48 V torque. It is evident that the 12 V winding is able to maintain each of the requested torque reference despite of the 48 V torque reference changes. The same results can be observed for the 48 V torque reference. The 48 V torque reference is plotted as a function of both torque references in Fig. 4.27. These results confirm that the decoupling through current references is working as expected in the simulation environment. The next step is to verify the torque control on the test bench with the machine prototype.

4.4.5 Torque Control Measurements in the BS Range

The same test bench setup, as described in Subsection 3.2.8 from Chapter 3, is used also for the torque control measurements. A script in Python is implemented to automate the testing of the working points. The script tests in a sequence one combination of torque references at a time. The duration of the pulses is 5 sec and the torque references are ramped in and ramped out. This way it is possible to repeat all combinations of operating points from Figures 4.26 and 4.27 in a limited time. The measured quantities

are the same as already described in Subsection 3.2.8 from Chapter 3. Simulation results from three of the cases have been presented in Subsection 4.4.4. The very same cases are included in this subsection.

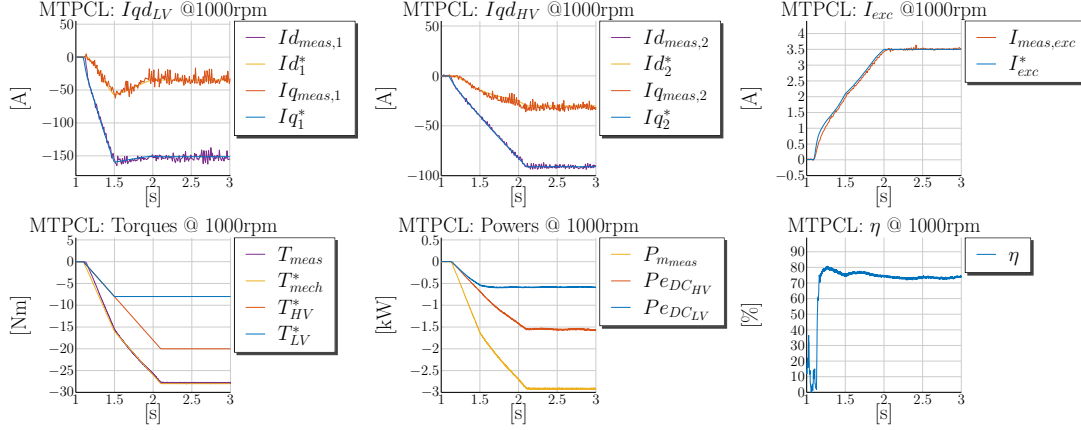


Figure 4.28 – Measurements @1000rpm: $T_{e12V} = -8\text{Nm}$, $T_{e48V} = -20\text{Nm}$ MTPCL Control

The first simulated case from Fig. 4.22 shows the dual-voltage machine in a torque control mode, when both sides are operated in generator mode. The 12V winding is operated at -8Nm and the 48V winding at -20Nm . The corresponding measurement is illustrated in Fig. 4.28. The plots show how the torque references are ramped in, held in their steady state and then ramped out. All three top plots show the five current references required to set the torque references of -8Nm and -20Nm . The top left plot of Fig. 4.28 shows the 12V d - and q -axis currents. The top middle plot shows the d - and q -axis currents of the 48V winding. The top right plot shows the field winding current and its reference. The bottom left plot shows both torque references, 12V and 48V, and the measured mechanical torque. Both air-gap torques cannot be measured on the test bench and the only way to verify the model is through the measured mechanical torque. Figure 4.28 shows that in the presented case the measured mechanical torque matches the sum of both references: $T_{e12V}^* + T_{e48V}^*$. In the middle bottom plot the mechanical and electrical 12V and 48V powers are illustrated. The mechanical power is directly calculated through the measured mechanical torque and the measured mechanical speed in radians. Both electrical powers are calculated through the measured DC voltages and currents at both sides. The measurements show that in both stator windings electrical power is generated. The 12V side is supplied with around 0,6 kW and the 48V side with approximately 1,5 kW. The ratio of both torque references and the measured electrical powers is the same: $\frac{1,5\text{kW}}{0,6\text{kW}} = \frac{20\text{Nm}}{8\text{Nm}} = 2.5$. This indicates that the applied air-gap torque references are set correctly. The last plot of Fig. 4.28 shows the calculated efficiency. The efficiency is calculated as a function of the mode the machine is operated. In this case the generated torque is mechanical and therefore the efficiency is calculated as the ratio between the sum of both electrical powers divided through the mechanical power. The efficiency is illustrated in percents and is around 75 % in steady state. It has to be noted

that the speed of 1000 rpm is not the optimal speed in terms of efficiency, as this speed is below the corner speed of 1500 rpm. Best efficiencies are achieved when the machine is operated around the corner speed. The presented measurement correlates with the performed simulation.

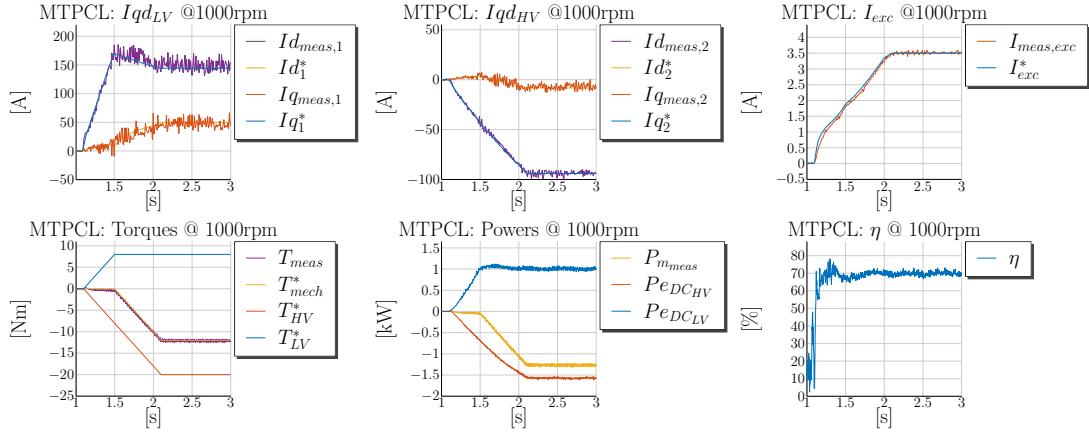


Figure 4.29 – Measurements @1000rpm: $T_{e12V} = 8 \text{ Nm}$, $T_{e48V} = -20 \text{ Nm}$ MTPCL Control

The next case, simulated in Fig. 4.23, represents a combined mode, where the 12V winding is controlled in motor mode to a reference of 8 Nm and the 48V winding is controlled to -20 Nm . Figure 4.29 illustrates the corresponding measurement. The 12V current references are illustrated in the left top plot. The current references are the same as the ones used in the simulation and it is evident, how the 12V winding changes its d -axis reference from negative values to a positive value of 50 A. This way a *cross-reluctance* torque of the 12V winding is generated and contributes to the torque generation of the 12V winding. The 48V winding reduces its d -axis current to -10 A . The resulting *cross-reluctance* torque is also negative, according to Fig. 4.20 around $-0,6 \text{ Nm}$, and contributes to the -20 Nm torque reference of the 48V winding. The 12V and 48V torque references are shown in the left bottom plot of Fig. 4.29. The resulting mechanical torque reference is the sum of both and is also illustrated in the same plot. It matches well to the measured torque from the test bench. The torque references from the bottom left plot of Fig. 4.29 are ramped with the same slew rate. Therefore, in-between seconds 1 and 1,5, both torques cancel each other and the resulting mechanical torque is zero. Once the 48V torque continues to increase up to -20 Nm , the negative mechanical torque is generated. The calculated powers are plotted in the bottom middle plot and confirm this behavior. The 12V winding draws positive power from the 12V source of around 1 kW and the 48V winding generates negative power into the 48V side of around 1,6 kW. In a sum, a negative mechanical power of around 1,25 kW is generated. The efficiency in this case is also calculated with the mechanical power in the denominator. The efficiency drops from around 75 % from the previous case to 70 %, because the power of the 12V winding is transformed through the air-gap to the 48V winding. This way the electrical power from the 12V winding is not used to generate a positive mechanical output power, but is used

to transfer power from the 12V side to the 48V side. More losses are generated, because the electrical power used is once converted into electromechanical air-gap torque and then again into electrical power supplied to the 48V winding. This power conversion in the air-gap of the machine is accompanied with higher losses. The illustrated measurements for this case correlate good with the corresponding simulation previously.

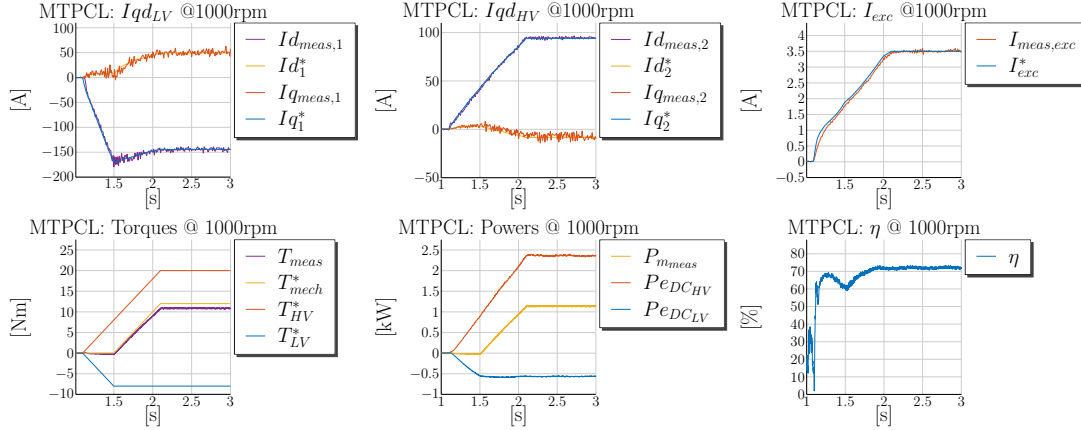


Figure 4.30 – Measurements @1000rpm: $T_{e12V} = -8$ Nm, $T_{e48V} = 20$ Nm MTPCL Control

The simulated third studied case from Fig. 4.24 sets the 48V winding in motor mode with a reference of 20 Nm and the 12V winding remains in generator mode with a reference of -8 Nm. The corresponding measurement is presented in Fig. 4.30. Both windings are operated in opposite modes. Therefore the 12V d -axis current is set to a positive value of 50 A to generate a cross-reluctance torque, which contributes to the 12V negative torque reference of -8 Nm. The current references are set to the same values as in the simulation. The 48V torque reference from the bottom left plot is ramped up to 20 Nm and the 12V torque reference to -8 Nm. Again in the first half of the second, the generated mechanical torque is zero, because the sum of both air-gap torques is zero. From the bottom left plot of Fig. 4.30 is evident that the mechanical torque is not set as accurately as in the previous both cases. There is a deviation of around 1 Nm between predicted mechanical torque and measured one. One reason for this deviation may be a non-perfect alignment of the d - and q -axis of the machine in the software despite the calibration techniques applied from Chapter 3. This means that the real d -axis of the machine deviates slightly from the performed calibration in the control software. Another reason for this deviation is, that the iron losses of the machine are not considered in the calculation of the working points for the presented measurements. Therefore the measured mechanical torque in motor mode is less than expected. The deviation is most likely a combination of both effects. The middle bottom plot of Fig. 4.30 shows the calculated powers. The power drawn from the 48V source is around 2,4kW and the power generated into the 12V side is around 0,6 kW. In a sum the mechanical output power is positive and a positive mechanical torque is generated. The efficiency in this case is calculated with the electrical power in the denominator.

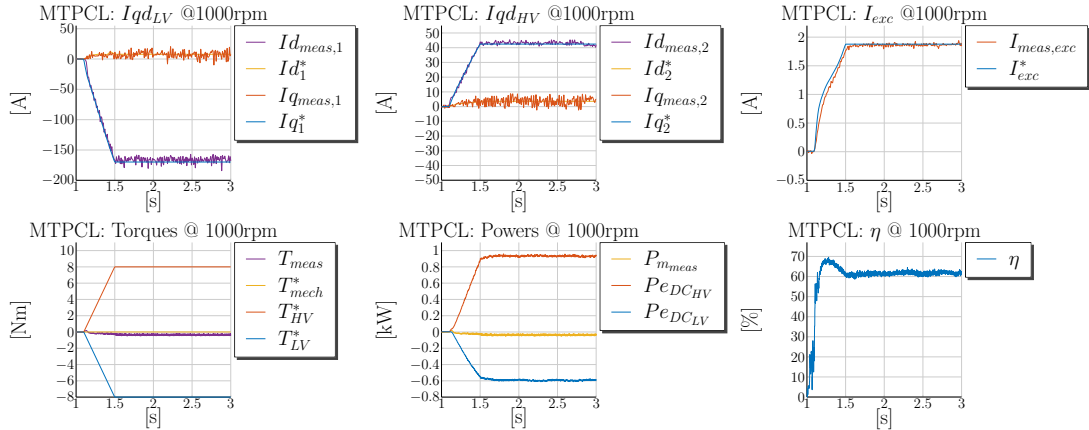


Figure 4.31 – Measurements @1000rpm: $T_{e12V} = -8\text{ Nm}$, $T_{e48V} = 8\text{ Nm}$ MTPCL Control

One last case is presented, where both sides are operated with exactly the same torque reference but with opposite signs. Figure 4.31 represents this case. The 48V winding is in motor mode with a torque reference of 8 Nm and the 12V winding is in generator mode with a torque reference of -8 Nm . The bottom left plot of Fig. 4.31 shows that both torque references are of the same magnitude but with opposite signs. The generated mechanical torque is close to zero but does not match exactly the zero reference. This is a result of the fact that the iron losses are not considered in the calculation of the working points. The efficiency is also decreased and around 60 %. The efficiency is calculated as the ratio between 12V electrical power and 48V electrical power.

From the presented measurements is evident that in some of the cases the measured torques match very well the requested reference. The torque references in generator mode are matched very well, but the measured torque in motor mode is always less than the reference. In order to check all measurements, a script is programmed, which selects only the mean values from the pulses and generates a graphic with all data points.

Figure 4.32 shows the measured mechanical torque values as a function of both torque references. The left plot shows the measured torques as a function of the 12V torque reference and a crosswise dependency of the 48V torque reference. The right plot shows the measured mechanical torque values depending on the 48V torque reference and a *crosswise* dependency of the 12V torque reference. From the left plot is evident that the measured mechanical torque increases linearly with the change of the 12V torque reference from -8 Nm to 8 Nm . In dependency of the 48V torque reference the curves are shifted along the y -axis as expected. All measured points look plausible and confirm the pre-calculated points. The right plot shows also a linear dependency of the measured torque from the 48V torque reference. The influence of the 12V torque reference is smaller and the curves are shifted along the y -axis in accordance to the requested 12V torque reference. Both presented plots from Fig. 4.32 illustrate that the implemented torque control based on offline calculated points and the parameterized machine model shows

4.4 Simulations and Measurements in the BS Range

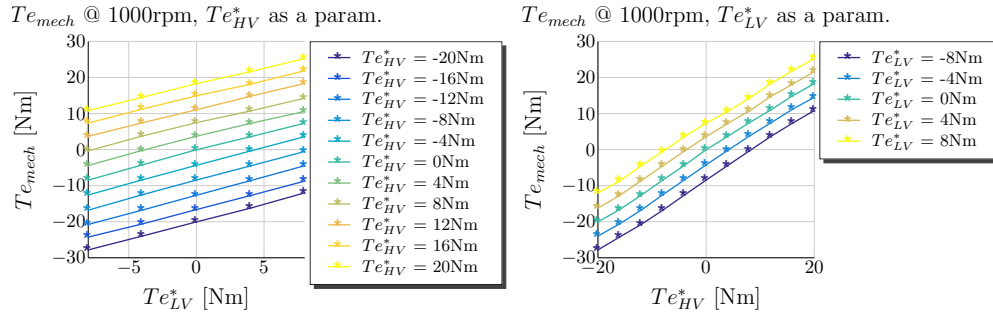


Figure 4.32 – Measurements for Torque Control MTPCL: T_{meas}

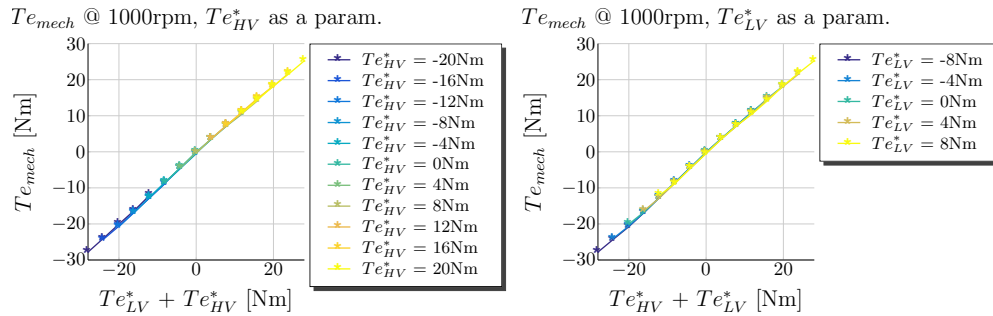


Figure 4.33 – Measurements for Torque Control MTPCL: T_{meas}

good results. The measured data look smooth and no glitches are present. However both curves do not show clearly how good the measured torque matches with the sum of both torque references, $T_{e_{12V}}^* + T_{e_{48V}}^*$. Therefore the measured torque is plotted also in dependency of the sum of both torque references.

Figure 4.33 shows all data points of the measured mechanical torque in dependency of the sum of both torque references. The left plot of Fig. 4.33 represents the measured mechanical torque in dependency of the 12V torque reference, to which for each curve the corresponding 48V varying parameter is added. This way the mechanical torque is illustrated in dependency of the sum of both. The right plot illustrates the measured mechanical torque as a function of the 48V torque reference, to which for each variation of the 12V torque reference a corresponding offset is added. Both curves show clearly that for all measured combinations of $T_{e_{12V}}^*$ and $T_{e_{48V}}^*$, the measured torque corresponds to the sum of both references. In order to quantify the error between the measured torque and the sum of both references the difference of both is plotted in Fig. 4.34

Both plots from Fig. 4.34 show that the error increases with higher torque references in motor mode. The reason for the torque error results from the fact that the iron losses are not considered in the offline calculation. Reference [61] shows based on measurements for an IPM machine, that the iron losses of the machine can result in an inaccurate alignment of the d - and q -axis in the software. The alignment of the d -axis is performed, when a

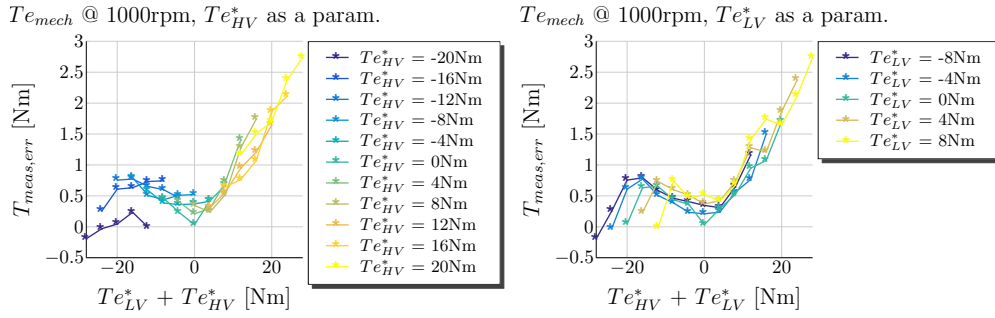


Figure 4.34 – Measurements for Torque Control MTPCL: $T_{meas,err} = T_{mech} - (Te_{LV}^* + Te_{HV}^*)$ [Nm]

certain field winding current is set and the stator currents are controlled to zero. Then the offset in the transformation matrix is adjusted, so that only q -axis voltage is measured. This procedure is performed prior to the torque control measurements during the current control testing. The cited reference proves that due to the iron losses of the machine not only a voltage along the q -axis is generated, but also in the d -axis. When the machine is excited and rotated at no-load conditions also a very small voltage along the d -axis is produced. For the claw-pole machine this effect is amplified, because the iron losses are greater in percentage in comparison to an IPM machine. Unfortunately at this step of the project the time at the test bench was very limited and no further calibration could have been done in order to repeat the measurements. Not only the aforementioned factors can influence the torque accuracy. The accurate representation of the saturation of both d - and q -axis is crucial to the torque prediction. The saturation behavior is simplified through an arcustangens function. The anisotropic factor between both inductances, L_{dd} and L_{qq} , is assumed to be constant for all saturation levels. These two simplifications can impact negatively the model accuracy in terms of torque prediction. Unfortunately no Finite Element Method (FEM) data for the main inductance is available for the machine and the only available data is the measured saturation behavior from Section 2.4 from Chapter 2.

4.4.6 Summary of the Torque Control Results in the BS Range

The presented simulation and measurement results show that an offline non-linear optimization can be employed to calculate working points for the torque control of the dual-voltage machine and achieve promising results. Though the problem is a complex five dimensional one, the non-linear optimization is able to find optimal working points. The working points have been checked for plausibility before they are tested in the simulation and on the test bench. The behavior of the curves is explained based on the torque equations for both air-gap torques derived in Chapter 2, which describes the modeling. The performed simulations afterwards show that the predicted torque by the offline optimization matches the simulated torque from the programmed machine.

These results prove that the derived machine theory in Chapter 2 is applied correctly also in the non-linear search. Multiple combinations of various 12V and 48V torque references are simulated and prove that the pre-calculated working points set correctly the requested 12V and 48V torques. Afterwards the same working points are tested in an automated manner on a test bench with the prototype machine. The presented measurements show good correlation with the simulation results. In some regions a greater deviation from the predicted mechanical torque is observed. Especially in motor mode the measured mechanical torque deviates in its extreme areas of up to 10 %. The correlation in the whole generator mode is very good and below 3 %. An explanation for the observed inaccuracies is provided. The mismatch can be due to multiple reasons: one reason is a non-perfect alignment of the d - and q -axis in the software, a second reason is the neglecting of the iron losses and a third reason is the performed approximation of the main inductance saturation through an arcustangens function. In order to improve the whole torque accuracy all three effects have to be considered in the torque control development.

4.5 Power Control - Voltage Angle Control in the FW Range

The proposed optimization from Subsection 4.3.2 is used to test only working points in the BS range of the machine, where the voltage limits do not restrict the choice of the optimal current references. The script is able also to find working points in the FW region and the proposed control structure for the FW region from Fig. 4.13 has been successfully verified in the simulation environment. Afterwards the same working points pre-calculated for the FW region have been tested also on the test bench. Unfortunately the results from the test bench did not match the simulation results. The reason for this lies in the previously explained deviation between measured and predicted torque from Subsection 4.4.6. The implemented model is not able to perfectly match the d - and q -axis inductance values of the machine prototype. This results in the BS range only in some deviation between torque references and measured mechanical torque. The machine is connected to an external electronic, which adds an additional leakage inductance. This leads to an increased back-emf voltage due to the added leakage inductances and saturation of the current controllers in the FW region.

Based on the performed observations a different approach is pursued for the FW operation, which relies less on machine parameters. For this purpose a literature review on various FW control strategies is performed. Reference [8] provides a review and comparison of different control techniques in the field weakening range. The reference classifies the techniques in three different categories. One category are the Vector Current Control (VCC) techniques, which control the phase angle of the currents vector in the machine to weaken the flux produced by the rotor. These techniques use the calculated MTPA current references and increase the field weakening angle of the currents vector to maintain the maximum voltage generated by the machine under a certain limit. A voltage feedback

controller is often employed, which amplifies the required field weakening angle as a function of the error between maximum available DC link voltage, $V_{\max,DC}$, and the voltage generated by the machine $|V_{\text{mach}}|$. There are different approaches of employing the VCC techniques described in reference [8]. One drawback of the technique is that often two controllers are required: one to control the flux through a field weakening angle β_{fw} and another to control the torque through the stator currents vector $|\vec{i}^*|$. The controllers may get unstable because both torque and flux are not decoupled from controllers point of view and the change in the flux due to the need for field weakening demands also a change in the current magnitude to hold the torque reference.

Another method, described in reference [8], to control a machine in the field weakening area is called a Torque Flux Control (TFC). This technique controls the voltage generated by the machine to the maximum available voltage by adjusting the requested flux and torque from the machine. The current references, i_{ds} and i_{qs} , are read out from look up tables based on the commanded torque and flux. The look up tables store the non-linear dependency between both, flux and torque, and currents. Then the current references are forwarded to the inner control loops. The required flux command is calculated from the error between the requested voltages from the current controllers and the maximum available DC link voltage. Afterwards, based on the so calculated flux and the commanded torque, the i_{ds} and i_{qs} current references are adapted.

Both group of techniques, the VCC and the TFC, have in common that they use the underlying inner current control loop and the current references are adjusted such that the machine is operated along the maximum voltage. Nevertheless, always a certain voltage margin has to be reserved for the current controllers such that these are able to adjust the current references [8]. There are two main drawbacks in these methods: the tedious calibration of the current controllers due to the not fully decoupled torque and flux and the inability to exploit fully the available DC link voltage. Both are handled by a third different approach described in the reference. The third method is called a Single Current Controller (SCR) + Voltage Angle Control (VAC). It uses the d -axis current error between the measured d -current and the MTPA d -current reference to calculate an FW angle through an integration. The FW angle is directly applied on the voltage vector. Through the rotation of the voltage vector the control mechanism is able to weaken the rotor flux. This method, in contrast to the others, applies the FW angle directly to the voltage instead to rotate the current vector. An advantage of this method is that the voltage is exploited fully but a transition between both control structures is required. This third method is originally presented in reference [74], where also stability analysis are performed for the method.

Reference [67] improves the voltage angle control method presented in reference [74] and uses instead of the d -axis current error, the q -axis current error to generate a field weakening angle. The PI controller is replaced also through a pure integrator. The q -axis current error is multiplied by an integral factor K_i and by the electrical angular speed ω_e and then integrated to generate a certain field weakening angle α_1 . A feed-forward part is added also to the control path. The feed-forward path generates a second angle

α_2 based on a low-pass filtering of the d -axis current and a proportional factor K_f . Thus, the whole angle of the voltage vector, required to set the torque in the FW range, is calculated as a sum of both angles α_1 and α_2 .

All three methods are explained in detail with schematics in reference [8] and the cited other references. The reader is referred to the corresponding papers in case of a greater interest.

Reference [36] presents the voltage phase angle method to control the machine torque. A Proportional Integral Derivative (PID) controller is employed to control directly the field weakening voltage angle. Feed-forward voltages are calculated based on the inversion of the machine model and based on the requested torque. The angle of the calculated feed-forward voltages is added to the output of the PID controller. The PID controller accepts as an input the difference between requested torque and the calculated torque from measured quantities. The machine torque is calculated based on the d - q voltages, v_{qs} and v_{ds} , on the d - q currents, i_{qs} and i_{ds} , and on the electrical angular speed ω_e . The whole field weakening angle is the sum of the feed-forward angle and the angle calculated by the PID controller.

The performed brief literature research shows that besides the field weakening control strategies based on controlling the stator current phase angle, also a direct manipulation of the voltage phase angle is possible. This idea is adopted here and is applied as a direct control of the torque or power based on the voltage phase angle in the field weakening range. The VAC is performed only in the field weakening area and therefore a transition mechanism between the FOC in the base speed range and the VAC in the field weakening range is required. The required machine theory for the VAC is explained in Subsection 4.5.1 and applied to the dual-voltage machine.

4.5.1 Voltage Angle Control Theory

In the field weakening range the operation of the machine is characterized with the fact that the DC link bus voltage is fully utilized. The reason for this is, that the back-emf voltage generated by the machine is higher than the available DC link voltage from the voltage source. This way the maximum available voltage is exploited. The voltage vector required to control the machine can be plotted as a space vector inside the SVM hexagon. For the dual-voltage machine the voltage vectors are plotted in two hexagons as illustrated in Fig. 4.35. The left one illustrates the voltage control vector for the 12V side and the right plot shows the 48V voltage vector. The employed voltage vectors are smaller than the maximum possible voltage vector, when both sides are operated in the BS range. Some example voltage vectors during a FOC operation in the BS range are illustrated in Fig. 4.35 in magenta. Each of the voltage vectors increases towards the border of the inner circle of the hexagons when the speed increases. Though the voltage vectors are coupled due to the back-emf produced by the field winding current, they may reach their maximum length at different times. Once a vector reaches its maximum amplitude,

the only way of control is to rotate the vector either clockwise \odot or counterclockwise \ominus . Though the idea of this control principle is simple, couple of challenges arise during the control development. One issue is the fact that the voltage vectors can reach their maximum length at any arbitrary angle. In Fig. 4.35 both angles are denoted with β_1 for the 12V side and β_2 for the 48V side. The direction and the angle step sizes, $\Delta\beta_1$ and $\Delta\beta_2$, should be determined such that the requested powers are regulated. The decoupling of the power control should be also considered during the analysis, so that the power at each side is not affected by reference changes of the other. The VAC derivation for the dual-voltage machine involves a detailed investigation of the machine equations in order to adequately address these issues.

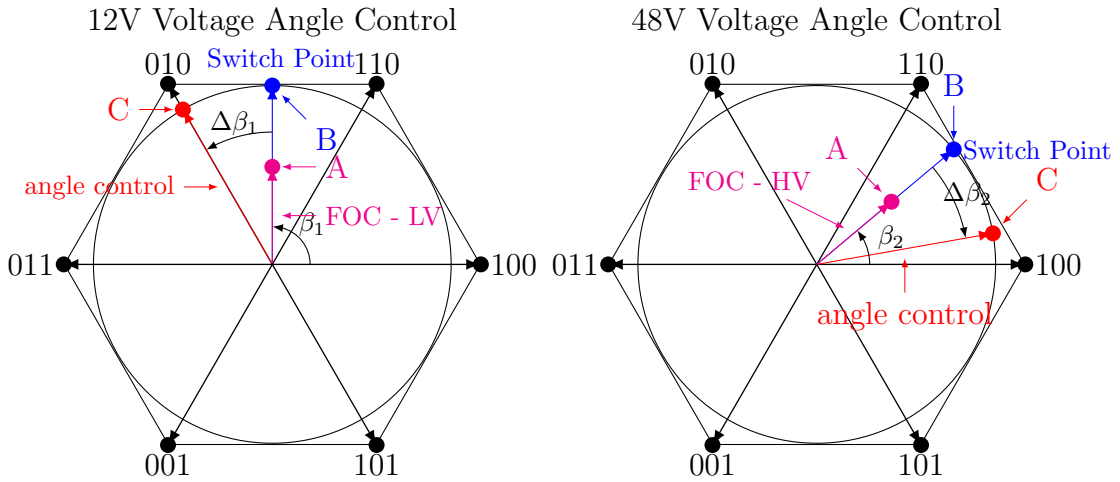


Figure 4.35 – Angle Control Principle with 12V and 48V Voltage Vectors

The presented idea is applied to control the power at both sides but can be applied in a similar way to control the torque. One reason to apply this principle for a power control is that the electrical power can be calculated only from internal measured quantities. The torque command can be converted to a corresponding power command with the measured mechanical speed and a knowledge of the machine efficiency. The active power of each side can be expressed through the d - and q -axis voltages and currents as shown in equations (4.5.1.1) and (4.5.1.2) [2]. The electrical power for the 12V side is calculated from the 12V d - q voltages and currents, v_{qs1} , i_{qs1} , v_{ds1} and i_{ds1} , and the electrical power at the 48V side is calculated from the 48V d - q voltages and currents, v_{qs2} , i_{qs2} , v_{ds2} and i_{ds2} . The formulas for deriving the active power in the d - q frame from the instantaneous power equation in the a - b - c frame are provided in reference [2].

$$P_{e12V} = v_{us1}i_{us1} + v_{vs1}i_{vs1} + v_{ws1}i_{ws1} = \frac{3}{2}(v_{qs1}i_{qs1} + v_{ds1}i_{ds1}) \quad (4.5.1.1)$$

$$P_{e48V} = v_{xs1}i_{xs1} + v_{ys1}i_{ys1} + v_{zs1}i_{zs1} = \frac{3}{2}(v_{qs2}i_{qs2} + v_{ds2}i_{ds2}) \quad (4.5.1.2)$$

The d - q voltages in equations (4.5.1.1) and (4.5.1.2) are in Cartesian form and should be transformed into a polar representation. The arbitrary plotted voltage vectors from Fig.

4.35 are considered without losing generality. The tip of both vectors, symbolizing an operation in the BS range, are marked with the point A. The d - q voltages are rewritten through their magnitudes, $| \vec{v}_{s1} |$ and $| \vec{v}_{s2} |$, and angles, β_1 and β_2 , in equation (4.5.1.3).

$$\begin{aligned} v_{qs1} &= | \vec{v}_{s1} | \sin \beta_1 & v_{ds1} &= | \vec{v}_{s1} | \cos \beta_1 \\ v_{qs2} &= | \vec{v}_{s2} | \sin \beta_2 & v_{ds2} &= | \vec{v}_{s2} | \cos \beta_2 \end{aligned} \quad (4.5.1.3)$$

The expressions from equation (4.5.1.3) can be substituted into equations (4.5.1.1) and (4.5.1.2) to remove the d - q voltage dependency. This way equations (4.5.1.4) and (4.5.1.5) are derived.

$$P_{e12V} = \frac{3}{2} (| \vec{v}_{s1} | \sin \beta_1 i_{qs1} + | \vec{v}_{s1} | \cos \beta_1 i_{ds1}) \quad (4.5.1.4)$$

$$P_{e48V} = \frac{3}{2} (| \vec{v}_{s2} | \sin \beta_2 i_{qs2} + | \vec{v}_{s2} | \cos \beta_2 i_{ds2}) \quad (4.5.1.5)$$

The power equations from (4.5.1.4) and (4.5.1.5) depend on the voltage vector magnitudes, the voltage phase angles and the stator currents. The goal is to find expressions also for the stator currents, so that the power equations will depend only on the voltage vectors. Therefore the d - q voltage equations are written out again in their stationary form in the system of equations shown in (4.5.1.6).

$$\begin{aligned} v_{qs1} &= r_{s1} i_{qs1} + \omega_e \left((L_{dd1} + L_{ls1}) i_{ds1} + \frac{L_{dd1}}{N_{s12}} i_{ds2} + \frac{2L_{dd1}}{3N_{s1f}} i_{fd} \right) \\ v_{ds1} &= r_{s1} i_{ds1} - \omega_e \left((L_{ls1} + L_{qq1}) i_{qs1} - \frac{L_{qq1}}{N_{s12}} i_{qs2} \right) \\ v_{qs2} &= r_{s2} i_{qs2} + \omega_e \left(\left(L_{ls2} + \frac{L_{dd1}}{N_{s12}^2} \right) i_{ds2} + \frac{L_{dd1}}{N_{s12}} i_{ds1} + \frac{2L_{dd1}}{3N_{s12}N_{s1f}} i_{fd} \right) \\ v_{ds2} &= r_{s2} i_{ds2} - \omega_e \left(\left(L_{ls2} + \frac{L_{qq1}}{N_{s12}^2} \right) i_{qs2} - \frac{L_{qq1}}{N_{s12}} i_{qs1} \right) \end{aligned} \quad (4.5.1.6)$$

The system of voltage equations from (4.5.1.6) can be solved after the stator currents: i_{qs1} , i_{ds1} , i_{qs2} and i_{ds2} . The solutions after the stator currents from (4.5.1.6) consist of very long and tedious terms because of the stator resistances. Therefore one simplification is performed. In the field weakening area the back-emf terms are much greater than the voltage drops over the stator resistances. Therefore the voltage equations are simplified to the ones written out in equation (4.5.1.7).

$$\begin{aligned} v_{qs1} &= \omega_e \left((L_{dd1} + L_{ls1}) i_{ds1} + \frac{L_{dd1}}{N_{s12}} i_{ds2} + \frac{2L_{dd1}}{3N_{s1f}} i_{fd} \right) \\ v_{ds1} &= -\omega_e \left((L_{ls1} + L_{qq1}) i_{qs1} - \frac{L_{qq1}}{N_{s12}} i_{qs2} \right) \\ v_{qs2} &= +\omega_e \left(\left(L_{ls2} + \frac{L_{dd1}}{N_{s12}^2} \right) i_{ds2} + \frac{L_{dd1}}{N_{s12}} i_{ds1} + \frac{2L_{dd1}}{3N_{s12}N_{s1f}} i_{fd} \right) \\ v_{ds2} &= -\omega_e \left(\left(L_{ls2} + \frac{L_{qq1}}{N_{s12}^2} \right) i_{qs2} - \frac{L_{qq1}}{N_{s12}} i_{qs1} \right) \end{aligned} \quad (4.5.1.7)$$

The system of equations from (4.5.1.7) is solved after the stator currents. The solution is provided in equation (4.5.1.8). It is evident that also with the performed simplification

of ignoring the stator resistance voltage drops, the terms are complex and lengthy. Nevertheless, the expressions for the stator currents through the voltages are valid and can be used further in the derivation of the VAC. The d - q voltages are still present in their Cartesian form in the system of equations shown in (4.5.1.8). Therefore the d - q voltages are substituted with their polar form. This way the currents from equation (4.5.1.8) depend only on the voltage vector magnitudes, $|v_{s1}^{\vec{}}|$ and $|v_{s2}^{\vec{}}|$, and both angles, β_1 and β_2 . The expressions for the currents are substituted in the power equations for the 12V and 48V side shown in equations (4.5.1.4) and (4.5.1.5), which eliminates the current dependency of the power.

$$\begin{aligned}
 i_{qs1} &= -\frac{(L_{ls2}N_{s12}^2 + L_{qq1})v_{ds1} - L_{qq1}v_{ds2}N_{s12}}{\omega_e(L_{ls1}L_{qq1} + L_{ls1}L_{ls2}N_{s12}^2 + L_{ls2}L_{qq1}N_{s12}^2)} \\
 i_{ds1} &= \frac{(3L_{dd1}N_{s1f} + 3L_{ls2}N_{s12}^2N_{s1f})v_{qs1} - 3L_{dd1}N_{s12}N_{s1f}v_{qs2} - 2L_{dd1}L_{ls2}N_{s12}^2i_{fd}\omega_e}{3N_{s1f}\omega_e(L_{dd1}L_{ls1} + L_{dd1}L_{ls2}N_{s12}^2 + L_{ls1}L_{ls2}N_{s12}^2)} \\
 i_{qs2} &= -\frac{N_{s12}((L_{ls1}N_{s12} + L_{qq1}N_{s12})v_{ds2} - L_{qq1}v_{ds1})}{\omega_e(L_{ls1}L_{qq1} + L_{ls1}L_{ls2}N_{s12}^2 + L_{ls2}L_{qq1}N_{s12}^2)} \\
 i_{ds2} &= -\frac{N_{s12}(3L_{dd1}N_{s1f}v_{qs1} - (3L_{dd1}N_{s12}N_{s1f} - 3L_{ls1}N_{s12}N_{s1f})v_{qs2} + 2L_{dd1}L_{ls1}i_{fd}\omega_e)}{3N_{s1f}\omega_e(L_{dd1}L_{ls1} + L_{dd1}L_{ls2}N_{s12}^2 + L_{ls1}L_{ls2}N_{s12}^2)}
 \end{aligned} \tag{4.5.1.8}$$

The power equations from (4.5.1.4) and (4.5.1.5) are then transformed to the expressions shown in equations (4.5.1.9) and (4.5.1.10).

$$\begin{aligned}
 P_{e12V}(\beta_1, \beta_2) &= |v_{s1}^{\vec{}}| \cos \beta_1 \left(\frac{3L_{dd1}N_{s1f}|v_{s1}^{\vec{}}| \sin \beta_1 - 2L_{dd1}L_{ls2}N_{s12}^2i_{fd}\omega_e}{2N_{s1f}\omega_e(L_{dd1}L_{ls1} + L_{dd1}L_{ls2}N_{s12}^2 + L_{ls1}L_{ls2}N_{s12}^2)} \right. \\
 &\quad \left. + \frac{3L_{ls2}N_{s12}^2N_{s1f}|v_{s1}^{\vec{}}| \sin \beta_1 - 3L_{dd1}N_{s12}N_{s1f}|v_{s2}^{\vec{}}| \sin \beta_2}{2N_{s1f}\omega_e(L_{dd1}L_{ls1} + L_{dd1}L_{ls2}N_{s12}^2 + L_{ls1}L_{ls2}N_{s12}^2)} \right) \\
 &\quad - |v_{s1}^{\vec{}}| \cos \beta_1 \frac{3|v_{s1}^{\vec{}}| \sin \beta_1 (L_{ls2}|v_{s1}^{\vec{}}| \cos \beta_1 N_{s12}^2)}{2\omega_e(L_{ls1}L_{qq1} + L_{ls1}L_{ls2}N_{s12}^2 + L_{ls2}L_{qq1}N_{s12}^2)} \\
 &\quad - |v_{s1}^{\vec{}}| \cos \beta_1 \frac{-L_{qq1}|v_{s2}^{\vec{}}| \cos \beta_2 N_{s12} + L_{qq1}|v_{s1}^{\vec{}}| \cos \beta_1}{2\omega_e(L_{ls1}L_{qq1} + L_{ls1}L_{ls2}N_{s12}^2 + L_{ls2}L_{qq1}N_{s12}^2)}
 \end{aligned} \tag{4.5.1.9}$$

The power generated by each stator winding depends on both voltage vectors in a complex way. The angle dependency is included in cosine and sine functions. The power equations depend only on both voltage angles, α_1 and α_2 , and both voltage magnitudes $|v_{s1}^{\vec{}}|$ and $|v_{s2}^{\vec{}}|$. The decoupling of both power equations in terms of angle control is not straightforward because the voltage angles are included in sine and cosine terms. Both power equations, (4.5.1.9) and (4.5.1.10), show that, the 12V and the 48V powers, P_{e12V} and P_{e48V} , are both dependent on both voltage magnitudes and both angles: $|v_{s1}^{\vec{}}|$, $|v_{s2}^{\vec{}}|$, β_1 and β_2 . The goal is to be able to control the power at each side as far as possible independently from the power and voltage vector of the other side. Therefore a decoupling algorithm and a control structure is required, which can achieve this task. In the FW area, both voltage vectors are fixed at their maximum possible values: $|v_{s1}^{\vec{}}| = \frac{V_{DC1V}}{\sqrt{3}}$

and $|v_{s2}^{\vec{}}| = \frac{V_{DCHV}}{\sqrt{3}}$. Therefore, a decoupling control based on both voltage angles is investigated, while the voltage vector magnitudes are set to their maximum values.

$$\begin{aligned}
 P_{e48V}(\beta_1, \beta_2) = & -3N_{s12} |v_{s2}^{\vec{}}| \sin \beta_2 \frac{(L_{ls1}N_{s12} |v_{s2}^{\vec{}}| \cos \beta_2 - L_{qq1} |v_{s1}^{\vec{}}| \cos \beta_1)}{2\omega_e (L_{ls1}L_{qq1} + L_{ls1}L_{ls2}N_{s12}^2 + L_{ls2}L_{qq1}N_{s12}^2)} \\
 & - 3N_{s12} |v_{s2}^{\vec{}}| \sin(\beta_2) \frac{L_{qq1}N_{s12} |v_{s2}^{\vec{}}| \cos \beta_2}{2\omega_e (L_{ls1}L_{qq1} + L_{ls1}L_{ls2}N_{s12}^2 + L_{ls2}L_{qq1}N_{s12}^2)} \\
 & + N_{s12} |v_{s2}^{\vec{}}| \cos \beta_2 \frac{(3L_{dd1}N_{s1f} |v_{s1}^{\vec{}}| \sin \beta_1 + 2L_{dd1}L_{ls1}i_{fd}\omega_e)}{2N_{s1f}\omega_e (L_{dd1}L_{ls1} + L_{dd1}L_{ls2}N_{s12}^2 + L_{ls1}L_{ls2}N_{s12}^2)} \\
 & + N_{s12} |v_{s2}^{\vec{}}| \cos \beta_2 \frac{(-3L_{dd1}N_{s12}N_{s1f} + 3L_{ls1}N_{s12}N_{s1f}) |v_{s2}^{\vec{}}| \sin \beta_2}{2N_{s1f}\omega_e (L_{dd1}L_{ls1} + L_{dd1}L_{ls2}N_{s12}^2 + L_{ls1}L_{ls2}N_{s12}^2)}
 \end{aligned} \tag{4.5.1.10}$$

The voltage vectors at both switch points B in Fig. 4.35 are considered in order to derive the angle control in the field weakening area. The switch points denote the time, where the voltage vectors generated by the current controllers first reach their maximum length. From this point on the voltage vector has to be rotated with an angle $\Delta\beta$. The examples shown in Fig. 4.35 rotate the 12V voltage vector counterclockwise with the angle $\Delta\beta_1$ and the 48V voltage vector clockwise with the angle $\Delta\beta_2$. In order to investigate how the power at both sides is influenced due to the rotation of both angles, β_1 and β_2 , to their new values, $\Delta\beta_1 + \beta_1$ and $\Delta\beta_2 + \beta_2$, the new angle values are substituted in equations (4.5.1.9) and (4.5.1.10). Then the power equations at both C points from Fig. 4.35 is expressed as: $P_{e12V}(\beta_1 + \Delta\beta_1, \beta_2 + \Delta\beta_2)$ and $P_{e48V}(\beta_1 + \Delta\beta_1, \beta_2 + \Delta\beta_2)$. The powers at both B points are respectively equal to $P_{e12V}(\beta_1, \beta_2)$ and $P_{e48V}(\beta_1, \beta_2)$. The power changes ΔP_{e12V} and ΔP_{e48V} from points C to points B can be expressed then through equations (4.5.1.11) and (4.5.1.12).

$$\Delta P_{e12V} = P_{e12V}(\beta_1 + \Delta\beta_1, \beta_2 + \Delta\beta_2) - P_{e12V}(\beta_1, \beta_2) \tag{4.5.1.11}$$

$$\Delta P_{e48V} = P_{e48V}(\beta_1 + \Delta\beta_1, \beta_2 + \Delta\beta_2) - P_{e48V}(\beta_1, \beta_2) \tag{4.5.1.12}$$

Equations (4.5.1.11) and (4.5.1.12) are implemented in Matlab and trigonometric simplifications are performed, so that the angle sums are excluded from the sine and cosine functions. This way the incremental powers, ΔP_{e12V} and ΔP_{e48V} , depend on the sine and cosine of the incremental angles $\Delta\beta_1$ and $\Delta\beta_2$. The sine and cosine functions of incremental angle values can be approximated according to equation (4.5.1.13).

$$\sin(\Delta\beta_1) \approx \Delta\beta_1 \quad \cos(\Delta\beta_1) \approx 1 \quad \sin(\Delta\beta_2) \approx \Delta\beta_2 \quad \cos(\Delta\beta_2) \approx 1 \tag{4.5.1.13}$$

A linearization is performed through the approximations from equation (4.5.1.13). Equations (4.5.1.11) and (4.5.1.12) are not written out here in their full form for readability purposes. The equations contain also the squares of the incremental angles $\Delta\beta_1^2$ and $\Delta\beta_2^2$ and their cross-multiplication $\Delta\beta_1 \cdot \Delta\beta_2$. The incremental angles $\Delta\beta_1$ and $\Delta\beta_2$ are assumed to be very small, which leads to the approximation that their squares and cross-multiplication tilt to zero. Thus they are substituted with zero. This way,

equations (4.5.1.11) and (4.5.1.12) become linear with respect to $\Delta\beta_1$ and $\Delta\beta_2$. This way the differential power equations linearized with respect to both incremental angles are derived in equation (4.5.1.14).

$$\begin{bmatrix} \Delta P_{e12V} \\ \Delta P_{e48V} \end{bmatrix} = \overbrace{\begin{bmatrix} A11 & A12 \\ A21 & A22 \end{bmatrix}}^A \cdot \begin{bmatrix} \Delta\beta_1 \\ \Delta\beta_2 \end{bmatrix}$$

$$\begin{aligned} A11 &= \frac{N_{s12} |v_{s1}^{\vec{}}| (+6(L_{qq1} - L_{dd1}) L_{ls2}^2 N_{s12}^3 N_{s1f} |v_{s1}^{\vec{}}| \cos 2\beta_1}{+ (4L_{dd1} L_{ls1} L_{ls2} L_{qq1} N_{s12} + 4L_{dd1} L_{ls2}^2 (L_{qq1} + L_{ls1}) N_{s12}^3) i_{fd}\omega_e \sin \beta_1} \\ &\quad + \frac{3(L_{qq1} - L_{dd1}) L_{ls1} L_{ls2} N_{s12}^2 N_{s1f} |v_{s2}^{\vec{}}| \cos(\beta_1 + \beta_2) + (6L_{dd1} L_{ls1} L_{qq1} N_{s1f}\omega_e \cdot (L_{dd1} L_{ls1} + L_{dd1} L_{ls2} N_{s12}^2 + L_{ls1} L_{ls2} N_{s12}^2))}{4N_{s1f}\omega_e \cdot (L_{dd1} L_{ls1} + L_{dd1} L_{ls2} N_{s12}^2 + L_{ls1} L_{ls2} N_{s12}^2)} \cdot \\ &\quad + \frac{3L_{ls1} L_{ls2} (L_{qq1} + L_{dd1}) N_{s12}^2 + 6L_{dd1} L_{ls2} L_{qq1} N_{s12}^2}{(L_{ls1} L_{qq1} + L_{ls1} L_{ls2} N_{s12}^2 + L_{ls2} L_{qq1} N_{s12}^2)} N_{s1f} |v_{s2}^{\vec{}}| \cos(\beta_1 - \beta_2)) \\ A12 &= - \frac{3N_{s12} |v_{s1}^{\vec{}}| |v_{s2}^{\vec{}}| ((L_{dd1} - L_{qq1}) L_{ls1} L_{ls2} N_{s12}^2 \cos(\beta_1 + \beta_2)}{4\omega_e (L_{dd1} (L_{ls1} + L_{ls2} N_{s12}^2) + L_{ls1} L_{ls2} N_{s12}^2)} \cdot \\ &\quad + \frac{(L_{ls1} L_{ls2} (L_{qq1} + L_{dd1}) N_{s12}^2 + 2L_{dd1} L_{qq1} (L_{ls2} N_{s12}^2 + L_{ls1})) \cos(\beta_1 - \beta_2)}{((L_{ls1} + L_{ls2} N_{s12}^2) L_{qq1} + L_{ls1} L_{ls2} N_{s12}^2)} \\ A21 &= - \frac{3N_{s12} |v_{s1}^{\vec{}}| |v_{s2}^{\vec{}}| ((L_{dd1} - L_{qq1}) L_{ls1} L_{ls2} N_{s12}^2 \cos(\beta_1 + \beta_2)}{4\omega_e (L_{dd1} (L_{ls1} + L_{ls2} N_{s12}^2) + L_{ls1} L_{ls2} N_{s12}^2)} \cdot \\ &\quad + \frac{(L_{ls1} L_{ls2} (L_{qq1} + L_{dd1}) N_{s12}^2 + 2L_{dd1} (L_{ls2} N_{s12}^2 + L_{ls1}) L_{qq1}) \cos(\beta_1 - \beta_2)}{((L_{ls1} + L_{ls2} N_{s12}^2) L_{qq1} + L_{ls1} L_{ls2} N_{s12}^2)} \\ A22 &= \frac{N_{s12} |v_{s2}^{\vec{}}| (6(L_{qq1} - L_{dd1}) L_{ls1}^2 N_{s12} N_{s1f} |v_{s2}^{\vec{}}| \cos 2\beta_2 +}{(6L_{dd1} L_{qq1} (L_{ls2} N_{s12}^2 + L_{ls1}) + 3(L_{dd1} + L_{qq1}) L_{ls1} L_{ls2} N_{s12}^2) N_{s1f} |v_{s1}^{\vec{}}| \cos(\beta_1 - \beta_2)} \\ &\quad + \frac{3L_{ls1} L_{ls2} (L_{qq1} - L_{dd1}) N_{s12}^2 N_{s1f} |v_{s1}^{\vec{}}| \cos(\beta_1 + \beta_2)}{4N_{s1f}\omega_e \cdot (L_{dd1} (L_{ls1} + L_{ls2} N_{s12}^2) + L_{ls1} L_{ls2} N_{s12}^2)} \cdot \\ &\quad + \frac{(4L_{dd1} L_{ls1}^2 L_{ls2} N_{s12}^2 + 4L_{dd1} L_{ls1}^2 L_{qq1} + 4L_{dd1} L_{ls1} L_{ls2} L_{qq1} N_{s12}^2) i_{fd}\omega_e \sin \beta_2}{((L_{ls1} + L_{ls2} N_{s12}^2) L_{qq1} + L_{ls1} L_{ls2} N_{s12}^2)} \end{aligned} \tag{4.5.1.14}$$

Equation (4.5.1.14) describes how an incremental change in both angles of the stator voltage vectors, $\Delta\beta_1$ and $\Delta\beta_2$, influences the power changes at both stator windings,

ΔP_{e12V} and ΔP_{e48V} . The cross-coupling terms $A12 \cdot \Delta\beta_2$ and $A21 \cdot \Delta\beta_1$ describe how the power at the neighboring side is influenced when one of the voltage angles is changed. Both terms $A12$ and $A21$ in the matrix are equal. It has to be noted that the coupling is present also in the terms $A11$ and $A22$ because both angles, β_1 and β_2 , are present in the matrix entries. The matrix A represents how an incremental change in both angles, $\Delta\beta_1$ and $\Delta\beta_2$, results in an incremental change in the power at both sides, ΔP_{e12V} and ΔP_{e48V} . The matrix is based on the sine and cosine terms, which are functions of the current voltage phase angles: β_1 and β_2 . This means that a certain incremental angle change, for example $\Delta\beta_1$, results in different power changes, ΔP_{e12V} , as a function of the current operating points of the voltage angles: β_1 and β_2 .

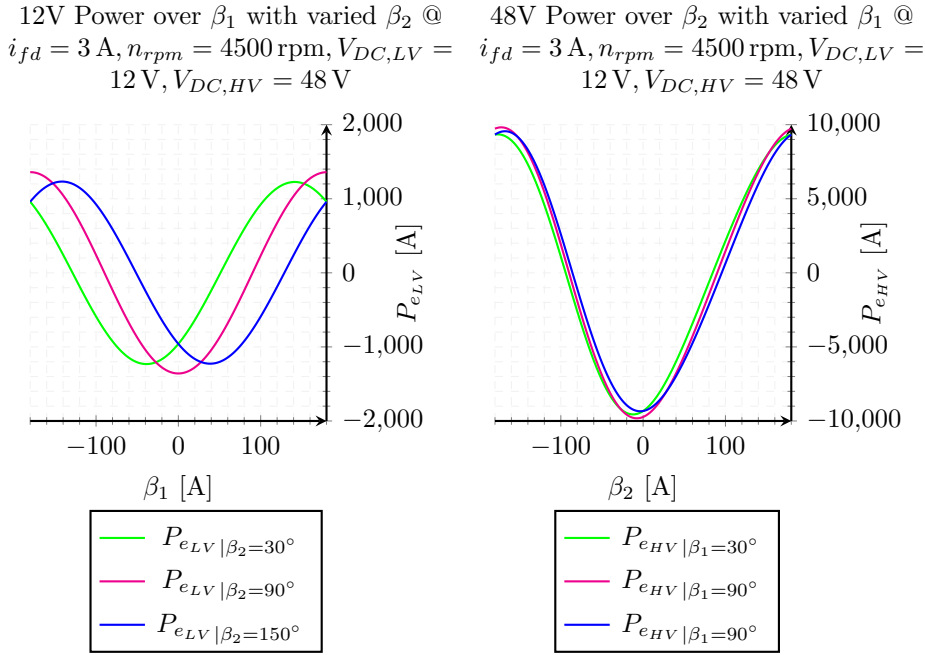


Figure 4.36 – Power as a Function of the Voltage Angles.

The 12V and 48V powers are plotted in Fig. 4.36 as functions of the voltage angles β_1 and β_2 . The 12V power is plotted in the left plot as a function of the 12V stator voltage angle β_1 . The 48V power is plotted to the right in dependency of the 48V stator voltage angle β_2 . The crosswise dependency from the other system is illustrated as a varying parameter for three different values. For the 12V power equation the 48V voltage angle β_2 is set to three different values: $\beta_2 = 30^\circ, 90^\circ$ and 150° . For the 48V power equation the 12V angle is varied correspondingly with the same three values. An angle β_2 of 90° represents a voltage vector fully aligned with the q -axis v_{qs2} . This plot is illustrated in magenta color in Fig. 4.36 for the 12V power. The 48V side in this case does not generate power, because the q -axis voltage compensates only the back-emf resulting from the d -axis flux¹⁰.

¹⁰Except for the cross-reluctance torque which is neglected in this consideration.

This is confirmed through the second plot on the right illustrated in magenta color in Fig. 4.37. It is obvious that for a 90° voltage angle the generated 48V power is around zero. The power plots in the Fig. 4.36 show clearly the cosine dependency of the voltage angle β_1 . When the voltage angle of the 48V side is varied, the cosine curve of the 12V power is shifted either to left or to the right. The magenta 12V power curve is linear around the angle of 90° : $\beta_1 = 90^\circ$. This is conceivable, as a voltage vector with an angle of 90° compensates fully the rotor flux and does not generate power. If the voltage vector is rotated right or left from 90° a generative or motoring power is produced respectively. When the 12V angle β_1 is increased close to the angle of 180° or decreased close to an angle of 0° , the relationship between voltage angle and power becomes highly non-linear and is even reversed due to the periodic character of the cosine function. This non-linear angle dependency of the power from the voltage angles is described through the matrix A of equation (4.5.1.14). The minimum and maximum possible voltage angles should be adequately considered in the control, in order to avoid instability issues during the angle control.

The two other curves from the left plot of Fig. 4.36 show the 12V power, when the 48V voltage angle is changed from 90° . The voltage angle of the 48V side β_2 is changed from 90° to 30° , which corresponds to the 12V power curve from Fig. 4.36 plotted in green. A negative power of around -7500 W is generated at the 48V side with a 30° angle of the 48V voltage vector¹¹. The power curve for the 48V side at an angle of 30° is illustrated in the right plot of Fig. 4.37 in green color. The green 12V power curve is shifted left from the magenta power curve in the left plot of Fig. 4.36. This means that the linear angle dependency of the 12V power from the 12V angle β_1 is not anymore around the angle of 90° but less. The graph shows that the maximum possible 12V power is reduced due to the change in the 48V voltage angle. Both limits, the maximum possible power and the maximum angles, have to be adjusted during the control. If the 48V angle is changed to 150° the 12V power curve shifts to the right with respect to the magenta curve in Fig. 4.36. This curve is plotted in blue in Fig. 4.36. In this case the linear area of the 12V power control is moved towards greater angles than 90° . Again the maximum possible power is reduced in comparison to the magenta curve. The right plot of Fig. 4.37 shows the 48V power at an angle of $\beta_2 = 150^\circ$ in blue color. The generated 48V power is around 7500 W .

The right plot of Fig. 4.36 shows the 48V power dependency of the 48V voltage angle β_2 . It is obvious that the power control of the 48V side is far less dependent from the 12V voltage angle β_1 . The linear area of the 48V power angle control is around 90° .

Both plots from Fig. 4.37 illustrate the crosswise dependency of both powers from the voltage angle of the other stator system. The left plot shows the 12V power as a function of the 48V angle β_2 and a parametrization of the 12V voltage angle β_1 . The right plot shows the 48V power as a function of the 12V angle β_1 and a parametrization of the 48V

¹¹The exact value of the power generated is in reality not -7500 W as the presented curves do not consider saturation

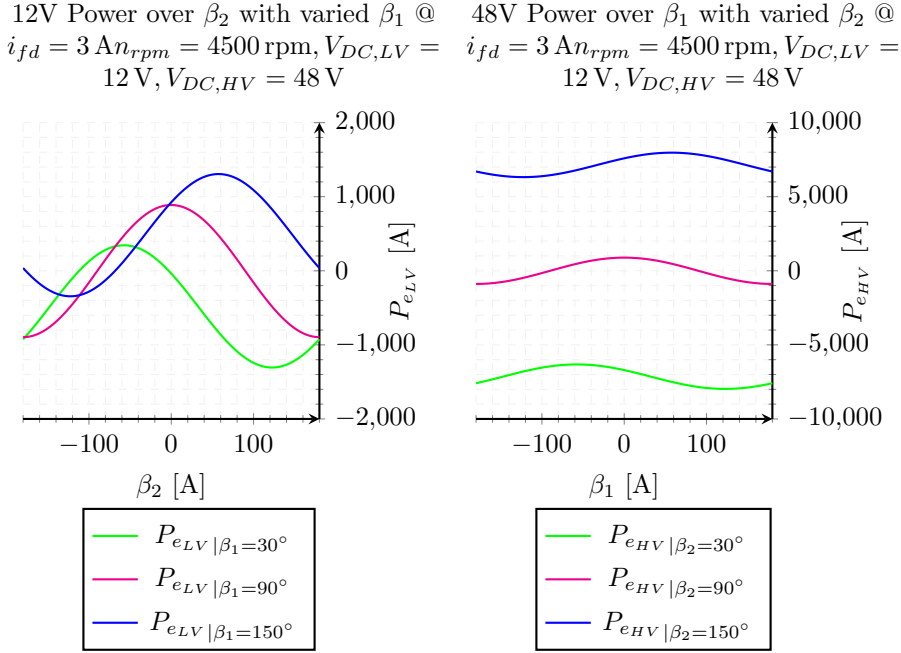


Figure 4.37 – Power as Function of Voltage Angles.

angle β_2 . The parametrization is done again for three different angles: 30° , 90° and 150° . All three plots show that if the 12V voltage angle is fixed at a certain value and the 48V angle β_2 is varied, the generated 12V power is highly disturbed. Therefore the 12V power control has to be able to counteract the disturbance resulting from the power control of the 48V system. The control of the 12V power through the 12V voltage angle β_1 has also a disturbing effect on the generated 48V power as it is evident from the right plot of Fig. 4.37. The effect is not as influential as for the 12V side. Nevertheless the 12V power control has to be compensated also at the 48V side.

The illustrated power curves from Figures 4.36 and 4.37 show that the matrix \mathbf{A} from equation (4.5.1.14) depends on the current angles of the voltage vectors β_1 and β_2 . The matrix \mathbf{A} thus relates the incremental angle changes, $\Delta\beta_1$ and $\Delta\beta_2$, with the incremental power changes ΔP_{e12V} and ΔP_{e48V} . However a power control structure requires the reverse relationship. The voltage angles, β_1 and β_2 , should be adjusted such, that the requested powers P_{e12V}^* or P_{e48V}^* are controlled. For this purpose the inverse relationship is shown in equation (4.5.1.15).

$$\begin{bmatrix} \Delta\beta_1 \\ \Delta\beta_2 \end{bmatrix} = \begin{bmatrix} B11 & B12 \\ B21 & B22 \end{bmatrix} \cdot \begin{bmatrix} \Delta P_{e12V} \\ \Delta P_{e48V} \end{bmatrix} = \frac{1}{\det(\mathbf{A})} \overbrace{\begin{bmatrix} A22 & -A12 \\ -A21 & A11 \end{bmatrix}}^{\text{adj}(\mathbf{A})} \cdot \begin{bmatrix} \Delta P_{e12V} \\ \Delta P_{e48V} \end{bmatrix} \quad (4.5.1.15)$$

A control structure can be derived based on equation (4.5.1.15). An integral action has to be applied on the incremental angles $\Delta\beta_1$ and $\Delta\beta_2$ in order to calculate the angles

β_1 and β_2 . The angle control structure is presented in Fig. 4.38. The inputs on the left

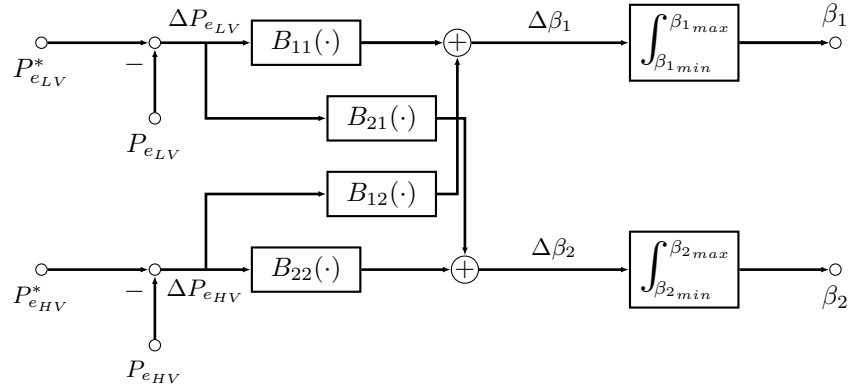


Figure 4.38 – Block Diagram Power Voltage Angle Control

side represent the requested 12V and 48V powers. The feedback for both controllers are the calculated powers, P_{e12V} and P_{e48V} , based on the internal voltages and currents in the d - q frame according to equations (4.5.1.1) and (4.5.1.2). In case the alignment of the d - and q -axis is not perfect, this would result in an error between calculated and generated power. There are also alternative ways to calculate the DC power at both sides. The DC powers can be calculated through the measured DC link voltage and a reconstruction of the DC current from the measured phase currents. An investigation of other alternative ways to calculate the DC powers will go out of the scope of the work. The focus of this chapter lies on the angle control concept and intends to prove its feasibility. If a deviation between calculated power and measured power is observed this has to be corrected through a time intensive calibration of the d - and q -axis alignment.

The presented theory show that an angle control for both sides should be feasible in the field weakening region. The presented control structure in Fig. 4.38 decouples the control of both axis before the inputs, $\Delta\beta_1$ and $\Delta\beta_2$, are forwarded to the integrators. The terms, B_{11} , B_{12} , B_{21} and B_{22} , depend on the current stator voltage angles β_1 and β_2 . Therefore the voltage angles from the inner current control loop should be employed into the angle control structure and used to calculate the terms. There is a delay introduced due to the feedback loop. The integral actions should be able to handle uncertainties in the model and additional time delays. When the fed back angles, β_1 and β_2 , do not correspond to the current angles, the control operates at a slightly different place on the power curves plotted in Fig. 4.36. As long as the fed back angles, β_1 and β_2 , do not drastically deviate from the real ones, such that the operating point is no longer in the linear range, the control structure should be able to handle these uncertainties.

The presented control structure takes care of the power control only in the field weakening area. The current controllers are active in the BS range before the stator voltages reach their maximal values. Therefore some control switching mechanism is required in order

to be able to use the proposed VAC. The switching mechanism is discussed in Subsection 4.5.2.

4.5.2 Switching Method between the Field Oriented Control and the Voltage Angle Control

The presented angle control exploits fully the DC link voltage and sets the voltage vectors of both stator system to their maximum lengths. In the BS range of the machine the voltage vectors are still below their maximal values and therefore it is logical to switch to the VAC, when the FOC control reaches for the first time the maximum modulation index. The switching condition can be encompassed with a speed condition, such that the VAC is only activated at speeds above the corner speed. A low-pass filter has to be applied on the modulation index, such that transients reaching the maximum modulation index for only short time due to dynamical reference changes do not activate the VAC. The filtered modulation index is the trigger for activating and deactivating the VAC control. A hysteresis has to be introduced around the maximum modulation index in order to prevent toggling between both control areas. The control should switch again to the FOC control, when the modulation index falls below a certain threshold: the maximum modulation index minus the hysteresis. The logic for activating and deactivating the VAC is illustrated in Fig. 4.39. The state machine, which describes how both control algorithms are selected is illustrated in Fig. 4.40.

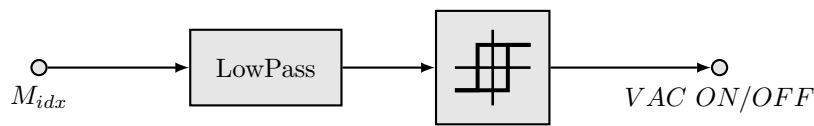


Figure 4.39 – Activation and Deactivation of the VAC based on M_{idx}

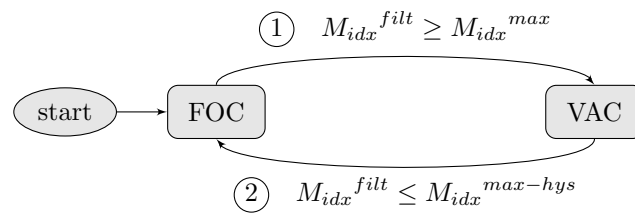


Figure 4.40 – Switching Mechanism between FOC and VAC

According to Fig. 4.40 the control initializes in the FOC mode and once the filtered modulation index M_{idx}^{filt} reaches the maximum possible modulation index M_{idx}^{max} , the VAC is activated. This switching mechanism is possible, because during the FOC mode the PI current controllers can regulate the length of the voltage vectors. The VAC control starts to be active from the last voltage vector set by the current controllers during the FOC. The principle is illustrated in Fig. 4.41. The blue voltage vector is the last one from the

FOC in the BS range. This one is used as an initial voltage vector for the VAC. The VAC rotates the voltage vector during the control in the field weakening area around an additional field weakening angle α in order to set the requested power.

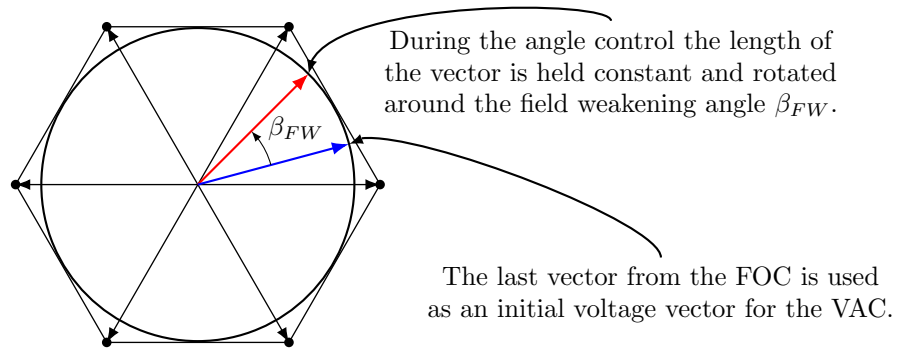


Figure 4.41 – Transition from VAC to FOC

This switching mechanism is feasible for the transition from FOC to VAC. However during the VAC only the angle of the voltage vector is controlled and the voltage vector is fixed at its maximum length. Therefore the second condition for switching back to the FOC cannot be fulfilled just by rotating the voltage vector. In order to be able to

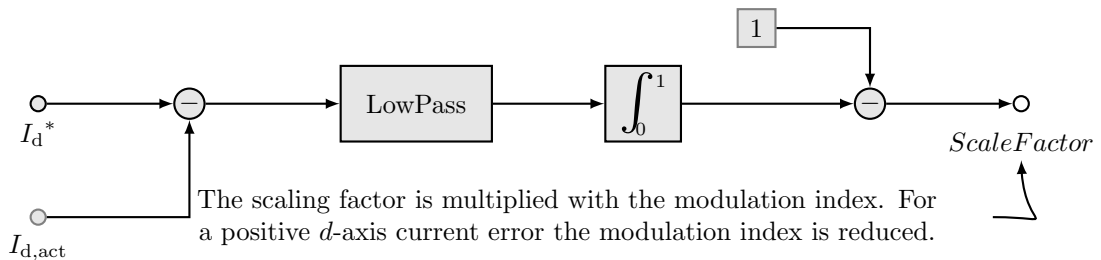


Figure 4.42 – Transition from VAC to FOC

fulfill the second condition from Fig. 4.42 a way is required to detect that no more FW action is required and the maximum modulation index can be reduced. In case the VAC returns to working points close to the BS range, it should be possible to set the requested working points also with the current controllers. If the VAC is no longer required for a FW control the d -axis and q -axis currents are adjusted close to their reference values. The d -axis current error can be used in order to detect that no more FW action is required. A mechanism to reduce the maximum modulation index is illustrated in Fig. 4.42. The difference between requested d -axis current and measured d -axis current is calculated and passed through a low-pass filter. When the FW action is required, the difference between requested and measured d -axis current should be negative. Therefore the output of the low-pass filter is also negative. This result is fed into an integrator, which has as a lower limit a zero. Therefore as long the difference between requested and measured d -axis

current is negative, the integrator will be saturated at its lower limit. Then the outcome of the integrator is subtracted from one. The result is a scaling factor, which is multiplied by the maximum modulation index. Therefore when the VAC is required, the outcome of the integrator is zero and the scaling factor 1. The maximum modulation index remains unaffected because it is multiplied by 1. Once the VAC controls the power such, that no more field weakening action is required, the difference between reference and measured d -axis current becomes positive. This results in an output from the integrator greater than zero, which results in a scaling factor smaller than 1. A positive d -axis current error is equivalent to the fact that no more FW action is required. In this case, the d -axis current controller can regulate the requested reference and the modulation index is reduced. Figure 4.42 presents a transition mechanism, which reduces the modulation index M_{idx} , when no field weakening action is required. This way condition 2 from Fig. 4.40 becomes feasible.

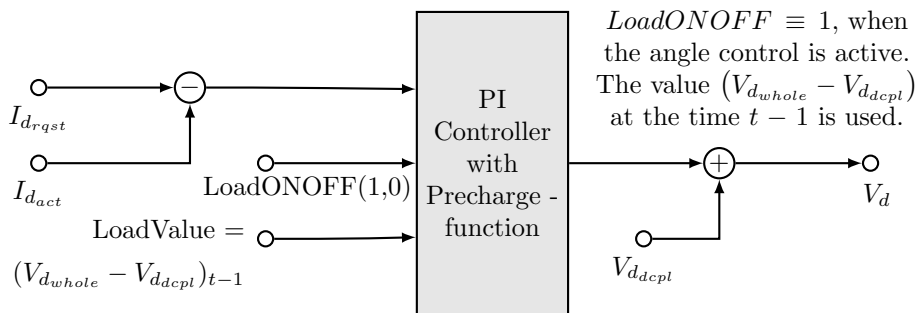


Figure 4.43 – PI Controller with a Pre-Charge Function

Another challenge during the transition back to the FOC control is the re-activation of the PI controllers. During the FW control, the PI controllers are always saturated, because the d - and q -axis current errors fed into the PI controllers cannot be influenced through the current controllers action. Therefore a mechanism is required, which passes the control from the VAC to the PI current control. The only common element both kinds of control have is the voltage vector as the actuator, which controls the requested power or torque. Therefore it is logical to consider a mechanism, which passes the voltage vector at the time of transition to the other control mechanism. The PI controllers should be loaded with the voltage vector from the last time step, when the VAC control was active. Figure 4.43 illustrates a PI controller with a pre-charge function. The illustrated PI controller is applied for a d -axis current control. There is an input denoted in the figure with $LoadONOFF(1,0)$, which is a boolean and is always true, when the VAC is active. This means that the controller is always loaded with a certain value during the VAC, so once the VAC is deactivated it can take over the control of the current error from the voltage vector loaded in the controller. The voltage vector is loaded with the difference between the whole voltage along the d -axis, denoted by $V_{d,whole}$, and the decoupling voltage $V_{d,dcpl}$, which is the output from the decoupling network. The way the PI controller is loaded is not straightforward. Only the integral part of the PI controller

has to be pre-charged, as the proportional part is always calculated from the current difference between I_d^* and I_d^{meas} and the proportional factor K_p : $(I_d^* - I_d^{meas}) \cdot K_p$. Therefore the integrator is pre-charged with the difference shown in equation (4.5.2.1).

$$V_d^{int,precharge} = V_{d,whole} - V_{d,dcpl} - (I_d^* - I_d^{meas}) \cdot K_p \quad (4.5.2.1)$$

The integral part of the PI controller is initialized with the value from equation (4.5.2.1). This way no overshoot in the currents is caused, when the PI controllers take over the control from the VAC control.

Though most of the time, when one of two stator sides switches into the FW region also the other is operated in the FW region, the transition from one region to the other can generally occur at different times. It shall be evaluated in the simulation and through measurements if this is an issue for the proposed angle control. Because the terms from the matrix \mathbf{A} include both, voltages and voltage angles, the developed control should be able to handle also the mixed mode of operation.

Though the stator control is achieved through the angle adjustment, this control is not possible if the field winding current is not high enough to set the requested power. Therefore the offline pre-calculation for the field winding current has to be performed for the whole speed range of the machine. The field winding current references are calculated with the optimization script described from Subsection 4.3.2. Based on the requested powers P_{e12V}^* and P_{e48V}^* and the current speed n_{rpm} the field winding current reference is selected and forwarded to the current control loop. If the field winding current is too small for the requested power references, then the requested powers are not physically feasible and the VAC will fail and get unstable. Therefore it is better to rather request more field winding current than less in order to assure that the requested powers can be regulated. The requested points for the stator currents are the same ones used in Subsections 4.4.4 and 4.4.5 in the BS range. The stator current controllers are active only in the BS range, while the field winding current controller is always active.

The current subsection explained the switching mechanisms between the VAC employed in the FW range and FOC operation used in the BS range. The explained theory is implemented in the control and applied in a simulation environment to the programmed machine model from Chapter 2. Subsection 4.5.3 shows simulation results, which verify the presented VAC and the switching mechanism.

4.5.3 Simulation Results with the Voltage Angle Control

The VAC is initially tested in the simulation for a couple of working points to figure out the appropriate integral factors K_i for both integrators from Fig 4.38. A factor of $K_i = 100$ delivers good results in the simulation environment and therefore the automatic testing of the working points is performed with this value. Due to the limited time at the end of the project stability analysis for the proposed control structure couldn't be performed. This may be addressed in some future work on this topic.

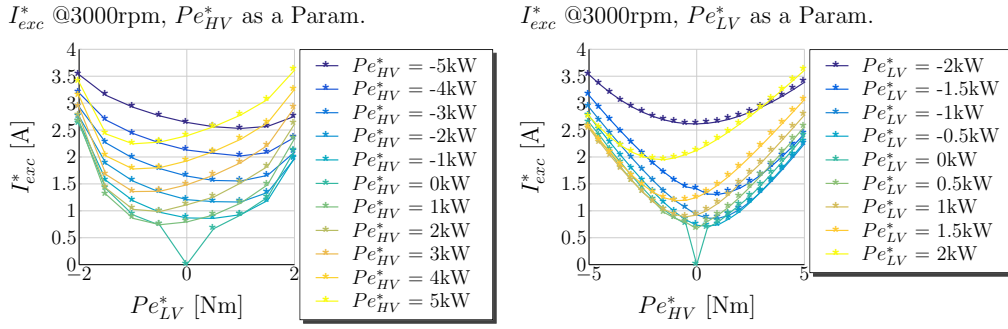


Figure 4.44 – Working Points for MPPF: I_{exc}

The proposed VAC is tested for different combinations of requested powers at a certain speed. A matlab script is used to perform all simulations and store the results from each simulation in separate files. Afterwards a plotting script is used to generate plots of the simulated data. The tests are performed at a speed of 3000 rpm, which is around 1500 rpm above the corner speed of the machine. At this speed the transitions between the VAC and the FOC can be tested, because the machine is operated in the beginning of the pulse in the FOC mode and after the maximum modulation index is reached the VAC takes over the control. At the end of the pulse the references are reduced again to zero and the FOC control takes over the control, when no more FW action is required. The calculated working points for the field winding current at this speed are illustrated in Fig. 4.44. The left plot illustrates the field winding current as a function of the 12V power references P_{e12V}^* and a crosswise dependency of the 48V power references P_{e48V}^* . The right plot shows the field winding current as a function of the 48V power reference P_{e48V}^* and a crosswise dependency of the 12V power reference P_{e12V}^* .

Figure 4.45 shows the simulation results for power references of -4 kW for the 48V side and 0 kW for the 12V side. The left top plot, (1, 1), shows the requested power references and the simulated ones. The simulated powers are calculated according the sampled d - and q -axis voltages and currents internally in the control software based on equations (4.5.1.1) and (4.5.1.2). The plot shows that the control is able to set the requested 48V power reference. The middle top plot, (1, 2), shows the whole angle of the 12V voltage vector β_1 and the field weakening angle applied by the VAC β_1^{FW} during the operation with maximum voltage vector. The top right plot, (1, 3), shows the voltage vector angle of the 48V side β_2 and the field weakening angle β_2^{FW} generated by the VAC of the 48V side. The left plot in the second row of the figure, (2, 1), shows the simulated torques of both windings T_{e12V} and T_{e48V} . The middle plot, (2, 2), shows the 12V d - and q -axis voltage vectors and their vector sum. The right most plot, (2, 3), shows the 48V d and q -axis voltage vectors and their vector sum. The third row of Fig. 4.45 illustrates the d - and q -axis currents of the machine and the field winding current. The most left plot, (3, 1), shows the field winding current, the middle plot, (3, 2), illustrates the 12V stator currents and the right most plot, (3, 3), shows the 48V stator currents.

4 Torque and Power Control Development

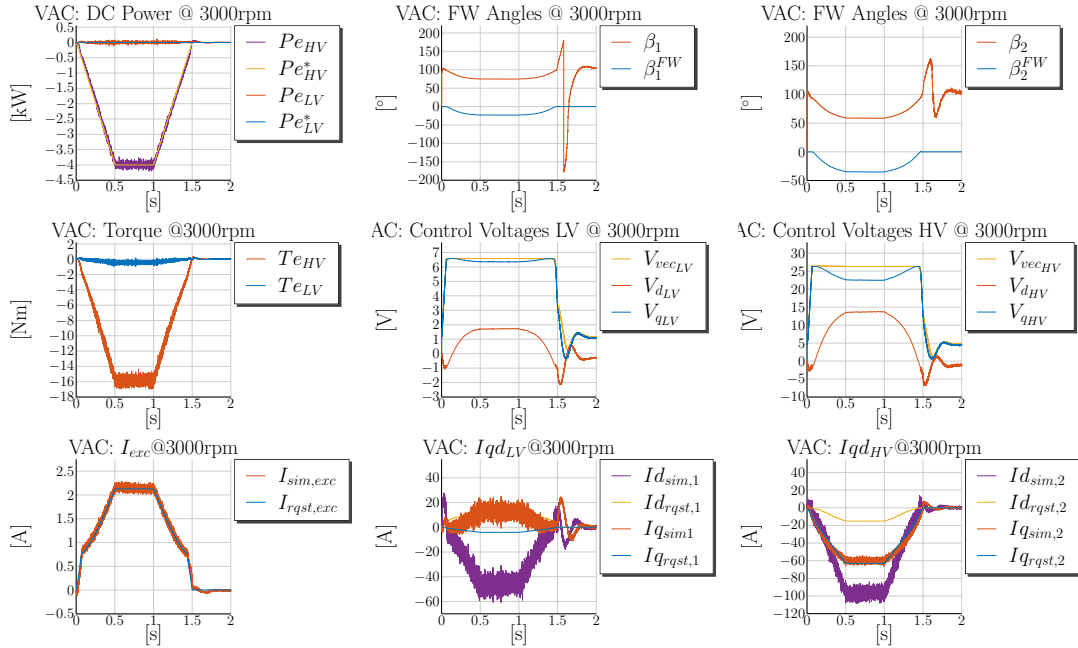


Figure 4.45 – VAC Simulation @3000rpm: $P_{e_{12V}} = 0$ W, $P_{e_{48V}} = -4000$ W

During the first 50 m sec of the simulation the FOC control is active and the modulation index increases. This is evident from the plots in the second row of Fig. 4.45, which show the applied voltage vectors to the machine. The middle plot, (2, 2), shows that the whole voltage vector of the 12V side is increased and that the d - and q -axis voltages are adjusted in order to weaken the d -axis flux. Then the voltage vector is held constant and the VAC of the 12V side is activated. It is obvious from the plot that the magnitude of the whole voltage vector remains fixed, while the vector is rotated and thus the lengths of the d - and q -axis components are changed. During the voltage vector rotation the field weakening effect can be explained based on the behavior of the d - and q -axis voltages. Though the field weakening angle is small the field weakening mechanism is observable in the graphs. While the q -axis voltage is decreased, the d -axis voltage is increased. The decrease of the q -axis voltage is equivalent to the weakening of the magnetizing flux. The increase of the d -axis voltage enables the increase of the q -axis current. In the middle plot of the third row, (3, 2), the 12V currents are illustrated. It is clear, that the d -axis current is increased much more to the negative values than its reference value from the BS range in order to weaken the flux. The graph shows that during the VAC the stator current references are not followed and the power is directly controlled by the rotation of the 12V voltage vector. The 12V voltage vector is rotated back to its previous values, when the power references are decreased. From the plotted field weakening angle of the 12V side is obvious, that a hysteresis in the modulation index is considered in the control, before the FOC control is activated again. When the error of the d -axis current becomes positive, the modulation index of the 12V side is reduced. After ca. 1,6 sec the VAC is

deactivated and the FOC control is activated again. It is visible from the middle plot in the second row, (2, 2), illustrating the 12V voltage vectors, and the middle plot in the third row, (2, 3), illustrating the d - and q -axis currents, that no overshoot is present, when the current controllers are activated again. Both transition mechanisms, from the FOC to the VAC and backwards, are successfully verified through the simulation results.

Similar behavior is observed also for the 48V side, which is represented by the plots in the third column of Fig. 4.45. The top right plot, (1, 3), shows the angle of the 48V voltage vector β_2 and the applied FW angle β_2^{FW} . The 48V VAC is activated in the same time as the 12V VAC, because the maximum voltage vectors are reached simultaneously. The 48V field weakening action behaves in a similar way as the 12V one. The voltage vectors are illustrated in the right most plot of the second row, (2, 3). While the whole length of the vector remains fixed, the q -axis voltage of the 48V side is decreased to weaken the flux produced by the rotor. This results in an increase of the d -axis current to greater negative values. This is evident from the bottom right plot of Fig. 4.45, (3, 3). The d -axis voltage is increased, which results in an increase of the 48V q -axis current into the negative values. This way the reference of -4 kW can be set. After the reference of -4 kW is reached the power is ramped back to 0 kW . The VAC control rotates back the voltage vector during the power reduction. When the error of the d -axis current controller becomes positive, the modulation index of the 48V side is reduced and the FOC control is activated again. The 48V PI controllers are pre-charged with the voltage vector from the VAC before they are activated and therefore no overshoot is present in the stator currents.

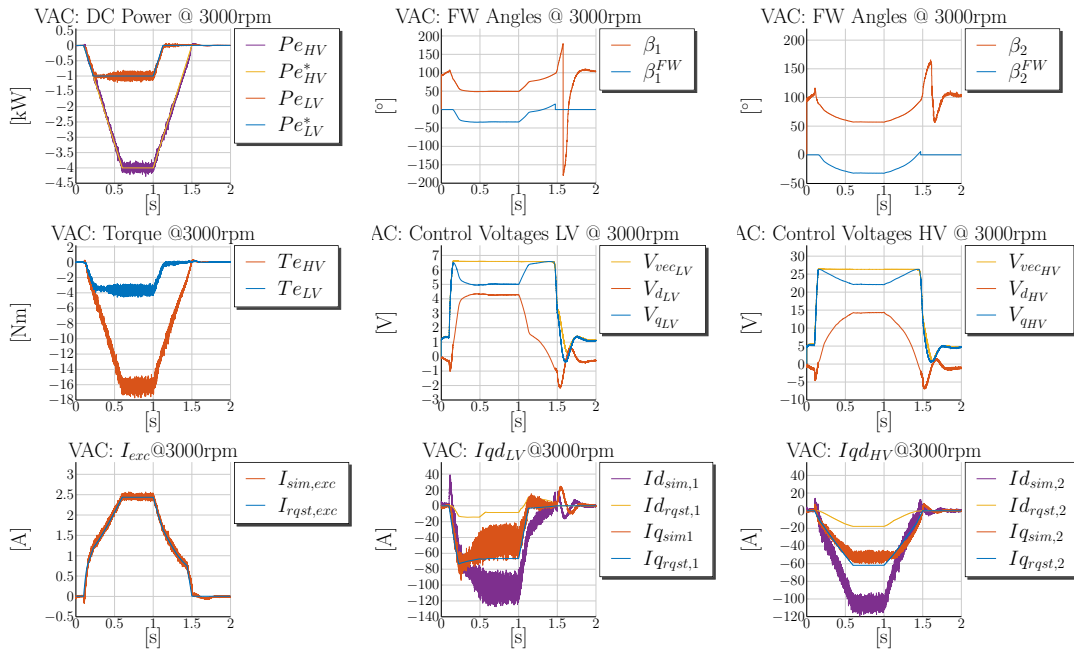


Figure 4.46 – VAC Simulation @3000rpm: $P_{e_{12V}} = -1000\text{ W}$, $P_{e_{48V}} = -4000\text{ W}$

Figure 4.46 shows the simulation results of a -1 kW reference for the 12V side and a -4 kW power reference for the 48V side. The top left plot, (1, 1), shows the requested power references and the simulated ones. The simulated power at both sides follow smoothly the requested power references. The middle top plot, (1, 2), shows the 12V voltage angle β_1 and the 12V field weakening angle β_1^{FW} . The 12V voltage vector is rotated in the same direction as in the previous case illustrated in Fig. 4.45 in order to weaken the rotor flux. The corresponding control voltages are illustrated in the middle plot of the second row of Fig. 4.46, (2, 2). The q -axis voltage is reduced more than in the previous case to weaken the d -axis flux and leave a margin for the q -axis voltage. This way the q -axis voltage can be increased in order to set the requested power, which is achieved through the setting of the q -axis current. The 12V currents are illustrated in the bottom middle plot, (3, 2). The negative d -axis current is increased up to -120 A to achieve the field weakening effect. The 12V q -axis current is increased up to -40 A to control the negative power reference of -1 kW.

The 48V reference of -4 kW is set through the angle control of the 48V side. The FW angle is negative and is illustrated in the top right plot of Fig. 4.46, (1, 3). The 48V voltages are illustrated in the second row and the right most plot, (2, 3). The whole vector length remains constant and the q -axis voltage is decreased to weaken the rotor flux. The d -axis voltage is increased to positive values in order to set the negative q -axis current required to set the reference of -4 kW¹². The transition mechanism back to the FOC control is working properly and the modulation index is reduced at the end of the pulse. The presented simulation results show that the VAC is able control the powers of both windings simultaneously.

The illustrated simulation results prove that the introduced theory from Section 4.5 can be practically applied and used to control the dual-voltage machine in the field weakening area. The VAC and the transition mechanisms are tested successfully for variations of working points. An automatic script performed simulations at 3000 rpm for the following combinations of power references: $P_{e12V}^* = -2$ kW, $-1,5$ kW \dots 2 kW and $P_{e48V}^* = -5$ kW, -4 kW \dots 5 kW. All test cases are successfully verified in the simulation. The plots of all performed simulations are not included in the subsection in order not to negatively impact the readability of the thesis.

4.5.4 Measurements with the Voltage Angle Control

The proposed VAC is implemented on the dSpace Autobox and various working points are tested on the test bench described in Fig. 3.24. The speed is set to 3000 rpm. Multiple operating points are tested Through a Python automation script.

One important observation is made during the initial tests of the new field weakening algorithm. The calculated powers from the d - and q -axis voltages and currents according

¹²In order to understand the logic behind the voltage vector behavior, a look at the machine voltage equations is helpful.

4.5 Power Control - Voltage Angle Control in the Field-Weakening Range

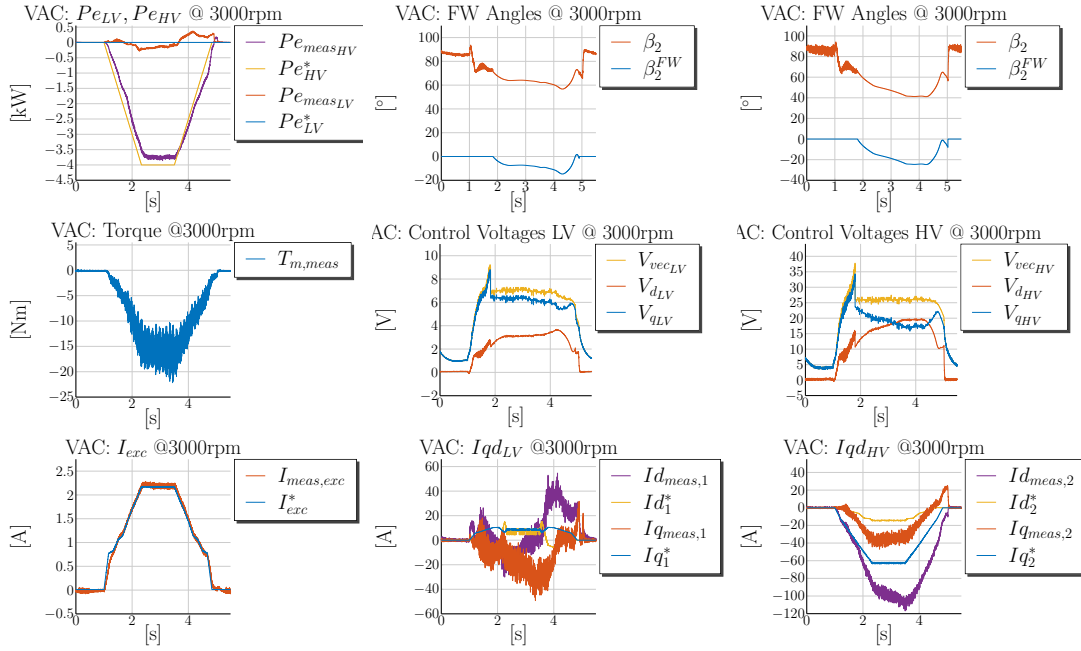


Figure 4.47 – Voltage Angle Control Measurement @3000rpm: $P_{e12V} = 0\text{ W}$, $P_{e48V} = -4000\text{ W}$

the formulas provided in equations (4.5.1.1) and (4.5.1.2) are very noisy due to quantisation effects and inaccuracies in the rotor position measurement. Therefore a low-pass filter with 300 Hz corner frequency is applied to the calculated powers. The integral factors from the power control structure illustrated in Fig. 4.38 are reduced also down to $K_i = 10$ for both stator systems due to the filtering of the calculated powers. This side effect deteriorates the performance of the presented angle control. However these adaptation are necessary in order to achieve a stable power control on the test bench. Due to the filtering of the calculated powers the control loops become slower and therefore the integral factors have to be reduced.

Figure 4.47 shows the measurement results for a 12V power reference of 0 kW and a 48V power reference of -4 kW . The top left plot, (1, 1), illustrates the filtered 12V and 48V powers and the requested references. It is evident that the angle control is able to control the 12V power around the zero reference, while the 48V power is ramped to -4 kW . Due to the low-pass filtering effect and the reduction of the K_i factor the filtered 48V power is slightly below the reference value. A fast dynamic cannot be achieved due to the required low-pass filters applied on the power references. The measurements serve as a proof of concept for the developed VAC, which can be fine tuned and improved in a future work. A better solution for the calculation of the DC powers has to be developed in order to eliminate the need for low-pass filtering.

The left plot in the second row, (2, 1), shows the measured mechanical torque of around -15 Nm . The negative torque corresponds with the negative power reference of -4 kW .

The middle top plot, (1, 2), shows the 12V voltage angle β_1 and the applied field weakening angle β_1^{FW} . The VAC is activated after 1,8 sec and rotates the voltage vector in order to maintain a 0 kW power reference. The middle plot in the second row, (2, 2), illustrates the applied d - and q -axis voltages to the machine. It is noticeable, that due to the low-pass filtering of the modulation index, the VAC is activated with a delay and the q -axis voltage exceeds the maximum possible voltage limit. The behavior is observable at ca. 1,8 s. After the VAC is activated the maximum possible voltage vector is limited. The q -axis voltage, plotted in blue, is slightly reduced to counteract the back-emf from the rotor. The d -axis voltage is slightly increased to be able to control the q -axis current. The middle bottom plot, (3, 2), shows the oscillation of the q - and d -axis currents around zero.

The 48V control is described through the quantities illustrated in the right most column. The top right plot, (1, 3), illustrates the voltage vector angle of the 48V side β_2 and the applied FW angle β_2^{FW} by the VAC. It is noticeable that the applied FW angle at the 48V side is greater than the one at the 12V side. This observation is understandable, as the power at the 48V side is raised to -4 kW. The right most plot in the second row, (2, 3), illustrates the 48V voltages. The VAC is activated after 1,8 s. Before the VAC is activated the q -voltage exceeds the maximum possible voltage limit, due to the decoupling action of the PI controllers and the low-pass filtering of the modulation index according to Fig. 4.39. The VAC is activated after the filtered modulation index reaches its maximum value. The q -axis voltage is reduced to weaken the rotor flux. This corresponds also to the negative d -axis current plotted in the bottom right plot, (3, 3). The q -axis voltage is increased in order to increase the q -axis current. There is a drift visible in the q - and d -axis currents, because the q -axis current is increased and the d -axis current is decreased. This can be caused by the low-pass filter added to the control loop. The excitation current is shown in the left bottom plot of Fig. 4.47, (3, 1).

Figure 4.48 shows another case for the voltage angle control of the dual-voltage machine, where both references are changed to negative values. The 12V power reference is changed to -1 kW and the 48V reference to -4 kW. The top left plot, (1, 1), shows the calculated powers and the power references. Before second 1,8 the 12V power is increased only due to the current references. After that the FW control is activated and the angle control starts to increase the power to the requested reference value. The middle plot in the first row, (1, 2), shows the 12V voltage angle β_1 and the 12V field weakening angle β_1^{FW} . The 12V voltages are plotted in the middle plot of the second row, (2, 2). The q -axis voltage is reduced to weaken the flux and the d -axis voltage is increased to set a larger negative q -axis current for the power reference of -1 kW. The maximum length of the voltage vector stays the same. It is evident from the plot of the 12V currents, shown in the middle plot of the third row, (3, 2), that the q -axis current is smaller in magnitude in comparison to the simulation from Fig. 4.45. This is due to the fact that the alignment of the d - and q -axis is not perfect on the test bench and therefore the d - and q -axis currents cannot be perfectly set at higher speeds. A more accurate rotor position sensor can be employed to improve the accuracy of the d - and q -axis voltages and currents calculation in order to improve the control performance.

4.5 Power Control - Voltage Angle Control in the Field-Weakening Range

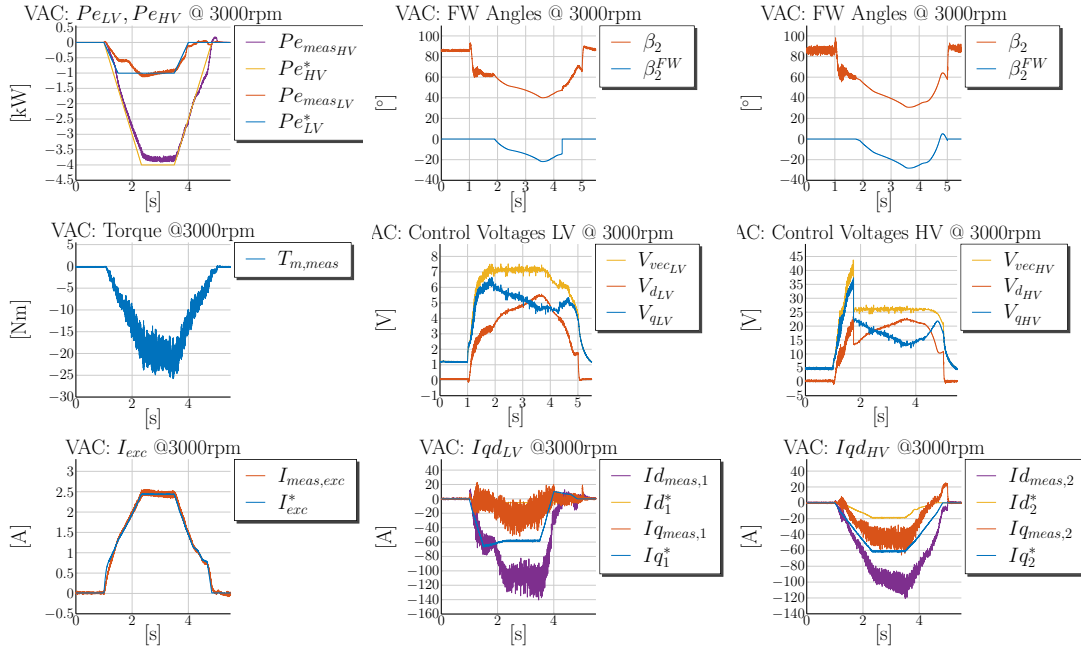


Figure 4.48 – Voltage Angle Control Measurement @3000rpm: $P_{e_{12V}} = -1000$ W, $P_{e_{48V}} = -4000$ W

The 48V voltage angle β_2 and the 48V field weakening angle β_2^{FW} are plotted in the right plot of the first row of Fig. 4.48, (1, 3). The VAC is activated after 1.8 seconds and the maximum voltage vector is limited. The 48V voltages are plotted in the right plot of the second row, (2, 3). The q -axis voltage is reduced to weaken the rotor flux and induce a negative d -axis current. The d -axis voltage is increased, which leads to an increase of the q -axis current into the negative direction. The drift, caused due to low-pass filtering effects, is also evident in the 48V q - and d -axis current's plot.

The presented measurements of both cases demonstrate that the proposed VAC is able to control the power at both stator windings in the field weakening area. The developed transition mechanisms, from the FOC to the VAC and backwards, are also successfully verified. At the end of the pulses the VAC rotates the voltage vector back to the initial values and a positive d -axis current is adjusted. The positive d -axis current error leads to the reduction of the modulation index and the reactivation of the FOC as described through the schematic from Fig. 4.42.

Through an automatic Python script various combinations of working points are tested. Due to speed limitation of the test bench the algorithm could not be verified at higher speeds. Further observation shows that the right calculation of the 12V and 48V power from the d - and q -axis quantities is essential for the performance of the power control algorithm. Due to the introduced low-pass filtering and the inaccuracies in the rotor position measurement the control performance of the VAC deteriorates on the test bench.

In a future work the accuracy of the position measurement and the calculation of the d - and q -axis quantities have to be improved in order to achieve better results. Stability analysis for the proposed VAC have to be performed in order to exploit fully the new angle control and improve its dynamics. Nevertheless the performed measurements confirm the feasibility of the developed VAC algorithm. A further research could be focused on the fine-tuning of the integrator and the accurate power calculation.

5 Summary and Outlook

5.1 Summary

The presented new machine topology introduces a machine generating two voltage levels with the goal to replace a conventional 48V architecture, which includes a DC/DC converter as a power transfer component between the 12V and 48V electrical systems. The new topology integrates the DC/DC functionality in the machine itself and therefore requires a machine-specific control development. The control has to be able to control the mechanical torque as well as the power transfer occurring in the air-gap of the machine between both stator windings. The presented work addressed the main challenges arising from the employment of this new dual-voltage machine topology. The main challenge lies in the control development for this machine and the ability of the control to decouple both stator systems from each other. In order to be able to develop an appropriate decoupling control for the machine, the machine physics have to be investigated in detail.

The first part of the research, documented in Chapter 2, focuses on the **dynamic modeling** of the dual-voltage machine. The theory for the VBR and the DQ dual-voltage machine models is derived in the chapter. The presented machine model is able to reproduce accurately the **electromagnetic coupling** between the 12V stator system, the 48V stator system and the field winding. The electromagnetic coupling, replicated in the model, is tested in the simulation environment and also verified through measurements. The model includes also the **saturation** and **cross-magnetization** of the main inductance. As a result of the new findings a research paper in the Transactions on Energy Conversion, which describes a general $n \times 3$ -phase multi-voltage machine model, is published [29]. The performed measurements during the torque control development show that the claw-pole machine has excessive iron losses. Therefore, the model is extended to include the measured iron losses of the machine. The iron loss resistance is added to the model as a variable resistance placed in parallel to the d - and q -axis inductances. The resistance is realized through a LUT in dependence of speed and flux. The iron loss modeling is documented in a second research paper in the Transactions on Energy Conversion [28]. At the end of Chapter 2 a parametrization procedure is proposed for the derived model and the model is parametrized based on measurements of the machine at no-load.

A model-based control is developed for the dual-voltage machine with the knowledge of the machine equations and physics. The next step is to design the inner current control loops for the machine. The current controllers regulate **all five currents**: (i) the

12V q -axis current i_{qs1} , (ii) the 12V d -axis current i_{ds1} , (iii) the 48V q -axis current i_{qs2} , (iv) the 48V d -axis current i_{ds2} and (v) the field winding current i_{fd} . Chapter 3 handles the design of the PI current control loops. The **Modulus Optimum (MO)** criterion is applied for the tuning of all five current controllers. Stability analysis are performed to confirm the tuning. In order to counteract the speed and the coupling action between the axis, a **decoupling network** based on the machine voltage equations and under consideration of the saturation behavior of the machine is implemented. The decoupling network improves the control performance of the current controllers at speed and reduces the disturbances in the currents, caused by reference changes on the other controllers. This is confirmed through the performed simulations and measurements. The **stability** of the current controllers is verified through the testing of variations of current references in the BS range. The performed simulations during the current control tests correlate with the measurements and verify the developed dynamic model in Chapter 2. Though the decoupling network improves the control performance, the simulations as well as the measurements show, that it is unable to counteract the **dynamic disturbances** caused on the rest of the controllers. In order to improve the decoupling control of the machine a new **dynamic decoupling control** is developed for the dual-voltage machine based on the control theory for Multiple-Input Multiple-Output (MIMO) systems. This new art of control is able to **predict** the action of each of the PI controllers, when a current reference is changed, and applies a **contra-action** on the other controllers, such that the dynamic disturbance during the reference change is almost eliminated. Due to the discrete art of the control and the presumed linearity of the inductances during the dynamic control design, there is still some very small and negligible disturbance left. The new control is based on the **inversion of the dynamic machine model** and achieves a full decoupling control. The dynamic control is able to reduce the disturbances by a factor of at least 5 when compared to the static decoupling techniques. The new decoupling control is introduced in this work under the abbreviation Dynamic Decoupling Matrix (DDM). The dynamic control algorithm is tested only in the simulation environment. The previously performed measurements with the static decoupling network match very well to the corresponding simulations, which is a strong indication, that the DDM will deliver the same promising results also during future measurements on a test bench. In the author's point of view, the presented dynamic decoupling control is one of the main contributions of this thesis.

The last main chapter focuses on the torque and power control development for the dual-voltage machine. Chapter 4 introduces in the beginning some state of the art torque control methods for three-phase machines like Maximum Torque-per-Ampere (MTPA) and Maximum Torque-per-Flux (MTPF) control. The second half of the chapter handles the torque control development in the BS range of the dual-voltage machine. The developed Maximum Torque-per-Copper Losses (MTPCL) torque control method minimizes the copper losses of the dual-voltage machine under the boundaries of two torque references: T_{e12V}^* and T_{e48V}^* . The magnetic coupling and saturation are considered during the search for optimal current references. Various simulations and measurements with the torque control at a speed of 1000 rpm are performed to verify the offline calculated

operating points. The performed simulations and measurements confirm that the torque control with two separate air-gap torques, is feasible and can be used to control the torque in the BS range. The error between predicted mechanical torque and measured mechanical torque is greater in motoring mode than in generator mode. This leads to the presumptions, that the alignment of the d - and q -axis of the machine is not perfect. The inaccuracies in the rotor position sensor, as a result of the employed encoder, lead to this non-perfect alignment of the d - and q -axis. Another reason for the observed deviation is the simplification of the saturation modeling achieved through an analytic arcustangens function and the neglect of the iron losses. The reported very good results between simulation and measurement in Chapter 3 are related to the dynamic performance of the model. The results from the torque control measurements leave potential for the model to be improved in its stationary behavior.

Due to the observed stationary mismatch between model and machine prototype a new concept for the **Field Weakening (FW)** control of the dual-voltage machine is developed. The new control relies less on offline pre-calculated working points. For this purpose a **new Voltage Angle Control (VAC)** is derived for the dual-voltage machine at the end of Chapter 4. The VAC makes use of the fact, that in the FW area the maximum voltage vectors at both stator systems are reached. The only possibility to control actively the power at both sides is to **rotate the voltage vectors**, such that the rotor flux is weakened and the requested power is controlled. The VAC is implemented based on the machine model and the calculated electrical power in the d - q frame. The angle control with a **decoupling structure** is derived and implemented successfully in the simulation. A **switching mechanism** between both control methods - FOC in the BS range and VAC in the FW range - is also developed. This switching mechanism is based on the **maximum modulation indices** of both stator systems for the transition from FOC to VAC and on the **d -axis current error** for the transition from VAC to FOC. The switching mechanism between both control areas is verified successfully in the simulation and through measurements. The developed VAC is implemented on a dSPACE Autobox and tested on the test bench and its feasibility is confirmed. Unfortunately, no detailed testing could be performed with the VAC due to the time limit at the end of the project. The performed measurements show promising results. Some drawbacks are noticed during the performed measurements for the VAC. The calculated power in the d - q frame is afflicted with noise, which affects badly the control performance of the VAC. Therefore the calculated power has to be strongly filtered, such that it can be used in the angle control. Due to this observation, the K_i factors employed for the integral controllers for the VAC are reduced by a factor of 10 in order to achieve a stable VAC control.

5.2 Outlook

Although the performed research on the modeling and control of the dual-voltage machine is detailed and thorough, there are some topics which can be addressed in a future work. Regarding the modeling of the machine, a further research could be focused on the detailed analysis of the iron loss modeling through analytical formulas. The saturation modeling is simplified through an arcustangens function and a constant anisotropic factor α . Future work could investigate different saturation modeling methods, which are able to reproduce more accurately the inductances along the d - and q -axis and thus improve the steady state accuracy of the machine model. In general the stationary behavior of the model can be improved and the presented iron loss modeling can be verified with various working points at different speeds.

A new dynamic decoupling current control for the machine is presented and verified in the simulation environment. In a further research the developed control can be tested on a test bench with the machine prototype in order to verify the presented simulation results.

The developed VAC shows promising results as well in the simulation as during the performed measurements. Due to some inaccuracies and jitter in the rotor position measurement the calculated power has to be filtered, which deteriorates the performance of the control. Further research can focus on the correct and non-noisy calculation of the power and perform stability analysis for the derived VAC.

In general, a more accurate position sensor can be employed in future work to eliminate control performance issues resulting from the drawbacks of the employed resolver.

A Calculating Inductances of a Three-Phase Machine

A.1 Deriving the Inductances of a Three-Phase Linear Machine Model

This appendix derives all flux linkage equation for the three-phase synchronous machine plotted in Fig. A.1. The following assumptions are made for the machine.

- the stator windings are sinusoidally distributed
- the field winding is sinusoidally distributed
- the machine has two poles
- the end turns of the windings are neglected

The following symbols are used in the machine equations.

- r mean air-gap radius
- l axial length of stator
- g air-gap length
- θ_r rotor angle to u_s -axis
- ϕ_s angle from u_s -axis in counterclockwise manner
- ϕ_r angle from f_q -axis in counterclockwise manner
- $d\phi_s$ integrative angle from u_s -axis in counterclockwise manner
- $d\phi_r$ integrative angle from f_q -axis in counterclockwise manner

The flux linkage equations will be derived taking into account the position of the coils of the stator phases u_s , v_s and w_s and the rotor displacement relative to the u_s -axis. The rotor angle position is fixed to the f_q axis and is denoted with ϕ_r . This angle is used in the integration, when deriving the flux linkage in the rotor coil. The angle ϕ_s is used for the integration over the stator circumference. The flux linkage is calculated for each coil when the flux density is integrated over the area covered by the coil with the assumption for sinusoidal distribution. The integration over each stator coil is done by integrating over the angle ϕ_s related to u_s . It is assumed that the other windings are displaced by 120° . When the flux linkage is calculated for winding v_s , 120° are added to ϕ_s : $\pi + \frac{2\pi}{3} \leq \phi_s \leq 2\pi + \frac{2\pi}{3}$. For winding w_s the integration is done over the stator

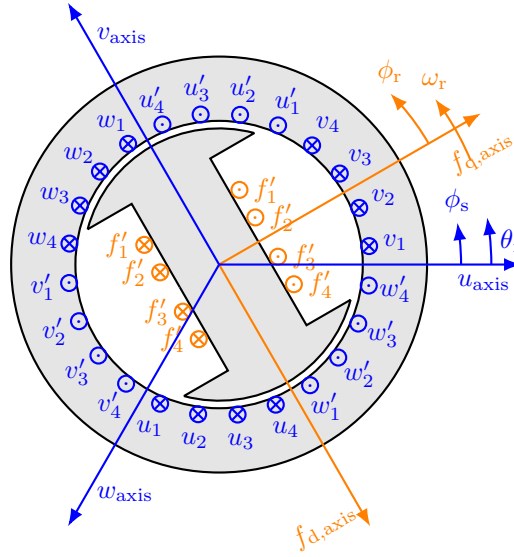


Figure A.1 – Schematic Drawing of a Three-Phase Salient-Pole machine

circumference for angle $\pi - \frac{2\pi}{3} \leq \phi_s \leq 2\pi - \frac{2\pi}{3}$. Over these parts of the circumference is assumed the corresponding coil has sinusoidal distribution.

- integration angle for coil u_s : $\pi \leq \zeta \leq 2\pi$
- integration angle for coil v_s : $\pi + \frac{2\pi}{3} \leq \zeta \leq 2\pi + \frac{2\pi}{3}$
- integration angle for coil w_s : $\pi - \frac{2\pi}{3} \leq \zeta \leq 2\pi - \frac{2\pi}{3}$
- integration angle for coil f_d : $\phi_r \leq \zeta \leq \phi_r + \pi$

The distribution of the turns over the stator or respectively rotor circumference for each winding derived from Fig. A.1 is then given in (A.1.0.1) - (A.1.0.4). The sinusoidal distribution of the field winding (A.1.0.4) is represented with a cosine function over $\frac{\pi}{2} \leq \phi_r \leq \frac{3\pi}{2}$, because the angle ϕ_r is fixed to the f_q -axis and not the f_d -axis.

$$u_s : -\frac{N_s}{2} \sin(\phi_s) \quad \pi \leq \phi_s \leq 2\pi \quad (\text{A.1.0.1})$$

$$v_s : -\frac{N_s}{2} \sin(\phi_s + \frac{2\pi}{3}) \quad \pi + \frac{2\pi}{3} \leq \phi_s \leq 2\pi + \frac{2\pi}{3} \quad (\text{A.1.0.2})$$

$$w_s : -\frac{N_s}{2} \sin(\phi_s - \frac{2\pi}{3}) \quad \pi - \frac{2\pi}{3} \leq \phi_s \leq 2\pi - \frac{2\pi}{3} \quad (\text{A.1.0.3})$$

$$f_d : \frac{N_f}{2} \cos(\phi_s) \quad \frac{\pi}{2} \leq \phi_r \leq \frac{3\pi}{2} \quad (\text{A.1.0.4})$$

$$(\text{A.1.0.5})$$

In order to derive the flux linkage of a winding a double integral has to be used. One integral integrates the magnetic flux density over one turn of the coil and the second one sums up all flux linkages of each turn. Since a sinusoidal distribution is assumed, the summation is also done via integral over the circumference, which the corresponding

winding spans over. When the flux linkage is defined as function of each current with all other currents set to zero the corresponding self or mutual inductances are derived. The flux linkage equations and inductance equations will be set first for the coil u_s , then for v_s , w_s and at last for the field winding f_d . The magnetic flux density is calculated for each winding according equation (A.1.0.6). The magnetomotive force of each winding is calculated according Ampere's law (A.1.0.7).

$$B_r(\phi_s) = \mu_0 H_r(\phi_s) \qquad B_r = \mu_0 \frac{MMF}{g} \qquad (A.1.0.6)$$

$$\int \vec{H} \, d\vec{L} = i \qquad (A.1.0.7)$$

When both expressions are applied on each winding we get the equations (A.1.0.8) - (A.1.0.11).

$$\lambda_{us} = L_{ls} i_{us} + \int N_{us}(\phi_s) \int_{\phi_s}^{\phi_s+\pi} B_r(\zeta, \theta_r) r l d\zeta d\phi_s \qquad (A.1.0.8)$$

$$\lambda_{vs} = L_{ls} i_{vs} + \int N_{vs} \left(\phi_s + \frac{2\pi}{3} \right) \int_{\phi_s + \frac{2\pi}{3}}^{\phi_s + \pi + \frac{2\pi}{3}} B_r(\zeta, \theta_r) r l d\zeta d\phi_s \qquad (A.1.0.9)$$

$$\lambda_{ws} = L_{ls} i_{ws} + \int N_{us} \left(\phi_s - \frac{2\pi}{3} \right) \int_{\phi_s - \frac{2\pi}{3}}^{\phi_s + \pi - \frac{2\pi}{3}} B_r(\zeta, \theta_r) r l d\zeta d\phi_s \qquad (A.1.0.10)$$

$$\lambda_{fd} = L_{lf} i_{fd} + \int N_{fd}(\phi_r) \int_{\phi_r}^{\phi_r+\pi} B_r(\zeta, \theta_r) r l d\zeta d\phi_r \qquad (A.1.0.11)$$

When equations (A.1.0.6) and (A.1.0.7) are applied on each winding along the stator or rotor circumference we get the flux linkages and thereafter the self- and mutual-inductances. These expressions will be calculated for each coil of the three phase machine. All integrations were performed by the Matlab Symbolic Toolbox [49]. The flux λ_{us} , produced due to the current i_{us} with all other currents set to zero is given in (A.1.0.12).

$$\lambda_{us}(i_{us}) = L_{ls} i_{us} + \int_{\pi}^{2\pi} -\frac{N_s}{2} \sin(\phi_s) \int_{\phi_s}^{\phi_s+\pi} \mu_0 r l \frac{N_s}{2} i_{us} \cos(\zeta) (\alpha_1 - \alpha_2 \cos(2(\zeta + \theta_r))) d\zeta d\phi_s \qquad (A.1.0.12)$$

The self-inductance is given after integration of (A.1.0.12) in (A.1.0.13).

$$L_{l,us} = L_{ls} + \overbrace{\frac{N_s^2}{2} \pi r l \mu_0 ((\alpha_1 - \frac{\alpha_2}{2} \cos(2\theta_r)))}^{L_{us}} \qquad (A.1.0.13)$$

The flux λ_{us} , produced due to the current i_{vs} with all other currents set to zero is given in (A.1.0.14).

$$\lambda_{us}(i_{vs}) = \int_{\pi}^{2\pi} -\frac{N_s}{2} \sin(\phi_s) \int_{\phi_s}^{\phi_s+\pi} \mu_0 r l \frac{N_s}{2} i_{us} \cos\left(\zeta - \frac{2\pi}{3}\right) (\alpha_1 - \alpha_2 \cos(2(\zeta + \theta_r))) d\zeta d\phi_s \quad (\text{A.1.0.14})$$

The self-inductance is given after integration of (A.1.0.14) in (A.1.0.15).

$$L_{usvs} = -\frac{N_s^2}{2} \pi r l \mu_0 \left((\alpha_1 - \frac{\alpha_2}{2} \cos(2\theta_r + \frac{\pi}{3})) \right) \quad (\text{A.1.0.15})$$

The flux λ_{us} , produced due to the current i_{ws} with all other currents set to zero is given in (A.1.0.16).

$$\lambda_{us}(i_{ws}) = \int_{\pi}^{2\pi} -\frac{N_s}{2} \sin(\phi_s) \int_{\phi_s}^{\phi_s+\pi} \mu_0 r l \frac{N_s}{2} i_{us} \cos\left(\zeta + \frac{2\pi}{3}\right) (\alpha_1 - \alpha_2 \cos(2(\zeta + \theta_r))) d\zeta d\phi_s \quad (\text{A.1.0.16})$$

The mutual-inductance is given after integration of (A.1.0.16) in (A.1.0.17).

$$L_{1,usus} = -\frac{N_s^2}{2} \pi r l \mu_0 \left((\alpha_1 - \frac{\alpha_2}{2} \cos(2\theta_r + \frac{2\pi}{3})) \right) \quad (\text{A.1.0.17})$$

The flux λ_{us} , produced due to the current i_{fd} with all other currents set to zero is given in (A.1.0.18).

$$\lambda_{us}(i_{fd}) = \int_{\pi}^{2\pi} \frac{N_s}{2} \sin(\phi_s) \int_{\phi_s}^{\phi_s+\pi} \mu_0 r l \frac{N_f}{2} i_{fd} \sin(\zeta - \theta_r) (\alpha_1 - \alpha_2 \cos(2(\zeta - \theta_r))) d\zeta d\phi_s \quad (\text{A.1.0.18})$$

The mutual-inductance is given after integration of (A.1.0.18) in (A.1.0.19).

$$L_{usfd} = \frac{N_f N_s}{2} \pi r l \mu_0 (\alpha_1 - \frac{\alpha_2}{2}) \sin \theta_r \quad (\text{A.1.0.19})$$

The flux λ_{vs} , produced due to the current i_{vs} with all other currents set to zero is given in (A.1.0.20).

$$\lambda_{vs}(i_{vs}) = L_{ls} i_{vs} + \int_{\pi+\frac{2\pi}{3}}^{2\pi+\frac{2\pi}{3}} -\frac{N_s}{2} \sin\left(\phi_s + \frac{2\pi}{3}\right) \int_{\phi_s+\frac{2\pi}{3}}^{\phi_s+\pi+\frac{2\pi}{3}} \mu_0 r l \frac{N_s}{2} i_{vs} \cos(\zeta) (\alpha_1 - \alpha_2 \cos(2(\zeta + \theta_r + \frac{2\pi}{3}))) d\zeta d\phi_s \quad (\text{A.1.0.20})$$

The self-inductance is given after integration of (A.1.0.20) in (A.1.0.21).

$$L_{l,vsvs} = L_{ls} + \overbrace{\frac{N_s^2}{2} \pi r l \mu_0 \left((\alpha_1 - \frac{\alpha_2}{2} \sin(2(\theta_r + \frac{\pi}{3}))) \right)}^{L_{vsvs}} \quad (\text{A.1.0.21})$$

The flux λ_{vs} , produced due to the current i_{us} with all other currents set to zero is given in (A.1.0.22).

$$\lambda_{\text{vs}}(i_{\text{us}}) = \int_{\pi + \frac{2\pi}{3}}^{2\pi + \frac{2\pi}{3}} -\frac{N_s}{2} \sin\left(\phi_s + \frac{2\pi}{3}\right) \int_{\phi_s + \frac{2\pi}{3}}^{\phi_s + \pi + \frac{2\pi}{3}} \mu_0 r l \frac{N_s}{2} i_{\text{us}} \cos\left(\zeta + \frac{2\pi}{3}\right) \left(\alpha_1 - \alpha_2 \cos\left(2\left(\zeta + \theta_r + \frac{2\pi}{3}\right)\right)\right) d\zeta d\phi_s \quad (\text{A.1.0.22})$$

The mutual-inductance is given after integration of (A.1.0.22) in (A.1.0.23).

$$L_{\text{vsus}} = -\frac{N_s^2}{2} \pi r l \mu_0 \left(\alpha_1 - \frac{\alpha_2}{2} \cos\left(2\theta_r + \frac{\pi}{3}\right)\right) \quad (\text{A.1.0.23})$$

The flux λ_{vs} , produced due to the current i_{ws} with all other currents set to zero is given in (A.1.0.24).

$$\lambda_{\text{vs}}(i_{\text{ws}}) = \int_{\pi + \frac{2\pi}{3}}^{2\pi + \frac{2\pi}{3}} -\frac{N_s}{2} \sin\left(\phi_s + \frac{2\pi}{3}\right) \int_{\phi_s + \frac{2\pi}{3}}^{\phi_s + \pi + \frac{2\pi}{3}} \mu_0 r l \frac{N_s}{2} i_{\text{ws}} \cos\left(\zeta - \frac{2\pi}{3}\right) \left(\alpha_1 - \alpha_2 \cos\left(2\left(\zeta + \theta_r + \frac{2\pi}{3}\right)\right)\right) d\zeta d\phi_s \quad (\text{A.1.0.24})$$

The mutual-inductance is given after integration of (A.1.0.24) in (A.1.0.25).

$$L_{\text{vsws}} = -\frac{N_s^2}{2} \pi r l \mu_0 \left(\alpha_1 - \frac{\alpha_2}{2} \cos(2\theta_r)\right) \quad (\text{A.1.0.25})$$

The flux λ_{vs} , produced due to the current i_{fd} with all other currents set to zero is given in (A.1.0.26).

$$\lambda_{\text{vs}}(i_{\text{fd}}) = \int_{\pi + \frac{2\pi}{3}}^{2\pi + \frac{2\pi}{3}} \frac{N_s}{2} \sin\left(\phi_s + \frac{2\pi}{3}\right) \int_{\phi_s + \frac{2\pi}{3}}^{\phi_s + \pi + \frac{2\pi}{3}} \mu_0 r l \frac{N_f}{2} i_{\text{fd}} \sin\left(\zeta - \theta_r + \frac{2\pi}{3}\right) \left(\alpha_1 - \alpha_2 \cos\left(2\left(\zeta - \theta_r + \frac{2\pi}{3}\right)\right)\right) d\zeta d\phi_s \quad (\text{A.1.0.26})$$

The mutual-inductance is given after integration of (A.1.0.26) in (A.1.0.27).

$$L_{\text{vsfd}} = \frac{N_f N_s}{2} \pi r l \mu_0 \left(\alpha_1 + \frac{\alpha_2}{2}\right) \sin\left(\theta_r - \frac{2\pi}{3}\right) \quad (\text{A.1.0.27})$$

The flux λ_{ws} , produced due to the current i_{ws} with all other currents set to zero is given in (A.1.0.28).

$$\lambda_{\text{ws}}(i_{\text{ws}}) = L_{\text{ls}} i_{\text{ws}} + \int_{\pi - \frac{2\pi}{3}}^{2\pi - \frac{2\pi}{3}} -\frac{N_s}{2} \sin\left(\phi_s - \frac{2\pi}{3}\right) \int_{\phi_s - \frac{2\pi}{3}}^{\phi_s + \pi - \frac{2\pi}{3}} \mu_0 r l \frac{N_s}{2} i_{\text{ws}} \cos(\zeta) \left(\alpha_1 - \alpha_2 \cos\left(2\left(\zeta + \theta_r - \frac{2\pi}{3}\right)\right)\right) d\zeta d\phi_s \quad (\text{A.1.0.28})$$

The self-inductance is given after integration of (A.1.0.28) in (A.1.0.29).

$$L_{\text{l,ws}} = L_{\text{ls}} + \overbrace{\frac{N_s^2}{2} \pi r l \mu_0 \left(\alpha_1 - \frac{\alpha_2}{2} \cos\left(\frac{\pi}{3} + 2\theta_r\right)\right)}^{L_{\text{ws}} \text{ws}} \quad (\text{A.1.0.29})$$

The flux λ_{ws} , produced due to the current i_{us} with all other currents set to zero is given in (A.1.0.30).

$$\lambda_{ws}(i_{us}) = \int_{\pi - \frac{2\pi}{3}}^{2\pi - \frac{2\pi}{3}} -\frac{N_s}{2} \sin\left(\phi_s - \frac{2\pi}{3}\right) \int_{\phi_s - \frac{2\pi}{3}}^{\phi_s + \pi - \frac{2\pi}{3}} \mu_0 r l \frac{N_s}{2} i_{us} \cos\left(\zeta - \frac{2\pi}{3}\right) \left(\alpha_1 - \alpha_2 \cos\left(2\left(\zeta + \theta_r - \frac{2\pi}{3}\right)\right)\right) d\zeta d\phi_s \quad (\text{A.1.0.30})$$

The mutual-inductance is given after integration of (A.1.0.30) in (A.1.0.31).

$$L_{wsus} = -\frac{N_s^2}{2} \pi r l \mu_0 \left(\alpha_1 - \frac{\alpha_2}{2} \cos\left(\frac{2\pi}{3} + 2\theta_r\right)\right) \quad (\text{A.1.0.31})$$

The flux λ_{ws} , produced due to the current i_{vs} with all other currents set to zero is given in (A.1.0.32).

$$\lambda_{ws}(i_{vs}) = \int_{\pi - \frac{2\pi}{3}}^{2\pi - \frac{2\pi}{3}} -\frac{N_s}{2} \sin\left(\phi_s - \frac{2\pi}{3}\right) \int_{\phi_s - \frac{2\pi}{3}}^{\phi_s + \pi - \frac{2\pi}{3}} \mu_0 r l \frac{N_s}{2} i_{vs} \cos\left(\zeta + \frac{2\pi}{3}\right) \left(\alpha_1 - \alpha_2 \cos\left(2\left(\zeta + \theta_r - \frac{2\pi}{3}\right)\right)\right) d\zeta d\phi_s \quad (\text{A.1.0.32})$$

The mutual-inductance is given after integration of (A.1.0.32) in (A.1.0.33).

$$L_{wsvs} = -\frac{N_s^2}{2} \pi r l \mu_0 \left(\alpha_1 + \frac{\alpha_2}{2} \cos(2\theta_r)\right) \quad (\text{A.1.0.33})$$

The flux λ_{ws} , produced due to the current i_{fd} with all other currents set to zero is given in (A.1.0.34).

$$\lambda_{ws}(i_{fd}) = \int_{\pi - \frac{2\pi}{3}}^{2\pi - \frac{2\pi}{3}} \frac{N_s}{2} \sin\left(\phi_s - \frac{2\pi}{3}\right) \int_{\phi_s - \frac{2\pi}{3}}^{\phi_s + \pi - \frac{2\pi}{3}} \mu_0 r l \frac{N_f}{2} i_{fd} \sin\left(\zeta - \theta_r - \frac{2\pi}{3}\right) \left(\alpha_1 - \alpha_2 \cos\left(2\left(\zeta - \theta_r - \frac{2\pi}{3}\right)\right)\right) d\zeta d\phi_s \quad (\text{A.1.0.34})$$

The mutual-inductance is given after integration of (A.1.0.34) in (A.1.0.35).

$$L_{wsfd} = \frac{N_f N_s}{2} \pi r l \mu_0 \left(\alpha_1 + \frac{\alpha_2}{2}\right) \sin\left(\theta_r + \frac{2\pi}{3}\right) \quad (\text{A.1.0.35})$$

The self-inductance of the field winding is calculated after integration of (A.1.0.36) and division by i_{fd} . The result is given in (A.1.0.37).

$$\lambda_{fd}(i_{fd}) = L_{lfd} i_{fd} + \int_{\frac{\pi}{2}}^{\frac{3\pi}{2}} \frac{N_f}{2} \cos(\phi_r) \int_{\phi_r}^{\phi_r + \pi} \mu_0 r l \frac{N_f}{2} i_{fd} \sin(\zeta) \left(\alpha_1 - \alpha_2 \cos(2(\zeta))\right) d\zeta d\phi_r \quad (\text{A.1.0.36})$$

$$L_{l,fd} = L_{lfd} + \overbrace{\frac{N_f^2}{2} \pi r l \mu_0 \left(\alpha_1 + \frac{\alpha_2}{2}\right)}^{L_{fdfd}} \quad (\text{A.1.0.37})$$

The mutual-inductance between the field winding and the stator winding i_{us} is calculated after integration of (A.1.0.38) and division by i_{us} . The result is given in (A.1.0.39).

$$\lambda_{fd}(i_{us}) = \int_{\frac{\pi}{2}}^{\frac{3\pi}{2}} \frac{N_f}{2} \cos(\phi_r) \int_{\phi_r}^{\phi_r+\pi} \mu_0 r l \frac{N_s}{2} i_{us} \cos(\zeta - \theta_r) (\alpha_1 - \alpha_2 \cos 2\zeta) d\zeta d\phi_r \quad (\text{A.1.0.38})$$

$$L_{fdus} = \frac{N_f N_s}{2} \pi r l \mu_0 (\alpha_1 + \frac{\alpha_2}{2}) \sin(\theta_r) \quad (\text{A.1.0.39})$$

The mutual-inductance between the field winding and the stator winding i_{vs} is calculated after integration of (A.1.0.40) and division by i_{vs} . The result is given in (A.1.0.41).

$$\lambda_{fd}(i_{vs}) = \int_{\frac{\pi}{2}}^{\frac{3\pi}{2}} \frac{N_f}{2} \cos(\phi_r) \int_{\phi_r}^{\phi_r+\pi} \mu_0 r l \frac{N_s}{2} i_{vs} \cos(\zeta - \theta_r + \frac{2\pi}{3}) (\alpha_1 - \alpha_2 \cos(2\zeta)) d\zeta d\phi_r \quad (\text{A.1.0.40})$$

$$L_{fdvs} = \frac{N_f N_s}{2} \pi r l \mu_0 (\alpha_1 + \frac{\alpha_2}{2}) \sin(\theta_r - \frac{2\pi}{3}) \quad (\text{A.1.0.41})$$

The mutual-inductance between the field winding and the stator winding i_{ws} is calculated after integration of (A.1.0.42) and division by i_{ws} . The result is given in (A.1.0.43).

$$\lambda_{fd}(i_{ws}) = \int_{\frac{\pi}{2}}^{\frac{3\pi}{2}} \frac{N_f}{2} \cos(\phi_r) \int_{\phi_r}^{\phi_r+\pi} \mu_0 r l \frac{N_s}{2} i_{ws} \cos(\zeta - \theta_r - \frac{2\pi}{3}) (\alpha_1 - \alpha_2 \cos(2\zeta)) d\zeta d\phi_r \quad (\text{A.1.0.42})$$

$$L_{fdws} = \frac{N_f N_s}{2} \pi r l \mu_0 (\alpha_1 + \frac{\alpha_2}{2}) \sin(\theta_r + \frac{2\pi}{3}) \quad (\text{A.1.0.43})$$

A.2 Saturation of the Main Inductance

$$i'_m = F(\lambda'_m) \quad (\text{A.2.0.1})$$

$$\Gamma'_{\text{diff}} = \frac{d}{dt} \frac{1}{L'_m} = \left(\frac{di'_m}{d\lambda'} - \Gamma' \right) \cdot \frac{1}{\lambda_m^2} \left(\lambda_{md} \frac{d}{dt} \lambda_{md} + \frac{1}{\alpha^2} \lambda_{mq} \frac{d}{dt} \lambda_{mq} \right) \quad (\text{A.2.0.2})$$

$$\begin{aligned} d\Gamma_{dd} &= \frac{1}{dL_{dd}} = \Gamma'_{\text{diff}} \frac{\lambda_{md}^2}{\lambda_m} + \Gamma' \frac{\lambda_{mq}^2}{\alpha \lambda_m} & d\Gamma_{qq} &= \frac{1}{dL_{qq}} = \frac{1}{\alpha^2} \left(\Gamma' \frac{\lambda_{md}^2}{\lambda_m} + \Gamma'_{\text{diff}} \frac{\lambda_{md}^2}{\lambda_m} \right) \\ d\Gamma_{qd} &= d\Gamma_{dq} = \frac{1}{dL_{qd}} = \frac{1}{\alpha} (\Gamma'_{\text{diff}} - \Gamma') \frac{\lambda_{md}}{\lambda_m} \frac{\lambda_{mq}}{\lambda_m} \end{aligned} \quad (\text{A.2.0.3})$$

$$\begin{aligned}
\tau_T &= \frac{f_T L_{md0}}{\lambda_T L_{mds}} & M_f &= \frac{1}{L_{md}} & M_i &= \frac{\left(\frac{1}{L_{md0}} - \frac{1}{L_{mds}} \cdot \left(\frac{1}{2} - \frac{\arctan(\tau_T \lambda_T)}{\pi}\right)\right)}{\left(\frac{1}{2} + \frac{\arctan(\tau_T \lambda_T)}{\pi}\right)} \\
M_d &= \frac{(M_f - M_i)}{2} & M_a &= \frac{(M_f + M_i)}{2} & \lambda'_m &= \sqrt{(\lambda_{md} + \lambda_{mag})^2 + \alpha \lambda_{mq}^2} \\
\frac{dF}{d\lambda'_m} &= \frac{2}{\pi} M_d \arctan(\tau_T (\lambda'_m - \lambda_T)) + M_a & \Gamma_q &= \frac{\alpha \cdot F}{\lambda'_m} & \Gamma_d &= \frac{F}{\lambda'_m} \\
F &= 2 \frac{M_d}{\pi} \left((\lambda'_m - \lambda_T) \arctan(\tau_T (\lambda'_m - \lambda_T)) + \lambda_T \arctan(-\tau_T \lambda_T) \right) \\
&\quad + \frac{M_d}{(\pi \tau_T)} \left(\log(1 + (\tau_T \lambda_T)^2) - \log(1 + (\tau_T (\lambda'_m - \lambda_T))^2) \right) + M_a \lambda'_m \\
d\Gamma_{qq} &= \frac{dF}{d\lambda'_m} \cdot \left(\frac{\alpha \lambda_{mq}}{\lambda'_m} \right)^2 + \alpha \frac{F}{\lambda'_m} \left(1 - \alpha \left(\frac{\lambda_{mq}}{\lambda'_m} \right)^2 \right) & d\Gamma_{qd} &= \left(\frac{dF}{d\lambda'_m} - \frac{F}{\lambda'_m} \right) \alpha \lambda_{mq} \left(\frac{(\lambda_{md} + \lambda_{mag})}{\lambda'_m} \right)^2 \\
\Gamma_{dd} &= \frac{dF}{d\lambda'_m} \cdot \left(\frac{(\lambda_{md} + \lambda_{mag})}{\lambda'_m} \right)^2 + F / \lambda'_m \cdot \left(1 - ((\lambda_{md} + \lambda_{mag}) / \lambda'_m)^2 \right) \\
\Gamma_{det} &= d\Gamma_{qq} d\Gamma_{dd} - d\Gamma_{qd}^2 & dL_{qq} &= \frac{d\Gamma_{dd}}{\Gamma_{det}} & dL_{qd} &= -\frac{d\Gamma_{qd}}{\Gamma_{det}} & dL_{dd} &= \frac{d\Gamma_{qq}}{\Gamma_{det}}
\end{aligned} \tag{A.2.0.4}$$

B Deriving State Space Representation for the Dual-Voltage Machine

A typical state space mode has the form of equation (B.0.0.1).

$$\begin{aligned}\dot{\mathbf{x}}(t) &= \mathbf{A}\mathbf{x}(t) + \mathbf{B}\mathbf{u}(t) \\ \mathbf{y}(t) &= \mathbf{C}\mathbf{x}(t) + \mathbf{D}\mathbf{u}(t)\end{aligned}\tag{B.0.0.1}$$

The quantities are type set in bold to denote matrices and vectors. The following notation holds typically for a state-space representation:

- \mathbf{A} is the state matrix
- \mathbf{B} is the input matrix
- \mathbf{C} is the output matrix
- \mathbf{D} is the feedforward matrix
- \mathbf{u} is the input vector
- \mathbf{x} is the state vector
- \mathbf{y} is the output vector

In a machine control, the currents of the machine are measured and transformed into the $q-d$ frame. Therefore, the output vector $\mathbf{y}(t)$ is equal to the measured currents in the $q-d$ frame $\mathbf{i}_{s,qd,12f}(t)$. The “input” vector $\mathbf{u}(t)$ applied on the machine terminals through the inverter is the voltage vector $\mathbf{v}_{s,qd,12f}(t)$. In reality, the voltages are transformed into the ABC frame and a modulation technique is used transform the desired ABC -voltages into duty cycles for the inverter end stages. For control purposes the analysis are made in the $q-d$ frame. The state space representation of the dual-voltage machine can be derived from the machine voltage equations (B.0.0.2)-(B.0.0.6).

$$\begin{aligned}v_{qs1} &= r_{s1}i_{qs1} + (L_{ls1} + L_{qq1})pi_{qs1} + \frac{L_{qq1}}{N_{s12}}pi_{qs2} \\ &\quad + \omega_e \left[(L_{ls1} + L_{dd1})i_{ds1} + \frac{L_{dd1}}{N_{s12}}i_{ds2} + \frac{2}{3} \frac{L_{dd1}}{N_{s1f}}i_{fd} \right]\end{aligned}\tag{B.0.0.2}$$

$$\begin{aligned}v_{ds1} &= r_{s1}i_{ds1} + (L_{ls1} + L_{dd1})pi_{ds1} + \frac{L_{dd1}}{N_{s12}}pi_{ds2} + \frac{2}{3} \frac{L_{dd1}}{N_{s1f}}pi_{fd} \\ &\quad - \omega_e \left[(L_{ls1} + L_{qq1})i_{qs1} + \frac{L_{qq1}}{N_{s12}}i_{qs2} \right]\end{aligned}\tag{B.0.0.3}$$

$$v_{qs2} = r_{s2}i_{qs2} + \left(L_{ls2} + \frac{L_{qq1}}{N_{s12}^2}\right) p i_{qs2} + \frac{L_{qq1}}{N_{s12}} p i_{qs1} + \omega_e \left[\left(L_{ls2} + \frac{L_{dd1}}{N_{s12}^2}\right) i_{ds2} + \frac{L_{dd1}}{N_{s12}} i_{ds1} + \frac{2}{3} \frac{L_{dd1}}{N_{s1f} N_{s12}} i_{fd} \right] \quad (\text{B.0.0.4})$$

$$v_{ds2} = r_{s2}i_{ds2} + \left(L_{ls2} + \frac{L_{dd1}}{N_{s12}^2}\right) p i_{ds2} + \frac{L_{dd1}}{N_{s12}} p i_{ds1} + \frac{2}{3} \frac{L_{dd1}}{N_{s1f} N_{s12}} p i_{fd} - \omega_e \left[\left(L_{ls2} + \frac{L_{qq1}}{N_{s12}^2}\right) i_{qs2} + \frac{L_{qq1}}{N_{s12}} i_{qs1} \right] \quad (\text{B.0.0.5})$$

$$v_{fd} = r_f i_{fd} + \left(L_{lf} + \frac{2}{3} \frac{L_{dd1}}{N_{s1f}^2}\right) p i_{fd} + \frac{L_{dd1}}{N_{s1f}} p i_{ds1} + \frac{L_{dd1}}{N_{s12} N_{s1f}} p i_{ds2} \quad (\text{B.0.0.6})$$

It is easier to derive the state space representation, when the voltage equations are written in matrix form. Then, through matrix manipulations the $(A - B - C - D)$ matrices of the state space model are derived. The voltage equations are written in matrix form with symbols given in (B.0.0.7).

$$\mathbf{v}_{s,\text{qd},12f} = \mathbf{R}_{s,12f} \cdot \mathbf{i}_{s,\text{qd},12f} + \mathbf{L}_{ls,\text{qd},12f} \cdot \frac{d}{dt} \mathbf{i}_{s,\text{qd},12f} + \omega_e \mathbf{P}_{m,\text{qd},12f} \mathbf{L}_{ls,\text{qd},12f} \cdot \mathbf{i}_{s,\text{qd},12f} \quad (\text{B.0.0.7})$$

$$\mathbf{R}_{s,12f} = \begin{bmatrix} R_{s1} & 0 & 0 & 0 & 0 \\ 0 & R_{s1} & 0 & 0 & 0 \\ 0 & 0 & R_{s2} & 0 & 0 \\ 0 & 0 & 0 & R_{s2} & 0 \\ 0 & 0 & 0 & 0 & R_f \end{bmatrix} \quad (\text{B.0.0.8})$$

$$\mathbf{L}_{ls,\text{qd},12f} = \begin{bmatrix} L_{qq1} + L_{ls1} & 0 & \frac{L_{qq1}}{N_{s12}} & 0 & 0 \\ 0 & L_{dd1} + L_{ls1} & 0 & \frac{L_{dd1}}{N_{s12}} & \frac{2}{3} \frac{L_{dd1}}{N_{s1f}} \\ \frac{L_{qq1}}{N_{s12}} & 0 & \frac{L_{qq1}}{N_{s12}^2} + L_{ls2} & 0 & 0 \\ 0 & \frac{L_{dd1}}{N_{s12}} & 0 & \frac{L_{dd1}}{N_{s12}^2} + L_{ls2} & \frac{2}{3} \frac{L_{dd1}}{N_{s12} N_{s1f}} \\ 0 & \frac{L_{dd1}}{N_{s1f}} & 0 & \frac{L_{dd1}}{N_{s12} N_{s1f}} & \frac{2}{3} \frac{L_{dd1}}{N_{s1f}^2} + L_{lf} \end{bmatrix} \quad (\text{B.0.0.9})$$

$$\mathbf{P}_{m,\text{qd},12f} = \begin{bmatrix} 0 & 1 & 0 & 0 & 0 \\ -1 & 0 & 0 & 0 & 0 \\ 0 & 0 & 0 & 1 & 0 \\ 0 & 0 & -1 & 0 & 0 \\ 0 & 0 & 0 & 0 & 0 \end{bmatrix} \quad (\text{B.0.0.10})$$

From the voltage equations in (B.0.0.7) is clear that the state vector $\mathbf{x}(t)$ is equal to the currents vector $\mathbf{i}_{s,\text{qd},12f}(t)$. From this insight is clear that the output matrix \mathbf{C} is

equal to the identity matrix. The voltage equations do not have a feed through path. Therefore the feedforward matrix \mathbf{D} is equal to zero. The remaining two matrices, the state matrix \mathbf{A} and the input matrix \mathbf{B} are derived when the voltage equation is solved after $\frac{d}{dt} \mathbf{i}_{s,\text{qd},12\text{f}}(t)$ or respectively in the laplace domain after $s \cdot \mathbf{i}_{s,\text{qd},12\text{f}}(s)$ (B.0.0.11).

$$s \cdot \mathbf{i}_{s,\text{qd},12\text{f}} = - \underbrace{\mathbf{L}_{\text{ls,qd},12\text{f}}^{-1} (\mathbf{R}_{s,12\text{f}} + \omega_e \mathbf{P}_{\text{m,qd},12\text{f}} \mathbf{L}_{\text{ls,qd},12\text{f}})}_{\mathbf{A}} \mathbf{i}_{s,\text{qd},12\text{f}} + \underbrace{\mathbf{L}_{\text{ls,qd},12\text{f}}^{-1} \mathbf{v}_{s,\text{qd},12\text{f}}}_{\mathbf{B}} \quad (\text{B.0.0.11})$$

Then the machine plant model can be derived according to equation (B.0.0.12).

$$\mathbf{y}(s) = \underbrace{(\mathbf{C} (s\mathbf{I} - \mathbf{A})^{-1} \mathbf{B} + \mathbf{D})}_{\mathbf{G}_p(s)} \mathbf{u}(s) \quad (\text{B.0.0.12})$$

C Tuning the Current Control Loops - Parameters and Nyquist Plots

This appendix includes all formulas used to tune the 5 current control loops and also figures of all Nyquist plots, showing the Phase Margin (PM) and the resulting bandwidths of the closed loops.

Equations (C.0.0.3) to (C.0.0.15) show the formulas used to tune the PI controllers, such that the closed loop transfer functions have a certain bandwidth. The time constants T_n , the proportional factors K_p and the integral factors K_i of all five PI controllers are given.

$$T_{n,iqs1} = (L_{ls1} + L_{qq1}) \cdot r_{s1}^{-1} \quad (C.0.0.1)$$

$$K_{p,iqs1} = (L_{ls1} + L_{qq1}) \omega_b \left(\sqrt{2T_{sw,ph}^2 \omega_b^2 + 1} - T_{sw,ph} \omega_b \right) \Rightarrow \overset{T_{sw,ph}=0}{\cong} (L_{ls1} + L_{qq1}) \omega_b \quad (C.0.0.2)$$

$$K_{i,iqs1} = \frac{K_{p,iqs1}}{T_{n,iqs1}} = r_{s1} \omega_b \left(\sqrt{2T_{sw,ph}^2 \omega_b^2 + 1} - T_{sw,ph} \omega_b \right) \Rightarrow \overset{T_{sw,ph}=0}{\cong} r_{s1} \omega_b \quad (C.0.0.3)$$

$$T_{n,ids1} = (L_{ls1} + L_{dd1}) \cdot r_{s1}^{-1} \quad (C.0.0.4)$$

$$K_{p,ids1} = (L_{ls1} + L_{dd1}) \omega_b \left(\sqrt{2T_{sw,ph}^2 \omega_b^2 + 1} - T_{sw,ph} \omega_b \right) \Rightarrow \overset{T_{sw,ph}=0}{\cong} (L_{ls1} + L_{dd1}) \omega_b \quad (C.0.0.5)$$

$$K_{i,ids1} = \frac{K_{p,ids1}}{T_{n,ids1}} = r_{s1} \omega_b \left(\sqrt{2T_{sw,ph}^2 \omega_b^2 + 1} - T_{sw,ph} \omega_b \right) \Rightarrow \overset{T_{sw,ph}=0}{\cong} r_{s1} \omega_b \quad (C.0.0.6)$$

$$T_{n,iqs2} = \left(L_{ls2} + \frac{L_{qq1}}{N_{s12}^2} \right) \cdot r_{s1}^{-1} \quad (C.0.0.7)$$

$$K_{p,iqs2} = \left(L_{ls2} + \frac{L_{qq1}}{N_{s12}^2} \right) \omega_b \left(\sqrt{2T_{sw,ph}^2 \omega_b^2 + 1} - T_{sw,ph} \omega_b \right) \Rightarrow \overset{T_{sw,ph}=0}{\cong} \left(L_{ls2} + \frac{L_{qq1}}{N_{s12}^2} \right) \omega_b \quad (C.0.0.8)$$

$$K_{i,iqs2} = \frac{K_{p,iqs2}}{T_{n,iqs2}} = r_{s2} \omega_b \left(\sqrt{2T_{sw,ph}^2 \omega_b^2 + 1} - T_{sw,ph} \omega_b \right) \Rightarrow \overset{T_{sw,ph}=0}{\cong} r_{s2} \omega_b \quad (C.0.0.9)$$

$$T_{n,ids2} = \left(L_{ls2} + \frac{L_{dd1}}{N_{s12}^2} \right) \cdot r_{s2}^{-1} \quad (\text{C.0.0.10})$$

$$K_{p,ids2} = \left(L_{ls2} + \frac{L_{dd1}}{N_{s12}^2} \right) \omega_b \left(\sqrt{2T_{sw,ph}^2 \omega_b^2 + 1} - T_{sw,ph} \omega_b \right) \Rightarrow \underbrace{\quad}_{T_{sw,ph}=0} \left(L_{ls2} + \frac{L_{dd1}}{N_{s12}^2} \right) \omega_b \quad (\text{C.0.0.11})$$

$$K_{i,ids2} = \frac{K_{p,ids2}}{T_{n,ids2}} = r_{s2} \omega_b \left(\sqrt{2T_{sw,ph}^2 \omega_b^2 + 1} - T_{sw,ph} \omega_b \right) \Rightarrow \underbrace{\quad}_{T_{sw,ph}=0} r_{s2} \omega_b \quad (\text{C.0.0.12})$$

$$T_n^{ifd} = (L_{lf} + L_{fd}) \cdot r_f^{-1} \quad (\text{C.0.0.13})$$

$$K_{p,ifd} = (L_{ls2} + L_{fd}) \omega_b \left(\sqrt{2T_{sw,f}^2 \omega_b^2 + 1} - T_{sw,f} \omega_b \right) \Rightarrow \underbrace{\quad}_{T_{sw,f}=0} (L_{lf} + L_{fd}) \omega_b \quad (\text{C.0.0.14})$$

$$K_{i,ifd} = \frac{K_{p,ifd}}{T_n^{ifd}} = r_f \omega_b \left(\sqrt{2T_{sw,f}^2 \omega_b^2 + 1} - T_{sw,f} \omega_b \right) \Rightarrow \underbrace{\quad}_{T_{sw,f}=0} r_f \omega_b \quad (\text{C.0.0.15})$$

$$T_n^{i0s2} = L_{ls2} \cdot r_{s2}^{-1} \quad (\text{C.0.0.16})$$

$$K_{p,is02} = L_{ls2} \omega_b \left(\sqrt{2T_{sw,ph}^2 \omega_b^2 + 1} - T_{sw,ph} \omega_b \right) \Rightarrow \underbrace{\quad}_{T_{sw,ph}=0} L_{ls2} \omega_b \quad (\text{C.0.0.17})$$

$$K_{i,i0s2} = \frac{K_{p,is02}}{T_n^{i0s2}} = r_{s2} \omega_b \left(\sqrt{2T_{sw,ph}^2 \omega_b^2 + 1} - T_{sw,ph} \omega_b \right) \Rightarrow \underbrace{\quad}_{T_{sw,ph}=0} r_{s2} \omega_b \quad (\text{C.0.0.18})$$

The figures below show the Nyquist plots of the open and closed loop transfer functions of the current control loops. The Nyquist plots for the current control loop for current i_{qs1} is already given in Subsection 3.2.2. Figure 3.7 shows the Nyquist plot of the open loop transfer function and Fig. 3.8 shows the Nyquist plot of the closed loop. Figures C.1 to C.8 show the rest of the Nyquist plots for the current control loops i_{ds1} , i_{qs2} , i_{ds2} and i_{fd} . The classical magnitude optimum tuning method with compensation of the small time constant T_σ results in a PM of $65,53^\circ$ for all stator current loops. The bandwidth tuning method shapes the closed loop to have a bandwidth of 200 Hz. The PM in this case is $83,66^\circ$. A greater PM provides robustness regarding model uncertainties (for example neglecting saturation effects) and coupling effects between the current axis. A further advantage of the bandwidth tuning method is that in case of instability problems the current control loops can be detuned only with the bandwidth frequency as a parameter $\omega_b = 2\pi f_b$. The field winding current controller is tuned with a bandwidth frequency of 8 Hz.

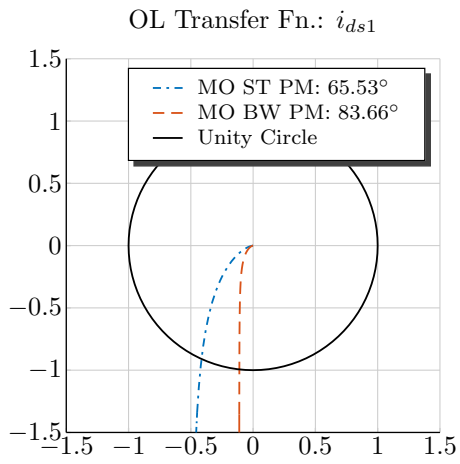


Figure C.1 – Nyquist Plot of the Open Loop Transfer Function i_{ds1}

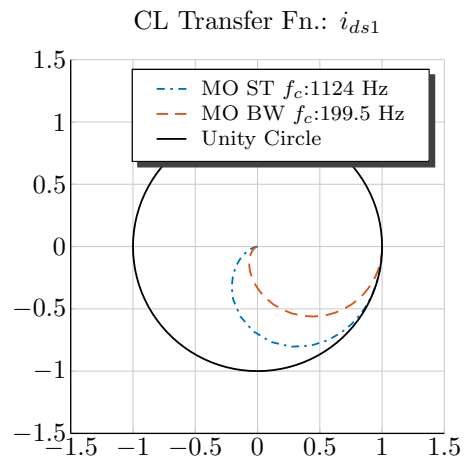


Figure C.2 – Nyquist Plot of the Closed Loop Transfer Function

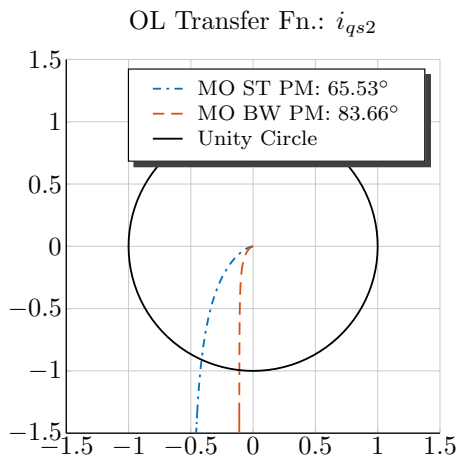


Figure C.3 – Nyquist Plot of the Open Loop Transfer Function i_{qs2}

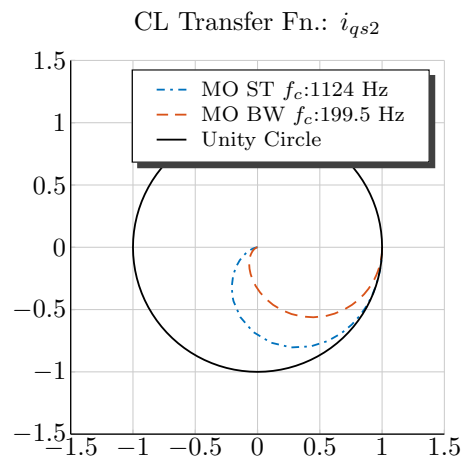


Figure C.4 – Nyquist Plot of the Closed Loop Transfer Function

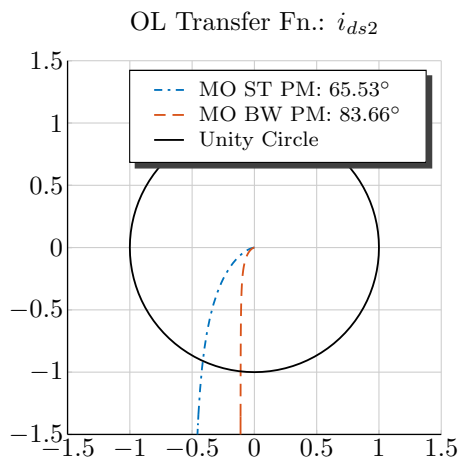


Figure C.5 – Nyquist Plot of the Open Loop Transfer Function i_{ds2}

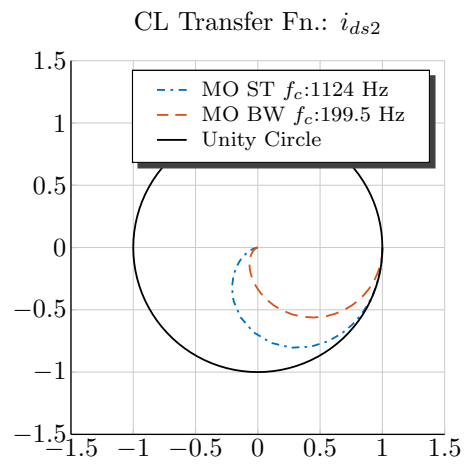


Figure C.6 – Nyquist Plot of the Closed Loop Transfer Function

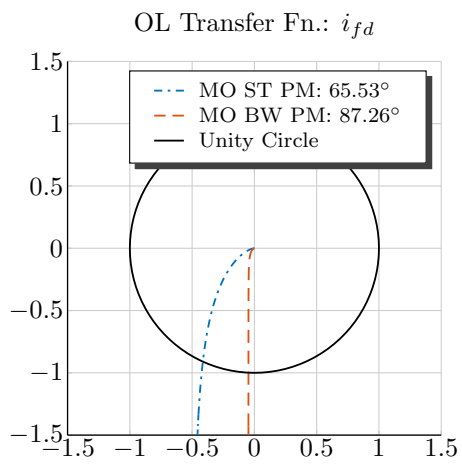


Figure C.7 – Nyquist Plot of the Open Loop Transfer Function i_{fd}

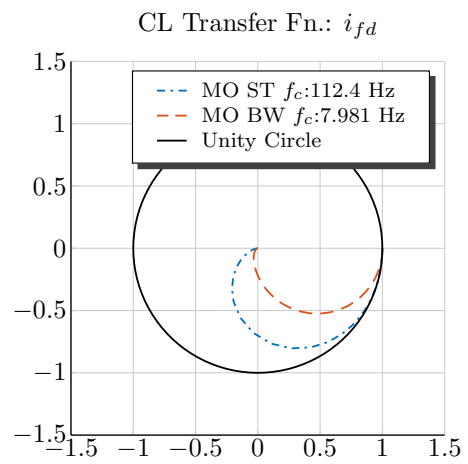


Figure C.8 – Nyquist Plot of the Closed Loop Transfer Function

D Simulation Results of the Controller Tests

This appendix includes the simulation results of all controller tests.

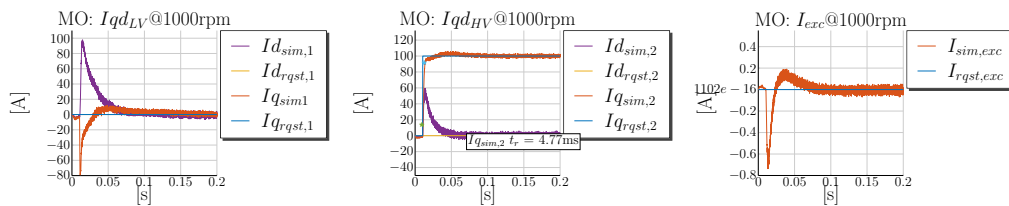


Figure D.1 – Simulation @1000rpm: $i_{qs1} = 0$ A, $i_{ds1} = 0$ A, $i_{qs2} = 100$ A, $i_{ds2} = 0$ A and $i_{fd} = 0$ A
MO Tuning

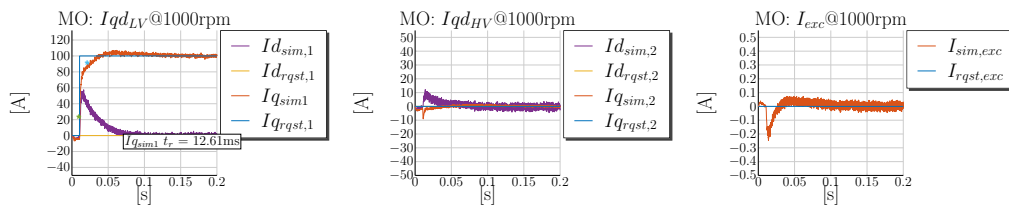


Figure D.2 – Simulation @1000rpm: $i_{qs1} = 100$ A, $i_{ds1} = 0$ A, $i_{qs2} = 0$ A, $i_{ds2} = 0$ A and $i_{fd} = 0$ A
MO Tuning

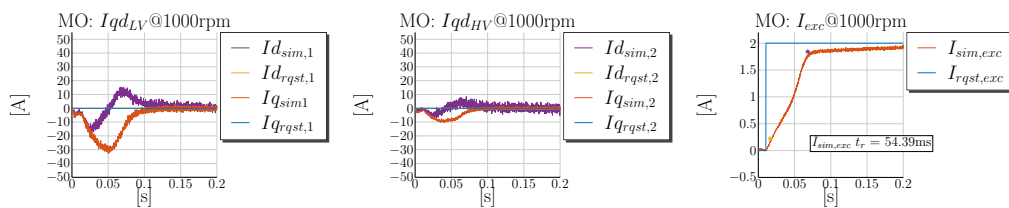


Figure D.3 – Simulation @1000rpm: $i_{qs1} = 0$ A, $i_{ds1} = 0$ A, $i_{qs2} = 0$ A, $i_{ds2} = 0$ A and $i_{fd} = 2$ A
MO Tuning

D Simulation Results of the Controller Tests

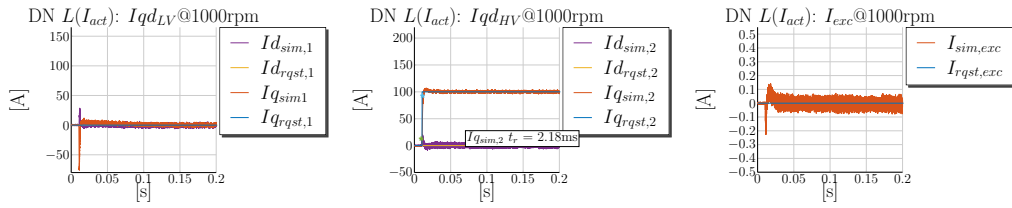


Figure D.4 – Simulation @1000rpm: $i_{qs1} = 0$ A, $i_{ds1} = 0$ A, $i_{qs2} = 100$ A, $i_{ds2} = 0$ A and $i_{fd} = 0$ A MO with a DN $L(I_{act})$

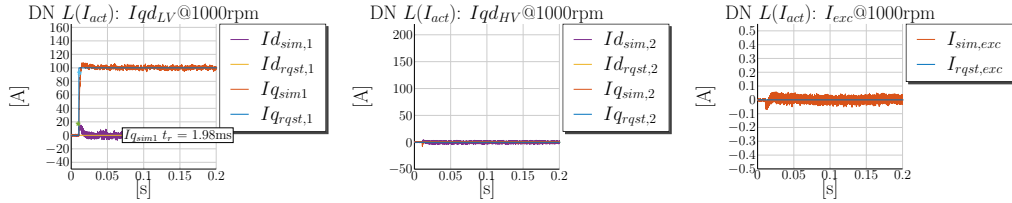


Figure D.5 – Simulation @1000rpm: $i_{qs1} = 100$ A, $i_{ds1} = 0$ A, $i_{qs2} = 0$ A, $i_{ds2} = 0$ A and $i_{fd} = 0$ A MO with a DN $L(I_{act})$

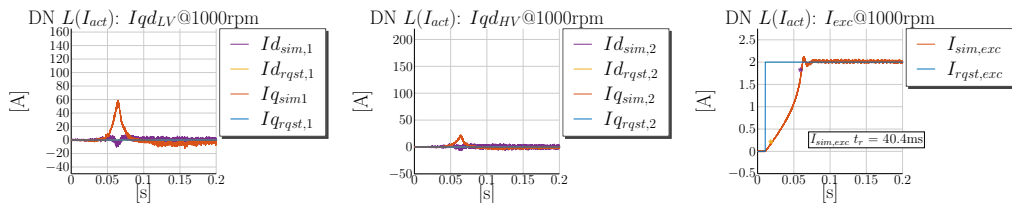


Figure D.6 – Simulation @1000rpm: $i_{qs1} = 0$ A, $i_{ds1} = 0$ A, $i_{qs2} = 0$ A, $i_{ds2} = 0$ A and $i_{fd} = 2$ A MO with a DN $L(I_{act})$

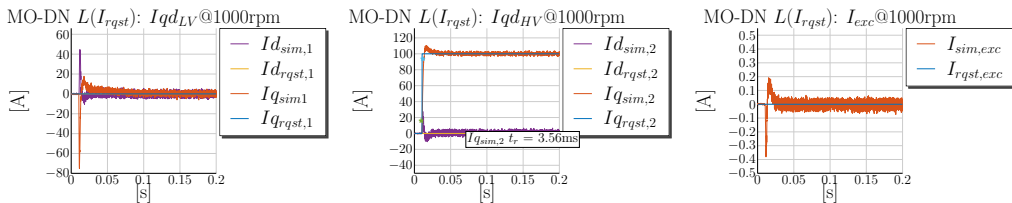


Figure D.7 – Simulation @1000rpm: $i_{qs1} = 0$ A, $i_{ds1} = 0$ A, $i_{qs2} = 100$ A, $i_{ds2} = 0$ A and $i_{fd} = 0$ A MO with a DN $L(I_{rqst})$

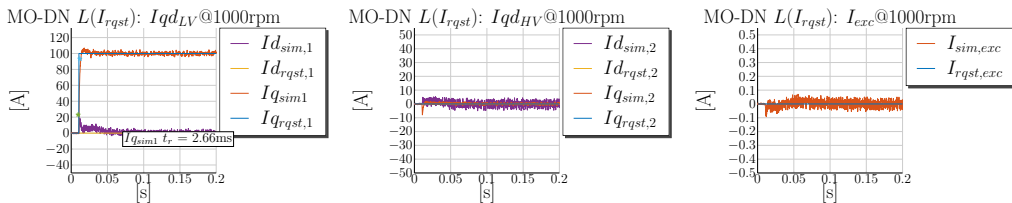


Figure D.8 – Simulation @1000rpm: $i_{qs1} = 100$ A, $i_{ds1} = 0$ A, $i_{qs2} = 0$ A, $i_{ds2} = 0$ A and $i_{fd} = 0$ A MO with a DN $L(I_{rqst})$

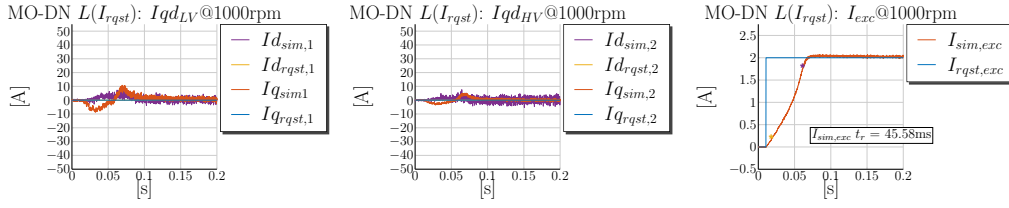


Figure D.9 – Simulation @1000rpm: $i_{qs1} = 0$ A, $i_{ds1} = 0$ A, $i_{qs2} = 0$ A, $i_{ds2} = 0$ A and $i_{fd} = 2$ A
MO with a DN $L(I_{rqst})$

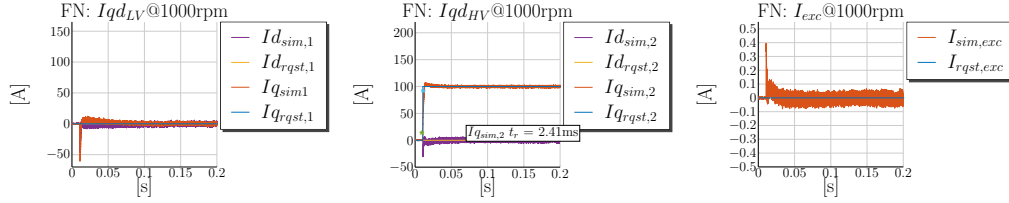


Figure D.10 – Simulation @1000rpm: $i_{qs1} = 0$ A, $i_{ds1} = 0$ A, $i_{qs2} = 100$ A, $i_{ds2} = 0$ A and $i_{fd} = 0$ A
MO-FN $L(I_{rqst})$

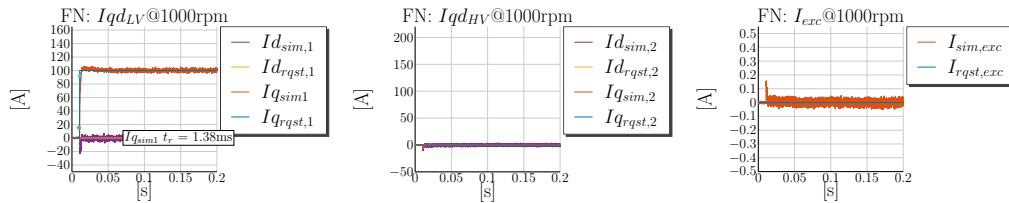


Figure D.11 – Simulation @1000rpm: $i_{qs1} = 100$ A, $i_{ds1} = 0$ A, $i_{qs2} = 0$ A, $i_{ds2} = 0$ A and $i_{fd} = 0$ A
MO-FN $L(I_{rqst})$

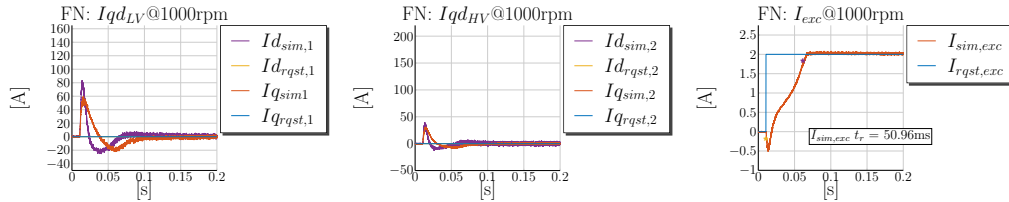


Figure D.12 – Simulation @1000rpm: $i_{qs1} = 0$ A, $i_{ds1} = 0$ A, $i_{qs2} = 0$ A, $i_{ds2} = 0$ A and $i_{fd} = 2$ A
MO-FN $L(I_{rqst})$

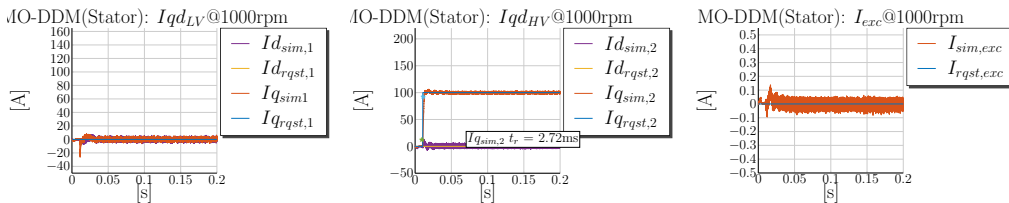


Figure D.13 – Simulation @1000rpm: $i_{qs1} = 0$ A, $i_{ds1} = 0$ A, $i_{qs2} = 100$ A, $i_{ds2} = 0$ A and $i_{fd} = 0$ A
MO with a DDM (Stator) $L(I_{rqst})$

D Simulation Results of the Controller Tests

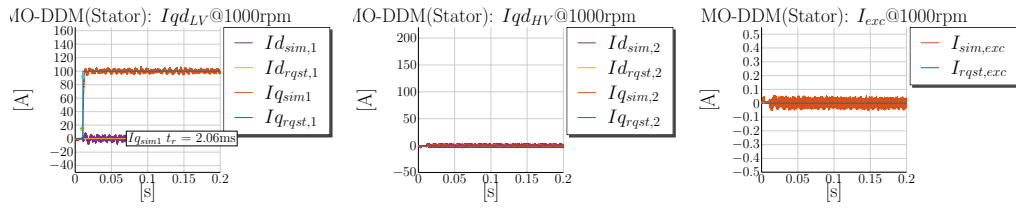


Figure D.14 – Simulation @1000rpm: $i_{qs1} = 100\text{ A}$, $i_{ds1} = 0\text{ A}$, $i_{qs2} = 0\text{ A}$, $i_{ds2} = 0\text{ A}$ and $i_{fd} = 0\text{ A}$ MO with a DDM (Stator) $L(I_{rqst})$

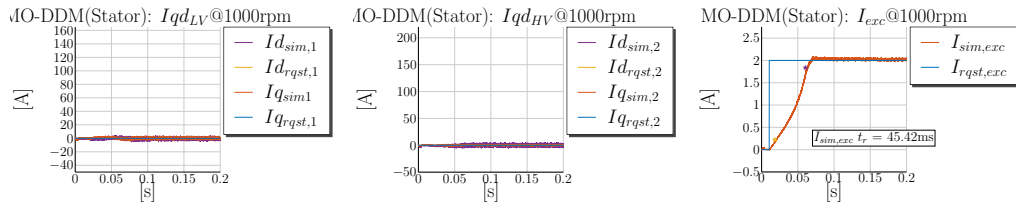


Figure D.15 – Simulation @1000rpm: $i_{qs1} = 0\text{ A}$, $i_{ds1} = 0\text{ A}$, $i_{qs2} = 0\text{ A}$, $i_{ds2} = 0\text{ A}$ and $i_{fd} = 2\text{ A}$ MO with a DDM (Stator) $L(I_{rqst})$

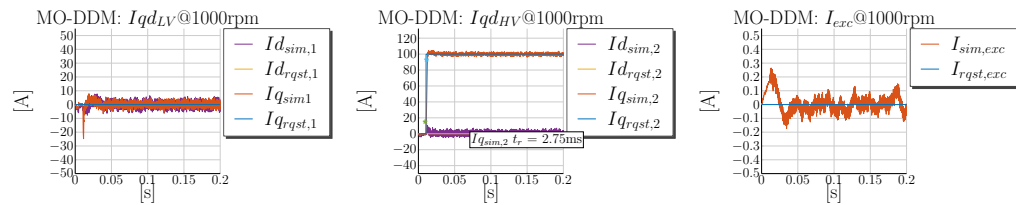


Figure D.16 – Simulation @1000rpm: $i_{qs1} = 0\text{ A}$, $i_{ds1} = 0\text{ A}$, $i_{qs2} = 100\text{ A}$, $i_{ds2} = 0\text{ A}$ and $i_{fd} = 0\text{ A}$ MO with a DDM $L(I_{rqst})$

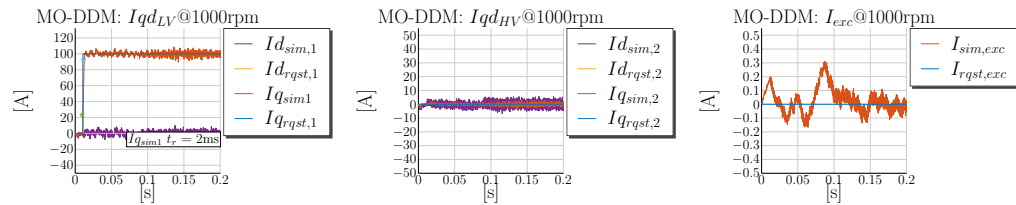


Figure D.17 – Simulation @1000rpm: $i_{qs1} = 100\text{ A}$, $i_{ds1} = 0\text{ A}$, $i_{qs2} = 0\text{ A}$, $i_{ds2} = 0\text{ A}$ and $i_{fd} = 0\text{ A}$ MO with a DDM $L(I_{rqst})$

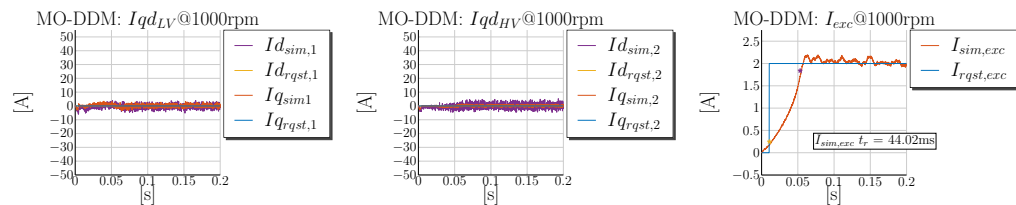


Figure D.18 – Simulation @1000rpm: $i_{qs1} = 0\text{ A}$, $i_{ds1} = 0\text{ A}$, $i_{qs2} = 0\text{ A}$, $i_{ds2} = 0\text{ A}$ and $i_{fd} = 2\text{ A}$ MO with a DDM $L(I_{rqst})$

E Star Point Current Controller - Tuning and Simulations

During standstill the dual-voltage machine can generate both electromagnetic torques T_{e12V} and T_{e48V} , but cannot transfer power between 12V and 48V through them. For this purpose the star point of the 48V phase winding is connected through a MOSFET switch, integrated in the power electronics, to the plus pole of the 12V side. This enables the power transfer at standstill through the control of the 48V star point current i_{0s2} . The DC/DC mode at standstill is schematically represented in Fig. E.1. The star point current controller is parametrized in an analogous way as the stator DQ current controllers. For the purpose of controller design the voltage equation of the star point current (E.0.0.1) is considered. The derivation of the plant transfer function from the voltage equation is straight forward and is shown in equation (E.0.0.2) and the inverse transfer function is shown in equation (E.0.0.3).

$$v_{0s2} = r_{s2}i_{0s2} + L_{1s2}p i_{0s2} \quad (\text{E.0.0.1})$$

$$G_{p,i_{0s2}}(s) = \frac{i_{0s2}}{v_{0s2}} = \frac{1}{r_{s2} + L_{1s2}s} = \frac{r_{s2}^{-1}}{1 + L_{1s2}r_{s2}^{-1}s} \quad (\text{E.0.0.2})$$

$$G_{p,i_{0s2}}^{-1}(s) = \frac{v_{0s2}}{i_{0s2}} = \frac{1 + L_{1s2}r_{s2}^{-1}s}{r_{s2}^{-1}} \quad (\text{E.0.0.3})$$

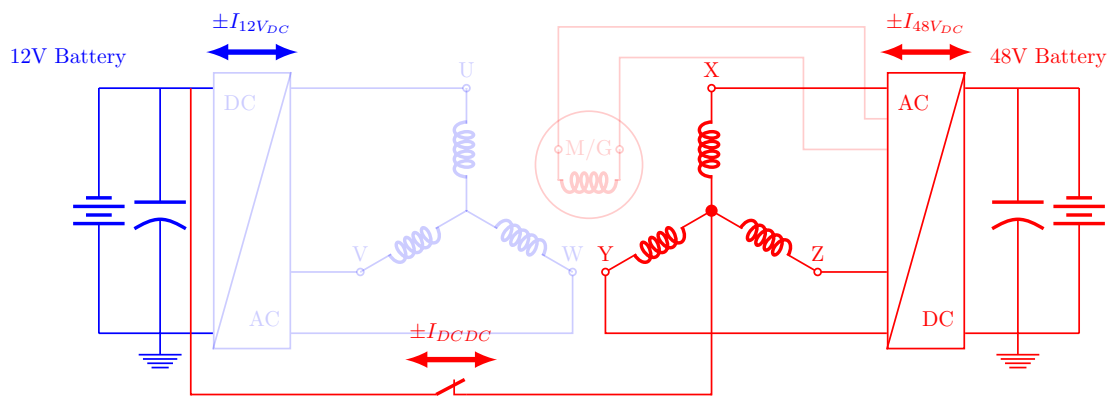


Figure E.1 – Dual-Voltage Machine with a Star Point Connected to 12V+

The current control loop for the star point current is illustrated in Fig. E.2. The goal for the current control of the star point current is to control the DC current at the 12V side. For this purpose the relationship between zero sequence current and the DC current is required. The DC current is the sum of all 48V phase currents. The relationship between phase currents and d - q currents is known through the d - q transformation shown in equation (2.1.3.15). The third row of the matrix shows the connection between between phase currents and star point current and is shown again in (E.0.0.4). In order to set the desired DC current correctly the reference star point current has to be scaled. From equation (E.0.0.4) is evident that $I_{48V,DC}^{ref}$ should be scaled with $\frac{1}{3}$ and forwarded as $I_{0,48V}^{ref}$ to the star point current controller. For example a 90 A DC 12V current is set through a star point reference current of 30 A: $I_{0,48V}^{ref} = \frac{1}{3} I_{48V,DC}^{ref}$. This relationship will be evident also in the performed simulations.

$$i_{0s2} = \frac{2}{3} \left(\frac{1}{2} i_{xs} + \frac{1}{2} i_{ys} + \frac{1}{2} i_{zs} \right) = \frac{1}{3} (i_{xs} + i_{ys} + i_{zs}) = \frac{1}{3} I_{48V,DC} \quad (E.0.0.4)$$

The MO tuning method is applied, as described in Chapter 3, to the tuning of the star point controller. The main inductance does is not evident in the star point voltage equation and therefore is also not considered in the tuning of the controller ¹. The controller parameters K_p and K_i are calculated through the formulas shown in (E.0.0.5).

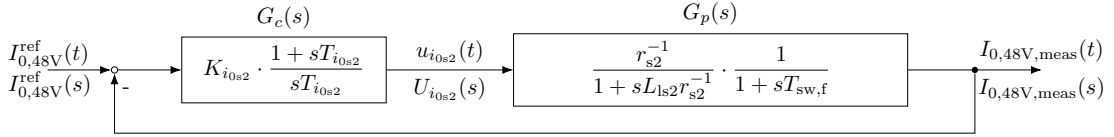


Figure E.2 – Star Point Current Control Loop

$$K_s = K_{i_{0s2}} = \frac{1}{r_{s2}} \quad T_1 = T_{i_{0s2}} = (L_{ls2}) r_{s2}^{-1} \quad T_\sigma = T_{sw,f} \quad (E.0.0.5)$$

$$K_{p, is02} = L_{ls2} \omega_b \left(\sqrt{2T_{sw,ph}^2 \omega_b^2 + 1} - T_{sw,ph} \omega_b \right) = 0.0428 \quad (E.0.0.6)$$

$$K_{p, is02} = r_{s2} \omega_b \left(\sqrt{2T_{sw,ph}^2 \omega_b^2 + 1} - T_{sw,ph} \omega_b \right) = 29.7575$$

Simulations with the tuned star point controller are performed. The power transfer the 12V side to the 48V side is tested through a step change of $I_{0,48V}^{ref} = 100$ A. A positive 48V star point current is equivalent to the boost mode of a DC/DC converter. The power is transferred from 12V to 48V. Figure E.3 shows the simulation results. The corresponding DC currents are plotted in the middle (unfiltered) and the most right plot (filtered) of the figure. A step change of $I_{0,48V}^{ref} = -100$ A is also performed to test an equivalent of a

¹The main inductance plays only a role in the torque building currents. The star point current does not have influence on the generated torque.

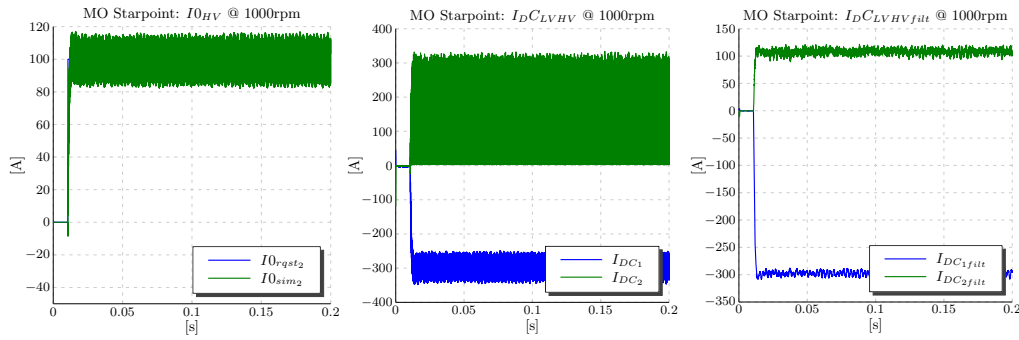


Figure E.3 – Controller Test: $i_{0s2} = 100 \text{ A}$, $I_{12\text{V,DC}}^{\text{ref}} = -300 \text{ A}$.

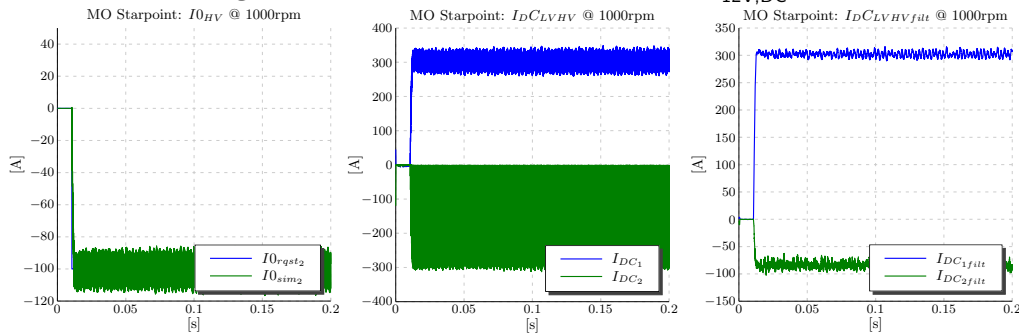


Figure E.4 – Controller Test: $I_{48\text{V,DC}} = -100 \text{ A}$, $I_{12\text{V,DC}}^{\text{ref}} = 300 \text{ A}$.

buck mode of a DC/DC converter. The power is transferred from the 48V to the 12V side. Figure E.4 shows the simulation results. In both tests the controller performs as expected without an overshoot. Reference [66] handles the tests of the star point current in detail and shows also measurements from a test bench. A special PWM technique is used to reduce the ripple of the star point current. The DC of the phases are not switched synchronously but in a sequence to reduce the ripple. Reference [31] explains this technique in detail. If all phases are switched synchronously the ripple increases 3 times.

F Offline Calculated Working Points

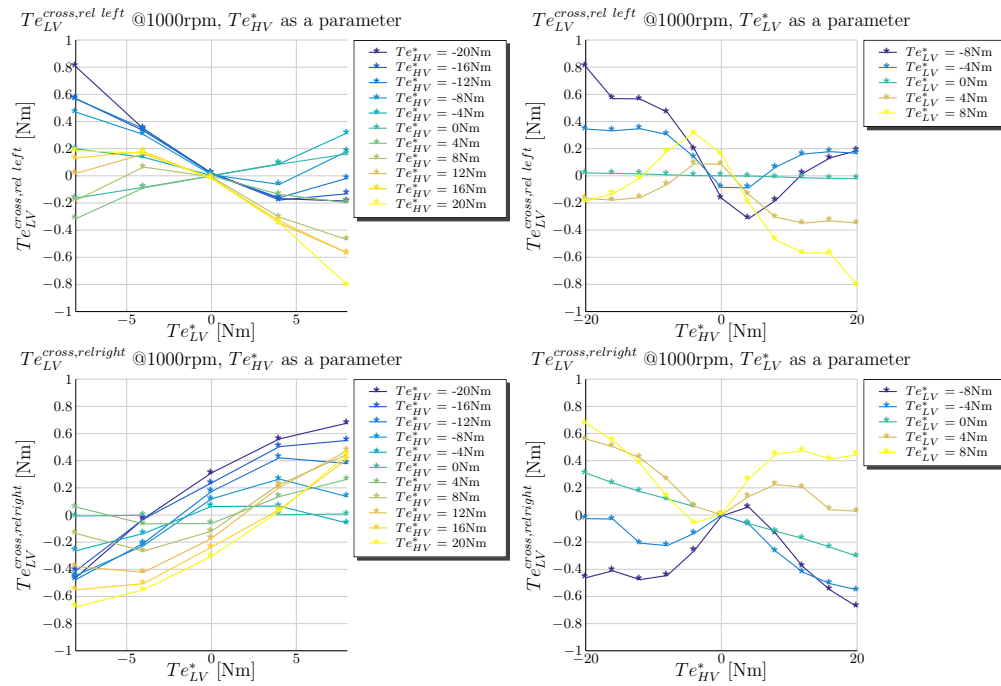


Figure F.1 – MTPCL: 12V Cross Reluctance Left Right Torques

F Offline Calculated Working Points

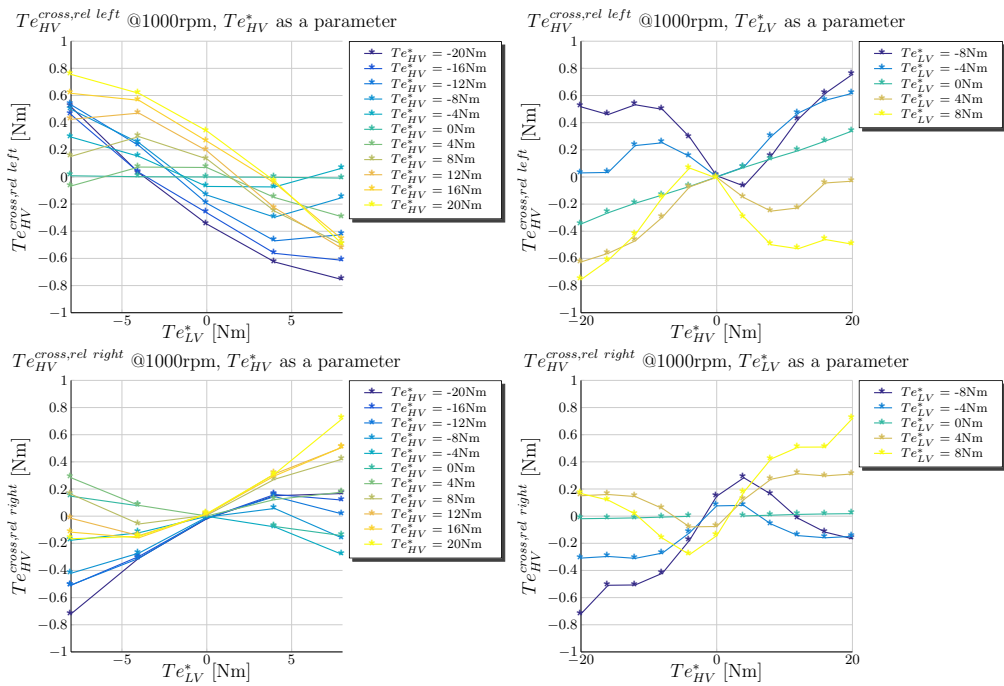


Figure F.2 – MTPCL: 48V Cross Reluctance Left Right Torques

References

- [1] *48/12V DC/DC converter*. [Accessed Mar. 1, 2020]. June 2015. URL: <https://pdrdrive-technologies.com/products/power-conversion/power-conversion-modules/dcdc-converters/dcdc-converter-4812v/>.
- [2] Akagi, H.; Aredes, M.: *Instantaneous power theory and applications to power conditioning*. John Wiley & Sons, 2017.
- [3] *ALABC: 48V mild hybrids can meet emission targets with CO₂ reductions of 15-20%*. [Accessed Mar. 1, 2020]. Jan. 2016. URL: <http://www.greencarcongress.com/2016/01/20160127-alabc.html>.
- [4] Aliprantis, D. C.; Sudhoff, S. D.; Kuhn, B. T.: “Genetic algorithm-based parameter identification of a hysteretic brushless exciter model”. In: *IEEE Transactions on Energy Conversion* 21.1 (Mar. 2006), pp. 148–154. ISSN: 0885-8969. DOI: [10.1109/TEC.2005.847967](https://doi.org/10.1109/TEC.2005.847967).
- [5] Amiri, N.; Chapariha, M.; Ebrahimi, S., ; et al.: “Constant parameter VBR model of permanent-magnet synchronous machine wind generation system”. In: *2015 IEEE Power Energy Society General Meeting*. July 2015, pp. 1–5. DOI: [10.1109/PESGM.2015.7286439](https://doi.org/10.1109/PESGM.2015.7286439).
- [6] Antonello, R.; Carraro, M.; Zigliotto, M.: “Maximum torque-per-ampere operation of anisotropic synchronous permanent-magnet motors based on extremum seeking control”. In: *IEEE Transactions on Industrial Electronics* 61.9 (Sept. 2014), pp. 5086–5093. ISSN: 0278-0046. DOI: [10.1109/TIE.2013.2278518](https://doi.org/10.1109/TIE.2013.2278518).
- [7] Astrom, K. J.; Hagglund, T.: *PID Controllers: Theory, Design, and Tuning*. 2nd ed. Instrument Society of America, Research Triangle Park, NC, 1995.
- [8] Bolognani, S.; Calligaro, S.; Petrella, R., ; et al.: “Flux-weakening in IPM motor drives: Comparison of state-of-art algorithms and a novel proposal for controller design”. In: *Proceedings of the 2011 14th European Conference on Power Electronics and Applications*. Aug. 2011, pp. 1–11.
- [9] Boyd, S.; Vandenberghe, L.: *Convex Optimization*. New York, NY, USA: Cambridge University Press, 2004. ISBN: 0521833787.
- [10] Capitan, C.: “Torque control in field-weakening mode”. [Accessed Mar. 1, 2020]. MA thesis. Aalborg University, June 2009. URL: http://projekter.aau.dk/projekter/files/17643253/PED4_1038C.pdf.

-
- [11] Chen, X.; Wang, J.; Sen, B., ; et al.: “A high-fidelity and computationally efficient model for interior permanent-magnet machines considering the magnetic saturation, spatial harmonics, and iron loss effect”. In: *IEEE Transactions on Industrial Electronics* 62.7 (July 2015), pp. 4044–4055. ISSN: 0278-0046. DOI: [10.1109/TIE.2014.2388200](https://doi.org/10.1109/TIE.2014.2388200).
- [12] Cheng, B.; Tesch, T. R.: “Torque feedforward control technique for permanent-magnet synchronous motors”. In: *IEEE Transactions on Industrial Electronics* 57.3 (Mar. 2010), pp. 969–974. ISSN: 0278-0046. DOI: [10.1109/TIE.2009.2038951](https://doi.org/10.1109/TIE.2009.2038951).
- [13] Chiniforoosh, S.; Davoudi, A.; Alaeinovin, P., ; et al.: “Dynamic modelling and characterisation of vehicular power system considering alternator iron core and rectifier losses”. In: *IET Electrical Systems in Transportation* 2.2 (June 2012), pp. 58–67. ISSN: 2042-9738. DOI: [10.1049/iet-est.2011.0031](https://doi.org/10.1049/iet-est.2011.0031).
- [14] *CO₂ reduction potentials for passenger cars until 2020*. [Accessed Mar. 1, 2020]. Dec. 2012. URL: <https://www.ika.rwth-aachen.de/en/research/projects/studies/1807-co%E2%82%82-reduction-potential-for-passenger-cars-until-2020.html>.
- [15] Corzine, K. A.; Kuhn, B. T.; Sudhoff, S. D., ; et al.: “An improved method for incorporating magnetic saturation in the q-d synchronous machine model”. In: *IEEE Transactions on Energy Conversion* 13.3 (Sept. 1998), pp. 270–275. ISSN: 0885-8969. DOI: [10.1109/60.707607](https://doi.org/10.1109/60.707607).
- [16] De Doncker, R.; Pulle, D. W. J.; Veltman, A.: *Advanced electrical drives: analysis, modeling, control*. Springer Science & Business Media, 2010.
- [17] dSpace: *DS1005 Power PC*. [Accessed Mar. 1, 2020]. URL: https://www.dspace.com/shared/data/bkm/catalog2014_en/files/assets/basic-html/page332.html.
- [18] dSpace: *DS2202 HIL I/O Board*. [Accessed Mar. 1, 2020]. URL: https://www.dspace.com/en/inc/home/products/hw/phis_hardware/i_o_boards/ds2202.cfm.
- [19] dSpace: *DS5203 FPGA Board*. [Accessed Mar. 1, 2020]. URL: https://www.dspace.com/en/inc/home/products/hw/phis_hardware/i_o_boards/ds5203_fpga_board.cfm.
- [20] Dueck, P.; Ponick, B.: “A novel iron-loss-model for permanent magnet synchronous machines in traction applications”. In: *2016 International Conference on Electrical Systems for Aircraft, Railway, Ship Propulsion and Road Vehicles International Transportation Electrification Conference (ESARS-ITEC)*. Nov. 2016, pp. 1–6. DOI: [10.1109/ESARS-ITEC.2016.7841432](https://doi.org/10.1109/ESARS-ITEC.2016.7841432).
- [21] Dumont, G. A.: *Decoupling of multiple-input-multiple-output systems*. Jan. 2011.

- [22] Ekanayake, S.; Dutta, R.; Rahman, M. F., ; et al.: “Deep flux weakening control of a segmented interior permanent magnet synchronous motor with maximum torque per voltage control”. In: *IECON 2015 - 41st Annual Conference of the IEEE Industrial Electronics Society*. Nov. 2015, pp. 004802–004807. DOI: [10.1109/IECON.2015.7392851](https://doi.org/10.1109/IECON.2015.7392851).
- [23] Ekanayake, S.; Dutta, R.; Rahman, M. F., ; et al.: “Operation along the maximum torque per voltage trajectory in a direct torque and flux controlled interior permanent magnet synchronous motor”. In: *8th IET International Conference on Power Electronics, Machines and Drives (PEMD 2016)*. Apr. 2016, pp. 1–6. DOI: [10.1049/cp.2016.0326](https://doi.org/10.1049/cp.2016.0326).
- [24] *Electrification of road transport*. [Accessed Mar. 1, 2020]. June 2012. URL: http://www.ertrac.org/uploads/documentsearch/id31/electrification_roadmap_june2012_62.pdf.
- [25] Gordon, G.; Tibshirani, R.: *KKT Conditions*. July 2010.
- [26] Goss, J.; Mellor, P. H.; Wrobel, R., ; et al.: “The design of AC permanent magnet motors for electric vehicles: a computationally efficient model of the operational envelope”. In: *6th IET International Conference on Power Electronics, Machines and Drives (PEMD 2012)*. Mar. 2012, pp. 1–6. DOI: [10.1049/cp.2012.0251](https://doi.org/10.1049/cp.2012.0251).
- [27] Gradev, S.; Findeisen, D.; Toennesen, T. L., ; et al.: “A voltage-behind-reactance model of a dual-voltage six-phase induction machine”. In: *2014 International Conference on Electrical Machines (ICEM)*. Sept. 2014, pp. 672–678. DOI: [10.1109/ICELMACH.2014.6960253](https://doi.org/10.1109/ICELMACH.2014.6960253).
- [28] Gradev, S.; Herzog, H.: “Integration of iron-loss resistance into dynamic models of 2×3-phase hybrid-excited synchronous machine”. In: *IEEE Transactions on Energy Conversion* (2018), pp. 1–1. ISSN: 0885-8969. DOI: [10.1109/TEC.2018.2841856](https://doi.org/10.1109/TEC.2018.2841856).
- [29] Gradev, S.; Reuss, J.; Herzog, H. G.: “A general voltage-behind-reactance formulation of a multivoltage n×3-phase hybrid-excited synchronous machine”. In: *IEEE Transactions on Energy Conversion* 31.4 (Dec. 2016), pp. 1452–1461. ISSN: 0885-8969. DOI: [10.1109/TEC.2016.2597258](https://doi.org/10.1109/TEC.2016.2597258).
- [30] Grune, R.; Einfeld, H.; Schäfer, U.: “Standstill frequency response tests for model identification of a synchronous machine”. In: *The XIX International Conference on Electrical Machines - ICEM 2010*. Sept. 2010, pp. 1–6. DOI: [10.1109/ICELMACH.2010.5608076](https://doi.org/10.1109/ICELMACH.2010.5608076).
- [31] Habermeyer, M.: “Modellbasierte Entwicklung eines Ansteuerverfahrens zur Energieübertragung zwischen Fahrzeugbordnetzen unter Verwendung einer Elektrischen Maschine”. MA thesis. University of Applied Science Munich, 2013.
- [32] Hu, D.; Zhu, L.; Xu, L.: “Maximum torque-per-volt operation and stability improvement of pmsm in deep flux-weakening region”. In: *2012 IEEE Energy Conversion Congress and Exposition (ECCE)*. Sept. 2012, pp. 1233–1237. DOI: [10.1109/ECCE.2012.6342675](https://doi.org/10.1109/ECCE.2012.6342675).

- [33] Im, J.; Kim, W.; Kim, K., ; et al.: “Inductance calculation method of synchronous reluctance motor including iron loss and cross magnetic saturation”. In: *IEEE Transactions on Magnetics* 45.6 (June 2009), pp. 2803–2806. ISSN: 0018-9464. DOI: [10.1109/TMAG.2009.2018663](https://doi.org/10.1109/TMAG.2009.2018663).
- [34] Jung Ho Lee; Jung Chul Kim; Dong Seek Hyun: “Effect analysis of magnet on Ld and Lq inductance of permanent magnet assisted synchronous reluctance motor using finite element method”. In: *IEEE Transactions on Magnetics* 35.3 (May 1999), pp. 1199–1202. ISSN: 0018-9464. DOI: [10.1109/20.767164](https://doi.org/10.1109/20.767164).
- [35] Junwei Jiang, B. M. M.: “Dual storage system and method with lithium ion and lead acid battery cells”. English. 20150050527. [Accessed Mar. 1, 2020]. Feb. 2015. URL: <http://www.google.ch/patents/US20150050527>.
- [36] Kashimura, T.; Morikawa, M.; Heo, J., ; et al.: “A method to design the controller of the voltage phase angle type torque feed-back control system for pmsm”. In: *2018 International Symposium on Power Electronics, Electrical Drives, Automation and Motion (SPEEDAM)*. June 2018, pp. 956–962. DOI: [10.1109/SPEEDAM.2018.8445419](https://doi.org/10.1109/SPEEDAM.2018.8445419).
- [37] Khandelwal, S.; Detroja, K. P.: “Optimal detuning parameter design for decentralized control of MIMO processes”. In: *TENCON 2017 - 2017 IEEE Region 10 Conference*. Nov. 2017, pp. 597–601. DOI: [10.1109/TENCON.2017.8227932](https://doi.org/10.1109/TENCON.2017.8227932).
- [38] Krause, P.; Wasynczuk, O.; Sudhoff, S. D., ; et al.: *Analysis of electric machinery and drive systems*. 2nd ed. John Wiley & Sons, 2002.
- [39] Kuo, B. C.: *Automatic control systems*. 5th. Upper Saddle River, NJ, USA: Prentice Hall PTR, 1987. ISBN: 0130550213.
- [40] LEM: *Automotive current transducer - HC5F400-S*. [Accessed Mar. 1, 2020]. URL: <https://www.lem.com/en/automotive-motor-control>.
- [41] LEM: *Automotive current transducer - HC5F800-S*. [Accessed Mar. 1, 2020]. URL: <https://www.lem.com/en/automotive-motor-control>.
- [42] LEM: *Automotive current transducer - LTS15-NP*. [Accessed Mar. 1, 2020]. URL: <https://www.lem.com/en/automotive-motor-control>.
- [43] LEM: *LEM - Automotive current transducers*. [Accessed Mar. 1, 2020]. URL: <https://www.lem.com/en>.
- [44] Levi, E.: “Saturation modelling in d-q axis models of salient pole synchronous machines”. In: *IEEE Transactions on Energy Conversion* 14.1 (Mar. 1999), pp. 44–50. ISSN: 0885-8969. DOI: [10.1109/60.749146](https://doi.org/10.1109/60.749146).
- [45] Levi, E.: “State-space d-q axis models of saturated salient pole synchronous machines”. In: *IEE Proceedings - Electric Power Applications* 145.3 (May 1998), pp. 206–216. ISSN: 1350-2352. DOI: [10.1049/ip-epa:19981786](https://doi.org/10.1049/ip-epa:19981786).
- [46] Levi, E.; Levi, V. A.: “Impact of dynamic cross-saturation on accuracy of saturated synchronous machine models”. In: *IEEE Transactions on Energy Conversion* 15.2 (June 2000), pp. 224–230. ISSN: 0885-8969. DOI: [10.1109/60.867004](https://doi.org/10.1109/60.867004).

-
- [47] Märgner, M.; Hackmann, W.: “Control challenges of an externally excited synchronous machine in an automotive traction drive application”. In: *2010 Emobility - Electrical Power Train*. Nov. 2010, pp. 1–6. DOI: [10.1109/EMOBILITY.2010.5668056](https://doi.org/10.1109/EMOBILITY.2010.5668056).
- [48] Mathworks: *fmincon*. [Accessed Mar. 1, 2020]. URL: <https://de.mathworks.com/help/optim/ug/fmincon.html>.
- [49] *Matlab symbolic math toolbox*. The MathWorks, Natick, MA, USA. 2013.
- [50] Mellor, P. H.; Wrobel, R.; Holliday, D.: “A computationally efficient iron loss model for brushless AC machines that caters for rated flux and field weakened operation”. In: *2009 IEEE International Electric Machines and Drives Conference*. May 2009, pp. 490–494. DOI: [10.1109/IEMDC.2009.5075251](https://doi.org/10.1109/IEMDC.2009.5075251).
- [51] Mochel, C.: “Li-ion batteries as replacement for standard lead-acid batteries in the 12v automotive powernet”. In: *Automotive Compilation 8* (2011). URL: www.atmel.com.
- [52] Moulahoum, S.; Touhami, O.: “A saturated induction machine model with series iron losses resistance”. In: IEEE, Apr. 2007. DOI: <http://ieeexplore.ieee.org/document/4380141/>. URL: <http://ieeexplore.ieee.org/document/4380141/>.
- [53] *Multiple input, multiple output process*. 2018.
- [54] Park, R. H.: “Two-reaction theory of synchronous machines generalized method of analysis-part I”. In: *Transactions of the American Institute of Electrical Engineers* 48.3 (July 1929), pp. 716–727. ISSN: 0096-3860. DOI: [10.1109/T-AIEE.1929.5055275](https://doi.org/10.1109/T-AIEE.1929.5055275).
- [55] Pekarek, S. D.; Wasynczuk, O.; Hegner, H. J.: “An efficient and accurate model for the simulation and analysis of synchronous machine/converter systems”. In: *IEEE Transactions on Energy Conversion* 13.1 (Mar. 1998), pp. 42–48. ISSN: 0885-8969. DOI: [10.1109/60.658202](https://doi.org/10.1109/60.658202).
- [56] Polyanin, A.; Manzhirov, A.: *Handbook of mathematics for engineers and scientists*. Taylor & Francis, 2006. ISBN: 9781584885023. URL: <https://books.google.de/books?id=ge6nk9W0BCcC>.
- [57] Rasmussen, H.; Vadstrup, P.; Borsting, H.: “Rotor field oriented control with adaptive iron loss compensation”. In: *Conference Record of the 1999 IEEE Industry Applications Conference. Thirty-Forth IAS Annual Meeting (Cat. No.99CH36370)*. Vol. 2. 1999, 1253–1258 vol.2. DOI: [10.1109/IAS.1999.801663](https://doi.org/10.1109/IAS.1999.801663).
- [58] *Reducing CO₂ emissions from passenger cars - before 2020*. [Accessed Mar. 1, 2020]. July 2016. URL: http://ec.europa.eu/clima/policies/transport/vehicles/cars/index_en.htm.
- [59] Renishaw: *RE36 series rotary encoders*.
- [60] Renishaw: *Renishaw Precision Measurement*. URL: <http://www.renishaw.com/en>.

- [61] Richter, J.; Dollinger, A.; Doppelbauer, M.: “Iron loss and parameter measurement of permanent magnet synchronous machines”. In: *2014 International Conference on Electrical Machines (ICEM)*. Sept. 2014, pp. 1635–1641. DOI: [10.1109/ICELMACH.2014.6960401](https://doi.org/10.1109/ICELMACH.2014.6960401).
- [62] SAE: *Testing Audi’s new e-booster reveals turbocharging’s future*. [Accessed Mar. 1, 2020]. Aug. 2014. URL: <https://www.sae.org/news/2014/07/testing-audis-new-e-booster-reveals-turbochargings-future>.
- [63] Schröder, D. ; et al.: *Elektrische antriebe-regelung von antriebssystemen [electrical drives- control of drivetrain systems]*. Vol. 2. Springer, 2009.
- [64] Šebest, M.; Hrabovcová, V.; Makyš, P.: “Optimization of the reluctance synchronous motor with barriers rotor”. In: *2016 ELEKTRO*. May 2016, pp. 374–378. DOI: [10.1109/ELEKTRO.2016.7512100](https://doi.org/10.1109/ELEKTRO.2016.7512100).
- [65] Skogestad, S.; Postlethwaite, I.: *Multivariable Feedback Control: Analysis and Design*. John Wiley, 2005. URL: <https://books.google.de/books?id=9pKznQAACAAJ>.
- [66] Steinberger, M.: “Modellbasierte Entwicklung einer Ansteuerung für eine neuartige 6-phasige Wechselrichter-topologie zur Versorgung von zwei unterschiedlichen Bordnetzspannungen im Fahrzeug”. MA thesis. Faculty of Electrical and Computer Engineering, University of Applied Science Konstanz, Oct. 2012.
- [67] Stojan, D.; Drevensek, D.; Plantić, Ž., ; et al.: “Novel field-weakening control scheme for permanent-magnet synchronous machines based on voltage angle control”. In: *IEEE Transactions on Industry Applications* 48.6 (Nov. 2012), pp. 2390–2401. ISSN: 0093-9994. DOI: [10.1109/TIA.2012.2227133](https://doi.org/10.1109/TIA.2012.2227133).
- [68] *The simulation platform for power electronic systems*. 4.3. [Accessed Mar. 3, 2020]. PLECS. 2019. URL: <https://www.plexim.com/files/plecsmanual.pdf>.
- [69] Urasaki, N.; Senjyu, T.; Uezato, K.: “A novel calculation method for iron loss resistance suitable in modeling permanent-magnet synchronous motors”. In: *IEEE Transactions on Energy Conversion* 18.1 (Feb. 2003), pp. 41–47. ISSN: 1558-0059. DOI: [10.1109/TEC.2002.808329](https://doi.org/10.1109/TEC.2002.808329). URL: <http://ieeexplore.ieee.org/document/1183711/>.
- [70] Wang, A.; Shi, W.: “A decoupling control strategy of IPM machine accounting for compensation of cross-saturation based on SVPWM technique”. In: *Proceedings of the 29th Chinese Control Conference*. July 2010, pp. 1672–1675.
- [71] Wang, L.; Jatskevich, J.; Pekarek, S. D.: “Modeling of induction machines using a voltage-behind-reactance formulation”. In: *IEEE Transactions on Energy Conversion* 23.2 (June 2008), pp. 382–392. ISSN: 0885-8969. DOI: [10.1109/TEC.2008.918601](https://doi.org/10.1109/TEC.2008.918601).
- [72] www.enginetechnologyinternational.com: *Continental reveals electrically heated catalyst*. Online. Tech. rep. [Accessed Mar. 1, 2020]. Sept. 2016. URL: <http://www.enginetechnologyinternational.com/news.php?NewsID=72899>.

-
- [73] Yamamoto, S.; Hirahara, H.; Tanaka, A., ; et al.: “Universal sensorless vector control of induction and permanent-magnet synchronous motors considering equivalent iron loss resistance”. In: *IEEE Transactions on Industry Applications* 51.2 (Mar. 2015), pp. 1259–1267. ISSN: 0093-9994. DOI: [10.1109/TIA.2014.2360962](https://doi.org/10.1109/TIA.2014.2360962).
- [74] Zhu, L.; Xue, S.; Wen, X., ; et al.: “A new deep field-weakening strategy of IPM machines based on single current regulator and voltage angle control”. In: *2010 IEEE Energy Conversion Congress and Exposition*. Sept. 2010, pp. 1144–1149. DOI: [10.1109/ECCE.2010.5617844](https://doi.org/10.1109/ECCE.2010.5617844).
- [75] Zhu, W.; Pekarek, S.; Jatskevich, J., ; et al.: “A model-in-the-loop interface to emulate source dynamics in a zonal DC distribution system”. In: *IEEE Transactions on Power Electronics* 20.2 (Mar. 2005), pp. 438–445. ISSN: 0885-8993. DOI: [10.1109/TPEL.2004.842973](https://doi.org/10.1109/TPEL.2004.842973).